VON KARMAN INSTITUTE FOR FLUID DYNAMICS
AERONAUTICS AND AEROSPACE DEPARTMENT

UNIVERSITÀ DEGLI STUDI DI ROMA
"LA SAPIENZA"
DIPARTIMENTO DI INGEGNERIA MECCANICA E AEROSPAZIALE

SAPIENZA
UNIVERSITÀ DI ROMA

Shock-Cell Noise Investigation on a Subsonic/Supersonic Coaxial Jet

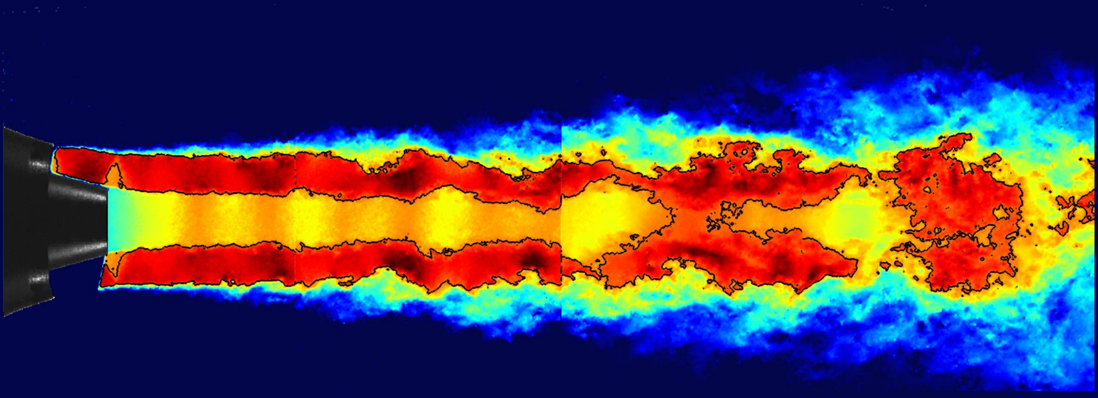

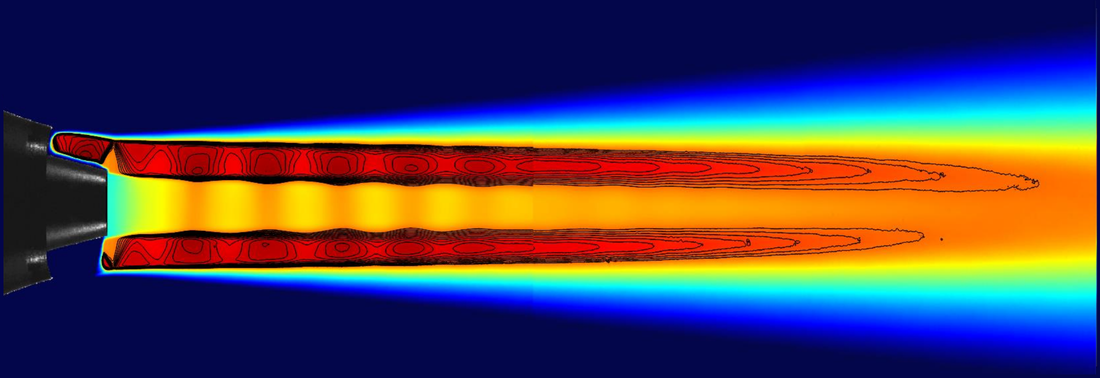

Daniel Guariglia

VON KARMAN INSTITUTE FOR FLUID DYNAMICS
AERONAUTICS AND AEROSPACE DEPARTMENT

UNIVERSITÀ DEGLI STUDI DI ROMA “LA SAPIENZA”
DIPARTIMENTO DI INGEGNERIA MECCANICA E AEROSPAZIALE

Shock-Cell Noise Investigation on a Subsonic/Supersonic Coaxial Jet

Front cover art: instantaneous velocity flow field of a subsonic/supersonic coaxial jet obtained through PIV. The black line is the M = 1 isocontour line (top). Averaged velocity flow field resulting from 1800 instantaneous fields. The black lines are Mach number isocontour lines in the range M = $[1 : 0.025 : 1.325]$ (bottom).
Back cover art: CAD drawing of the FAST facility, designed and built in the PhD framework.

Thesis presented by Daniel Guariglia in order to obtain the degree of Doctor of Philosophy in Tecnologie Aeronautiche e Spaziali, Università degli Studi di Roma “La Sapienza”, February 2017.

Promoter: Prof. Fulvio Stella (Università degli Studi di Roma “La Sapienza”, Italy)

Supervisor: Prof. Christophe Schram (von Karman Institute for Fluid Dynamics, Belgium)

Doctoral Committee:
Prof. Luciano Galfetti (Politecnico di Milano)
Prof. Christophe Schram (von Karman Institute for Fluid Dynamics)
Prof. Giovanni Bernardini (Università degli Studi Roma Tre)
Prof. Giuseppe Pucacco (Università degli Studi di Roma “Tor Vergata”)

A selection of doctoral theses published by the von Karman Institute:

Assessment of advanced numerical methods for the aero-thermal investigation of combustor-turbine interactions
(S. Vagnoli, Università degli Studi di Firenze, April 2016)

Aerothermodynamics of pre-flight and in-flight testing methodologies for atmospheric entry probes
(I. Sakraker, Université de Liege , February 2016)

Material response characterization of low-density ablators in atmospheric entry plasmas
(B. Helber, Vrije Universiteit Brussel, January 2016)

Development and applications of the Light Extinction Spectroscopy technique for characterizing small particles
(I. T. Horváth, Université Libre de Bruxelles, Ecole Polytechnique de Bruxelles, October 2015)

Numerical simulation of aerothermal flows through ablative Thermal Protection Systems
(P. Schrooyen, Université catholique de Louvain, November 2015)

Semi-analytical methodologies for airfoil noise prediction
(L. Dantas de Santana, KU Leuven, September 2015)

A full catalogue of publications is available from the library.

Shock-Cell Noise Investigation on a Subsonic/Supersonic Coaxial Jet

Keywords: Aeroacoustics, Shock-Cell Noise, Screech, Dual Stream Jet, Coaxial Jet, Supersonic Jet, Under-Expanded Jet, Facility Design.

D/2017/0238/680, T. Magin, Editor-in-Chief
Published by the von Karman Institute for Fluid Dynamics with permission.

ISBN 978-2-87516-113-0

Abstract

This work is aimed at the experimental investigation of shock-cell noise on a coaxial jet with subsonic primary stream and supersonic secondary stream. This kind of noise is nowadays an important component of the total noise emitted by aeronautic engines, particularly affecting cabin noise in cruise conditions. In this thesis, the design and commissioning of a new supersonic coaxial jet rig, at the von Karman Institute for Fluid Dynamics (BE), are discussed, with a specific focus on the design choices that have been made to obtain good flow quality, low background noise and the possibility to perform a variety of flow and acoustic measurements. The maximum achievable Mach number at the outlet of the primary (central) and secondary (annular) nozzles is equal to 2.2, with a baseline operating point being $M_p = 0.89, M_s = 1.21$. To commission the facility, several test campaigns on a supersonic single stream jet were conducted using PIV in synchronous with microphones mounted on a polar antenna. Multiple screech harmonics and subharmonics tones have been documented, showing a directivity pattern similarly to the supersonic broadband noise (BBSAN). Turbulence integral length scales have been computed using correlation functions. The average of Reynolds shear stress fields shows the presence of lobes in the jet near field which are the trace of a standing wave caused by the screech. Following the commissioning, the coaxial jet has been investigated. Multiple combinations of pressure conditions for the primary and secondary flows have been tested. Acoustic measurements have been performed in synchronous with the PIV, which has been applied for the first time in the literature on a supersonic coaxial flow. The presence of both screech and broadband noise was recorded in the majority of the tests, and a directivity pattern was recognized for the latter. For a certain pressure conditions, the screech tone naturally disappeared. Experimental evidences suggest this may be related to a complex shock interaction occurring at the end of the primary nozzle. A simple method to infer the screeching dynamics from the spatial correlation functions was proposed. The correlation suggests the presence of a pulsation (or breathing) motion of the internal jet, which is cause/effect of the screech. A second screech mode was also retrieved from acoustic data, for which, the correlation functions suggest the presence of a sinusoidal motion of the internal jet.

Acknowledgements

The “End of the beginning!”, this is how I would like to remember this moment in the coming years. And it was a quite looooong beginning...

For the people who know me a little bit, you know my difficulties in remembering names of people met just few days before. So, you can image how challenging is for me to try to thank everybody. But you also know, that I love challenges! ☺

I will try to do my best in remembering all of you, but please, if you don’t find your name here, don’t be offended. You just have a super forgetful friend... ☺

So let’s start with the unforgettable ones: the ones who loaned me money, without asking a refund date! And... no, Mom and Dad, you have a specific paragraph already! ☺☺☺

The European Commission is gratefully acknowledged for the financial support, provided in the framework of the FP7 Marie Curie ITN project AeroTraNet2 (Grant Agreement no 317142).

The von Karman Institute for Fluid Dynamics is gratefully acknowledged for the financial support in the realization of the FAST facility and for the PhD Fellowship.

Ok, fiuuuuu, now I feel much more relaxed. So let’s see, who will be the first one under the spotlight? Well, of course... the best aeroacoustic salsero in Belgium! My mentor: Prof. Christophe Frédéric Schram! Thank you so much for taking me with you. I am just sorry I was not able to teach you all my secret Napolitan steps... ☺ Jokes aside, it has been really a pleasure and a honor to study with you. I know it was tough, but I think, at the end, you were able to put something in this stubborn head, right?

Number two in my list, infinite thanks to my promoter in “La Sapienza”, Prof. Fulvio Stella! Thank you so much for assisting me from Rome, always with nice words and sympathy.

Thanks to my dear comrades in this cruise on the AeroTraNet2 ship: Alessandro, Carlos, Carina, Danilo, Elena, Francisco, Ilaria, Lior, Mohsin, Shreyas and Tobias. We navigated quite well together, I think. Also in hard times, with cold winds blowing against us, we stood together to get warmer, a lot warmer! ☺

Thanks so much also to the carpenters: Aldo, Alessandro, Choi-Hong, Christophe A., Christophe S., Edward, Guillome, Mario and Roberto. You built a very strong ship! I wish you all the best for your next ones!

What to say about VKI people? Dear friends, thanks so much to all of you for your support, and patience.
The fantastic aeroacoustic group, past and present: Andreas, Cansev, Gabriele, Julien, Korcan, Leandro, Lionel, Nicolas B., Nicolas V., and the students that I had the pleasure to follow during this adventure: Alejandro, Alessio and Nicolas C.. I wish to all of you guys all the best for your lives and your careers!
The wonderful professors, always ready to give me advices and support in those years: Fabrizio, Herman, Jeroen, Maria Rosaria, Olivier, Sergio, Tamas, Thierry and Tony. Thank you so much for lending me your experience.
The research engineers: Gertjan, Laura, Mathieu, Philippe and Sebastien. Thank you so much for helping me in solving all the small and big issues that occurred in the labs.
Previously I wrote: thank you for the patience, this is certainly referred to all the technical divisions of the VKI who supported my work (and tolerated my disastrous French!). From the Computer Center: Laurent, Natalie, Olivier, Quentin and Raimondo 'the Boss'. From the Drawing Office: Didier, Jean-Jacques and Michel. From the workshop: Christophe, José, Maurizio, Sebastien, Terence, Valentin, Vincent, Walter, Xavier and Yves. The Electronic Lab (I can't remember how many wires did you repaired...): Pierre and Remy. The Library: Christelle and Evelyne. Dears, how many papers I asked you... Thank you so much. The Accounting and the Secretariat: Bernard, Christian, Claire, Eddy, Eric, Dominique, Kris and Simone. The Photolab and the Canteen: Bintou, Claude, Houda, Maud and Miguel.
All the VKI technicians! And in particular: Alain, Antony, Pascal, Patrick and Pierre. You know well that without your hands I would not have completed this job. Thank you for all the expertize that you transmitted to me!
Finally, all my remaining friends! I really want to cite all of you, because you absolutely deserve it! So in the future years, when I will read again these pages, I will remember you! And, trying to not forget anybody, I'm reading the VKI phonebook! So, if your name is missing, you have to complain with the Secretariat, not with me! ☺☺☺. Mohamed, Giacomo, Zuheyr, Alejandro, Federico, Bruno, Georgios, Aurelie, Fabio B., Sophia, Bogdan, Florian, Christopher, Julien, Nicolas, Cis, Giulia, Claudia, Charline, Clara, Sara, Gian Luca, Guillaume, Bernd, Imre, Isil, Zdenek, Lilla, Delphine, Aude, Damien, Vincent, Silvania, Roberto, Davide, Ignacio, Miguel, Fernando, Laura, Fabio P., Jerome, Bayindir, Maria Teresa, Torsten, Alessia, Chiara, Orkun, Marco, Paride, Erik, Alessandro, Jorge, Ertan, Vincent, Alan and Agustin.

To my dear ex-flatmates Alessandro, Camille, Fabrizio, Philippe, I totally enjoyed the period that we spent together fighting against the landlady! ☺ We passed so many good moments, thank you for having shared a part of your path with me!

To Gianluca, Bahar, Paola and Gilles, I want to thank you for all the beautiful moments we spent together. All the delicious dinners, the cinema nights, and the matches at 7 Wonders!

Ai miei carissimi amici a Napoli: Chiara, Egidio, Umberto, Chiara, Federica e Piera! Anche se ci vediamo anche solo una o due volte all'anno, è sempre festa (proprio per definizione... ce verimm sulament ne' period e' fest... ☺)!

A tutta la mia famiglia (inclusa quella acquisita, eh ☺), vi voglio un mondo di bene. Potrei stare su un altro pianeta, ma questi sentimenti per tutti voi non cambieranno mai!

Grazie a mamma e a papà per avermi fatto così be... hem, benpensante! ☺ Vi voglio un mondo di bene, non scordatelo mai. Per i miei fratellini adorati. Ettoriño grazie per le chiacchierate, e per tutti i bellissimi libri che mi regali, mi hanno donato tanti attimi di gioia ed evasione. Per favore non smettere mai, che sennó se aspetto a Stefania sto fresco... ☺. Lolloló, lo sai, anche se a volte sono severo, è perché ti voglio davvero bene, e voglio che tu diventi un grande scienziato! Non come tuo fratello (a libera interpretazione a quale dei due mi riferisco ☺)!

Per Stefy, sei tu il traguardo più importante che ho raggiunto in questi anni. La fonte della mia forza e determinazione. Queste pagine non avrebbero senso, e probabilmente non esisterebbero nemmeno, senza di te. A te vanno tutti i miei ringraziamenti, per avermi amato, supportato (e sopportato) per tutto questo tempo. Grazie.

Contents

List of Figures

List of Tables

List of Symbols

Bibliography

Acronyms

A/D	Analog to digital
AeroTraNet2	Aeronautical Training Network 2
BBSAN	Broad-Band Shock-Associated Noise
BLOPWL	Band Limited Overall Sound Power Level
B&K	Brüel & Kjær
CFD	Computational Fluid Mechanics
DNS	Direct Numerical Simulations
FAST	Free jet AeroacouSTic laboratory
HBPR	High By-Pass Ratio
LDV	Laser Doppler Velocimetry
LES	Large Eddy Simulations
LIF	Laser Induced Fluorescence
NI	National Instruments
NPR	Nozzle Pressure Ratio
OASPL	Overall Sound Power Level ref. 10^{-12} W
PIV	Particle Image Velocimetry
PSD	Power Spectral Density
RMS	Root Mean Square
SCN	Shock-Cell Noise
SPL	Sound Pressure Level ref. $2 \cdot 10^{-5}$ Pa
SWL	Sound Power Level ref. $2 \cdot 10^{-12}$ W
VKI	von Karman Institute

Roman symbols

d	distance	m
D	diameter	m
f	frequency, focal length	Hz
L	length	m
T	temperature	K
p	pressure	Pa

Greek symbols

α	angle	^{o}
λ	wavelength	m
ρ	density	kg/m^3
σ	standard deviation	
θ	angle	^{o}

Subscript

n	nozzle
p	primary nozzle
s	secondary nozzle
sc	shock-cell
1	relative to nozzle 1
2	relative to nozzle 2

Preamble

This work is aimed at the experimental investigation of shock-cell noise, being nowadays an important component of the total noise emitted by aeronautic engines, particularly affecting cabin noise in cruise conditions. In this thesis, the design and commissioning of a new coaxial jet rig, with supersonic capability, are discussed, with a specific focus on the design choices that have been made to obtain good flow quality, low background noise and the possibility to perform a variety of flow and acoustic measurements. The maximum achievable Mach number at the outlet of the primary (central) and secondary (annular) nozzles is equal to 2.2, with a baseline operating point being $M_p = 0.89, M_s = 1.21$. Such conditions are not far from those simulated by Miller & Morris in [53]. Many studies are present in the literature on the shock-associated noise[70, 102, 33, 94, 57, 58, 93, 90]. These models have been applied with fair success, mostly to single stream supersonic jets, and the objective of this facility is progress further in complexity with a coaxial jet with subsonic primary and supersonic secondary flows. It should be stressed at this stage that the primary flow is unheated, leading to a reversed velocity profile to yield the desired Mach numbers in each stream. Nevertheless it is still a valuable benchmark for physical understanding and the validation of theoretical or numerical models because of the annular shock-cell pattern confined between two shear layers.

Motivations

The noise inside the cabin of an aircraft has become one of the most challenging issues for the aircraft manufacturers since it represents a threat for the passengers comfort and hardens the working conditions of the cabin crew. During cruise flight, which represents the longest segment of the overall flying profile, cabin noise is contributed externally by the turbulent boundary layer and the noise produced by the propulsive system [40]. Currently, most of the commercial aircraft are propulsed by High By-Pass Ratio (HBPR) engines because of their higher efficiency. At cruise, the fan stream of these engines operates in supersonic underexpanded conditions. In these circumstances, the flow adapts to ambient pressure through a shock cell pattern at the outlet of the nozzle [40].

The noise produced by the interaction of this shock-cell system with the turbulent structures of adjacent shear layers impinges on the fuselage, becoming one of the main sources of noise inside the cabin. For this reason, since the seminal study of Harper-Bourne and Fisher in the 70s [34], the noise originated from this interaction, generally called Shock-Cell Noise (SCN), has become the main focus of attention of a large number of researches. Nevertheless, there is not a clear explanation of the physical mechanisms involving this noise generation yet.

Typically, aircraft cabin noise is controlled by adding acoustic treatment to the cabin walls, which implies an increase of weight and a reduction on the payload of the aircraft. Cabin noise reduction through source control would therefore be a more attractive solution. Different methods have been proposed but none of them represent a ultimate solution since all have major drawbacks. The mechanical modification of the nozzle lips via tabs or chevrons suppose loss of engine thrust [121] and the injection of air or water at the nozzle exit does not guarantee a significant noise reduction [35]. Other technologies like the distributed exhaust nozzle concept or the nozzle misalignment are indeed effective ways to control and suppress jet noise but they are hard to implement at full scale [17].

Furthermore, since the physical mechanisms involving the production of the SCN are not yet understood, the models available in the literature have still limitations, such the lack of accuracy in the predictions and the strong dependence on empirical coefficients. These deficiencies prevent the application of the models to complex geometry problems usually found in the industry. Most of the researches in the literature have been focused on single stream jets, and therefore there is still a lack of experimental databases available for coaxial nozzles, which are representative of the modern turbofan engines. The Free jet AeroacouSTic facility (FAST) in the von Karman Institute, which allows the research of SCN on single and coaxial jets, has been commissioned as a part of this investigation.

Framework

This PhD thesis is enclosed in the AeroTraNet2 Project, a Marie Curie Action of the European Commissions 7th Framework Programme (FP7) between several laboratories and universities in Europe. The project aims at generating a ready to use model for shock-cell noise characterization. Six academic partners collaborate to address the common objective of modeling shock-cell noise in a wide-body aircraft engine configuration, from private sector partner Airbus France, by shock-tolerant numerical modeling for under-expanded jets (University of Leicester), large eddy simulations for turbulent jets with weak shocks (CERFACS), advanced flow-noise correlations (Università degli Studi Roma Tre), jet and near-field noise experiments (von Karman Institute for Fluid Dynamics), reduced-order modeling and flow control (Institut de Méchanique des Fluides de Toulouse, IMFT-INP), and advanced laser-based measurement techniques (the Italian Ship Model Basin, CNR-INSEAN). Knowledge output is synthesized through a dedicated knowledge capturing program by the University of Greenwich, which is used by private sector partner General Electric. In AeroTraNet2, the research output becomes itself object of knowledge management research, which is a novel supra-disciplinary element. AeroTraNet2 is the successor of AeroTraNet project which studied the unsteady flow in airframe fuel vents.

Aims of the Project

In the framework of the AeroTraNet2 project, the main goal is to characterize a subsonic/supersonic coaxial jet with flow field and acoustic measurements, at different test conditions. The database acquired will be used by partners for data post-processing and for the validation of aeroacoustic models based on CFD simulations. Measurements using microphones, Schlieren, Background-Oriented Schlieren (BOS), and Particle Image Velocimetry (PIV) have been considered to provide a comprehensive experimental database. In order to extract useful information on the shock-cell noise generation mechanisms, post-processing techniques such as wavelets, proper orthogonal decomposition, causality correlations and conditional techniques have been reasoned. The design and construction of a new experimental facility at the von Karman Institute (VKI), constituted also a challenging engineering goal. The key objectives of this study have been :

a) Outline a cost efficient and flexible configuration for a new facility to be installed at VKI.

b) Design the nozzles and perform a numerical simulation of the flow, using a commercial software, to validate the geometry.

c) Design a coaxial silencer and perform an acoustic simulation, using a commercial software, to assess its acoustic properties.

d) Supervise the detailed design and installation of the facility, including the procurement of technical equipment, sensors and the software control suit.

e) Commission the facility, using a supersonic single stream jet as benchmark.

f) Perform several test campaigns on a supersonic single stream jet, using PIV synchronized with microphones in the far-field, on two different nozzles. Analyze the flow fields and the acoustics, and compare with analogous results.

g) Perform for the first time a test campaign on a subsonic/supersonic coaxial jet, using PIV synchronized with microphones. Analyze the flow and acoustic measurements.

h) Perform an exploratory acoustic test campaign on the subsonic/supersonic coaxial jet variating the pressure condition in both primary (internal) and secondary (external) flow.

i) Collapse the Mach number axial profiles of the dual stream jet using a new scaling law.

j) Infer the screech modes of the dual stream jet from velocity autocorrelation functions based on PIV flow fields.

Outline

The manuscript is structured as follows. Chapter 1 introduces the reader to the dynamics of supersonic jets and the physics behind supersonic jet noise. Chapter 2 illustrates the design process and main characteristics of the FAST facility. Results of the CFD simulations of the coaxial jet, as well as the prediction of the silencer acoustic performances, are presented. Chapter 3 and Ch. 4 reports the results experimental investigation of an under-expanded single and dual stream jet respectively, obtained with PIV and microphones. In Chapter 5, the screech modes of both the single stream jet and the coaxial jet are inferred from velocity autocorrelation functions based on decorrelated PIV images. Last, the conclusions and perspectives of this work are presented in Chapter 6.

Chapter 1

Introduction

In this chapter, an introduction to the physics and acoustics of supersonic underexpanded jets is given. Single stream jets have been studied extensively in the past, due to their relatively simple way to be simulated and compared experimentally. Supersonic coaxial jets are far more complex, involving the presence of dual flows interaction, geometrical and scaling issues, difficulties to compare with analogous researches. All characteristics that limited aeroacoustic studies in the past, although they are largely used in modern commercial aviation.

1.1 Supersonic Underexpanded Jets

A jet is working in supersonic underexpanded condition when the pressure at the exhaust of the nozzle is higher than the ambient pressure. Under these circumstances, the adaptation of the flow to ambient conditions is accomplished by means of expansion and compression waves that trail downstream of the nozzle lip. Subsequent multiple internal reflections at the boundary of the jet produce a characteristic system of shock cells, as shown in Fig. 1.1.

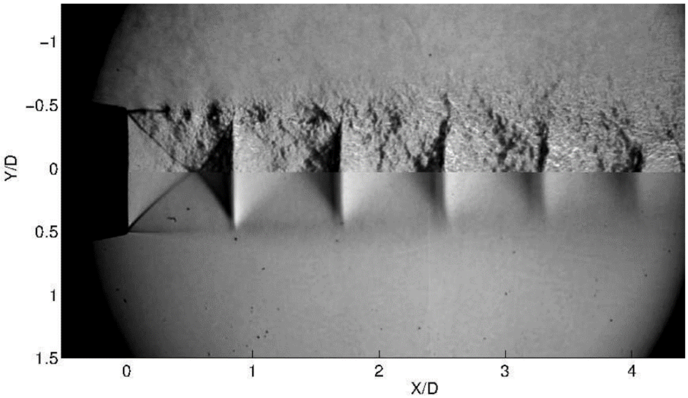

Figure 1.1: Schlieren visualization of an under-expanded jet operated at NPR = 2.5 : (top half) instantaneous and (bottom half) averaged view [78].

For a convergent nozzle, this condition is achieved when the Nozzle Pressure Ratio (NPR), defined as the ratio of total to ambient pressure, is higher than $p_0/p_\infty = 1.89$. Under this circumstance, the Mach number at the throat of the nozzle is equal to 1 and the mass flow is driven only by the NPR value, which controls the pressure mismatch at the exhaust of the nozzle. The fully expanded condition refers to a jet which would have expanded isentropically through a convergent-divergent nozzle. This label is widely used to compare different jets quantities. The fully expanded Mach number is defined by Equation 1.1.

$$M_j = \sqrt{\frac{2}{\gamma - 1}\left[\left(\frac{p_0}{p_\infty}\right)^{\frac{\gamma-1}{\gamma}} - 1\right]} \tag{1.1}$$

where p_0 and p_∞ are the total and atmospheric pressures, respectively, and γ is the heat capacity ratio.

The fully expanded jet exhaust velocity is thus derived as:

$$U_j = c_j\, M_j \tag{1.2}$$

where the fully expanded velocity of sound c_j is equal to $\sqrt{\gamma R T_j}$.

T_j and ρ_j are the fully expanded jet temperature and density, respectively, obtained from the isentropic relations:

$$T_j = T_0\left(1 + \frac{\gamma - 1}{2} M_j^2\right)^{-1} \tag{1.3}$$

$$\rho_j = \rho_0\left(1 + \frac{\gamma - 1}{2} M_j^2\right)^{\frac{-1}{\gamma-1}} \tag{1.4}$$

An important quantity used to compare different jets is the off-design parameter β, defined in Equation 1.5.

$$\beta = \sqrt{M_j^2 - M_d^2} \tag{1.5}$$

where M_d is the nozzle design Mach number. For all the convergent nozzles, $M_d = 1$, while for convergent-divergent nozzles $M_d > 1$. The parameter β gives a measure of how much the jet is imperfectly expanded. When the flow is underexpanded, the jet plume diameter is actually bigger than the diameter of the nozzle D. Tam and Tanna [95] derived an expression to calculate the fully expanded diameter of the jet D_j from the condition of conservation of mass flux:

$$\frac{D_j}{D} = \left[\frac{1 + 0.5(\gamma - 1)M_j^2}{1 + 0.5(\gamma - 1)M_d^2}\right]^{\frac{\gamma+1}{4(\gamma-1)}}\left(\frac{M_d}{M_j}\right)^{1/2} \tag{1.6}$$

1.1.1 Shock-Cell Structure

The underexpanded condition at the exhaust of the nozzle yields the flow to adapts to the ambient pressure through series of expansion fan and oblique shocks, originating a shock-cells pattern which is shown in figure 1.2. The pressure mismatch leads to expansion fans attached to the lip of the nozzle. They are refracted at the jet mixing layer as compression waves, which collapse forming an oblique shock. Both oblique shocks, one corresponding to the upper part of the jet and the other to the lower part, will meet at the interception point P. This point indicates the end of the expansion zone in the cell. The oblique shock will impinge on the jet boundary at the reflection point Q, marking the end of a cell.

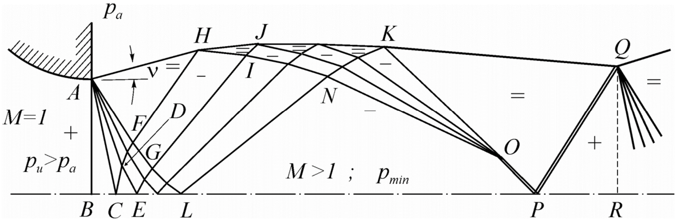

Figure 1.2: Schematics of the shock-cell structure. [16]

1.1.2 Models for the ShockCells

The modelling of the shock-cell associated perturbations is of primary importance for SCN models. The periodic succession of expansions and compressions generates an almost periodic, steady pattern of fluctuations that defines the main characteristics of the acoustic emission of imperfectly expanded jets. The first model dates back from Prandtl [71] later reworked by Pack [60], in the following simply referred to as the Prandtl & Pack model. In their work they proposed to model the shock-cell structure of slightly imperfectly expanded jets as small-amplitude disturbances superimposed on a perfectly expanded base flow, with this being represented as a uniform flow column bounded by a vortex sheet to reproduce shear layers. For a given pressure imbalance at nozzle exit $\Delta p = p_e - p_\infty$, with p_e the exhaust pressure, the linear, inviscid solution for shock-cell pressure perturbations was given in the form of a sum of shock-cell modes as

$$\frac{p'}{p_\infty} = \sum_{n=1}^{\infty} A_n \frac{1}{2} \left\{ e^{ik_{s_n}x} + e^{-ik_{s_n}x} \right\} \tag{1.7}$$

with k_{sn} being the wavenumber of the $n-th$ mode, calculated as:

$$k_{s_n} = \frac{2\mu_n}{D\beta} \tag{1.8}$$

where μ_n is the n-th zero of the $zero-th$ order Bessel function J_0, and

$$A_n = \frac{2\Delta p}{\mu_n p_\infty} \tag{1.9}$$

the amplitude coefficient of the $n-th$ mode. One comment can be readily done on this model: the mode wavenumber is a function of $k_{s_n} \propto \beta-1$ and the amplitude coefficient scales as $A_n \propto \Delta p \cong \beta^2$: an increase of the NPR hence generates, as expected, a stretching of the shock-cell and a strengthening of its fluctuations. The Prandtl & Pack models solution is however subject to the main limitation of the vortex sheet approximation. This is valid only in the near nozzle region as the jet shear region is relatively thin, but loses of accuracy further downstream. It is further not capable to reproduce the turbulence smoothing effect on the shock-cell fluctuations and these are represented as periodically oscillating quantities. At first approximation, however, the SCN source extension can be considered as of limited extent for that the approximation of constantly oscillating shock-associated flow quantities is still valid. The Prandtl & Pack model can be, then, still be considered as a useful tool to retrieve the wavenumber value and amplitude coefficient of the different modes that, can be introduced in noise models to reproduce the shock-cell component.

1.1.3 Shock-Cell Length

The cell length has a clear implication in SCN as it defines implicitly the frequency of its main peak. It is defined as the axial distance between two consecutive identical component of the shockcell (i.e. two compressions end-tips), and stretches as the off-design condition is increased. An estimation of its dimension was already obtained by the Prandtl & Packs model Equation 1.7, which first modes wavenumber,

$$k_1 = \frac{2\mu_1}{D_j \beta} \tag{1.10}$$

obtains, with $\mu_1 = 2.40483$, an average cell length of:

$$L_{sc} = \frac{2\pi}{k_1} \approx 1.306 D_j \beta \tag{1.11}$$

Harper-Bourne & Fisher [3] later proved the dependence by the jet diameter and off-design condition by physically measuring the average shock-cell length in a number of experiments, obtaining a similar relationship in the form of:

$$L_{sc} = kD\beta \tag{1.12}$$

where k is a fit coefficient (retrieved as k = 1.11) and D is the nozzle physical diameter (oppositely to Prandtl & Packs model discussed above which uses the fully expanded diameter D_j). In Harper-Bourne following publications, i.e. [34], the value of this fit coefficient was slightly revised, indicating that most probably the shock-cell length can be sensible to the experimental setup. Despite this, Equation 1.12 is usually found to give good first-order predictions for the average shockcell length. More than the average length also the actual cells length is important, as downstream in the plume the shock-associated fluctuation are smoothed out by turbulence effect and they tend to shorten. Neither Prandtl and Packs model nor Equation 1.12 can account for this aspect. Harper-Bourne [34], based on his experimental measurements, provided an empirical formulation for the cell shortening in the form of

$$L_n = L_1 - (n-1)\frac{\delta L}{L_1} \tag{1.13}$$

with L_n and L_1, respectively, the $n-th$ and first cell length. By fit of experimental data, the shortening factor was expressed as a percentage of the first cell length:

$$\frac{\delta L}{L_1} \simeq 6\% \tag{1.14}$$

to say that downstream cell shortens progressively of about the 6% of the first cell length. About this value authors argue that it shall be dependent on the degree of screech, which may increase the jet mixing rate and hence shock-cell smoothing, even if no physical justification on the proposed value was provided.

1.1.4 Mixing Layer

The mixing layer comprises an annular region surrounding the potential core of the jet, which is dominated by shear flow.

In addition to the shock cell pattern, the turbulent field also plays a role on the SCN. As Savarese [78] indicated, from all the different components contained in the turbulent field of the jet there is only one relevant from an acoustic point of view since only they present spatial-time coherence, the so-called wavepackets. Colonius *et al.* [18] argued that these advecting disturbances have a nearly constant convection velocity and their coherence over radial and axial length scales exceeds the integral scales of the turbulent field. Veltin and McLaughlin [110] derived the next relation between the convection speed of the wavepackets U_c and the off-design parameter from their measurements:

$$\frac{U_c}{U_j} = 0.75 - 0.0353\beta^8 - 0.008\beta^4 \tag{1.15}$$

It has also been found that wavepackets grow exponentially in the axial direction, followed by saturation and decay. Savarese [78] found through his experiments in supersonic single jets that the maximum amplitude of this disturbances is located between the third and the fourth shock cell.

1.2 Acoustics Of Supersonic Underexpanded Jets

Noise from underexpanded jets has two major sources: jet mixing noise and shock-cell noise. The former is due to the dynamics of the convected turbulent structures within the shear layer of the jet. This source dominates the low frequency acoustic spectrum and it can be considered as directional since it is mainly propagated downstream. The latter, which is the focus of this study, is due to the interaction between this downstream propagating turbulence structures and the shock cells in the jet plume [34] and it dominates the high frequency acoustic spectrum as it was pointed out by Tanna [102].

The typical acoustic footprint of a imperfectly expanded supersonic single jet is shown in figure 1.3. The two typical acoustic features of the SCN, broadband shock cell noise and screech tone, have been highlighted. In the following subsections the main characteristics of this two features will be briefly explained.

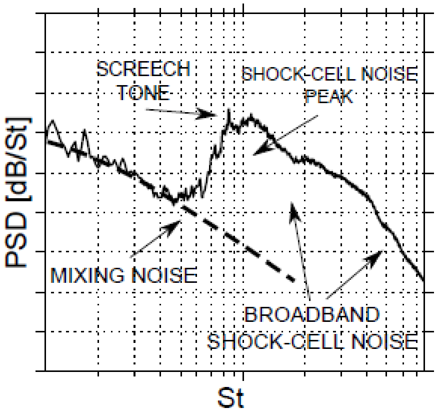

Figure 1.3: Example of jet noise spectrum characteristics. Savarese [78].

1.2.1 Broadband Shock Cell Noise

BBSAN was first identified by Harper-Bourne and Fisher [34] in 1974. They found that, in terms of overall intensity, the SCN is omnidirectional and is proportional to the fourth power of the off-design parameter β:

$$I \propto \beta^4 \tag{1.16}$$

For $\beta \leq 0.5$ the shock cells are weak and the jet mixing noise mechanism becomes the main contributor to the intensity of the noise, so the Lighthill's M^8 law is recovered [48]. Tam and Tanna [96] pointed out that the relation between the shock cell strength and the intensity of the BBSAN is also valid for dual stream jets. In their experiments they found that although the fan stream was supersonic, when the core stream became slightly supersonic no periodic shock cell pattern arose in the outer stream. The acoustic measurements showed that under that condition the BBSAN is led to a minimum.

Harper-Bourne & Fisher [34] also identified a broad BBSAN peak in the acoustic spectrum (Fig. 1.3), which has a directional character. The peak frequency decreases as the listener moves from downstream to upstream angles. They retrieved a peak frequency f_p prediction formula modeling the BBSAN by a phased array of monopole sources:

$$f_p = \frac{U_c}{L_{sc}(1 - M_c \cos\theta)} \tag{1.17}$$

where $M_c = U_c/c_\infty$ is the convective Mach number, c_∞ is the ambient speed of sound and θ is the angle with respect to the nozzle axis, where $\theta = 0^o$ is downstream direction. This relation is in agreement with experimental observations by Andr [2] reported in Fig. 1.4, by adjusting the value of the mean shock-cell spacing L_{sc}.

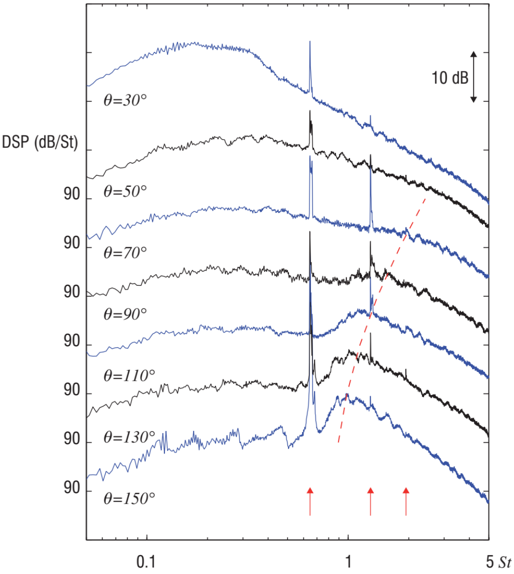

Figure 1.4: Narrow-band acoustic spectra of $M_j = 1.10$ jet, measured at r /D = 53.2 as a function of the Strouhal number St, and for different angular positions. The angle θ is taken from the downstream jet axis. The red dashed line corresponds to relation 1.17 and the red arrows indicate the fundamental screech frequency and its two first harmonics. From Bailly *et al.* [6]

1.2.2 Screech Tone

The presence of the shock cell pattern is also the cause of a tonal noise called screech. This tone was first studied by Powell [70] in 1953. He explained that the tone is generated because of a feedback loop involving non-linear instabilities originated at the nozzle lip region. These become unstable as they propagate downstream, and generate acoustic radiation as they interact with the shock cells. The acoustic waves reach the nozzle lip region, where they trigger new instabilities in the flow, closing the loop. He derived a simple formula to compute the screech frequency f_s based on a phased monopole sources model:

$$f_s = \frac{U_c}{L_{sc}(1 + M_c)} \tag{1.18}$$

where U_c is the convective velocity of the hydrodynamic fluctuations, L_{sc} is the average shock-cell length, and M_c is the Mach number of the convected hydrodynamic fluctuations. It is important to highlight that screech is rarely found in commercial jet engines.

A jet undergoing screech exhibits various oscillation modes [72]. These modes have already been characterized on the basis of the nature of the instabilities involved in the generation of the feedback loop. The already known modes are axisymmetric (A1, A2), sinuous (B), and helical (C). The difference between mode A1 and A2 is that the first one is stable with a single screech frequency, while for the second one the mode is unstable and the screech frequency is changing over time. Mode D initially resisted classification, but successively was identified as sinuous mode and called mode (b). A visual example of symmetric and helical mode is provided in Fig. 1.5.

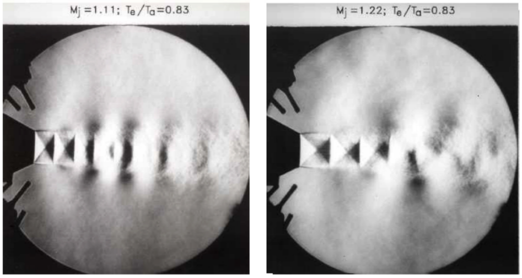

Figure 1.5: Schlieren visualization of a screeching jet : (left) axisymmetric mode and (right) helical mode, from Seiner [82]

A comparison of the data from various researchers on the wavelength of the screech stages was provided by Norum[56] and is shown in the figure 1.6. Two screech modes may be recorded at the same time for pressure conditions laying in the boundary region between the two modes, although it is not clear if the jet is swapping from one mode to the other one, or the two are coexisting.

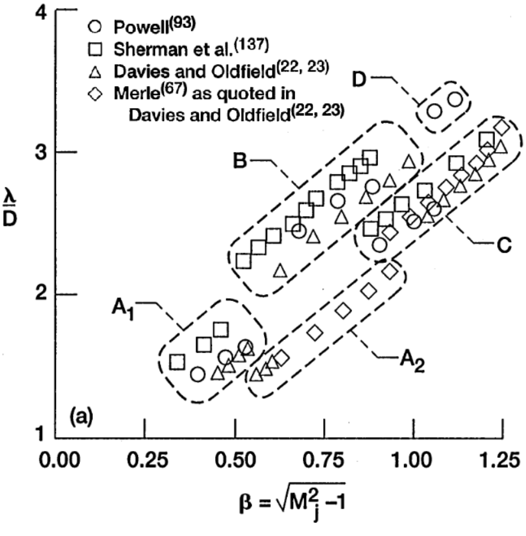

Figure 1.6: Modes of the screech tone. From Norum[56]

Recently, André *et al.* studied the flight effects on screech in supersonic jets [3]. They used an azimuthal array near the nozzle lip of the co-flow jet in order to identify changes in the screech modes. For the sinuous mode (B) they identified two azimuthal opposite components at slightly different frequencies, leading to a rotation of the oscillation plane. Adding the co-flow, this rotation was suppressed. For the other sinuous mode (b), instead, the oscillation plane is initially fixed, but, increasing the co-flow velocity, the oscillation plane started to rotate, and, keeping increasing, it stabilized again.

Westley and Woolley [115] showed that disturbances accelerated between shocks and decelerated as they approached a shock. Several factors could be responsible for the acceleration and deceleration of the instability wave. First, the shock/expansion train in an imperfectly expanded jet produces an alternating convergent and divergent flow boundary. Since the supersonic mean flow accelerates and decelerates as it passes by the convergent divergent 'channel' it is reasonable to expect that the disturbance velocity would also do the same. Second, shocks significantly modulate the velocity fluctuation amplitudes as it was shown in the experiments of Raman *et al.*[74].

An empirical prediction formula for circular jets was proposed by Ahuja [51], based on previous experiments. He suggested two equation to determine the frequency of the stable modes screech tones, such as the axisymmetric (A2) and the helical (C) modes. His formula are given in Equation 1.19, valid for $1 \leq M_j \leq 1.35$ and Equation 1.20, valid for $1.2 \leq M_j \leq 1.8$. It is important to note that the equations take into account the effect of the temperature in the frequency of the screech tone.

$$\frac{fD_j}{U_j} = 1.25\frac{0.63}{1.1(M_j^2-1)^{1.3}}\left[1+0.63M_j\left(1+\frac{\gamma-1}{2}M_j^2\right)^{-1/2}\sqrt{\frac{T_\infty}{T_0}}\right]^{-1} \tag{1.19}$$

$$\frac{fD_j}{U_j} = \frac{0.615}{1.1(M_j^2-1)^{1.3}}\left[1+0.615M_j\left(1+\frac{\gamma-1}{2}M_j^2\right)^{-1/2}\sqrt{\frac{T_\infty}{T_0}}\right]^{-1} \tag{1.20}$$

A reasonable agreement between his equations and experimental data is found, as it can be seen in Fig. 1.7.

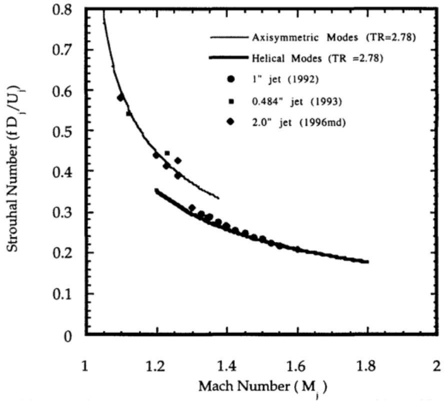

Figure 1.7: Prediction of the screech frequency. From Ahuja[51]

There are two analogies between screech and BBSAN. First, both of them take place only when a shock-cell structure arises from the jet. Second, both are produced by the interaction of the large-scale turbulent structures with the shock-cells. The difference between screech and BBSAN is that first is amplified by the aforementioned feedback. As Raman [72] explained, when shock noise from an array of shock-cells combines constructively and results in strong upstream radiation of sound that closes the resonant loop, the result is screech. Contrary to the BBSAN, instead, the screech frequency is independent of the location of the observer. Tam *et al.* [89] showed that both features could be closely related, since screech could be considered as a limiting case of broadband shock noise. Nevertheless, there are still many questions to be answered regarding this relation.

1.2.2.1 Near Field Standing Wave

To close the screech feedback loop, it is required the sound-generated downstream to propagate to the nozzle lip (feedback) and couple with the hydrodynamic disturbances in the shear layer (the process of receptivity). Feedback and receptivity are clearly important because although similar processes produce screech and broadband noise, it is possible to predict the amplitude of the latter but prediction of the former remains an elusive goal. A description of the acoustic near field is very crucial for understanding of feedback and receptivity processes.

Westley and Woolley [118][117][116][115] were the first to document details of the acoustic near field. The distinctive radiation pattern displays sound pressure levels that vary from 160 dB near the jet boundary to about 130 dB at a radial distance of 6D from the jet. Their data also illustrate the emergence of a standing-wave pattern. They suggested that the standing wave may result from the interaction between downstream-propagating hydrodynamic waves and upstream propagating acoustic waves. Further, reflection from an upstream flange could also produce an acoustic-acoustic standing wave that may also influence the former type of standing wave.

It should be noted that standing-wave formation is not specific to a shock-containing screeching jet. Lepicovsky and Ahuja [47] showed that a standing wave exists in the near field even for a subsonic edgetone situation. Westley and Woolley's [118][117][116][115] data also show lobes of high sound pressure levels between shocks that extend out normal to the jet with the strongest maxima occurring at shocks 3 and 4. Westley and Woolley [119] also documented the instantaneous pressure distributions in planes perpendicular to the jet axis that displayed the spiraling motion of the near-acoustic field during helical mode screech. Detailed phase-averaged measurements by Panda [61] show the downstream propagating hydrodynamic disturbances as well as upstream- and downstream-propagating acoustic waves for a round jet at $M_j = 1.19$ (Fig. 1.8).

In a movie based on Panda's data, the upstream-propagating acoustic waves exhibited a pause-and-go feature as they negotiated the standing wave. Similar data on the phase-averaged acoustic near field was reported by Raman *et al.* [73] for a rectangular jet (aspect ratio = 5, $M_j = 1.8$) with an upstream reflector located at a position that maximized screech. Panda [61] suggested that a standing wave pattern is expected with a resultant wavenumber $k_{sw} = k_s + k_h$.. If k_h is associated with the hydrodynamic fluctuations of wavelength $\lambda_h (k_h = 2\pi/\lambda_h)$, k_s with sound waves of wavelength λ_s, and k_{sw} with the standing waves of wavelength λ_{sw}, then one can represent L_{sw} as $1/L_{sw} = 1/\lambda_s + 1/\lambda_h$. Since $\lambda_s = c_\infty/f_s$ and $\lambda_h = u_c/f_s$, c_∞ is the ambient speed of sound, f_s is the screech frequency and u_c is the convective speed of the hydrodynamic disturbances, a frequency formula can be written that resembles Powell's [70] equation with the wavelength of the standing wave replacing the shock-cell length in Powell's original formula (equation 1.18).

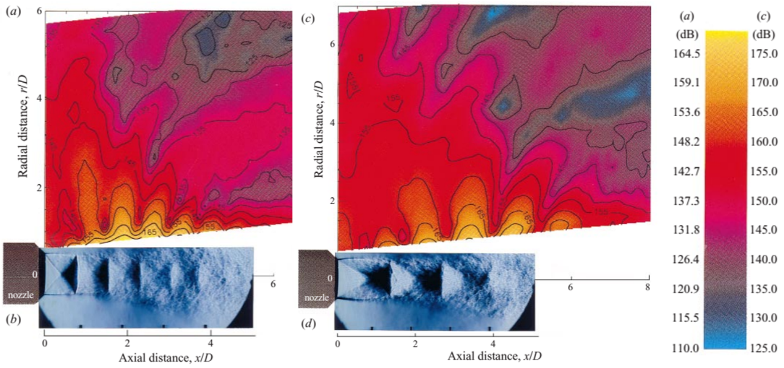

Figure 1.8: RMS pressure fluctuations at screech frequency and schlieren photograph for $M_j = 1.19$ and (c), (d) $M_j = 1.42$ jets. The superimposed contour levels are at 5 dB intervals. From Panda[61]

Panda *et al.* [62] demonstrated that the above relationship also applies to rectangular and elliptic jets.

1.2.3 Shock leakage theory

Although this phenomenon has not been investigated in this thesis, this theory is worthy of interest, and therefore it is briefly described in this section. Manning [50] introduced first the concept of shock leakage through vortex-ladden mixing layer. This mechanism was shown to play a fundamental role in shock noise emission. By means of geometrical acoustic theory, Suzuki & Lele [87] also supported the idea that the local vorticity behaves as a barrier against shocks while acoustic waves can leak near the saddle point between vortices. DNS on a 2D vortex-ladden supersonic mixing layer, showed the evolution of a shock-wave, impinging on the mixing layer, being initially deformed by a vortex, and then 'bouncing back' at the saddle point. A strong pressure wave is then generated and it starts propagating outside (Fig. 1.9).

Daviller *et al.* [25] confirmed the results with another plane 2D DNS of an oblique shock-wave impinging on a supersonic shear layer with forced periodic instabilities. Berland *et al.* [11] also evidenced the presence of sound waves 'leaking' from the third shock-cell in their LES of a planar supersonic underexpanded jet.

Unfortunately this phenomenon was never documented experimentally. Supersonic jets are surrounded by turbulent shear layers which make difficult the usage of Schlieren visualization, because of the light integration path. Modern fast PIV systems, with acquisition frequencies of the order of 10 kHz, may instead suffice, especially if using the screech as base frequency to

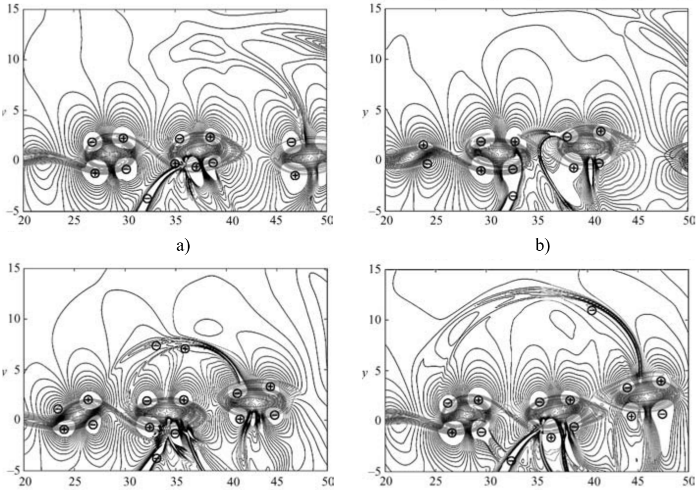

a)
b)
c)
d)

Figure 1.9: Dilatation fields showing the evolution of the shock-front calculated in DNS. From Suzuki & Lele [87]

perform a phase locked average.

1.3 Dual Stream Jets

The noise generated by dual stream jets has the same characteristics as the one generated by single jets. Although the jet topology is different, the mechanism at the base of shock-associated noise is the same. In comparison with single stream jets, dual stream jets have a larger number of parameters that can influence the acoustic output. A part for the two different NPRs, defined as Core Nozzle Pressure Ratio (CNPR) and Fan Nozzle Pressure Ratio (FNPR) for the core (primary) and fan (secondary) stream respectively, also temperature ratio and nozzles geometry play a major role. The acoustical properties of subsonic coaxial jet was investigated by Kuztnetsov & Munin [44] and Balsa & Gliebe [8] as the sum of the contribution of the annular flow and the core flow. Keeping the core flow speed constant, and increasing the fan flow speed, the overall noise pass trough a minimum level before to increase again.

The first studies on shock-cell noise for dual stream jets was carried out by Tanna *et al.* [105] in the seventies. In particular, Tanna *et al.* [104][103] and Tam *et al.* [96][97] showed that having a slightly supercritical primary jet would yield an almost complete destruction of the shock-cell system of the secondary stream, reducing the overall shock-cell noise. Dahl *et al.* [22][23] applied the instability wave noise generation model of Tam *et al.* [98][99] to supersonic dual jets having good agreement with experiments. The structure of the shock-cell system and the appearance and location of a shock-disk on the primary jet was studied by Rao [75]. The appearance of screech on dual stream jets was studied experimentally by Bent *et al.* [10]. They found that the 'tonal'shock-cell noise disappeared when the nozzle had bifurcations inside the secondary stream. This illustrates how the effect of a pylon and the internal struts of commercial turbofans would disengage screech from being present in commercial aviation. Dahl *et al.* [24] studied a perfectly expanded dual stream jet where they showed that the mixing noise can be also adapted by the similarity spectra used for single jets.

Viswanathan [111] investigated the effect of different combinations of CNPR and FNPR on the produced noise. When the primary jet is supersonic, the shock-associated noise is dominant at all the angles, and the contribution of the secondary shear layer is considered negligible. On the other side, when the secondary flow is supersonic, the shock-cell noise is increased in the downstream angles. Bhat *et al.* [12] conducted an extensive test campaign on a dual stream jet where the pylons and the central plug were installed in the nozzle, and the core flow was heated. They found that the shock-cell noise contribution was not monotonically increasing while the NPRs were increasing. In particular, for certain pressure conditions, the strength shock-cell pattern in the secondary stream was reduced, with a consequent decrease of the shock-associated noise.

Another extensive experimental campaign on subsonic and supersonic dual stream jets was performed by Viswanathan [112] and Viswanathan *et al.* [114] in order to carry out a parametric study on the effect of the primary and secondary nozzle pressure ratio, the secondary-to-primary jet velocity ratio and the secondary-to-primary nozzle area ratio. For a dual stream jet with shock-cells in the secondary flow, two possible sources of shock-cell noise are present: the inner (primary) shear layer, and the outer (secondary) shear layer. And both shear layers are also source of turbulent mixing noise. Tam *et al.*[92] showed that dual stream jets have two set of BBSAN, coming from the primary and secondary shear layer. Being the BBSAN frequency peak related to the wavepackets convective speed U_c, the two shear layers generate a different directivity pattern, as evidenced in Fig. 1.10. They stated that the first set was similar to the BBSAN peak produced in a single stream jet, radiating sound mainly in the upstream direction. The second set that radiated sound mainly in the downstream direction. From their mathematical analysis, using a simple model, they demonstrated how the first set was due to the interaction of the large turbulent structures with the shock cell pattern in the outer layer, while the second set was produced by the interaction of the turbulent structures with the shock cell pattern in the inner shear layer. The sound waves produced by the latter are firstly convected inside the supersonic stream before to propagate outside.

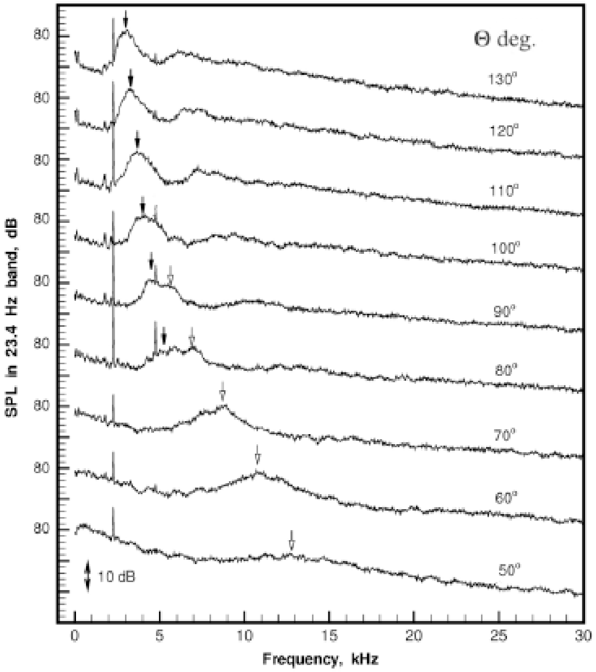

Figure 1.10: Directivity of the SCN peak for a dual stream jet, pointed out by the arrows. Black arrows are related to the secondary shear layer, while white arrows to the primary shear layer. Tam *et al.* [92].

1.4 Numerical Simulations of Supersonic Jets

The advances in computational power made possible the simulation of higher Reynolds number jets, as well as more complex geometries. Acoustics perturbations are by definition an unsteady process. Therefore, in order to be able to compute acoustic waves and sound phenomena computationally, an unsteady calculation or acoustic models are needed. Moreover, the errors committed by the numerical model and machine related errors must be lower than the acoustic perturbations itself. Two different methods can be used in order to simulate sound fields: direct computation of sound and hybrid methods [19]. Without going into details, the first one relies on Direct Numerical Simulations (DNS) or to Large Eddy Simulations (LES) to compute directly the sound sources. Due to the fine scales to be resolved, those methods are computationally expensive, and are usually limited to low Reynolds number. This also depending on the frequencies to be studied, because the mesh must be sufficiently fine to avoid dissipation, at least until a certain distance from the source, where Ffowcs-Williams and Hawkings surfaces can be used to propagate the sound into the far field.

Many examples of numerical simulations on single stream jets are present in the literature, but still few on coaxial jets. Lele *et al.* [46] compared LES results of a supersonic single stream jet with experimental results. Nicholson *et al.* simulated a complex geometry using a rectangular nozzle with chevrons [55]. Shur *et al.* simulated both a single and a dual stream jet in static and flight conditions [84]. Brès *et al.* described the advances in massively-parallel simulations for supersonic jets noise from complex nozzles. Pèrez Arroyo performed a LES of the coaxial nozzle studied in this thesis [67] and compared with the experimental measurements [66].
Hybrid approaches, instead, relies on the computation of the main flow features, and a second computation to retrieve the sound field. Miller and Morris used RANS simulations on a supersonic coaxial jet to predict the noise in the far field [53].

Further information on numerical simulations, models and implementations can be found in [66].

1.5 Modelling Shock Cell Noise

The first comprehensive experimental and theoretical study on shock-cell noise was due to Harper-Bourne & Fisher[34]. They proposed a source scenario composed of localized phased sources as an extension of Powells model [70] for the screech tone. Another approach was developed later by Tam *et al.* [95] [91], considering the interaction of instability waves with the steady shock cell pattern as a phased array of distributed sources, which are the cause of the BBSAN. A review of this methodology can be found in Savarese's thesis [78], where he assessed the influence of several model parameters and compared with experiments he performed on an underexpanded jet.

Tam & Tanna [95] found that for a convergent-divergent nozzle of design Mach number M_d, the acoustic intensity of BBSAN is proportional to $I \propto (M_j^2 - M_d^2)^2$. This expression is compatible with Harper-Bourne & Fishers result for convergent nozzles, for which $M_d = 1$. The interaction between convected turbulence and the shock-cell structure is also experimentally investigated in Pao & Seiner [64], and a critical review of the previous models is provided. Morris & Miller [53] have developed a numerical model to predict BBSAN, in extending what has been done for mixing noise within the framework of statistical modeling [7]. The inputs of such models are provided by a Reynolds-Averaged Navier-Stokes (RANS) solution. As a starting point, flow variables are split up among four contributions associated with the mean flow, the turbulent flow, the shock-cell structure and the fluctuations generated by the interaction between shocks and turbulence, including acoustic perturbations. The BBSAN component predicted by the statistical model is plotted in Fig. 1.11, as well as experimental results.

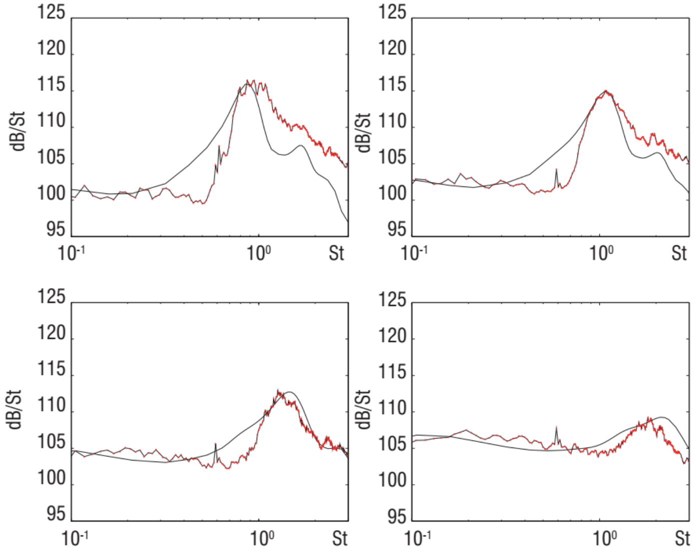

Figure 1.11: Acoustic spectra in dB/St as a function of the Strouhal number $St = fD/u_j$, of the $M_j = 1.15$ jet for an observer angle $\theta = 130^o$, 110^o, 90^o and 70^o; red line are the measurements [2], black lines predicted BBSAN component [36], which is expected to dominate in the rear quadrant. The observer angle θ is taken from the downstream jet axis. From Bailly *et al.* [6]

The peak frequency f_p is correctly captured numerically and the emergence of BBSAN increases in the inlet direction, as predicted by Equation 1.17.

1.5.1 BBSAN Prediction using PIV data

The model developed by Tam was applied by Rubio Carpio [77] using PIV data acquired during this project and presented in Ch. 3. The model showed overall good agreement with measured data when it was fed with specific empirical parameters for the calculation of the convection speed of the large turbulence structures, the wavenumbers of the shock cell pattern, the width of the Gaussian envelope of the wavepackets, the amplitude of the wavepackets and also the amplitude of the shock cell pattern modes among other fitting constants. Rubio Carpio, instead, retrieved part of the parameters directly from not time-resolved PIV measurements. The comparison between the measured and predicted Sound Pressure Level is exposed in Fig. 1.12. The model overestimates the SPL at low frequencies and underestimates it at high frequencies for all the test cases. However, the prediction retrieves successfully the frequency of the broadband shock cell peak for all the different polar positions in all measured test cases.

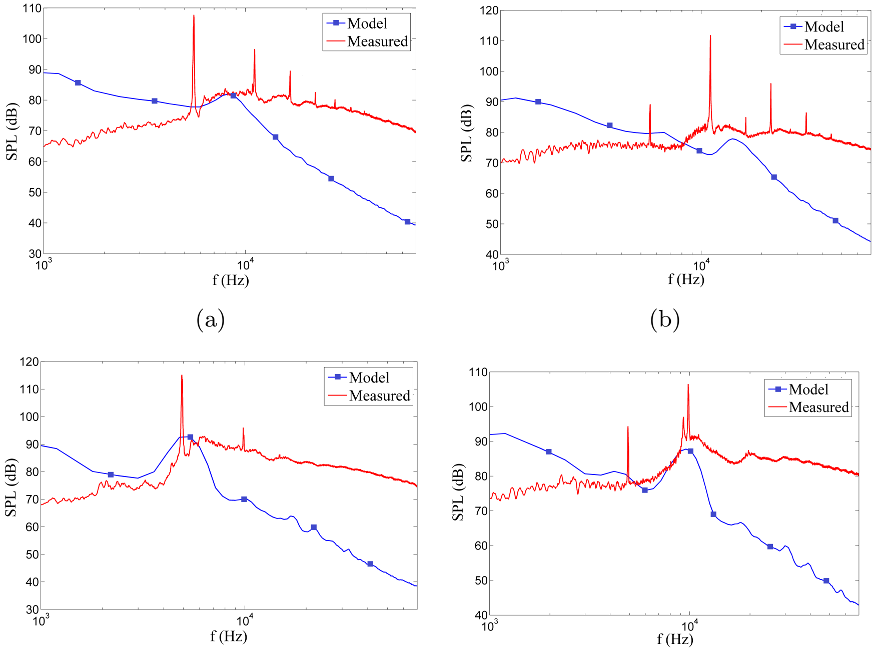

(a)

(b)

(c)

(d)

Figure 1.12: Comparison of measured and predicted far-field spectra at different observation angles for different CNPR values. White points indicate the measured shock associated noise peak. (a) $M_j = 1.25$ at $\theta = 30^o$. (b) $M_j = 1.25$ at $\theta = 80^o$. (c) $M_j = 1.50$ at $\theta = 30^o$. (d) $M_j = 1.50$ at $\theta = 80^o$

Chapter 2

FAST: Free jet AeroacouSTic facility

The design and implementation of a jet rig to simulate a supersonic dual stream jet is presented in this chapter. At VKI is present a semi-anechoic room (4 3 4) m^3 having a cut-off frequency of 350 Hz, already used for studies on single stream jet and dual stream jets, supplied either by a 7 bar pressure line or by a centrifugal fan. The air supply system is located in the basement under the anechoic room, with the jet blowing in vertical direction. An, extractor with a muffler, is present on the roof of the chamber. The previous configuration consists in a rectangular single stream jet supplied by a centrifugal fan described in the PhD thesis of De Santana [26]. This configuration was unsuitable for generating a high speed coaxial flow, and therefore a in-depth analysis was conducted for an efficient adaptation to high pressure jets.

2.1 Requirements and Constraints

The main purpose of this project is to generate a supersonic coaxial jet, which means to ensure to the rig a sufficient and stable pressure and mass flow rate. The desired test conditions for the coaxial flow were established together with Airbus, partner of AeroTraNet2, and used as reference for the whole design procedure. The pressure requirements in terms of Fan Nozzle Pressure Ratio (FNPR = $\mathrm{p}_{0s}/\mathrm{p}_a$) and Core Nozzle Pressure Ratio (CNPR = $\mathrm{p}_{0p}/\mathrm{p}_a$) are shown in Fig. 2.1 and explicitly represented in Tab. 2.1. This combination of parameters represents a possible working envelop for next generation HBPR turbofan engines.

Another requirement is the possibility to study the jet using using both non intrusive, optical techniques, such as PIV, LDV, Schlieren, as well as intrusive techniques, such as hot wires and pressure probes. A part from the Schlieren technique, which is usually performed with a high frame rate cameras, the other techniques listed above require a certain time lapse to be completed, because of their low frame rate (PIV) or because they are point-wise measurements, and thus adjustments to instrument positions must be made during the duration of the experiment. A suitable test duration is consequently essential. However, long time duration must not be detrimental for good quality flow, as well as reproducibility, which is very important in order to confute results over time. Safety and workability are also central,

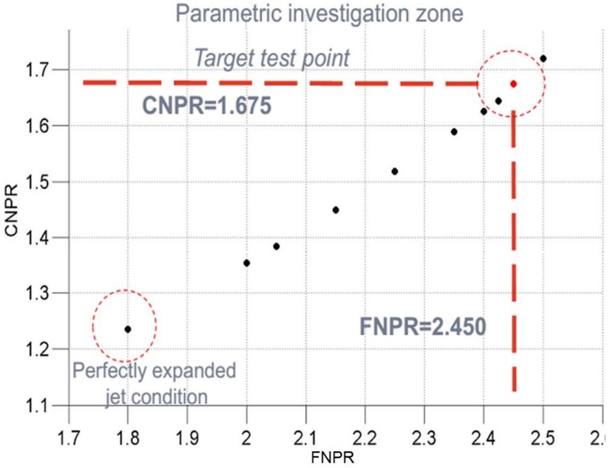

Figure 2.1: Reference test condition for the dual stream jet in terms of FNPR and CNPR.

and must be included from the start of the design process. A high pressure facility is potentially more dangerous to the user than a low pressure one, hence, specific regulations and guidelines must be followed. Finally, cost efficiency is highly desirable. A flexible installation may repay the initial investment among the years, and so future scenarios must be foreseen and included in the design process.

2.2 Design phase

To fulfill these requirements, an iterative design procedure was carried out to select the best configuration for the facility. Initially, two limit configurations were considered: a continuously running facility and a blow-down facility. The first kind, sketched in Fig. 2.2a, presents several advantages, the main one being the test duration. Using the VKI high pressure line, at 35 bar, the air is provided by the main institute tanks, with a nominal capability of 60 m^3. After a first pressure reduction, particles are added by means of a single seeding generator, and then fed through two lines into the anechoic room. This configuration would be cost efficient, due to the little number of components. However, it presents the drawback to be sensible to the pressure fluctuations coming from the feeding line, which is shared by the whole institute. Furthermore, there would be no room to mix the oil particles used for PIV, and thus a good flow quality would be not guarantee. In the second configuration, shown in Fig. 2.2b, the air for the two streams is supplied by two tanks that are filled using the main pressure line. A

Test	$FNPR$	$CNPR$	M_{fan}	M_{core}	BPR	BPR (CFD)
1	2.450	1.675	1.21	0.89	4.95	6.22
2	2.500	1.720	1.22	0.91	4.90	6.86
3	2.425	1.645	1.20	0.87	5.01	7.01
4	2.400	1.626	1.19	0.86	5.03	7.02
5	2.350	1.589	1.18	0.84	5.07	7.02
6	2.250	1.518	1.14	0.80	5.16	7.04
7	2.150	1.450	1.11	0.75	5.28	7.20
8	2.050	1.385	1.07	0.70	5.43	7.90
9	2.000	1.353	1.05	0.67	5.53	8.35

Table 2.1: The parameters of the test campaign with the related fully-expanded Mach number, the by-pass ratio obtained with isentropic relations, and using CFD RANS.

couple of seeding generators are used to fill the two tanks with particles, ensuring the best flow quality, without unwanted pressure fluctuations. The drawback of this setup would be the associated costs, due to the duplication of the components, plus the presence of two tanks. Furthermore, the test duration would be determined by the volume of the tanks and their pressure. Considering that high pressure vessels need to satisfy very strict safety regulations, and they are usually very expensive, this second solution would be prohibitive from the economic point of view.

2.2.1 Conceptual design

The proposed solution incorporates benefits of both edge designs presented above, while avoiding their disadvantages and keeping the facility costs low. The final configuration is shown in Fig. 2.3. The 35 bar line supplies a single seeding generator in parallel with a buffer tank, from which two lines for the primary and secondary flow depart. This setup allows continuous operation of the facility, with fluctuations damped by the buffer tank, enhancing the flow quality and providing uniform seeding. The number of components is reduced to the minimum, increasing the cost efficiency. A coaxial silencer is used to dump all the spurious noise produced by the feeding line, providing an anechoic termination, and also acting as a settling chamber for the primary and secondary flow, all without introducing asymmetries in the flow. The drawbacks of this design are the impossibility to change the total temperature ratio between the two streams, as well as to select a seeding concentration for the two jets individually.

Following this layout, a set of valves, pressure regulators and other components were chosen (Fig. 2.4). A brief overview of the technical solutions will be given hereafter, while for a detailed description of each component, the

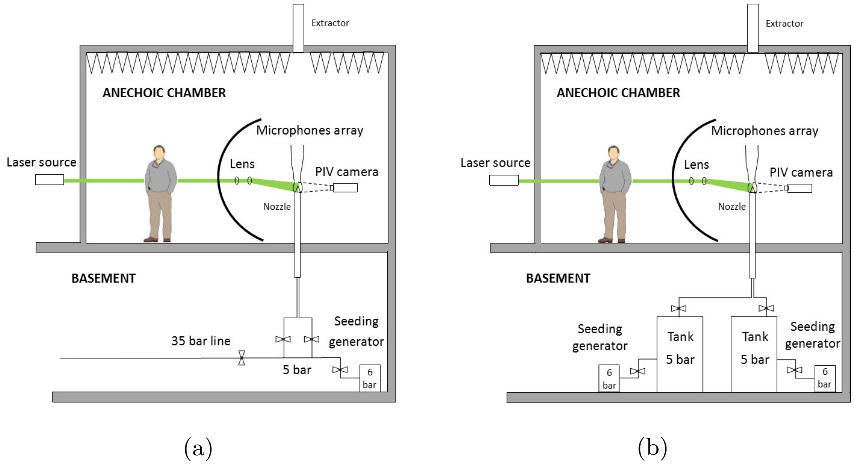

(a) (b)

Figure 2.2: a) Limit working configuration of a continuously running facility using the VKI high pressure line. b) Limit working configuration of a blow-down facility using two tanks to feed the dual stream jet.

reader is referred to Sec. 2.3.

The flow enters pressurized at 35 bar from the bottom left of the picture. An electrical ball valve with a safety return battery is used as main ON/OFF shutter. Four emergency buttons are placed strategically to cut the valve power supply, which will cause it to close automatically in approximately 10 seconds. A manual ball valve is placed upstream as backup. The pressure line is then lowered from 35 to 10 bar by two identical pressure regulators, because a single one would not have sustained the requested volumetric flow. At this point the flow splits in two lines. One goes to the buffer tank, after passing trough a pilot controlled pressure regulator, which lower the pressure from 10 to 5 bar. The other line goes inside the seeding generator, described in Sec. 2.2.3, which was mounted on the ground level. The seeded flow merges with the main stream in the buffer tank, from which two lines departs. Each line is independent and they mount the same components, except for one of them, which is supplied also with a conditioning orifice flow meter (described in Sec. 2.2.4). On each line, a fine pressure regulator controls a volume booster, ensuring higher precision together with high volumetric flow capabilities. The two lines and the buffer tank are all equipped with safety rupture disks, which will break in case the pressure would exceed the tank limit of 11 bar. Finally, the flow enters into the coaxial silencer (described in Sec. 2.2.5) trough 20 radially distributed inlets, 10 per each of the two circuits. Two conical flow distributors are used at this scope, each of them mounting 10 flexible pipes of the same length. The vertical coaxial ducts bring the flow into the anechoic chamber. Each of them is equipped with

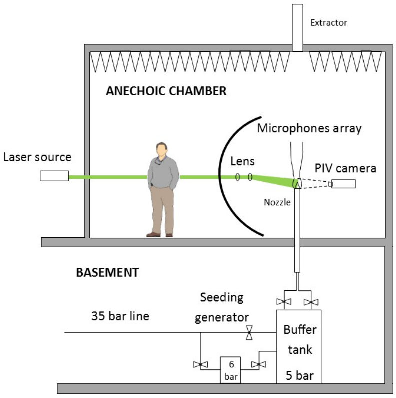

Figure 2.3: Selected layout of the facility. Advantages of the previous limit cases are joined together in a functional and cost efficient design.

honeycombs and three screens to uniform the streams.

In principle, the facility was intended to be controlled entirely in remote through electrical actuators, with the control room placed outside the anechoic room, near the PIV and the acquisition systems. This explain the presence of the seeding generator on the ground floor: to help the operator to control the seeding quantity while looking at the screens. However, the remote option was not exploited so far, due to excessive costs, and the seeding generator was moved downstairs, close to the buffer tank and the other pressure valves, where the operator must stay to control the facility. The latter can monitor and also operate on the computers upstairs through a screen and input devices placed near the feeding line. It is, anyway, highly recommended to update the facility to enable remote control. This would safeguard the operators from potentially harmful situations, including the exposure to a very noisy environment for long time.

2.2.2 Coaxial Nozzles

The designed coaxial nozzle is representative of next generation aeronautic engines with high by-pass ratio. The main geometry dimensions were proposed by Airbus. The outlet diameters are D$_{p1}$ = 24 mm and D$_s$1 = 55 mm for the primary and secondary jets, respectively, the nozzle lip thickness is t = 0.3 mm for both the nozzles. The primary outlet plane is 21 mm downstream of the plane of the secondary outlet, leading to a ratio of $A_s 1/A_p 1 = 3.35$. The secondary jet area contraction ratio is about 44, and the primary jet contraction ratio is 12. The primary nozzle has a simple conical shape, with the semi-aperture angle $\alpha_p = 14°$. The secondary nozzle profile follows a 3^{rd} order polynomial function, modified in the final section to have the throat at the exit. The exit semi-aperture angle for the secondary nozzle is $\alpha_s = 12°$.

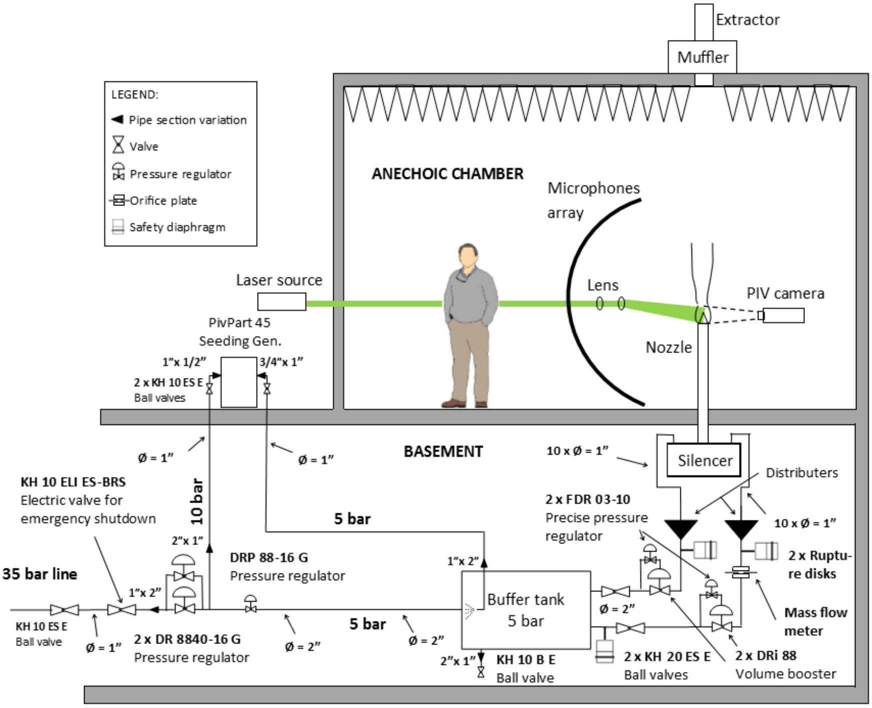

Figure 2.4: Detailed layout of FAST feeding line, including equipment. Product codes are referred to the supplier catalog [45].

A preliminary version of the nozzle (Fig. 2.5.a) was validated trough CFD, and tested for the initial commissioning of the facility, as well as for the experimental campaign of the single supersonic jet described in Sec. 3. A second, smaller, version was used for the experiments with dual flow. It is a 0.8 scaled version of the previous nozzle, and thus $D_{p2} = 19.2$ mm, $D_s 2 = 44$ mm and the primary outlet plane is 16.8 mm downstream of the plane of the secondary outlet (Fig. 2.5.b). Both nozzle sets were realized in stainless steel. In case it is needed, a cylindrical spacer under the secondary nozzle (violet element in Fig. 2.5) can be modified to adjust the protrusion length.

To control and eventually correct the position of the internal nozzle, three screws were placed in the external duct at the level of the roof. A centering tool was designed and manufactured to check the correct positioning (Fig. 2.6). This tool can fit the nozzles only if their axes are aligned. A small rectangular window is used to check that the primary nozzle is touching the tool upper surface, meaning that also the protrusion length is correct.

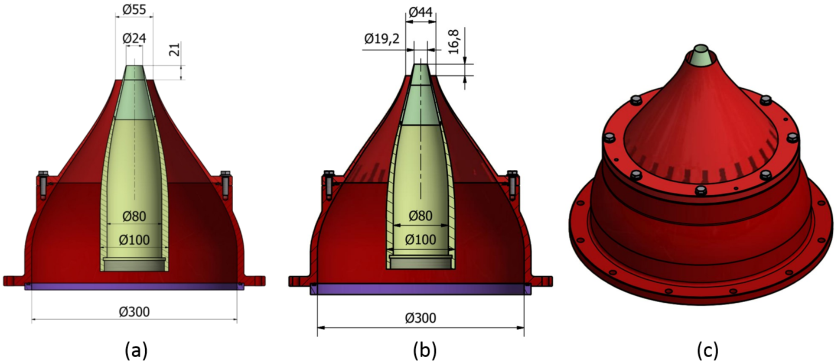

Figure 2.5: CAD drawing of the manufactured coaxial nozzle sets. Dimensions are in mm. a) Preliminary version, used for CFD and single stream jet experiments. b) Final version, used for dual stream experiments. c) 3D view.

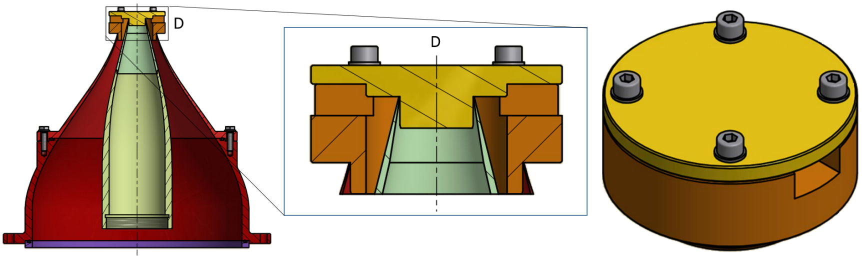

Figure 2.6: CAD drawings of the centering tool designed to ensure the coaxiality of the two nozzles.

2.2.3 Seeding Generator

The seeding generator was selected taking into account the requirements in terms of particles density and size. In presence of shock-waves, the inertia of the particles must be small enough to follow the strong decelerations across the shocks. The motion of a particle in a fluid was studied by Oseen [59] and Tchen [106], who derived the fundamental equations. Jeronimo [42] computed the time response for different sizes of vegetable oil particles in an open jet at Mach $M = 4$. She concluded that particles size should be limited to $\varnothing = 1$ μm or smaller, for this kind of investigation. PivPart-45M by PIVTEC Gmbh has therefore been used for the experiments. It is a seeding generator composed by 45 Laskin nozzles, with 5 bar as maximum outlet pressure. The manufacturer User Manual[69] reported a peak in the particle size distribution function around $\varnothing = 1$ μm for vegetable oil (Fig. 2.7). However,

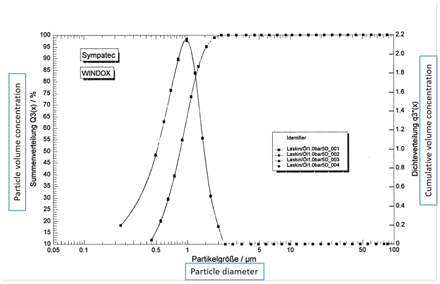

Figure 2.7: Particle volume density distribution for vegetable oil provided by PIVTEC Gmbh at 1 bar input pressure.

the seeding used is industrial oil Shell Ondina-919, and so discrepancies from the manufacturer data sheet have to be expected. This seeding was used because of commonality with others VKI experiments, and because of the high purity level. Mandon [49], a posteriori of our experiments, conducted an extensive characterization of the seeding created by the very same generator used for the test campaigns. Using Laser Extinction Spectroscopy and Phase Doppler Interferometry, he retrieved seeding size distribution curves depending on the pressure in input, and number of Laskin nozzles opened. His results demonstrate that the peak of the number of density is lower than 1 μm and close to 0.5 μm (Fig. 2.8).

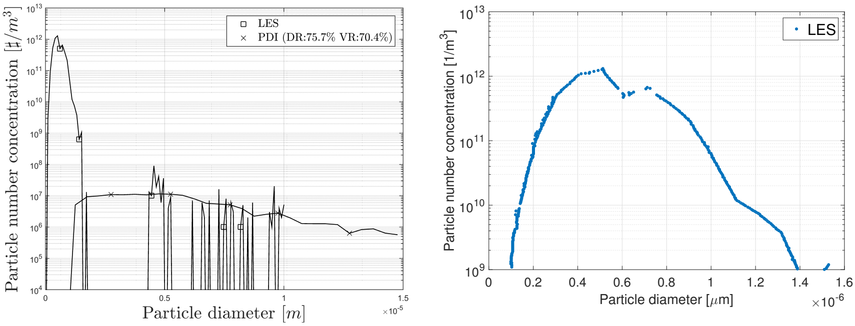

Figure 2.8: Number of particles per volume distribution using LES and PDI[49] (left) and zoom in (right), at 5 bar input, all the valves open.

Since his investigation was limited to study the particles at atmospheric pressure, and therefore particle concentration is unknown at 7 bar input and 5 bar output, the conditions used during the tests. It is not clear, in fact, if the distribution is sensitive to the pressure difference between inlet and outlet, or to the pressure ratio. Anyway, in case the distribution is the one shown in Fig. 2.8, it would be positive for the measurement accuracy, because of the smaller time lag in comparison with the initially considered 1 μm particles. However, too small particles size will negatively affect the visualization of the droplets on the PIV images, since the scattered light per droplet will fall below the noise threshold of the camera sensor.

2.2.4 Conditioning Orifice Flow Meter

The primary mass flow rate must be measured because it cannot be determined in other ways due to the flow topology, as explained in Sec: 2.4.5.1 and 4.2.1. Several technical solutions were thus considered. Flow meters with different working principles are present on the market. They can be grouped into four categories:

- **Mass Flow.** These instruments determine directly the mass flow passing through the meter. Two types deserve mention here: Coriolis flow meters provide a direct mass flow measurement based upon the deflection force of the fluid moving through a vibrating tube. These meters are highly accurate with high turn-down capabilities and are independent of fluid properties. They are also extremely expensive to purchase and install, and are not suitable for larger pipe sizes. Thermal mass flow meters measure the mass flow based on heat transfer from a heated element. The measurement is in mass flow, and additional pressure and temperature correction is not required. They also provide excellent accuracy and repeatability and are easy to install.

- **Velocity.** In a velocity meter type, the rate of the medium passing through the meter determines the measurement. Turbine flow meters measure volumetric flow based on fluid flowing passed a free-spinning rotor; each revolution corresponding to a specific volume of fluid. The meters have high turn-down and accuracy. Unfortunately, because of the meters moving parts its use is limited to clean dry gases only, and pressure and temperature compensation are required. Ultrasonic flow meters measure the difference in transit time of pulses that travel from a downstream transducer to the upstream transducer, compared to the time from the upstream transducer back to the downstream transducer. This style of meter is very accurate but very expensive, and pressure and temperature measurement are required. Vortex flow meters have a bluff object or shedder bar that is placed in the flow path, and as gas flows around the shedder bar, vortices are cyclically generated from opposite sides of the bar. The frequency of vortex generation is a function of the gas velocity. The frequency of vortex shedding is independent of fluid composition. The meter, however, requires pressure and temperature compensation and needs a minimum flow rate to produce vortices.

- **Differential Pressure Meters.** Differential pressure flow meters calculate flow by measuring the pressure drop over an obstruction inserted in the flow path. Common types of flow elements are orifice plates, flow nozzles, venturi tubes and averaging Pitot tube. The orifice plate is a differential pressure meter frequently used for natural gas measurement. It measures volumetric flow, not mass flow. Limitations of this meter include poor low flow sensitivity, limited turn-down, and it also creates a pressure drop, which impacts operating costs. Additionally, since the meter only provides information about the volume flow, mass flow can only be computed with additional pressure and temperature data. An averaging Pitot tube is a differential pressure flow measurement device commonly used for combustion air measurement. The device has limitations with gas flow; especially low flow sensitivity and turn-down The measurement relies upon quantifying velocity pressure, which is only possible above certain flow rates.

- **Positive Displacement.** Positive displacement meters require fluid to mechanically displace components, and measure volumetric flow at the operating pressure and temperature. While they have sufficient accuracy, pressure and temperature compensation are required to achieve mass flow, and since they have moving parts, gas cleanliness needs to be considered. A positive displacement meter is called a PD flow meter or a volumetric flow meter. An example of of such a device is the diaphragm meter.

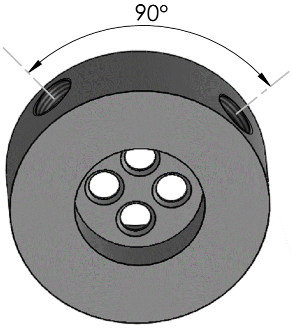

Figure 2.9: Conditioning orifice plate with four holes.

To remain cost efficient, a conditioning orifice plate was chosen as differential meter, since its pressure losses can be considered negligible, for the implemented test matrix. Positioning the meter after the tank and before the final pressure regulator leads to have high pressure and thus low velocity inside the device. The main drawback of such meters is the required length of straight pipe before and after the plate, depending on the upstream pipe geometry. A four holes conditioning orifice plate by EMERSON (Fig. 2.9) was chosen as its requirements in terms of pipe length are less than those of a single orifice plate [41]. Authors [28] tested the device extensively with good results, showing that it requires only a pipe length $L_{pipe} = 2D_{pipe}$ fore and aft to measure mass flow.

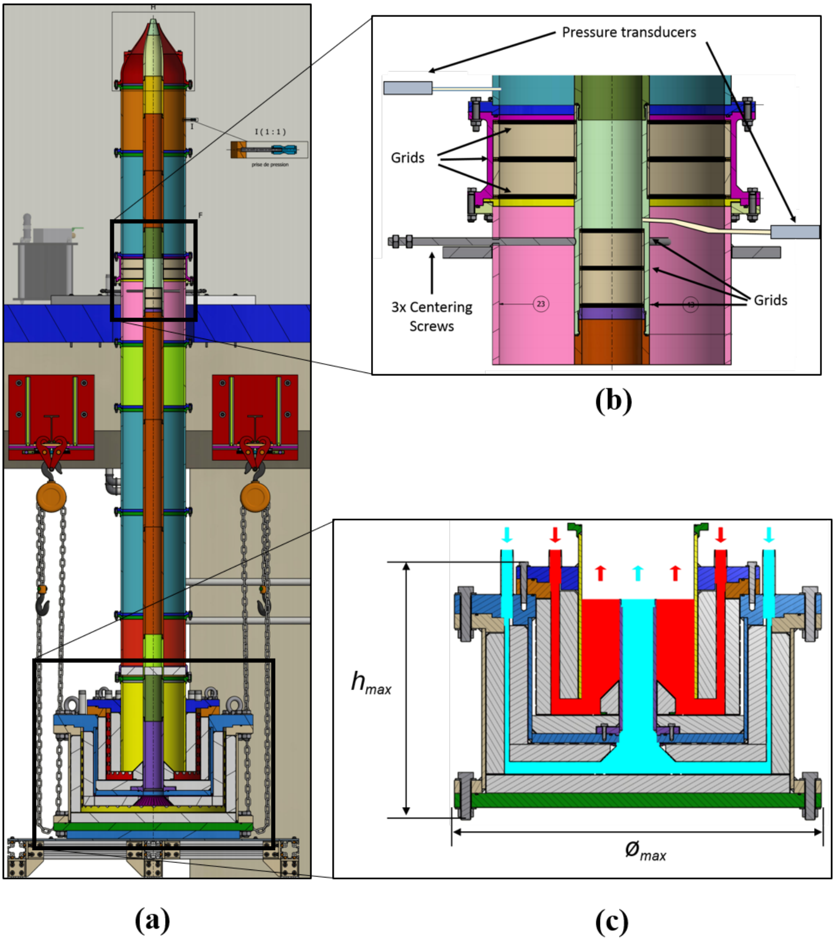

Figure 2.10: a) Section of the silencer and coaxial ducts. b) Detail of the ducts. The pressure tap of the primary flow is located below the grids of the secondary one, thus decreasing the risk of introducing vortex shedding noise. c) Detail of the coaxial silencer. The clean passage areas for the primary and secondary flow are colored in cyan and red, respectively. The gray zones represents the phono-absorbent material. The overall dimensions are $h_{max} = 0.76$ m, $\varnothing_{max} = 0.98$ m, weight $m \approx 1200$ Kg.

2.2.5 Silencer

The silencer is designed to feature a coaxial, U-turning flow in annular sections, in order to maximize the area of damping material exposed to the incident acoustic field, while minimizing the flow velocity and associated pressure losses. The air enters the circuit from the top plate through ten equally-spaced inlets. The colored zones in Fig.2.10c) represent the clean passage areas, while the gray dashed zones depict the acoustic absorbent material. Due to space constraints, it was decided to use a fixed thickness for all the absorbent layers, equal to $l_{abs} = 50$ mm. The clean passage areas were sized in order to not exceed flow velocities of 10 m/s and thus reduce both pressure losses and extra noise production. The chosen absorbent material is composed by very fine stainless steel wool (type #000). The wool is hold by four metal canisters. The maximum working pressure is 11 bar.

2.2.6 Coaxial Duct

From the silencer, a 4 m long coaxial duct brings the flow into the semi-anechoic chamber through a circular hole in the roof. An overview of the CAD assembly is shown in Fig. 2.10a). The external duct is composed by several flanged steel cylinders of internal diameter $\varnothing = 0.3$ m. No gap is present between the jointed pieces. The internal duct, instead, is composed by screwed steel cylinders, without gaps in both inner and outer surfaces. The inner and outer diameters are $\varnothing_{in} = 0.08$ m and $\varnothing_{in} = 0.10$ m. A 0.05 m thick honeycomb was mounted at the exit of the silencer, for both circuits, to dump the transversal velocity fluctuations. At the level of the roof, a special section is present, to host the centering screws, the primary flow pressure tap and the turbulence grids (Fig. 2.10b). Three M10 screws are used to center correctly the inner duct. The screws head was rounded, and a small round bed was made on the outer surface of the internal duct, to avoid the screws to slip on the duct walls. Above the screws, holes were drilled in both ducts to make the pressure tap. Small metal tubes were welded on both sides of the walls, and a flexible tube of $\varnothing = 5$ mm is used to connect the internal duct with a pressure sensor located outside the external duct. Three turbulence grids were installed to dump velocity fluctuations in both flows. The primary flow grids were placed below the pressure tap, to not bias the measure, while the secondary flow grids were installed above both the centering screws and the pressure tap tube. In such a way, the vortex shedding caused by the latter should be attenuated, and thus the spurious noise generated.

2.2.7 FAST Overview

The complete CAD design of FAST, including each component, was carried out by Didier De Backer, under de supervision of Jean-Jacques Delval, both from VKI drawing office, which are gratefully acknowledged. An overall view of the facility is depicted in Fig. 2.11. The manufacturing of the majority of the components, and the installation of such complex facility was studied and executed together with the VKI technicians, which are gratefully acknowledged for their professionalism and precision. In Fig. 2.12 is presented the Free jet AeroacouSTic facility completely installed, while in Fig. 2.13 a detail of the technical solution adopted is shown.

In Fig. 2.12 is presented the Free jet AeroacouSTic facility completely installed, while in Fig. 2.13 a detail of the technical solution adopted is shown.

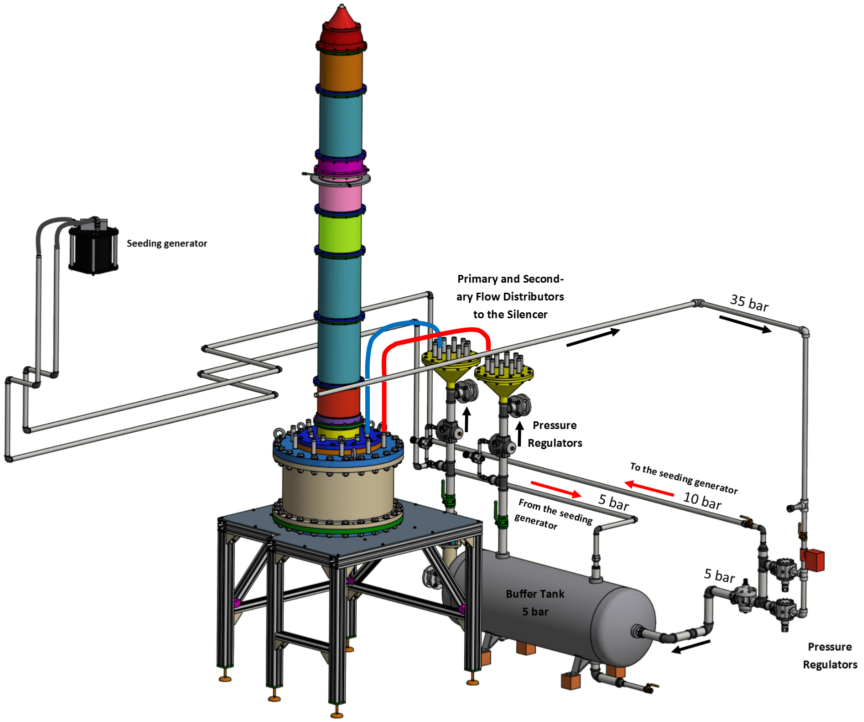

Figure 2.11: CAD overview of FAST facility.

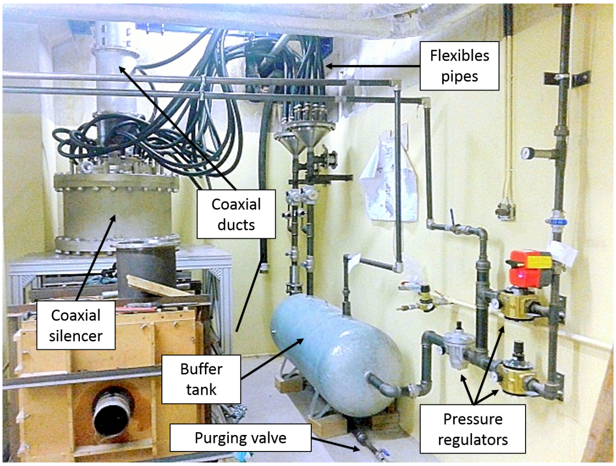

Figure 2.12: Picture of the FAST facility ready for testing.

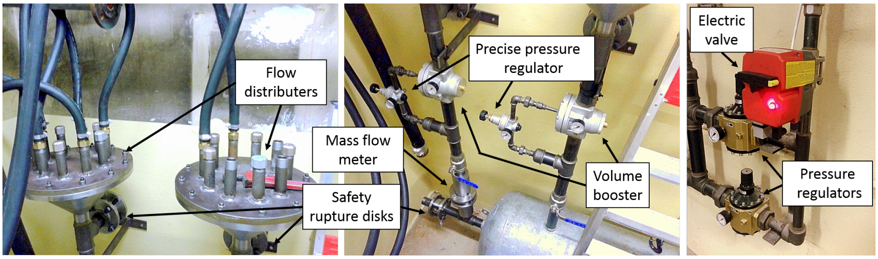

Figure 2.13: Details of the installed equipment.

2.3 FAST Equipment Description

In this section, details on the equipment installed in the FAST facility and present in Fig. 2.4 are provided. The code number refer to the manufacturer atlas [45]. A quick guide on the pressure regulators working principles is also given.

2.3.1 Pressure Regulators: Operative Principles

A pressure regulator is a mechanical device which primary function is to match the fluid flow demand through it, whilst maintaining a constant output pressure.

If the load flow decreases, then the regulator flow must decrease also. If the load flow increases, then the regulator flow must increase in order to keep the controlled pressure from decreasing due to a shortage of gas in the pressure system.

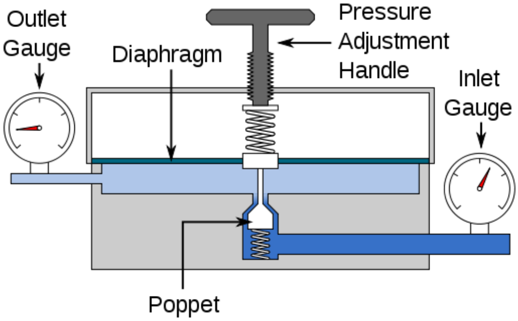

Figure 2.14: Sketch of a single stage pressure regulator. From Wikipedia [120].

A pressure regulator includes a restricting element, a loading element, and a measuring element (Fig. 2.14):

- The restricting element is a valve that can provide a variable restriction to the flow, such as a globe valve, butterfly valve, poppet valve, etc.
- The loading element is a part that can apply the needed force to the restricting element. This loading can be provided by a weight, a spring, a piston actuator, or the diaphragm actuator in combination with a spring.
- The measuring element functions to determine when the inlet flow is equal to the outlet flow. The diaphragm itself is often used as a measuring element; it can serve as a combined element.

High pressure gas from the supply enters into the regulator through the inlet, and then through the restricting element, before leaving the regulator. When the outlet pressure lowers, and more flow rate is demanded, the diaphragm moves the poppet, opening the valve until equilibrium is re-established. On the contrary, when the outlet pressure increases, the valve closes, until the flow is fully stopped. In case of further outlet overpressure, in most of the regulators a safety relief valve opens in order to release the flow. In this process, the flow loses total pressure, in an omoenthalpic process, because there is no energy transfer outside the valve. Therefore the total temperature of the flow remains the same.

Each regulator is provided with a characteristic working curve, which is given by the manufacturer. A typical one is depicted in Fig.2.15. On the vertical axes is found the outlet pressure, usually in bar or in psig. On the horizontal axes, instead, the volumetric flow rate. The volumetric flow rate can be expressed in several units, depending on the manufacturer. The time unit can be expressed in minutes or hours, the volume in m^3, litres, or ft^3, and it can be in “standard”or “normal”condition. Unfortunately these last two definitions are not completely uniform across the globe. Standard Temperature and Pressure (STP) as defined by IUPAC (International Union of Pure and Applied Chemistry) is air at 0℃(273.15 K, 32 °F) and 10^5 Pa. STP commonly used in the Imperial and USA system of units is air at 60°F (520°R) and 14.696 psia (15.6℃, 1 atm). Standard volume of 1 mole of an ideal gas at STP is 22.4 liters. Normal Temperature and Pressure (NTP) is defined as air at 20℃(293.15 K, 68 °F) and 1 atm (101.325 kPa, 14.7 psia, 0 psig). Density 1.204 kg/m3 (0.075 pounds per cubic foot) [108]. Therefore, to use the graph, the target mass flow rate, or generically, the flow rate must be converted in one of these two formats.

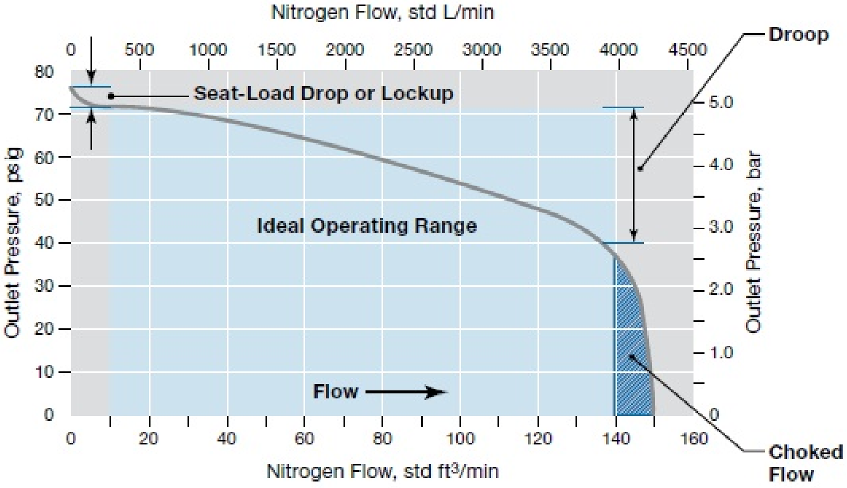

Figure 2.15: Example of valve working envelope. From [88]

The seat-load drop, or lock-up, is an undesired feature of mostly all valves for which, when the flow is stopped, the outlet pressure increases more than the pressure set initially. The droop curve is the pressure loss associated with a inlet and outlet pressure combination, while the flow rate is increasing. Lower is the slope of this curve, better is the valve. During the design, it is important to consider the pressure drop, and it can be studied in two ways. The first, is to consider to set pressure with the valve at zero flow rate, or lock-up point. When the fluid starts flowing, the pressure will drop following the curve, meaning that the output pressure will be lower than the one initially set. To correct it, the only solution is to act on the regulator in order to increase the pressure, and thus moving on another curve. This leads straight to the second point of view: if now the flow downstream the valve is stopped, the pressure fill follow back the curve until a new (higher) lock-up point is reached. This could be unwanted, or even dangerous, in case the circuit is operated at the limit point. Finally, the choked flow regime

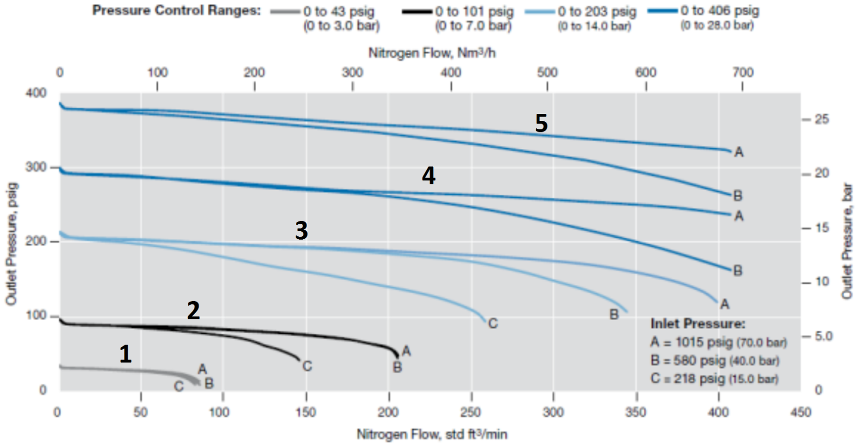

Figure 2.16: Example of effects of changing inlet and outlet pressure on the valve working envelope. From [88]

occurs at the limiting working point of the valve, where the valve reaches the maximum aperture, and the flow becomes sonic in the throat. No further increase of the flow rate is possible.

Each valve has an infinite number working points, or droop curves. Fig. 2.16 show the effect of changing the inlet and outlet pressure. Increasing the inlet pressure has the general effect to extend the curve, retarding the chocked regime, and to decrease the droop slope (curves 3-5). However, there is a limit in the flow rate that can be delivered at a given pressure, which depends on the valve design. For instance, in the point B on curve 2, doubling the inlet pressure does not produce any increment in the mass flow rate. On curve 1, the points A, B and C almost coincide. It happens that, given an inlet and outlet pressures for which the valve is fully opened and choked, the minimum pressure is achieved in the throat subsection (critical), and then the pressure will recover in the outlet subsection until the set p_2 pressure. This recovery factor, losses included, is defined by the geometry, which is now fixed, because the valve is fully open. For this reason, increasing the inlet pressure would necessarily cause an increase in the flow rate and in the pressure at the outlet beyond the set p_2, because of the fixed recovery factor. The regulator will react to this overpressure reducing the valve area, and thus keeping the outlet pressure and mass flow rate constant (curves 1-2).

Last effects to take into account, depending on the application, is the hysteresis. Almost all valves exhibits droop curves which are different depending on the positive or negative flow rate variation. Unfortunately hysteresis curves on manufacturers' datasheets are difficult to find unless for few points.

2.3.2 Manual Ball Valves KH10-ES-E and KH 20-ES-E

Those simple manual ball valves, 1.0″and 2.0″size, are made in stainless steel, full throughway, PN 63 (Fig. 2.17a).

2.3.3 Electric Ball Valve KH 10-ELI-24

This ball valve, 1.0″size, made in stainless steel and full throughway, is actuated electrically (220 V) and it is equipped with a safety return battery. The motor opens and close the valve in approximately 10 seconds, and it can be bypassed to actuate the valve manually. In case of electrical cut the safety battery automatically powers the motor to close the valve. Three emergency buttons have been installed on the valve electrical circuit in order to cut the current and close the valve. Two buttons are strategically located in basement, one in the anechoic room, and another one outside the room, on the operator's desk.


(a)

(b)

Figure 2.17: a) Manual ball valve KH 10-ES-E. b) Electrical ball valve KH 10-ES-E .

2.3.4 High Pressure Regulators DR 8840-16-G

Two high pressure regulators are mounted in parallel to ensure a sufficient amount of mass flow rate 2.18a. The maximum inlet pressure is $p = 40$ bar and the maximum outlet is $p = 25$ bar. The volumetric flow rate diagram in Fig. 2.18b is used to calculate the mass flow rate depending on the outlet pressure. The target mass flow rate for FAST, based on the nozzle diameters and target pressure conditions, was estimated in $\dot{m} = 1.06$ kg/s, which corresponds to $5.28 \cdot 10^4$ Nl/min, or $3.17 \cdot 10^3$ Nm^3/h. The curve corresponding at the nominal working pressure in this project is 10 bar, for which the curve is plotted up to 32500 Nl/min, which is inferior to the estimated normal flow rate. However, the curves are based on $p_1 = p_2 + 2$ bar, while the flow pressure before the regulator is 35 bar, and thus the admissible flow rate would be surely larger, like for the curve 2 in Fig. 2.16. Unfortunately, it is impossible to know from the graph the maximum flow rate, and therefore, it has been decided to use two identical pressure regulator in parallel. This would also guarantee flexibility for future upgrades of the facility.

Operative instructions. When pressurizing, turn the knots of the two regulators contemporary until the desired pressure in output is reached. In case of unbalance, one of the two regulators will start venting the pressurized air into the atmosphere. If this happens, turn the knot of the venting regulator in order to increase the set pressure until the venting valve is closed.

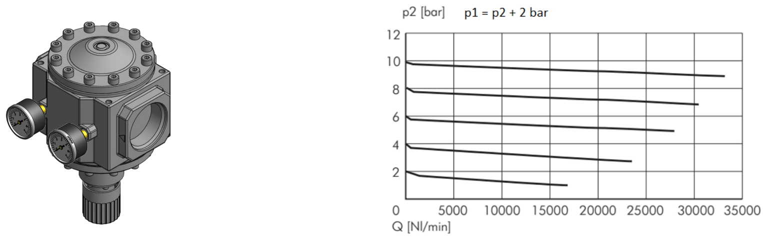

(a)

(b)

Figure 2.18: a) CAD illustration of the DR 8840-16 G high pressure regulator and b) the relative droop curves.

2.3.5 Pilot Controlled Pressure Regulators DRP-88-G

The pilot controlled regulators do not use a spring to regulate the outlet pressure, but compressed air. The source of compressed air can be an external actuator, or, like in this case, the outlet pressure itself (Fig. 2.19a). The advantage of this solution is to reduce the amplitude of the hysteresis curve, and to guarantee more stable conditions in the buffer tank. The characteristic curves of the regulator are shown in Fig. 2.19b. The maximum inlet pressure is 25 bar. Considering the estimated normal flow rate of $3.17 \cdot 10^3$ Nm^3/h, and an inlet pressure of 10 bar, this regulator works in its limit point. However because of the limitations in the mass flow rate of the 40 bar line, this limit is actually not reachable. Nevertheless, this valve may constitute a bottleneck for future increments in the mass flow rate. Increasing the inlet pressure and the output pressure would for sure make it possible, however, special care must be taken. For the inlet pressure, the maximum admissible for the pipes is 15 bar. For the outlet, the maximum pressure for the buffer tank is 11 bar, and the **lockup** must be taken in consideration.

Operative Instructions. When pressurizing, simply turn the knots until the desired pressure is reached.

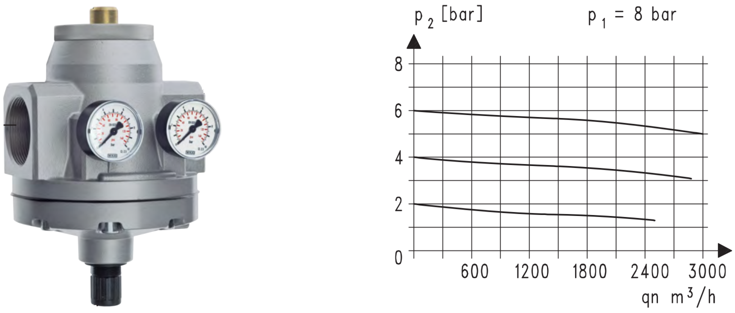

(a) (b)

Figure 2.19: Sa) CAD illustration of the DRP 88-16 G pilot controlled pressure regulator and b) the relative droop curves.

2.3.6 Buffer Tank

This tank has a capacity of 500 l, operative temperature range between -11 and 80, and it is certified up to 11 bar. The vessel was subjected to a hydraulic test up to 1.5 the operative pressure, corresponding to 16.5 bar. The tank size was selected in order to increase the settling time of the gas, to increase the mixing with the oil particles which are injected here. Given the estimated mass flow rate, at 5 bar the speed inside the tank does not exceed V_{tank} 0.6 m/s, meaning a residence time of the order of t_{tank} 3 s. This has been thought to be a good compromise considering costs and space occupied. Six 2″ports with G thread are present, and one 1/4″G thread (Fig. 2.20a). In the upper port closer to the tank inlet is located the seeding diffuser, which is a closed-end straight pipe, with 40 holes disposed circumferentially along it.

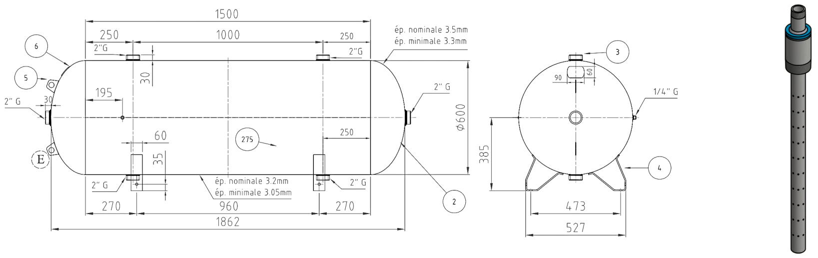

(a) (b)

Figure 2.20: a) Technical drawing of the buffer tank. b) CAD drawing of the seeding diffuser inserted inside the tank. Dimensions in mm.

2.3.7 Volume Booster DRi-88

This regulator is a copy of the previous pilot controlled DRP-88, with the difference that the knot is absent, and the source pressure must be necessarily external (Fig. 2.21a). This device is usually coupled with another, smaller, pressure regulator and it is used to increase the flow rate, hence the name "booster". In Fig. 2.21b are represented two possible configurations of feedback loop. In the first one, a precise regulator is used to set the outlet pressure of the volume booster, which is acted in order to achieve that value. In the second configuration, instead, the target pressure can be at any point downstream the volume booster. The precise regulator will act on the volume booster in order to achieve that value without knowing what is in between. This is a very interesting solution that could be implemented in order to have a directly the target pressure in the ducts, without considering the effects of the silencer. The current configuration is similar to the one shown before, except that there is no feedback loop. A precise regulator DRF-03-10 controls the DRi-88. It must be noted that being both inlet and outlet pressure lower than for the DRP-88, it is doubtful that a single DRi-88 could sustain entirely the design flow rate.

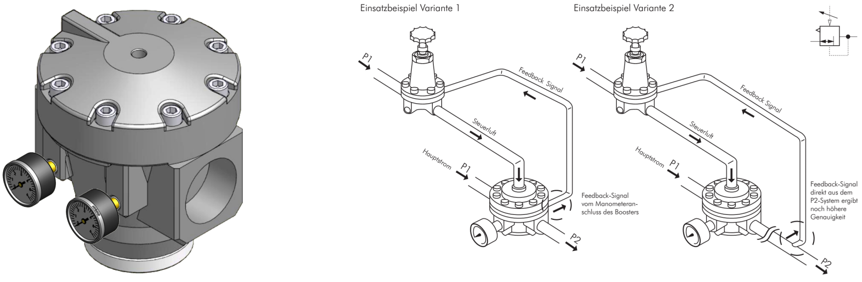

(a) (b)

Figure 2.21: a) Technical drawing of the buffer tank. b) CAD drawing of the seeding diffuser inserted inside the tank. Dimensions in mm.

2.3.8 Precise Regulator FDR-03-10

This small pressure regulator has been chosen to finely tune the volume booster (Fig. 2.22). The maximum inlet pressure is $p = 16$ and max outlet pressure $p = 10$ bar. Since the flow rate is zero, it has no meaning to consider the droop curve.

Operative Instructions. Simply turn the knot until the desired pressure conditions are reached.

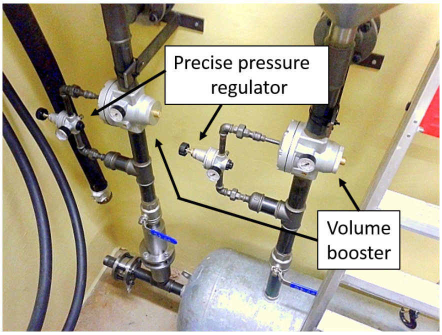

Figure 2.22: Picture of the precise regulators FDR-03-10 and the volume boosters DRi-88.

2.3.9 Flow Distributors

Before entering the silencer, the flow is split into 20 flexible pipes by two flow distributors. Those pieces are made in stainless steel in a shape of a cone, with ten 1″pipes welded on the top plate. Inside, a small conical canister has been realized using the same perforated plate used for the silencer, and filled with metallic foam. The idea at the base was to address the flow through the ten outlet and at the same time to absorb some noise from the valves.

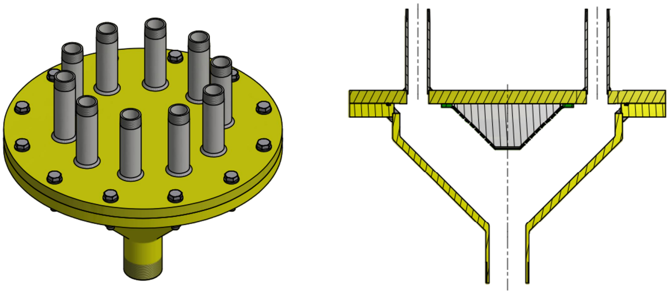

Figure 2.23: CAD drawing of the flow distributor. On the left, an isometric view. On the right, a section.

2.4 RANS Simulation of the Coaxial Jet

Before to proceed with the construction of the facility, simulations of the dual jet were performed in order to validate the nozzle geometry and to have a first insight of the flow field. The simulated geometry represents the preliminary nozzle design (shown in Fig. 2.5.a) and the results are considered extendibles also to the definitive version once scaled appropriately. The computations were carried out with COMSOL Multiphysics® 4.4 using linear triangular Finite Elements, 2D axisymmetric flow assumption and k-ϵ turbulence model. Being the primary nozzle walls only 0.3 mm thick near the outlet, the fluid dynamic problem was coupled with the heat transfer in solids model, with the aim to verify possible influences of the heat transfer, across the walls on the shock-cells system. Furthermore, the Solid Mechanics interface was used to verify the walls resistance to deformations due to the combined stresses of the shear stress, pressure and thermal stress. It should be enforced here that the goal of the simulations were only to validate the nozzle design and to provide insights of the flow fields useful for the development of the experimental setup.

2.4.1 Fluid Dynamics Model

The simulation of the coaxial flow was carried out by means of the interface High Mach Number Flow using a k-ϵ model. The computational domain is rectangular, extending for 18 D_s after and 6 D_s before the nozzle in the axial direction, 5.5 D_s in the radial direction. The ambient pressure was p_a = 101325 Pa and the initial temperature was set to 293.15 K. Three boundaries 'Inlet' are present at the bottom of the domain, two boundaries inside the nozzles (p_{01}, p$_{02}$, T_{01}=T_{02}=293.15 K, M_1=M_2=0.01) and the third outside (p_3=101325 Pa, T_3=293.15 K, M_3=0.01). The boundaries 'Outlet' are the side and top edge of the domain with $p_{a,outlet}$=101325 Pa. The default model 'Wall', no slip, is applied to all surfaces of the nozzle. The simulations were carried out varying only the total pressure at the two nozzle inlets. The test conditions are the same of Tab. 2.1.

2.4.2 Heat Transfer Model

The reason to apply the model is because a heat transfer through the thin walls of the nozzle is expected; in particular from the internal flow (warmer) to the external one (colder). It is well known that positive heat flux has destabilizing effects on the boundary layer, and so, also on the development of the supersonic region (in particular the position of the first shock-wave). Two materials currently in use at VKI for manufacturing were selected from the COMSOL material library: brass and structural steel. These metals have significantly different thermal conductivity as well as Young's module and yielding stress. As boundary conditions a fixed temperature, T_m = 293.15 K, was imposed at the bottom edge of the nozzles, as well as initial temperature inside the material.

2.4.3 Structural Model

A load function was created with the pressure extracted from the CFD results and applied to the nozzle walls. As other boundary conditions, fixed constraints was imposed to the bottom edge of the nozzle.

2.4.4 Mesh Sensitivity

For the mesh sensitivity, the feature 'Physics Controlled Mesh', with the 'Extremely fine' option, was firstly used. However, it was assessed the mesh was not sufficiently refined in the supersonic region. Consequently, other two meshes with higher resolution were created and tested with the same pressure conditions. An example of the Mesh 1 and Mesh 2 in the nozzles exit region is shown in Fig. 2.24. A Mesh 3, omitted for clarity, was created with a maximum element size being half of Mesh 2. Details on the three meshes are shown in Tab. 2.2.

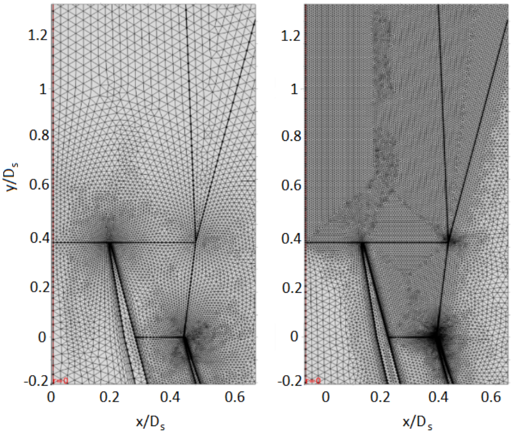

Figure 2.24: Comparison of 'Physics Controlled' Mesh 1 and 'User-defined' Mesh 2.

	Maximum element size in the shock region	Total number of elements
Mesh 1	0.002	$3.4{\cdot}10^5$
Mesh 2	0.0005	$2.7{\cdot}10^5$
Mesh 3	0.00025	$6.0{\cdot}10^5$

Table 2.2: Meshes main characteristics

The comparison between the three meshes was done by plotting the Mach number along a line starting at the beginning of the supersonic region. The graph in Fig. 2.25 shows how the results for Mesh 1 has poor resolution in

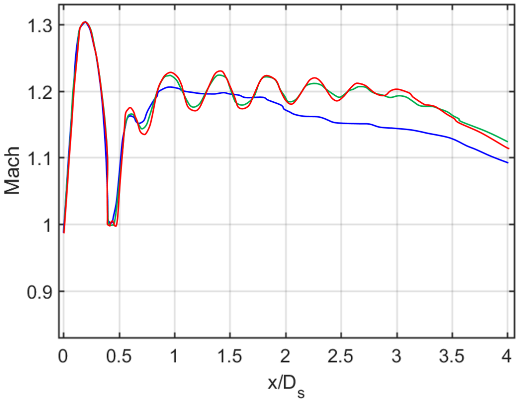

Figure 2.25: Comparison of ’Physics Controlled’ Mesh 1 and ’User-defined’ Mesh 2 and Mesh 3. Data was extracted from the dashed line in Fig. 2.27.

comparison of Mesh 2 and Mesh 3. The Mesh 2 is capable to calculate the first peak in accord with Mesh 3, but the amplitude for the other peaks is slightly different. In conclusion, because of the relatively high computational cost of Mesh 3, it was decided to carry out all the simulations using the Mesh 2.

2.4.5 Results

A shock-cells system is present starting from the exit of the secondary nozzle, surrounding the primary jet. For all the simulated condition, a strong, conical, shock-wave is present, starting from the lip of the primary nozzle and refracting back into the flow when reaching the external shear layer. After the shock, the flow is locally subsonic, becoming again supersonic after a few distance, leading to the formation of annular shock-cells in the wake, between the internal shear layer and the external shear layer. The main result of this simulation was, however, the assessment of the coaxial nozzle geometry, which, in fact, was initially not correct. Fig. 2.26a) shows that the sonic throat was not at the exit of the secondary nozzle, leading, effectively, to a convergent/divergent geometry. An ‘ad hoc’modification was thus adopted to solve the problem, as visible in Fig. 2.26b) , and successively this second geometry was used to manufacture the real nozzles.

All the test conditions were simulated, but, for brevity, only some of them would be presented. Condition 01 was established to be the reference test condition for the AeroTraNet2 network. Pérez Arroyo performed LES [67], in parallel with this project, using the same nozzle geometry and test conditions, and compared its results with the PIV measurements described in Sec. 4. Fig. 2.27a) shows the velocity field together with M ¿ 1 isocontour lines. The

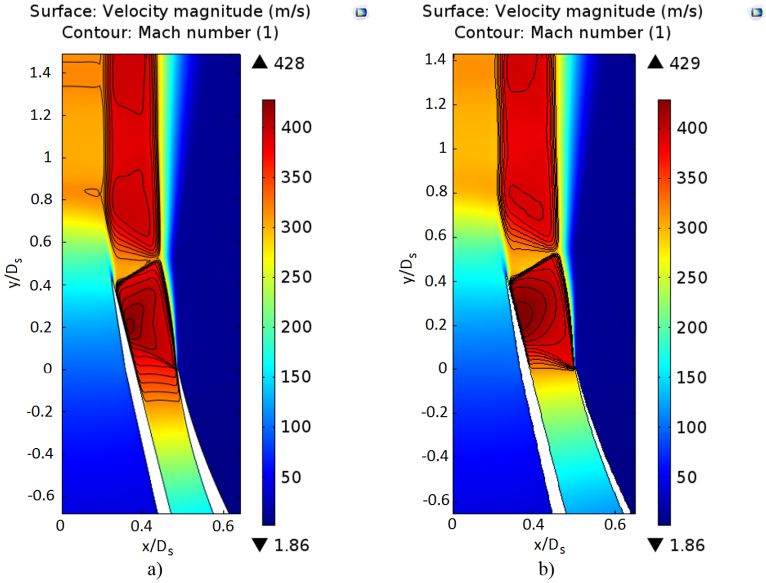

Figure 2.26: Comparison of the preliminary nozzle geometry a) with the final optimized geometry b). In the preliminary version the sonic throat was inside the nozzle, leading to a convergent-divergent shape. Subsequently, the inner profile was thinned leading to the final version, where the sonic throat is at the nozzle exit.

primary flow velocity appears to be modulated in space following the series of expansions and compressions of the annular shock-cells. This appears even more evident if the pressure field is observed (Fig. 2.27b)). The pressure pattern in the secondary flow is transmitted radially into the primary stream apparently without obstacles. The presence of the primary flow shear layer, in fact, is not detectable with this view, thus supporting the hypothesis that the secondary stream is effectively guiding the primary one. This pattern remains substantially unchanged from Cond.01 to Cond.06, a progressive reduction on the length of the shock-cells, due to the total pressure reduction, as expected. Cond.07, instead, shows a very different pressure pattern, as visible in Fig. 2.27c). The color scale is enlarged to highlight small pressure differences. A complete shock-cell is formed also in the region between the external shear layer and the wall of the internal nozzle, while the starting point of the shock-cells in the wake is shifted downstream. This may suggest a destructive interaction between the conical shock-wave refractions and the expansion waves related to the underexpansion factor. Furthermore, the primary jet pressure is not modulated anymore following the secondary stream. This behavior was successively confirmed by PIV measurements, relatively to the velocity field (Sec. 4.2.2). Further lowering the total pressure, shock-cells between the secondary shear layer and the primary nozzle wall are still present, while a large subsonic region is developing after the oblique shock-wave, becoming supersonic again much downstream the primary nozzle exit (Fig. 2.27.d). No further shock-cells are visible in the wake. PIV measurements, show, instead the presence of weak shock-cells also in the wake, but confirm the complex shock-waves interaction downstream the primary nozzle.

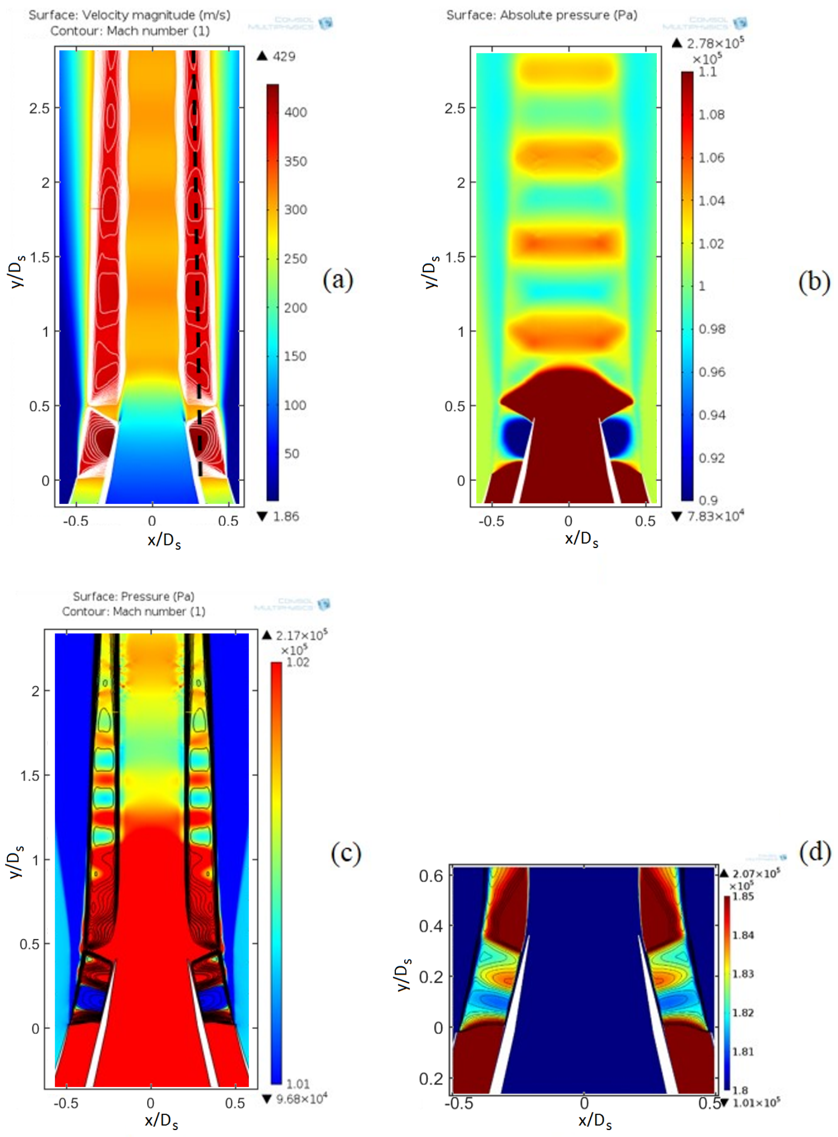

Figure 2.27: RANS simulation of the coaxial jet at several test conditions. Axes units are non-dimensionalized by the secondary diameter. (a) the velocity field and (b) the pressure field for Cond.01. Mach > 1 contour lines in white are superimposed. Data extraction is performed along the dashed black line. (c) Pressure field at Cond.07 and Cond.08 (d). Mach > 1 contour lines in black are superimposed.

Mach number profiles for all tests were extracted along an arbitrary line (black dashed line in Fig. 2.27.a) and compared in Fig. 2.28. The reason for this location follows the difficulties to identify univocally the place of maximum velocity variation in the shock-cells, and therefore a physical reference in the space was preferred. The same approach was applied also by Miller&Morris in [54]. The profiles show a progressive reduction of the Mach number oscillations and shock-cell length. For Cond.08 and Cond.09 no shock-cells are visible in the wake, but two are present before the primary nozzle exit.

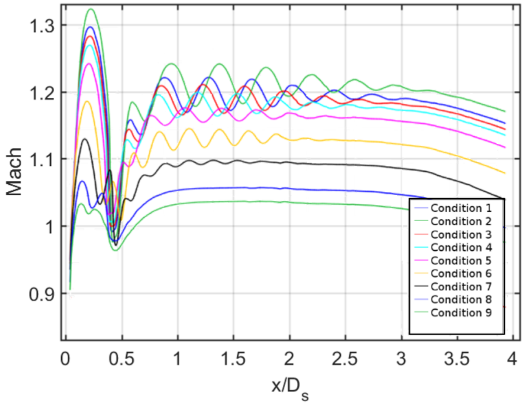

Figure 2.28: Comparison of Mach number of all test IDs along a line described in Fig. 2.27 and projected on the jet axis non-dimensionalized by the primary nozzle diameter.

2.4.5.1 Effects of the conical shock-wave

Another important result of this investigation is the identification of a deviation of the computed mass flow rates, compared with the expected ones, obtained using the isentropic relations. Especially for the mass flow rate of the primary nozzle, important differences were found for all the test conditions, which are summarized in Tab. 2.3. The reason for this behavior can be attributed to the strong re-compression at the end of the primary nozzle due to the oblique shock-wave generated by the secondary stream. This analysis led the choice to directly measure the primary mass flow rate with the orifice plate described in Sec. 2.2.4. From a macroscopic point of view, the major impact would be, of course, in the by-pass ratio, which would sensibly increase as shown in the previous Tab. 2.1. The reduction in the mass flow rate for the secondary stream, instead, may be due to the presence of the boundary layers. It is believed, however, that this variation is overestimated, due to the discretization and the model used for the boundary layer.

	mass flow rate isentropic		mass flow rate COMSOL		Variation respect to isentropic relations in percentage	
Test ID #	$\dot{m}_1$ [Kg/s]	$\dot{m}_2$ [Kg/s]	$\dot{m}_1$ [Kg/s]	$\dot{m}_2$ [Kg/s]	$\Delta\dot{m}_1$ %	$\Delta\dot{m}_2$ %
1	0.173	0.860	0.118	0.817	-31.9	-4.9
2	0.179	0.877	0.121	0.834	-32.1	-4.9
3	0.170	0.850	0.115	0.809	-32.1	-4.9
4	0.167	0.842	0.114	0.801	-31.9	-4.9
5	0.162	0.825	0.111	0.784	-31.6	-5.0
6	0.152	0.790	0.104	0.750	-31.9	-5.0
7	0.143	0.754	0.091	0.716	-36.5	-5.1
8	0.132	0.719	0.082	0.681	-38.4	-5.3
9	0.127	0.702	0.077	0.664	-39.3	-5.4

Table 2.3: Mass flow rate comparison between the theoretical values obtained with the isentropic relations and those calculated with COMSOL

2.4.5.2 Effects of the heat transfer and structural deformations

Concerning the influence of the heat transfer, simulations with and without the heat flux through the walls were carried out with two materials, brass and steel. It was shown how with both materials, despite being good heat conductors, the difference of temperature is not sufficient to influence the shock-cells pattern. To further assess this, it was tried increasing the total temperature in the primary flow up to T_{0p}= 1000 K. Only in this case, the conical shock-wave slightly moved upstream due to a small enlargement of the separation zone at the end of the nozzle lip.

The structural simulations were carried out separately, using the pressure loadings on the walls retrieved by the previous CFD tests. In Fig. 2.29 the von Mises stress (colors) and displacements (magnified 14000 times in the figure) are shown. Results are related to Cond.02, which is the most loaded condition, using brass as material. The maximum stress is well below the yielding point of the material ($\sim 8 \cdot 10^7$ Pa for commercial brass), despite the small thickness of the lip edge. The maximum displacement, at the secondary nozzle lip, are of the order of $3.5 \cdot 10^{-4}\%$ of the secondary nozzle diameter, in both axial and radial direction, and thus are considered negligible. A simulation using steel was not, thus, performed.

The reality, unfortunately, told a different story. As explained in Sec. 4.1.2, during the experiments a not negligible vertical displacement of the whole secondary nozzle and duct was experienced. This was not found in the simulation because the focus was only on the nozzle lip deformation, and not on the duct. The latter, for simplicity, was represented more thicker than the real one, and much shorter.

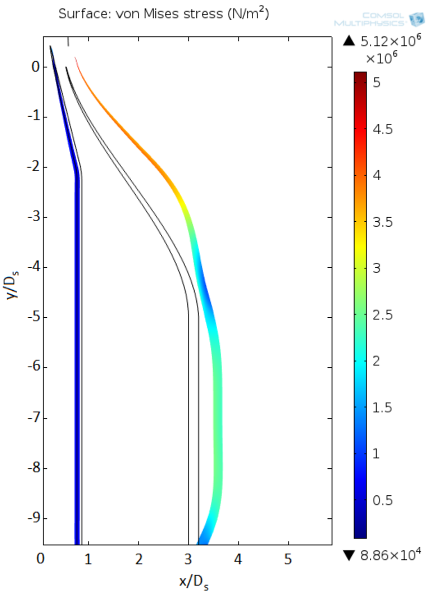

Figure 2.29: von Mises stresses and displacements magnified 14000 times for condition 2. Axes units in m, colorbar in Pa

2.5 Acoustic Simulations of the Silencer

The acoustic performances of the silencer were also simulated with COMSOL Multiphysics® 5.0. The acoustic module of the software was used to compute the transmission loss between the ten inlets and the silencer outlet, including the effects of the phono-absorbent material and the canisters holding it in position.

It is assumed that the flow is not moving inside the silencer, so no sound production and no convection effect take place. This hypothesis is justified by the small Mach number inside the silencer (M $\simeq$ 0.01), thus small noise production is expected in comparison with the noise emissions generated by the valves, where the flow is choked. The problem was solved in the frequency domain using the Pressure Acoustics module, Frequency Domain interface. The model equation is a slightly modified version of the Helmholtz equation for the acoustic pressure p:

$$\nabla \cdot \left(-\frac{\nabla p}{\rho} \right) - \frac{\omega^2 p}{c^2 \rho} = 0, \tag{2.1}$$

where ρ is the density, c is the speed of sound, and ω is the angular frequency.

For the steel wool, modeled as a Poroacoustic domain, the damping is introduced into the equations as a complex speed of sound, $c_c = \omega/k_c$, and a complex density, $\rho_c = k_c Z_c/\omega$, where k_c is the complex wave number and Z_c equals the complex impedance. With this equivalent fluid model for the porous domain, the losses are modeled in a homogenized way. For a highly porous material with a rigid skeleton, the well-known model of Delany and Bazley estimates these parameters as functions of frequency and flow resistivity. Using the original coefficients of Delany and Bazley[27], the expressions are:

$$k_c = k_a \cdot \left(1 + 0.098 \cdot \left(\frac{\rho_a f}{R_f} \right)^{-0.7} - i \cdot 0.189 \cdot \left(\frac{\rho_a f}{R_f} \right)^{-0.595} \right), \tag{2.2}$$

$$Z_c = Z_a \cdot \left(1 + 0.098 \cdot \left(\frac{\rho_a f}{R_f} \right)^{-0.734} - i \cdot 0.189 \cdot \left(\frac{\rho_a f}{R_f} \right)^{-0.732} \right), \tag{2.3}$$

where R_f is the flow resistivity, c$k_a = \omega/c_a$ and $Z_a = \rho_a/c_a$ are the free-space wave number and impedance of air, respectively. Flow resistivity can be estimated using the tables developed by [21] (the chosen option) or by measurement. For glass-wool-like materials, Bies and Hansen [13] give an empirical correlation:

$$R_f = \frac{3.18 \cdot 10^{-9} \cdot {\rho_{ap}}^{1.53}}{{d_{av}}^2}, \tag{2.4}$$

where ρ_{ap} is the material apparent density and d_{av} is the mean fiber diameter. For grade #000 fine steel wool d_{av}=35 μm, ρ_{ap}=166 kg/m^3 and R_f=6472 kg/(m^3·s).

For the perforated plate, containing the steel wool, COMSOL Multiphysics calculates the transfer impedance using the following model expression by Bauer [9]:

$$\frac{Z}{\rho_c c_c} = \left(\frac{1}{\sigma}\sqrt{\frac{8\mu k_{eq}}{\rho_c c_c}}\left(1 + \frac{t_p}{d_h}\right) + \theta_f\right) + i\frac{k_{eq}}{\sigma}\left(t_p + \delta_h\right), \tag{2.5}$$

where μ is the dynamic viscosity. The area porosity σ is the hole's fraction of the boundary surface area, a dimensionless number between 0 and 1. For the present design σ=0.4, t_p=1.5 mm is the plate thickness, d_h=4 mm is the holes diameter. d_h is the end correction to the reactance, (the default is 0.25d_h), θ_f=0 is the flow resistance, which is a contribution to the resistive part of the impedance which takes into account effects of a mean flow, or nonlinear effects at large sound pressure levels.

The boundary conditions are of three types: solid boundaries, inlet and outlet. At the solid boundaries, such as the outer walls of the silencer and the pipes, the model uses sound hard (wall) boundary conditions. The condition imposes a normal velocity of zero. The boundary condition at the inlet involves a combination of incoming and outgoing plane waves [30]. This boundary condition is valid as long as the frequency is kept below the cutoff frequency for the second propagating mode in the tube, as it happens in the case studied. At the outlet boundary, the model specifies a radiation condition for an outgoing plane wave, a valid assumption in the case studied. The whole silencer, plus a limited portion of the ducts (for computational efficiency) and the nozzles were included into the computation. Because of the area contraction of the nozzles, for the simulated frequencies, the plane wave boundary condition is respected due to the contraction. The only requirement to apply to the ducts is that they shall be long enough to allow the modes to fully develop. The presence of the honeycomb, as well as the screens installed in the ducts, is neglected, as it is not expected to influence sound propagation significantly, other than some noise reflection and dumping effects. The length of the ducts should not take a relevant role, until they are sufficiently long to guarantee the modes fully development. The other simplification is to neglect the presence of the honeycomb and the screens which are installed in the ducts. The domain was meshed with tetrahedral linear elements, with the maximum element length equal to $1/10^{th}$ of the smallest computed wavelength.

Simulations were carried out for fifty frequencies in the range $100 \leq f_s \leq 5000$. The upper limit of 5000 Hz was chosen since the higher frequencies are expected to be efficiently damped. The amplitude of the forcing at the 10 inlets is 1 Pa. It is expected to find in such range several duct or resonant modes. This has been assessed using COMSOL, and a very large resonant

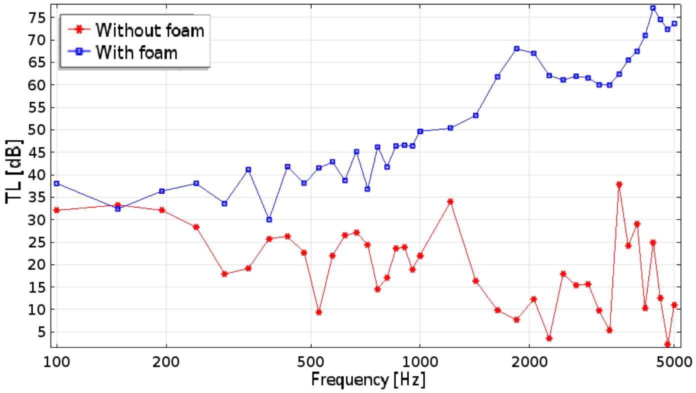

Figure 2.30: Transmission Loss of the silencer for the primary flow.

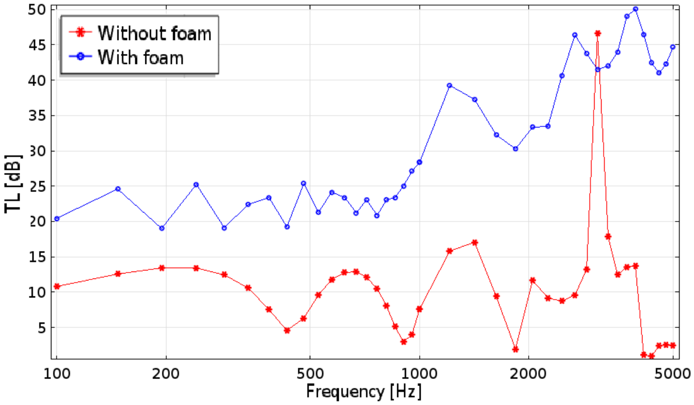

Figure 2.31: Transmission Loss of the silencer for the secondary flow.

modes were found, due to the complex geometry. The number of modes was, in fact, too large to be investigated on a single basis. Furthermore, how it will be shown hereafter, including the poroacoustic material and the perforated plate in the model, there are not such deeps in the transmission loss to justify further investigation. The transmission loss is defined as the ratio between the incoming and outgoing acoustic energy. The attenuation TL (in dB) of the acoustic energy is defined by the following equation:

$$TL = 10\log\left(\frac{w_{in}}{w_{out}}\right). \tag{2.6}$$

where w_{in} and w_{out} denote the incoming power at the inlet and the outgoing power at the outlet, respectively. It is possible to calculate each of these quantities as an integral over the corresponding surface:

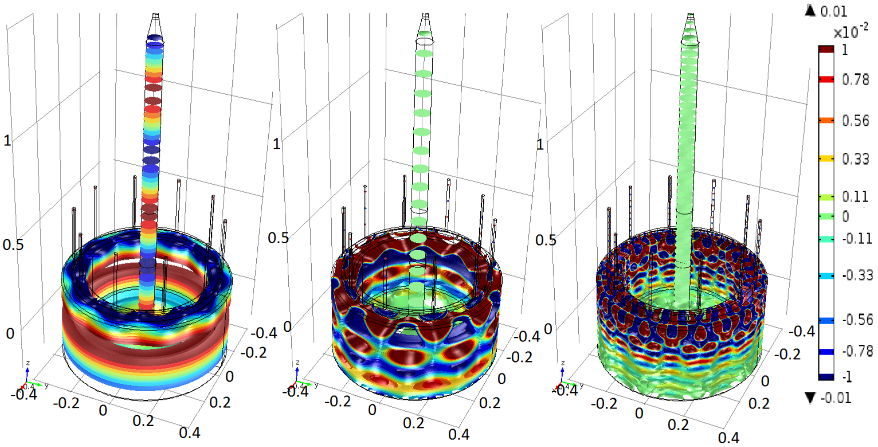

Figure 2.32: Acoustic pressure field isosurfaces in the primary flow circuit at 570 Hz (left), 1840 Hz (center) and 5000 Hz (right). The scale (in Pa) enhances the modes visualization that otherwise would be very faint at full scale. The forcing amplitude is 1 Pa on each inlet. Axes units are in m.

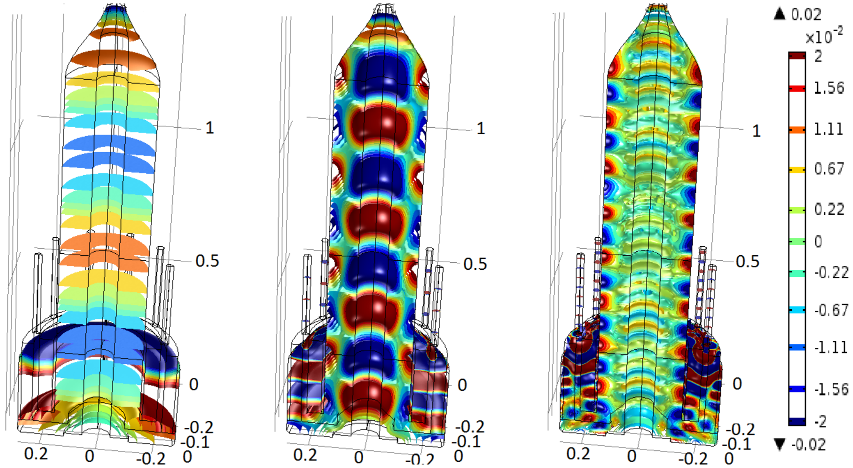

Figure 2.33: Acoustic pressure field isosurfaces in the secondary flow circuit at 480 Hz (left), 2050 Hz (center) and 4790 Hz (right). The scale (in Pa) enhances the modes visualization that otherwise would be very faint at full scale. The forcing amplitude is 1 Pa on each inlet. Axes units are in m.

$$\omega_{out} = \int_{\delta\Omega} \frac{|p|^2}{2\rho c} dA \quad \text{and} \quad \omega_{in} = \int_{\delta\Omega} \frac{{p_0}^2}{2\rho c} dA \tag{2.7}$$

The results of the simulations are shown in Figs. 2.30 and 2.31. From the two graphs it is possible to see how the damping without foam is already effective at low frequencies, with some negative peaks that should represent the cavity resonant modes, at higher frequencies. With the foam, instead, the damping is much more effective especially at higher frequencies, thus confirming the design choices.

In Figs. 2.32 and 2.33 pressure waves propagating at different frequencies. With increasing frequency, more modes are developing in the silencer and in the conduits, especially for the secondary flow circuit. However, as they approach the convergent nozzle, the acoustic waves become planar again, avoiding spurious reflection at the boundary.

To verify that this effect is not due to the boundary condition imposing a wave planarity to the flow, another simulation was carried out without the nozzle. Fig. 2.34 shows how higher modes are leaving the domain without modification.

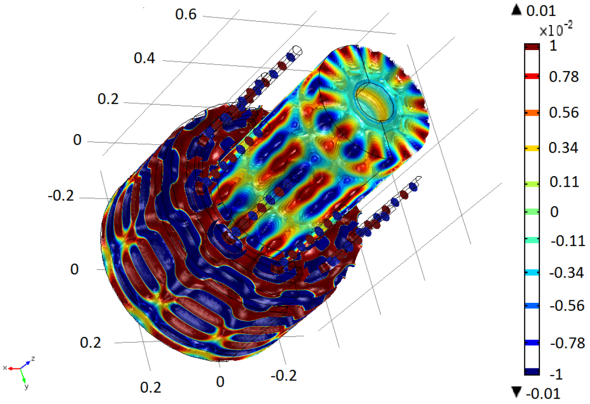

Figure 2.34: Acoustic pressure field isosurfaces in the secondary flow circuit at 4370 Hz, with a short conduit trait and no nozzle. We can observe at this enhanced scale how the mode propagation at the exit is not forced to plane wave mode by the boundary condition. The scale (in Pa) enhances the modes visualization that otherwise would be very faint at full scale. The forcing amplitude is 1 Pa on each inlet. Axes units are in m.

2.6 Control Equipment

In this section, the installed control equipment, such the acquisition system, pressure probes and thermocouples, is described.

2.6.1 Pressure Probes

Two OMEGA pressure sensors model PXM419 are used to measure the static pressure in the ducts for both the core and the fan nozzles. Due to the large area ratio between the ducts and the nozzle exits, equal to $AR_p = 11.6$ and $AR_s = 50$ for the primary and secondary flow respectively, the Mach number is limited to M ¡ 0.05. Therefore, the pressure measured is assumed to be the total pressure with an uncertainty inferior to 0.2%. The pressure range of the sensors is from 0 until 4.5 bar, with a standard accuracy of 0.08% according to the data sheet. Since newly purchased probes were used, only a check with a calibrator at the maximum pressure range was performed. The data signal was recorded using a National Instruments 9215 analog to digital converter placed in a NI cDAQ-9174 4 slot chassis. The sampling rate is set to 51.2 kHz with low-pass analog filter at 25.6 kHz, imposed by the acquisition module. From the manufacturer data-sheet, the frequency response of the instrument is of the order of 1 kHz, and thus data samples are acquired over 1 s periods, numerically filtered above 1 kHz, and finally averaged and stored. Ambient pressure is retrieved from the measurement of a Druck DPI 150 precision pressure indicator located near the anechoic room.

2.6.2 Thermocouples

Two OMEGA KMQSS-IM150U-150 K-type thermocouples are used to measured the ambient temperature of the room and the total temperature of the two streams. In order to measure the ambient temperature of the room, one thermocouple is attached to one of the walls of the anechoic chamber. The second thermocouple is located downstream the mass flow meter described in Sec. 2.2.4. The thermocouple is mounted in the middle of the pipe section, where the Mach number, according to the primary nozzle area ratio $AR_p = 4$, is at maximum M = 0.14. Assuming a homoenthalpic flow in the valves, the temperature measured corresponds to the total temperature of the flow for both circuits. The signals from the thermocouples were acquired through a NI 9211 24-bit resolution analog to digital converter. The module is specifically designed to support K-type thermocouples. The module was installed in the same 4 slot NI 9174 chassis used for the pressure sensors.

The thermocouples were calibrated before each test campaign. After it was discovered that the temperature can fall below 0^oC, the thermocouple was calibrated to cover this range as well. The calibration was carried out using a oil bath and a mercury thermometer as a reference temperature indicator.

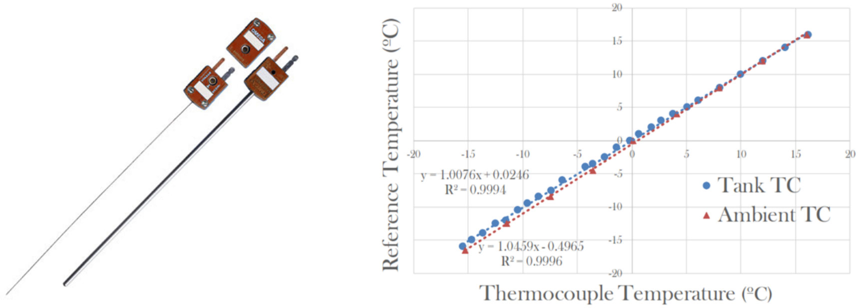

(a) (b)

Figure 2.35: a) Picture of the thermocouples OMEGA KMQSS type K installed into the mass flow meter and into the anechoic chamber. b) Calibration curve of the thermocouples [77].

When a first calibration attempt using pure oil proved to be unfeasible, since the oil became too viscous and temperature distribution inhomogeneous, it was decided to carry out the calibrations using a mixture of 50% water - 50% ethanol. The calibration curves are shown in figure 2.35.

2.7 FAST Limitations and Upgrades Analysis

In this section, an analysis on the performances of the facility, and how to improve them, is presented. Under the word ”performances”, many parameters could be ascribed, such as: energetic efficiency, safety, acoustics, reliability, etc... Three parameters, however, have the highest impact on the capability of the facility to simulate a jet (single or dual stream): mass flow rate, pressure and temperature.

2.7.1 Mass Flow Rate

The mass flow rate is a limiting factor which impact mainly the size of the jet rig. It is straightforward to think that, for constant exit speed and temperature, higher the jet area, higher is the demanded flow rate. The same is valid for increasing the jet speed.

$$\dot{m} = \rho V A \tag{2.8}$$

Where $\dot{m}$ is the mass flow rate, ρ is the density, V is the flow velocity and A is the flow passage area. Being the mass flow rate directly dependent on the flow density, increasing the pressure would automatically increase the mass flow rate in a certain section of the circuit. For a given section, is also straightforward to compute the maximum mass flow rate that can pass through it, corresponding to the choked condition:

$$\dot{m}^* = \rho^*(T^*)c(T^*)A^* \tag{2.9}$$

Where the * denotes the critical condition, and $c(T*)$ is the speed of sound at the critical temperature. The boundary layer, is not considered in this formulation, and thus this formula always overestimate the real mass flow rate. Given the Eq. 2.9, it is possible to compute for each section the maximum mass flow rate, depending on the local pressure and temperature. The problem arise in determining the correct pressure and temperature in a duct, considering that pressure losses occur in the line. Given a certain mass flow rate at the pipe inlet, with the pipe having adiabatic walls, after a certain length the pressure would drop because of friction. The pressure would thus decrease, and consequently, because of mass conservation, the flow must accelerate. Because the pressure drops are proportional to the square of the velocity, the flow would accelerate more rapidly and, if the pipe is sufficiently long, it would reach sonic speed at the pipe outlet. This happened in the initial phases of the commissioning, when the nozzle shown in Fig. 2.5a) was tested, and the 40 bar line choked. Eq. 2.9 can be rearranged in order to give:

$$\dot{m} = \frac{p_0 A^*}{c_0}\Psi^* \tag{2.10}$$

where $\Psi* = 0.8102$ is the critical efflux factor, which is valid for choked flows. Using this formula, the maximum available mass flow rate for $1''$ pipe, with $p_0 = 35$ bar, $T_0 = 273.15$ K, should have been $\dot{m} = 4.68$ Kg/s. Instead, the maximum stable condition reachable was Cond. 07 in Tab. 2.3, corresponding to $\dot{m} \sim 0.90$ Kg/s. When the gas started flowing, the static pressure gauge on the 40 bar line dropped from 35 to 19 bar, and after several minutes it reached the value of 7 bar, which is the minimum to operate the seeding generator correctly, and finally to 3 bar, which is the minimum to have supersonic flow conditions in the nozzle. When the flow was stopped, the static pressure gauge returned total pressure of p_0 25 bar.
This is a very limiting factor, considering the facility was designed to work in a range of $15 \leq p_0 \leq 35$ bar. The time at disposal of the researcher to perform the measurements is reduced by more than a half. Furthermore, for higher conditions the pressure rapidly drop under the working limit of the seeding generator, making impossible to use PIV.

A posteriori, this behavior was found to agree very well with the Fanno theory.

2.7.1.1 Fanno flow theory

The Fanno equations are valid for a steady, 1-D, constant area, adiabatic flow with no external work but with friction. The hypothesis at the base are:

- $h = const$, since adiabatic walls, no work;
- $\rho V = const$, since A is constant;
- $H = h + V^2/2 = const$, by construction;

where H is the total enthalpy, h is the sensible enthalpy.

Without going into details, from the momentum conservation it is possible to derive the following equation:

$$dI = dp + \rho V dV = -4f\frac{1}{2}\rho V^2 \frac{dx}{D_e} < 0 \tag{2.11}$$

where dI is the total impulse variation, f is the Fanning coefficient, D_e is the equivalent duct diameter and dx is the variation in the x direction. While the impulse decrease, the entropy, instead, increase. Because of the fluid dynamics equations, the behavior of the flow of the subsonic and supersonic regimes, is opposite: in subsonic regime the flow is accelerating, while in supersonic regime it is decelerating.

This is synthesized in Fig. 2.36, where a normalized Fanno curve is depicted in the Gibbs plane (top) and in a Mach-specific entropy plane (bottom). Given a starting point on a subsonic or supersonic branch of the curve, the point can evolve only towards the right of the graph, because entropy can only increase. Isocore curves are also plotted and labeled respect to the point they refer (A, B, C, etc...) . Following the subsonic arm, from the point A to C, it can be appreciated the loss of the total pressure, because the isocore p_{0C} is under the curve for p_{0B}, and p_{0B} is under p_{0A}. The same behavior occur for the supersonic branch, from point D to C, except that the static pressure is, instead, increasing (isocore p_C is above isocore p_E and p_D).

It is important to note that equations do not forbid to jump from one arm to the other given that the second thermodynamic principle is not violated. This means that a flow, initially supersonic, can became subsonic inside a duct when a steady shock-wave is present, and then continuing in the subsonic branch.

After further mathematical derivation, it is possible to arrive to Eq. 2.12, which is a differential equation linking the variation of the Mach number with the variation of the non-dimensional length $4f dx/D_e$, which can be used to determine the flow conditions after a certain pipe length L_{12}, given the initial Mach number M_1.

$$\frac{M^2 - 1}{\gamma M^2 \left(1 + \frac{\gamma - 1}{2} M^2\right)} \frac{dM^2}{M^2} = -4f\frac{dx}{D_e} \tag{2.12}$$

All the characteristic ratios can be derived based on the non-dimensional duct length. Fig. 2.37 shows all the curves in function of the initial Mach number and the critical non-dimensional parameter $4fL^*/D_e$, where L^* is

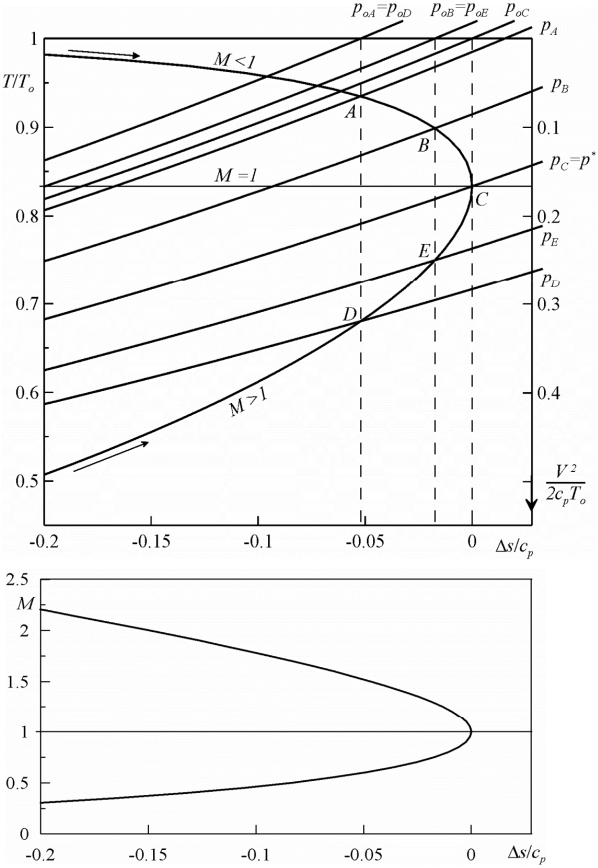

Figure 2.36: Normalized Fanno curve plotted in the Gibbs plane, together with isocore curves (top). The arrows on the curve shown the direction of the flow evolution in a duct. The equivalent curve in the Mach-specific entropy plane. Taken from [16].

the duct length for which the flow reaches the speed of sound, given an initial Mach number. All these values can be found in tables.

A question may arise: what happens to the flow when the pipe is longer than L^*? The answer is that the flow can be sonic only at the exit of the pipe, therefore, if the non-dimensional parameter $4fL^*/D_e$ increases for some reason (increment of friction due to dust deposits, or reduction of the equivalent area), a new, lower, initial Mach number is set, and therefore, also the mass flow rate will be lower.

A practical example on how to use the Fanno theory is shown in Fig. 2.38. A straight duct is attached to an isentropic convergent nozzle, which is used set up an initial Mach number. The pressure at the outlet is lower enough

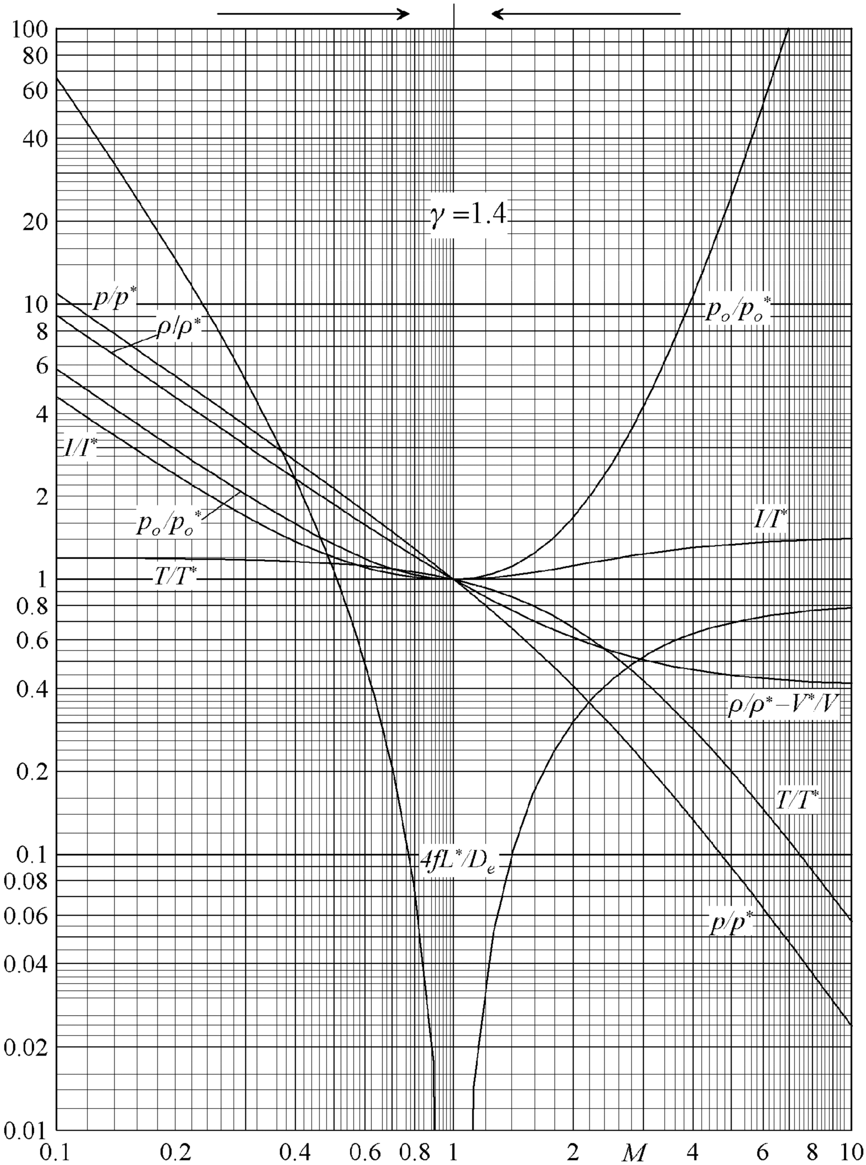

Figure 2.37: Chart of the characteristic ratios in Fanno flows. Taken from [16].

to guarantee sonic conditions.
Without the duct ($4fL^*/D_e = 0$), the flow accelerates isentropically until the sonic condition, following the curve a in Fig. 2.38b) and c). On the

Fanno curve in Fig. 2.38d), the flow passes from the point O to A, without an entropy increment.
When a short piece of duct is added $4fL^*/D_e = 0.3$, the initial Mach number must be $M_1 = 0.66$, as shown in 2.38b) and thus the mass flux must be also lower. On Fig. 2.38d) the flow accelerates isentropically from point O to B, and then on the Fanno curve from B to E. The Fanno curve is more external than the previous one, meaning lower mass flux, and $p_E < p_A$.
Further increasing the duct length, the initial Mach number progressively decreases, as well as the outlet pressure.

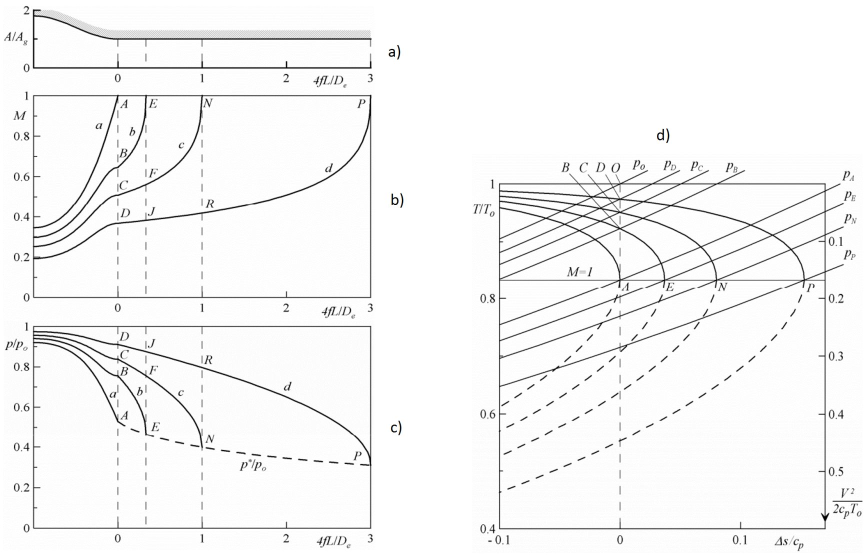

Figure 2.38: Chart of the characteristic ratios in Fanno flows. Taken from [16].

2.7.1.2 Mass flow rate limit calculation using the Fanno theory

The theory has been used to compute the mass flow rate of the facility given the initial total pressure, measured at the gauge upstream the electric valve, the static pressure with the gas flowing, and the circuit characteristics.

The FAST facility is located at the very end of the 40 bar line circuit. The majority of the distance between the VKI tanks and the installation is equipped with 2.5″ pipes, and only for the last trait 1″ pipe is used. Unfortunately, a detailed map of the VKI pipeline was not available, and therefore the length of each segment was measured using a laser meter. A sketch of the circuit is provided in Fig. 2.39.

The total length of the 2.5″ pipe is estimated to be $l_{3''} = 100 \pm 2$ m, while for the 1″ line $l_{1''} = 40.5 \pm 0.5$ m. For the scope of this exercise, the pressure

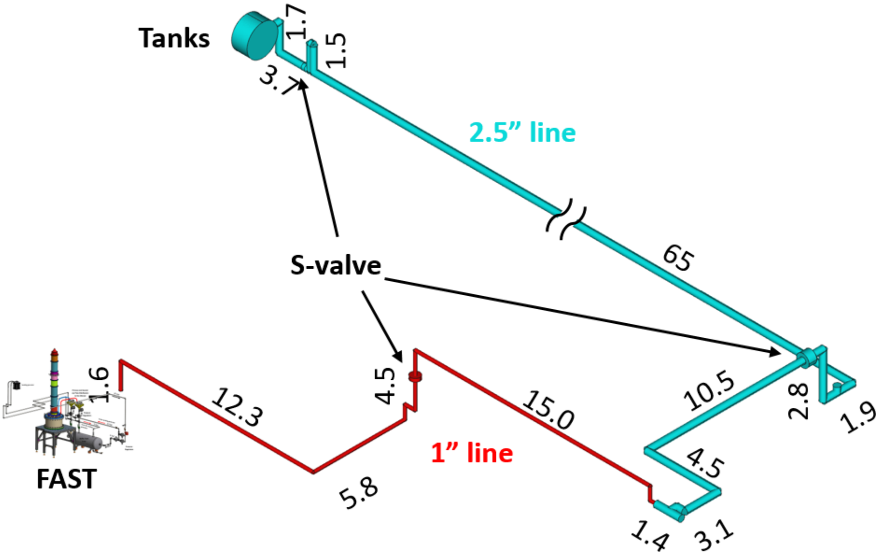

Figure 2.39: Sketch of the VKI 40 bar line. Dimensions are in m.

losses due to the pipe bending and control valves is not considered, and thus the pressure losses are underestimated.

The Fanning coefficient was calculated starting from the pipe rugosity, which was measured using a rugosimeter. The average of 15 measures on a $1''$ pipe internal wall is $\epsilon = 3.28 \cdot 10^{-6}$ m, leading to a non-dimensional rugosity $\epsilon/D_{1''} = 1.26 \cdot 10^{-4}$.
As initial guess, $\dot{m} = 0.7$ Kg/s was used. Based on that, and using the isentropic relations, the estimated Mach number was $M_{1''} = 0.087$ and $M_{2.5''} = 0.015$, for the $1''$ and $2.5''$ pipes respectively. For the $2.5''$ pipe, based on the initial Mach number the non-dimensional length is of the order of $4fL^*/D_e = \mathcal{O}(3 \cdot 10^3)$, and thus the flow acceleration inside the duct was considered negligible.
By exclusion, this means that the main limiting factor is the $1''$ pipe. The estimated Reynolds was $Re_{1''} = 1.85 \cdot 10^6$. However, in reality, the flow accelerates up to $M = 1$, with associated $Re_{1''} = 1.90 \cdot 10^7$. Therefore a wider range of Reynolds number must be taken into account.

From the Moody's diagram (Fig. 2.40), for $\epsilon/D_{1''} = 1.26 \cdot 10^{-4}$, in the aforementioned Reynolds band the Fanning coefficient is bounded by $0.012 \lesssim 4f \lesssim 0.014$, therefore, an average value of $4f = 0.013$ was chosen. This leads to a non-dimensional length for the $1''$ trait of $4fL_{12}/D_{1''} = 20.25$, assuming $D_{1''} = 26$ mm. The subscript (12) meaning the physical length between inlet and outlet.

From the Fanno tables, for such non-dimensional length, the initial Mach number of $M_1 = 0.174$ is extracted. This value is what the theory says to

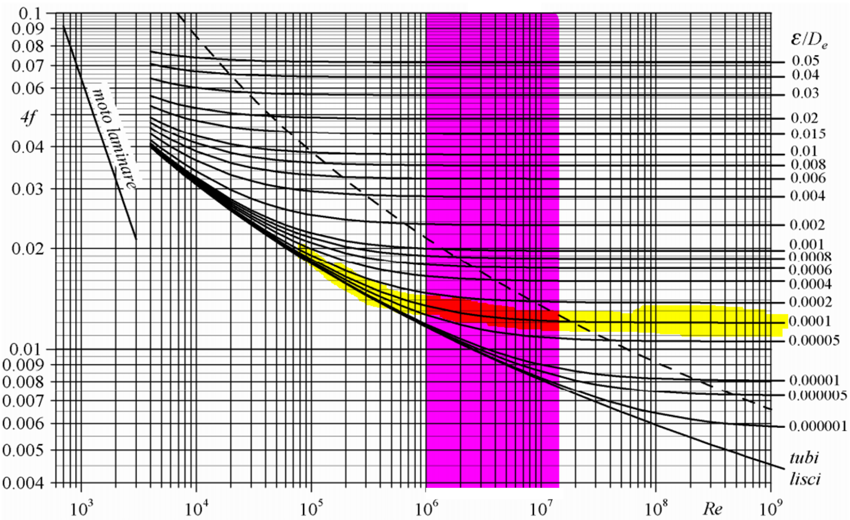

Figure 2.40: Picture of the Moody's diagram. The colored areas evidence the operative conditions of the facility.

be the maximum inlet Mach number, also corresponding to the maximum flow rate that can pass through this pipe. For a total pressure of 33 bar, the equivalent mass flow rate would be $\dot{m} = 1.24$ Kg/s, the pressure at the pipe end would be $p^* = \frac{p^*}{p_0^*} \cdot \frac{p_0^*}{p_0} \cdot p_0 = 0.528 \cdot 0.300 \cdot 34 \cdot 10^5 = 5.2 \cdot 10^5$ Pa. This value are inferior to the one measured (19 bar), and thus we can conclude the flow did not reach sonic conditions, hence the initial Mach number and mass flow rate must be lower.

To find the correct value in subcritical conditions, one must proceed by trials and errors, guessing the outlet Mach number.
$M_{2''} = 0.40$ is taken as first guess. From the Fanno tables, the non-dimensional length relative to this Mach number is $4fL_2^*/D_{1''} = 1.07$. This value is used to compute a second non-dimensional number $4fL_1^*/D_{1''} = 4fL_2^*/D_{1''} + 4fL_{12}/D_{1''} = 21.32$, with associated $M_1 = .169$. The reason to make this is to use the following ratios chain to compute the outlet pressure, having the inlet total pressure:

$$p_2 = \frac{p_2}{p^*} \cdot \frac{p^*}{p_1} \cdot \frac{p_1}{p_{01}} \cdot p_{01} = 2.696 \cdot \frac{1}{6.600} \cdot 0.980 \cdot 34 \cdot 10^5 = 13.61 \cdot 10^6 \text{ Pa} \quad (2.13)$$

The values for the ratios in Eq. 2.13 are taken from the Fanno tables (reported in Tab. 2.4) and from isentropic relationship.
This guess returned a value p_2 which is lower than the one measured, and thus the outlet Mach number must be lower.

M	p/p^*	ρ/ρ^*	T/T^*	p_0/p_0^*	$4fL^*/D$
.15	7.287	6.099	1.195	3.910	27.93
.16	6.829	5.720	1.194	3.673	24.20
.17	6.425	5.385	1.193	3.464	21.12
.18	6.066	5.088	1.192	3.278	18.54
.27	4.028	3.406	1.183	2.238	6.983
.40	2.696	2.138	1.163	1.590	2.308

Table 2.4: Values from the Fanno tables.

As second guess, $M_2 = 0.27$ is taken. Repeating the same procedure, the non-dimensional length relative to this Mach number is $4fL_2^*/D_{1''} = 7.00$. This value is used to compute a second non-dimensional number $4fL_1^*/D_{1''} = 4fL_2^*/D_{1''} + 4fL_{12}/D_{1''} = 27.25$, with associated $M_1 = 0.151$. Using the same ratios chain, with the new values, one can obtain:

$$p_2 = \frac{p_2}{p^*} \cdot \frac{p^*}{p_1} \cdot \frac{p_1}{p_{01}} \cdot p_{01} = 4.028 \cdot \frac{1}{7.150} \cdot 0.984 \cdot 34 \cdot 10^5 = 18.84 \cdot 10^6 \text{ Pa} \quad (2.14)$$

which is a good approximation of the measured value of 19 bar ($20{\cdot}10^5$ Pa). One can thus conclude that the initial Mach number at the inlet of the $1''$ pipe was $M_1 \simeq 0.15$, which correspond to a mass flow rate of $\dot{m} = 1.06$ Kg/s. This value, is still higher than the one on Tab. 2.3 for Cond.07, but it can be justified in two ways. The first one is that, in this exercise, pressure losses due to bends were not taken into account, meaning that the initial Mach number must be lower than the one calculated. The second is that it has been verified that the secondary nozzle (shown in Fig. 2.5b) and reported in Sec. 4.1.2) experience a vertical displacement when the facility is turned on, increasing the throat passage area. This phenomenon may produce an increment of the mass flow rate up to the 4.5%.

A further check was done considering the final working point, when the total pressure was $p_0 = 25$ bar and $p_2 = 3$ bar. Assuming the flow was choked in the line, $4fL_{12}/D_{1''} = 4fL^*/D_{1''} = 20.25$ and $M_1 = 0.174$. The pressure at the outlet would be then:

$$p_2 = p^* = \frac{p^*}{p_{01}^*} \cdot \frac{p_{01}^*}{p_{01}} \cdot p_{01} = 0.528 \cdot \frac{1}{3.50} \cdot 26 \cdot 10^5 = 3.92 \cdot 10^6 \text{ Pa} \quad (2.15)$$

which is exactly the measured value.

We can conclude that the Fanno theory is a useful tool which fits quite well the facility behavior, and it can thus be used as cheap tool to roughly estimate the capabilities for future upgrades.

2.7.2 Pressure

The maximum operative pressure is related to the chosen components of the facility. Concerning the pipes, both 1″ and 2″ size can sustain pressures up to 50 bar.
The limiting pressure regulator is the model DRP-88-G (Sec. 2.3.5) and DRi-88 (Sec. 2.3.7), which can both sustain up to 25 bar as inlet pressure. The buffer tank, the silencer and the flow distributors have been designed in order to sustain up to 11 bar, and both the silencer and the tank have been tested under pressure up to 16 bar.
Concerning the vertical ducts, the inner one has very thick walls (10 mm) and small inner diameter (80 mm), and thus it is virtually insensible to the pressure at such range. For the outer duct, instead, the walls are thinner and the internal diameter is larger (300 mm). Although the cylinder itself should resist at the working pressure of 11 bar, concerns arise from the flanges, which appears thin, especially for the duct traits recycled from the previous facility. A pressure test with water, up to 16 bar, is thus recommended.

2.7.3 Temperature

Also for the temperature, the limitations are related to the materials and components of FAST. Valves and flexible pipes cannot sustain heated flow above 60°C.
The silencer and the ducts may in principle sustain high temperature flow up to 300°C, assuming the proper O-rings are installed. The rubber pipes connecting the pressure taps with the sensors must be replaced with metallic ones, and filled in the last trait with oil to avoid damaging the transducers with the heat.

2.8 Conclusions

A new facility to study supersonic coaxial jets was designed and built at the von Karman Institute for Fluid Dynamics. The chosen layout merges efficiently the benefits of a continuously running facility with a blow-down one, which are mainly the long test duration and good flow quality. The valves components and the seeding generator were chosen in order to assure flexible, safe and easy usage, allowing to operate the facility even by a single person. A security system to shut down the flow in 10 seconds was implemented, with four emergency button located in strategic points, and three rupture disks were installed to further enhance security. The installation was completely designed making use of a CAD software, enhancing the overall conception process, and leading to a simplification of the procedures for maintenance and further upgrading. An innovative coaxial silencer was realized to eliminate all spurious noise from piping and valve system, and to act as an anechoic termination for the ducts. The main advantage of this configuration is to avoid any kind of aerodynamic interference between the inner duct and the outer ducts. The U turns shape combined with the presence of stainless steel wool leads to an effective sound damping, validated through COMSOL® acoustic simulation. The nozzles geometry was validated through CFD simulations using COMSOL®, where all the planned test conditions were tested. The preliminary nozzle geometry was found unsuitable, and was thus modified to obtain the final shape. Results show a complex flow pattern, with a conical shock wave present at the end of the primary nozzle. From the simulations, the effect of the conical shock-wave is to sensibly reduce the primary flow stream, creating an over-pressurized zone. This discovery led to the installation of a mass flow meter for the primary stream to directly measure the mass flow rate. It was also found that this shock-wave could interact with the shock-cells pattern in the wake, if certain geometric and pressure requirements are met.

During the commissioning, it was found the main actual limitation is constituted by the pipe diameter of the 35 bar line, which became chocked with a mass flow rates around 0.7 kg/s. As future improvement, in order to achieve higher mass flow rates, it is mandatory to substitute this line with at least 2.5″pipes. Furthermore, the implementation of an electric actuator to control the two streams pressure valves is also recommended, to move the control station from the basement up to the ground floor. Despite the degree of safety, high pressure devices remain a source of hazards for the users, including ear damage provoked by the long exposure to valve noise.

Chapter 3

Single stream jet

In this chapter are exposed the techniques that have been used to investigate a supersonic underexpanded single stream jet, and the results achieved. This constitutes a preliminary approach to the study shock-cell noise, permitting at the same time to validate the facility and the methodology. Synchronized microphones and Particles Image Velocimetry (PIV) measurements have been performed, which have been compared with the literature. This part of the work was carried out in collaboration with Rubio Carpio [77],who is gratefully acknowledged.

3.1 Experimental Setup

A vertical microphone polar array is located in the anechoic room to proceed with the acoustic measurements. The array comprises 11 microphones, equally spaced to cover a range of polar angles from 30^o to 130^o. The PIV optical bench containing all the devices necessary to generate the laser light sheet and the cameras to record the images is also placed inside the anechoic chamber. The laser head and its cooling system are kept outside of the room, since they are source of spurious noise. A sketch of the final set-up of the facility is shown in Fig. 3.1. The nozzles used are the first set built, described in Sec. 2.2.2, with $\varnothing_{p,inner} = 23.3$ mm and $\varnothing_{s,inner} = 55$ mm for the primary and secondary jets, respectively. For this study, both the nozzles were installed, but only the primary flow was used.

3.2 Operating Conditions

Three measurement campaigns were conducted. In the first one, PIV and microphones measurements were performed synchronously, for a range of NPR and Mach numbers indicated in Table 3.1. However, the microphones had their protection grid, causing an alteration of the spectra for frequencies above ∼10 kHz (Fig. 3.11). For this reason, acoustic measurements, without the protective grid, were repeated and extended for lower and higher Mach numbers, as indicated in Table 3.1. The last acoustic measurement campaign was executed using a new manufacture nozzle with a smaller diameter, for the sake of verifying the experimental repeatability. The conditions have been chosen in order to establish a comparative study with the previous

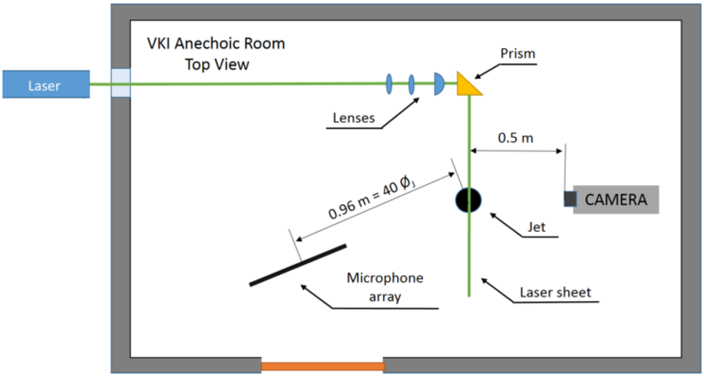

Figure 3.1: Sketch of the experimental setup. The laser equipment, usually source of unwanted noise, was located outside the anechoic room. Two spherical lenses and one cylindrical lens have been used to create the laser sheet. The microphones antenna is placed in the lower left corner. This was the only possible solution to guarantee to be in the jet acoustic far field, avoiding to be too close to the chamber walls.

research of Savarese [79] and André *et al.* [5]. These conditions are presented in the Table 3.1:

The conditions cover a wide range of operating points of the supersonic jet. It was found that for the two tested nozzle, the Mach number for the onset of double screech was different, and also the for the same nozzle, with and without the PIV equipment. Therefore, a fine test matrix has been implemented to document this behavior.

3.3 PIV Measurements

A quantitative measurement of the flow field of the jet was achieved through PIV. The Particle Image Velocimetry is a non-intrusive optical method, which principle has been described extensively in the literature [1]. In order to characterize the flow field, the use of non-intrusive methods reveals to be more adequate since the intrusive techniques alter significantly the flow pattern and subsequently the acoustic footprint of the jet [4].

The application of this technique to supersonic flows involves raise specific problems such as the difficulty of achieving a uniform seeding concentration, or the velocity lag between the air and the seeding particle. Jeronimo [43] showed that the correct choice of the particle size and the seeding generator leads to good results in terms of flow feature identification of shock-cells geometry and location.

NPR	M_j	PIV & Nozzle 1	Nozzle 1	Nozzle 2
1.8	0.96			x
1.9	1.0		x	x
2	1.05		x	x
2.13	1.1		x	x
2.26	1.15		x	
2.30	1.16	x	x	x
2.36	1.18	x	x	x
2.40	1.19	x	x	x
2.46	1.21			x
2.50	1.22	x	x	x
2.60	1.25	x	x	x
2.70	1.28	x	x	x
2.96	1.35	x	x	x
3.67	1.50	x	x	x
4	1.56		x	x

Table 3.1: Overview of the test conditions investigated during the three campaign carried out using PIV and microphones. Nozzle 1 has D = 0.024 m, while nozzle 2 has D = 0.019 m.

3.3.1 PIV Acquisition Procedure

In order to achieve statistical convergence within the PIV measurements it is necessary to take a certain amount of samples (images). The exact quantity depends on the turbulence intensity of the flow measured following the figure 3.2. André *et al*, in previous research in similar conditions used 2000 images [5]. Due to computer memory limitations, pairs of particles images can be acquired in batches of 600 only. It was decided to acquire 1800 samples and to verify turbulence intensity statistical convergence a posteriori. The acquisition of pairs of particles images was performed at a sampling rate of 15 Hz. Consecutive fields can thus be assumed to be decorrelated. Each acquisition of 600 images lasted 40 seconds, with a pause of ca 5 minutes to store data on the hard drive. During this pause time, the facility was kept running at minimum mass flow rate, to not let the seeding stagnate inside the circuit. For this reason, small discrepancies ($< \pm 0.5\%$) in the NPR between the three runs could be present. The turbulence intensity in the mixing layer of the jet was calculated to be less than 20%. Assuming this value as an upper limit, it can be assumed that the number of samples taken allows to have a 1% error on the velocity mean value with a 99% of confidence (Fig. 3.2).

The acoustic acquisition was set to last 50 seconds, starting immediately before the PIV recording. In order to correlate both measurement techniques, the laser pulses have been acquired with the same acquisition system used

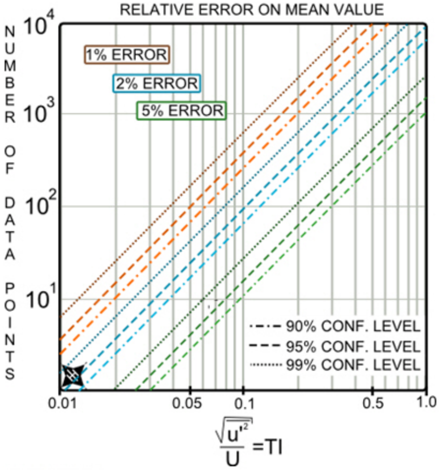

Figure 3.2: Number of samples *vs* TI for several confidence levels and percentage of error error [39].

for the acoustic measurements. In this way it is possible to know the instantaneous acoustic field that corresponded to each PIV sample.

3.3.2 PIV seeding

Jeronimo [42] showed that a particle size of $1\mu m$ is small enough to avoid the velocity lag even at higher speeds, but big enough to scatter a sufficient amount of light. Therefore, the flow was seeded with Shell Ondina 919 oil, with a peak in the particle diameter distribution function around of $1\mu m$, according to the manufacturer. The seeding was provided by a PIVTEC PivPart45-M with 45 Laskin Nozzles and a typical seed output of 10^8 particles per second, data taken from the data sheet. In contrast, Mandon [49], obtained a particle distribution peak of less than 0.5 μm, as already described in Sec. 2.2.3. There should thus not be any significant velocity lag and the measurements indicate that enough light was scattered by the particles to yield a good Signal-To-Noise Ratio (SNR) of the velocity correlation maps.

3.3.3 PIV equipment

The illumination is provided by laser pulses generated with a double-cavity Quantel CFR200 Nd:YAG system. This system provides a laser wavelength $532nm$ (green), with a maximum energy of $200mJ/pulse$ and a pulse duration of $12ns$. Since both lasers are running simultaneously, the flashlamp and the Q-switch are triggered externally to maintain predictable spacing between laser pulses from each laser head and to get the best pulse timing stability.

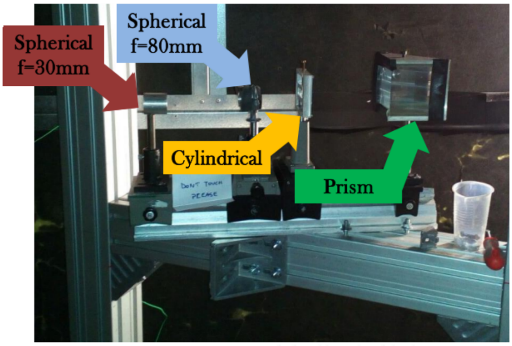

Figure 3.3: Picture of the optical bench. Rubio Carpio [77].

After a transmission of approximately 3 meters, the laser beam reaches the optical bench where the beam is reshaped a laser sheet. The optical bench consists of two spherical lenses, one with focal length $f = 30mm$ and the other one with $f = 80mm$, a cylindrical lens and a prism to turn the laser beam, as shown in Fig. 3.3. Being a single lens with a proper focal length unavailable, the combination of these two different spherical lenses supplied very well, guaranteeing the compactness of the optical test bench, to avoid disturbances in the acoustic measurements. After the cylindrical lens, the laser light sheet passes through the prism, where it is deviated 90^o in order to reach the test section. The distance between the prism and the test section is about 1 meter. This setup allowed to obtain a laser light sheet of about 1.5 mm thickness on a vertical plane containing the jet axis.

The recording system is composed of two LaVision Imager SX4M cameras located at a distance of 0.5 meters of the jet axis. Preliminary acoustic tests were carried out to ensure that at such a distance, the acoustic field emitted by the jet was not perturbed. The cameras are placed vertically in order to enlarge the total field of view in the axial direction of the jet, although a little overlapping between the field of view of both cameras was set up in order to allow the construction of the final one by joining them. The final field of view (depicted in Fig. 3.4) is of 10.5Dx4D (252x96 mm^2) with a digital resolution of 18 pixel/mm. A parametric study was carried out to choose the optimum separation time and seeding density for each case. The time delays between the laser pulses have been selected accordingly to the flow maximum velocity in order to have 1/4 displacement of the first interrogation windows (Table 3.2).

The main characteristics of the cameras are summarized in the table 3.3. The sampling frequency used is set to 15 Hz. Two Nikkor f/1.8 objectives of 50mm focal length are mounted. To avoid peak locking, the particle size on the sensor should be around 2 pixels. Known the pixel and the droplet size, and the magnification factor, it is possible to derive the focal number required to achieve such requirement.

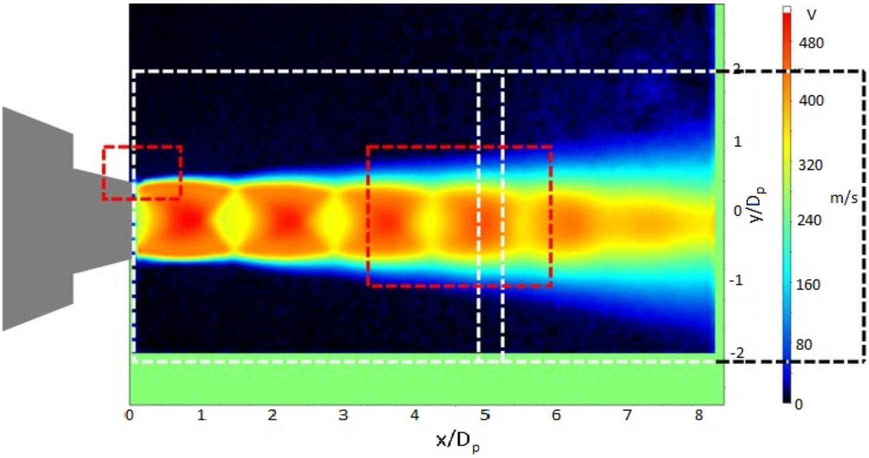

Figure 3.4: The fields of view investigated. In white, the contour to have an overall of the flow field. In red, two zoomed view, one of the boundary layer of the nozzle, and one of the shear layer.

Test	$CNPR$	$M_{j,core}$	Δt $[\mu s]$
1	2.30	1.16	1.5
2	2.40	1.19	1.5
3	2.50	1.22	1.2
4	2.60	1.25	1.2
5	2.70	1.28	1.2
6	2.96	1.35	1.2
7	3.67	1.50	1.0

Table 3.2: Test conditions for the single stream jet campaign, the relative fully-expanded Mach number and the separation time between two laser pulses.

Camera	Imager SX4M
Resolution	2360 x 1776 $pixel^2$
Sensor Format	12.98 x 9.76 mm^2
Pixel Size	5.5 x 5.5 μm^2
Framing Rate	30 Hz
Min. Δt	250 ns

Table 3.3: Camera parameters

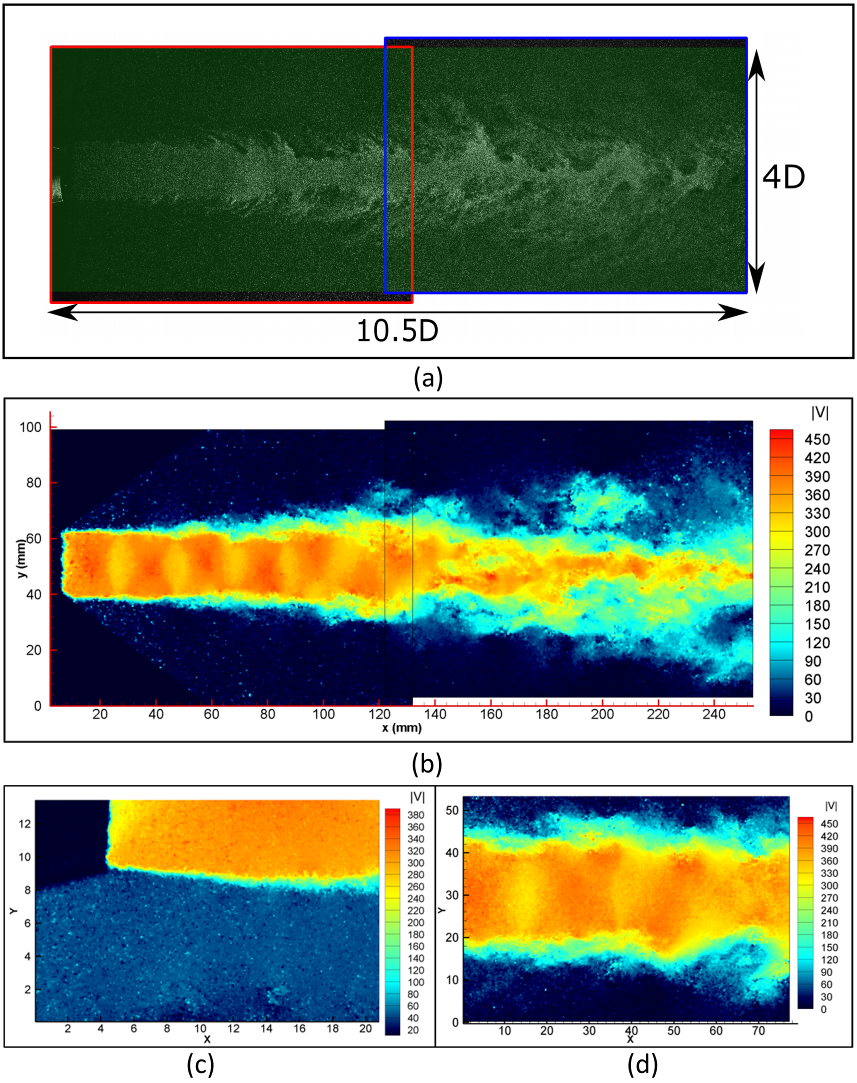

Figure 3.5: a) Example of instantaneous combined FOVs and b) instantaneous velocity fields, post-processed using Davis 8 12x12 pixel^2 final window with 75 % overlap for NPR = 2.50. The flow field shows a system of five shock-cells in line with the sixth and the seventh one oscillating in antisymmetric motion. c) Instantaneous velocity field, with higher magnification factor, near the nozzle lip region. d) Instantaneous velocity field, with higher magnification factor, at the shear layer.

A focal number $f^{\#} = 8$ was derived from the following equation to allow to focus the light scattered by the particles of 1 μm size:

$$d_{\tau} \approx \sqrt{d_s^2 + M_0^2 d_p^2} \tag{3.1}$$

with

$$d_s = 2.44(1 + M_0) f^{\#} \lambda \tag{3.2}$$

where d_{τ} is the desired dimension of the particle on the camera sensor (2 pixels), d_p is the particle size, M_0 is the magnification factor, λ is the laser wavelength and $f^{\#}$ is the focal number. The cameras were however slightly de-focused in order to increase the size of the particles on the image, since they were at the limit of 2 pixel per particle. A posteriori, this is probably due to the particles diameter, smaller than 1 μm.

In Fig. 3.5a, an example of combined row images is shown. The seeding outside the jet appears less concentrated than the jet itself, but still sufficient to have good signal to noise ratio. The following pictures 3.5b, 3.5c and 3.5d show first postprocessed velocity fields using the PIV software Davis 8.

3.3.4 Calibration Procedure

In order to proceed with the calibration of the PIV system, a metallic plate was placed in the test section with a geometric pattern attached to it, as shown in figure 3.6 (a). The geometric pattern in the plate, depicted in Fig.

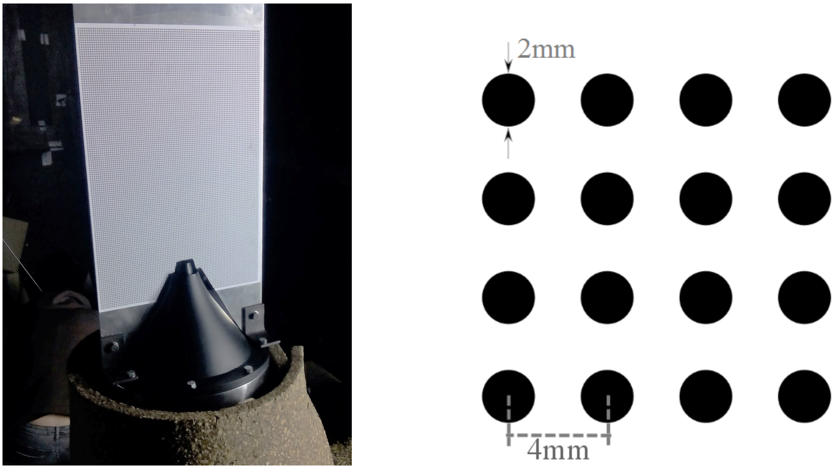

(a) (b)

Figure 3.6: Calibration procedure for the PIV system. (a) Calibration plate mounted on the nozzle. (b) Geometric pattern used for calibrate.

3.6 (b), was selected with the next constraints, imposed by the PIV software:

- After focusing the cameras on the plate, the size of the circles has to be approximately of 50 pixel in the image.
- There must be as many circles as possible inside the image, but the calibration software has to be able to make a difference between a circle and another one. The distance between circles was chosen to be the double of the circle diameter.

The calibration procedure was carried out using the LaVision Davis 8 software. This software has a predefined calibration procedure. After defining the characteristics of the geometric pattern in the test section, an algorithm localizes all the circles in the image and the position of each one is fitted with a 3rd order polynomial. This polynomial is used afterwards to correct the images. In order to assure a good calibration, the software prescribe to have the standard deviation, between the calibration pattern and the fitting polynomial, to be lower than 0.3, which was our case for both cameras. However, after several test run with both Davis 8 and WIDIM, it was decided to not include any image correction during the pre-processing. It was found, in fact, that the images corrected showed a significant distortion in the velocity field, particularly at lower speeds. The distortion consisted in the appearance of unphysical patterns both in the SNR and in the vector components maps. This was occurring for both images corrected with Davis 8 and images rotated using the VKI preprocessor Tucsok, but it was not occurring when no image transformation was applied (Fig. 3.7). For these reasons, the calibration was thus only used to check the camera orientation with the jet axis and to estimate the magnification factor. Finally, the laser sheet was aligned with the calibration pattern in order to make sure that the illuminated section coincides with the one of the calibrated plane.

3.3.5 Image Processing

The image pre-processing was carried out with Tucsok [38], the cross-correlation with WIDIM [80], a multi-grid FFT based algorithm, and the post-processing with Rabon [37]; all VKI-developed softwares. WIDIM uses an iterative interrogation procedure with window shifting and deformation. Image interpolation at sub-pixel positions is performed by a standard three-point Gaussian function [85]. The initial interrogation size was set according to the one-quarter rule. The final interrogation size was decided in order to have at least 10 particles in it. According to this, a 48x48 pixel^2 initial interrogation window is used with two iterations, resulting in a 12x12 pixel^2 final interrogation window. A 75% overlap is set resulting in a vector every 3 pixel (0.1687mm). In order to avoid spurious vectors in the statistics, a double filter on the images is present in Rabon. Those instantaneous flow

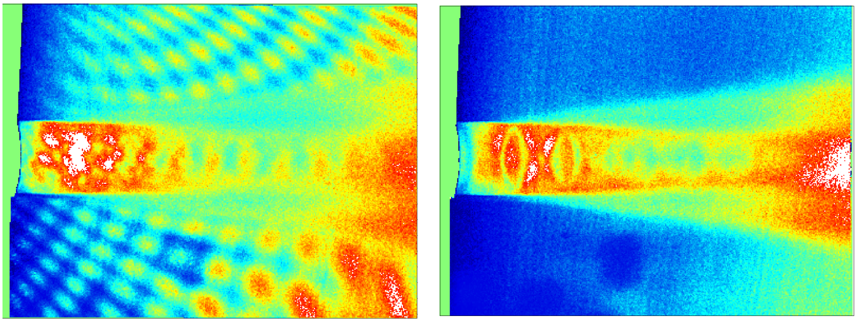

(a) SNR, corrected image

(b) SNR, no image correction

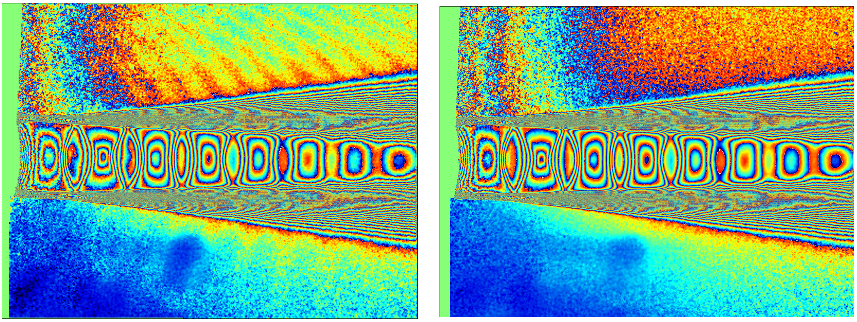

(c) V_{abs}, corrected image

(d) V_{abs}, no image correction

Figure 3.7: Effects of the image correction on the Signal-to-Noise Ratio and on the velocity field for NPR = 2.30, $\Delta t = 2$ μs. Cross correlation was performed using Davis8 with 12x12 final window size, 50% overlap. The pictures shown represent the averaged value over 600 samples. The velocity color range was reduced from 0 to 10 m/s and color wrapping was introduced to enhance shock-cells visibility.

fields with a signal to noise ratio lower than 1.5 or higher than 20 were automatically discarded. Unfortunately, the analysis of the mean of the velocity fluctuations for the 1800 samples reported noisy results. Because of this, a second post processing was tempted using a 64x64 pixel^2 initial window. Two iterations were carried out, resulting in a final interrogation window of 16x16 pixel^2, with 50% of overlap. In this case the spatial resolution is a vector each 8 pixels (0.44 mm) i.e. 55 vectors across the single supersonic jet diameter. In order to avoid spurious vectors, the same filter thresholds have been applied.

The comparison of both velocity fluctuation profiles is done in figure 3.8. The 16x16 pixel^2 final interrogation window returned a smooth profile while the 12x12 pixel^2 is more noisy. After this evidence, a second post-processing of the rest of the test cases was redone using the 16x16 pixel^2

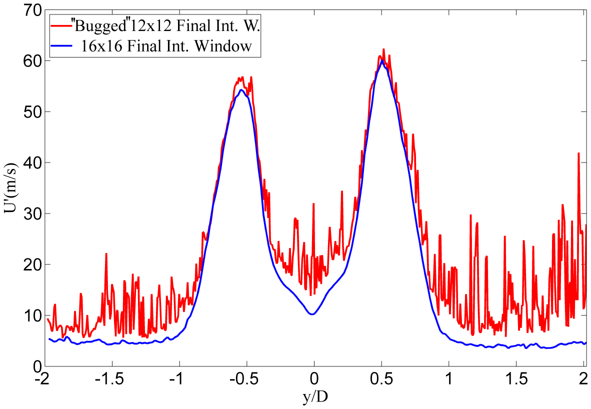

Figure 3.8: Mean velocity fluctuations $\overline{U'}$ profile at x/D=3.2 at $M_j = 1.25$. In red, data found with 12x12 pixel^2 final interrogation window. In blue, data found with 16x16 pixel^2 final interrogation window

final interrogation window.

The Signal to Noise Ratio (SNR) of the two different post-processing parameter sets are compared in figure 3.9. As it can be appreciated, the SNR given by the 16x16 pixel^2 final interrogation window is higher, especially at the end of the potential core of the jet. The histograms also show this increase. The majority of vectors in this case have a SNR close to 3, meanwhile with a 12x12 pixel^2 the majority are located at a SNR close to 2.5.

A posteriori, the noisy profile of the 12x12 pixel^2 final interrogation window (Fig 3.8) was attributed to a bug in the Rabon interface of WIDIM. This bug provokes an incorrect statistics, not taking into account the double filter for the SNR, as well as the mask in the cross-correlation (see Fig. 3.9b).

We verified a posteriori that the spatial resolution, provided by the 16x16 pixel^2 final interrogation window, was enough to compute the integral length scales of the turbulence in the mixing layer of the jet. Taking into account this and the increase in the SNR, a third post-processing using the 12x12 pixel^2 final interrogation window avoiding the Rabon bug was considered not to be necessary.

The peak locking effect in the measurements has also been checked. Peak locking is a bias error produced by the sub-interpolation step in the post-processing algorithm. It happens when the particle-image diameter falls below 2 pixel units. The measured particle-image displacement Δx then becomes biased towards integer-pixel values. The histograms presented in the figure 3.10 show displacement of the interrogation windows. The peak at very small pixel displacement corresponds to the particles in the entrainment zone of the jet. The separation time Δt was set to allow the particles in the

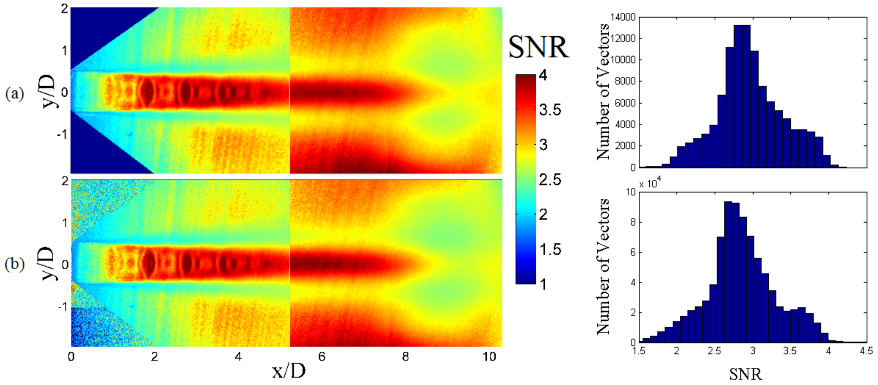

Figure 3.9: Signal to Noise Ratio at $M_j = 1.25$. The two post processing parameters sets are considered. (a) The final interrogation window is 16x16 pixel^2 with 50% of overlapping.(b) The final interrogation window is 12x12 with 75% of overlapping

core of the jet to move around 8 pixel. Since the velocity of the particles in the entrainment zone of the jet is much lower, their displacement between images is practically zero. On the second histogram of the figure 3.10 a zoom of the first image is shown. It can be appreciated that most of the particles have displaced around 9 pixel. As there is no peak at integer numbers, we can consider the images free of the peak locking effect.

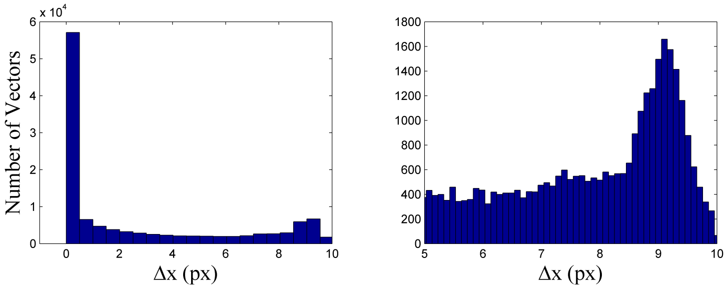

Figure 3.10: Peak locking checking at $M_j = 1.16$

3.4 Acoustic Measurements

3.4.1 Test Campaigns

As already anticipated, three different acoustic test campaigns have been performed, the first one synchronized with PIV and the last two with only the microphone array. For the first test campaign, the acquisition software consented a minimum sampling frequency of 800 kHz. This would have implied to record very large data files, for the requested time of 40 seconds. Therefore, it was decided to use two acquisition systems in parallel. One, with a sampling frequency of 51.2 kHz, was used to record the signals of 4 on 8 microphones and the laser pulses, for the entire acquisition period of 40 seconds. The first one, at 800 kHz, was used to obtain highly resolved data, with 8 microphones, limiting the acquisition period to only 5 seconds. The microphones' protective grids were not removed, leading to a spectra pollution above 15 kHz, as presented in Fig. 3.11.

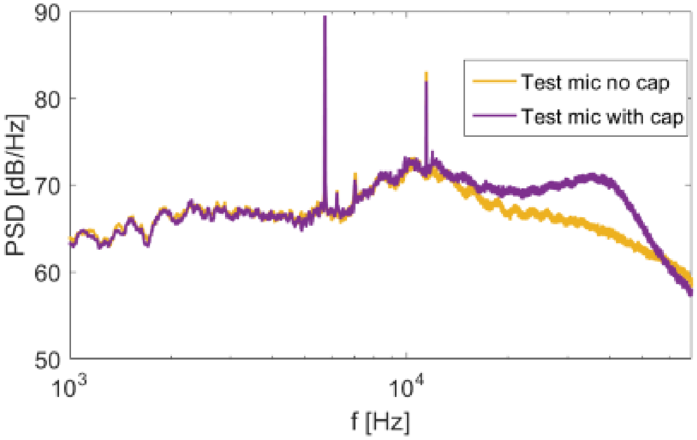

Figure 3.11: Example of the effect of the protective grid on the spectrum. Guariglia *et al.* [32]

For all these reasons, this acoustic dataset has not been exploited, and only the results of the other test campaigns will be presented.

3.4.2 Acoustic Equipment

A new microphone polar array, depicted in the Fig. 3.12, was designed to perform acoustic measurements.

The array allows to place the microphones at different angles, both upstream and downstream the jet, in order to retrieve the BBSAN peak variation with the angle. Special care was taken to avoid using large structures, which would eventually case acoustic energy scattering and therefore disturbances in the measurements.

In the first test campaign 8 microphones have been placed on the array covering an angular range from $\theta = 50^o$ to $\theta = 120^o$ (being $\theta = 0$ the downstream direction) with a microphone every 10^o at a distance of 0.96 m (40 D_p). In the second and third test campaign, 11 microphones were set,

Figure 3.12: Picture showing the polar array with 8 microphones mounted.

covering an angular range from $\theta = 30^o$ to $\theta = 130^o$ again with a microphone every 10^o, at a distance of 1.32 m (30 D_{s2}, 55 D_{p1} or 68.75 D_{p2}, as defined in Sec. 2.2.2).

The microphones used are Bruel & Kjaer 4938, 1/4 inch diameter, shown in Fig. 3.13 (a). These microphones are able to acquire in a wide frequency range from 4 Hz to 70000 Hz and their dynamical range is comprised between 30 and 172 dB ($P_{ref} = 20\mu Pa$). The signal of the microphones is amplified by a Bruel & Kjaer 2670 - 1/4-inch microphone preamplifier, depicted in Fig. 3.13 (b). A Bruel & Kjaer NEXUS Type 2690-A microphone conditioner, presented in Fig. 3.13 (c), is used to amplify and band-pass the signal.

3.4.3 Acquisition Systems

As introduced already in Sec. 3.4.1, two acquisition systems have used. For the acoustic and PIV synchronous measurements, two NI 9234 modules records the signal from 4 microphones and the laser trigger. The modules are placed in the NI cDAQ 9174 4 slots chassis, also used to record the pressure and temperature described in Sec. 2.6. The sampling frequency f_s is 51.2 kHz. The low pass filter, embedded in the NI 9234 A/D converter, is set to 25.6 kHz, following the Nyquist criteria

In parallel, a NI 5751 14-bit A/D converter together with NI PXIe-1073 chassis was used to convert the signal. This acquisition system can sample frequencies up to 1 MHz. The sampling frequency for the first test campaign was set 800 kHz, while for the following two campaigns it was lowered to 250 kHz. In all cases the band pass filter of the NEXUS system was set from 20 Hz to 100 kHz.

The selected acquisition parameters for every test campaign, including the


(a) (b) (c)

Figure 3.13: (a) B&K 4938 microphone. (b) B&K 2670 microphone preamplifier. (c) B&K NEXUS 2690 microphone conditioner.

acquisition time T_s, the sampling frequency f_s, the number of samples N_s and the frequency resolution Δf, are summarized in Table 3.4.

Acquisition Parameters					
Test Campaign	f_s (kHz)	N_s	T_s (s)	Δf (Hz)	D
1^{st} Sync. PIV	51.2	2560000	50	0.02	0.024
1^{st} Only mics	800	$2^{22} = 4'194'304$	5.24	0.191	0.024
2^{nd} Only mics	250	$2^{24} = 16'777'216$	67.11	0.015	0.024
3^{rd} Only mics	250	$2^{24} = 16'777'216$	67.11	0.015	0.019

Table 3.4: Acquisition Parameters

3.4.4 Data Processing

The data processing was carried out following the recommendations suggested in the Data Acquisition and Processing VKI course [81]. The Welch's Power Spectral Density of the signal was calculated. The Welch's PSD divides the whole acquired signal into segments of N_{PW} points and applies the FFT to each one of these segments. To avoid spectral leakage, a Hanning window is applied to every signal of N_{PW} points. After being normalized, obtaining so the PSD, all the segments are averaged resulting a mean PSD, which makes the spectral content of the signal much more readable. The drawback of this method is, since the PSD is applied to shorter pieces of the signal, there is a loss of frequency resolution. The final frequency resolution of the Welch averaged signal Δf_{PW} is thus given by equation 3.3.

$$\Delta f_{PW} = \frac{f_s}{N_{PW}} \tag{3.3}$$

The values of N_{PW} and the resolution in frequency after applying the Welch's Power Spectral Density are presented in Tab 3.5.

Acquisition Parameters			
Test Campaign	f_s (kHz)	N_{PW}	Δf_{PW} (Hz)
1^{st} Sync. PIV	51.2	$2^{15} = 32768$	1.56
1^{st} Only mics	800	$2^{15} = 32768$	24.41
2^{nd} Only mics.	250	$2^{15} = 32768$	7.63
3^{rd} Only mics.	250	$2^{15} = 32768$	7.63

Table 3.5: Processing Parameters

3.4.5 Calibration Procedure

The calibration procedure is achieved using a calibrated piston-phone emitting a pure tone of 94 dB at 1000 Hz, and it is used as reference to compute the microphone's sensitivity. From the manufacturer data-sheet, such kind of microphones have typically flat amplitude response in the range from 10 Hz to 20 kHz (Fig. 3.14). Above this frequency, the response is not flat anymore. However, the error is contained between ±2 dB. No correction was thus applied in the results presented in the following sections.

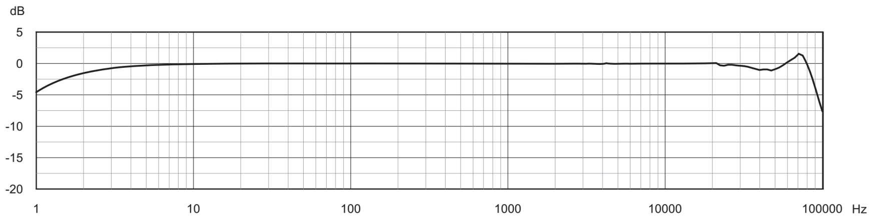

Figure 3.14: Typical amplitude dynamic response of B&K 4938 microphones.

3.5 Results: PIV

In this section the results obtained from the PIV measurements are presented and compared with previous research.

3.5.1 System Alignment Check

The position of the aerodynamic axis of the jet was calculated as follow:

$$y_0(x) = \frac{\int \overline{V_{abs}}(x,y)\, y\, dy}{\int ydy} \tag{3.4}$$

where x, y are the axial and radial coordinate, respectively, $y_0(x)$ is the radial coordinate of the jet center at the axial coordinate x, $\overline{V_{abs}}(x,y)$ is the averaged absolute velocity. The analysis revealed a slight deviation angle αbetween the geometric $(y = 0)$ and the aerodynamic axis of the jet. In Fig. 3.15 the deviation for the case $M_j = 1.35$ is shown. For the case exposed, $\alpha = 0.18^o$, which represents a deviation of 1.5 vector spacing at $x/D = 10$. For the other cases, the values of α are presented Tab. 3.6. The maximum deviation corresponds to the case $M_j = 1.16$ with a deviation of $\alpha = 0.37^o$ which corresponds to a deviation of 3 vectors at $x/D = 10$. It was concluded that this deviation has negligible effect on the jet aerodynamics or aeroacoustics.

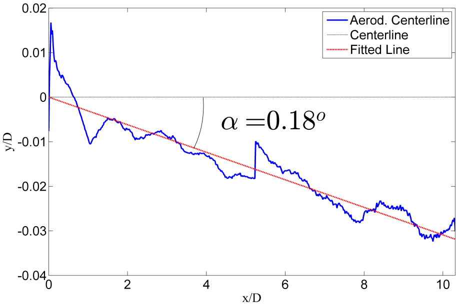

Figure 3.15: Deviation between the aerodynamic center line and the geometric one for the case $M_j = 1.35$.

M_j	1.16	1.19	1.22	1.25	1.28	1.35	1.50
Angle	0.37^o	0.23^o	0.20^o	0.20^o	0.17^o	0.18^o	0.15^o

Table 3.6: Angle α between the aerodynamic and the geometric center line for every case.

In Fig. 3.16 the averaged axial velocity component, $\overline{U}$, is shown. In order to verify the jet symmetry, some radial and axial velocity profiles, marked with white dashed lines, have been extracted and presented in Fig. 3.17.

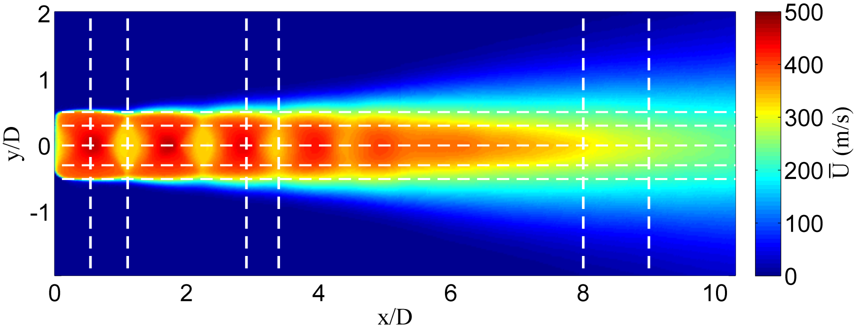

Figure 3.16: Contour plot of the average axial velocity component, $\overline{U}$, for the case $M_j = 1.35$. White dashed lines mark lines where the velocity profiles have been taken.

The higher gradient of axial velocity in the radial direction, $d\overline{U}/dy$, is located near the nozzle lip lines ($y = \pm 0.5$). Due to the PIV final windows size, it is expected to have higher uncertainty on the modulus around these positions.

The $\overline{U}$ axial profiles are shown in Fig. 3.17(b). The profiles corresponding to $y/D = \pm 0.3$ are expected to be still in the potential core of the jet, where the radial velocity gradient $d\overline{U}/dy$ is small; and thus, they coincide. For $y/D = \pm 0.5$, instead, the values for both profiles diverge slightly, but this can be due to the steep gradient. In fact, for $x/D > 6$, with a smoother gradient, the mismatch is reduced.

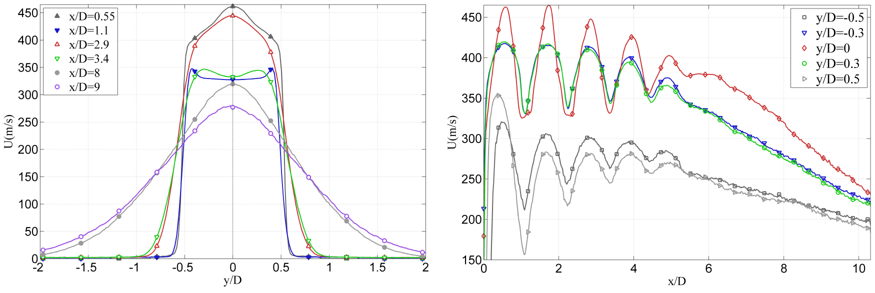

(a)

(b)

Figure 3.17: Averaged $\overline{U}$ velocity profiles for the case $M_j = 1.35$. (a) Radial profiles. (b) Axial profiles.

In Fig. 3.18 the upper half and the lower half radial profiles have been compared. Although there is a small difference between the values at $y/D < 0$ and $y/D > 0$, it was considered that the centerline identification method is not free from errors, as well as the post processing of the images.

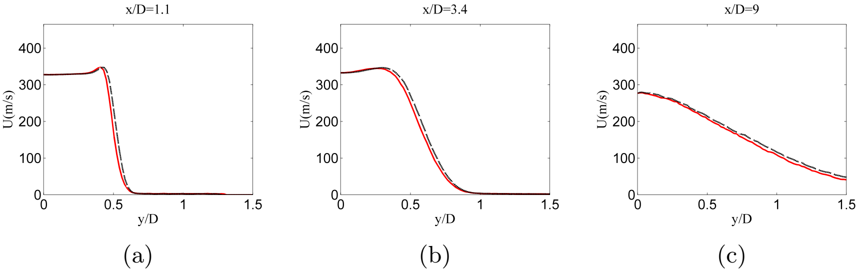

(a) (b) (c)

Figure 3.18: Symmetry of the transversal axial velocity profiles for different locations. Black dashed line corresponds to $y < 0$

3.5.2 Shock-cells length

The main characteristics of the shock-cell pattern have been retrieved from the PIV measurements. The axial velocity component of the mean flow, $\overline{U}$, is displayed in Fig. 3.19 together with the streamlines. The curvature of the streamlines, which comes from the lateral expansions and compressions of the jet plume, is induced by the underexpansion.

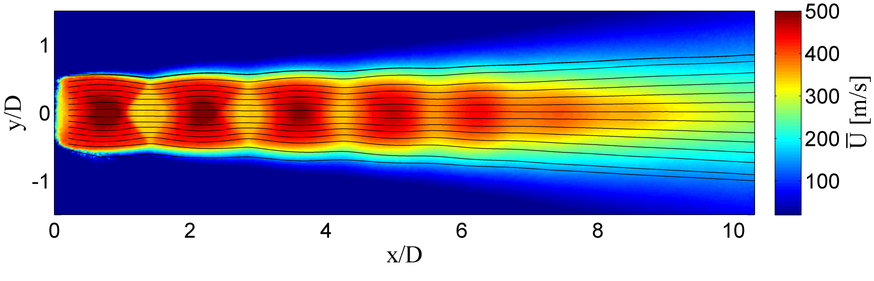

Figure 3.19: Velocity field for $M_j = 1.50$, NPR = 3.67. Black lines represent the streamlines.

Local Mach numbers can be computed from the PIV data assuming the total temperature does not change in the pipes, and it is and equal to the reservoir one. With the further assumption of isentropic flow the following formula was used [5]:

$$|M| = \sqrt{\frac{|U|^2}{\gamma R T_0 - |U|^2(\gamma - 1)/2}} \tag{3.5}$$

which is less and less valid as the shock-wave strength increases, and in the shear layer, as effect of entropy production. Pérez Arroyo, in his LES on a supersonic coaxial jet [67], found a difference $< 3\%$ between the Mach number extracted from the simulation and calculated using this method [65]. An overview of the average velocity fields for all the tested condition is presented in Fig. 3.20. The picture shows the progressive increment of the shock-cell length, but not the same for the total length of the supersonic region; sudden reductions of the number of the shock-cells periodically occur. It was already known from the literature [78][2] this is due to the effect of the screech acoustic feedback loop, which destroys the shock-cells system. For NPR = 2.30, an axisymmetric screech mode (A2) is present, from NPR = [2.40 2.50 2.60] a flapping mode (B) is onset, and finally for NPR = [2.7 2.96 3.67] an helical mode (C) is ongoing. Further information on the screech modes can be found in Sec. 3.6 and 5.

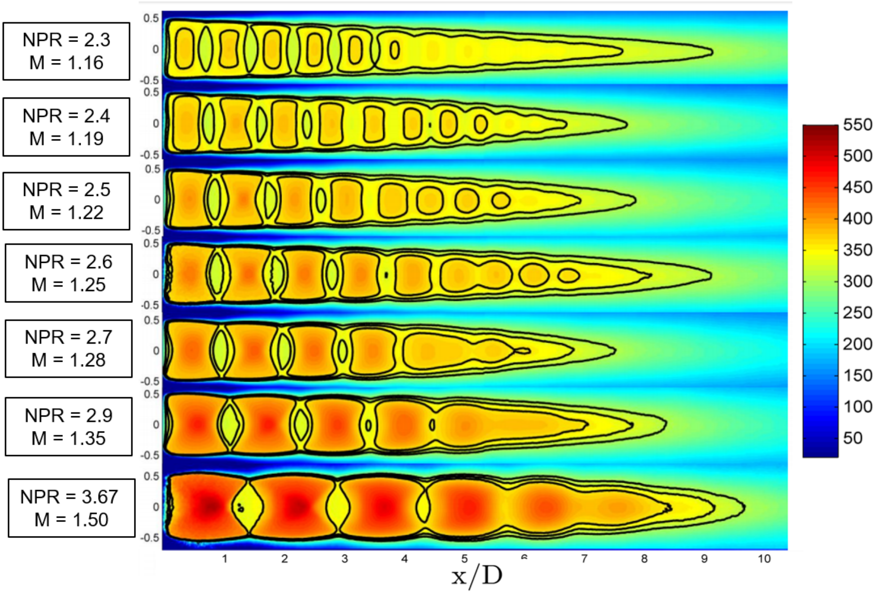

Figure 3.20: Overview of the averaged velocity field for all the conditions investigated. Black isocontour lines identify M = [0.9 1.0 1.1].

In Fig. 3.21, the variation of the absolute Mach number of the mean flow, in the center line, is shown. The amplitude of the fluctuations depends on the strength of the shocks present in the jet plume, and thus on the off design factor β. For this reason, the amplitude of the oscillations grows when the M_j is increased. The fluctuations intensity decreases as the distance from the exit of the nozzle is increases. A method to collapse all the fluctuations curves in the center line of the jet is proposed by Savarese [79] for his non-screeching jet. The shock cell length appears to be proportional to β and the amplitude of the fluctuations is proportional the pressure mismatch, which, in turn, appears to be proportional to β^2. Therefore, by dividing the length of the shock cells by the off design factor and the amplitude by β^2 a collapse of all the curves is tempted. The raw profiles and the collapsed ones are presented in Figs. 3.21 and 3.22.

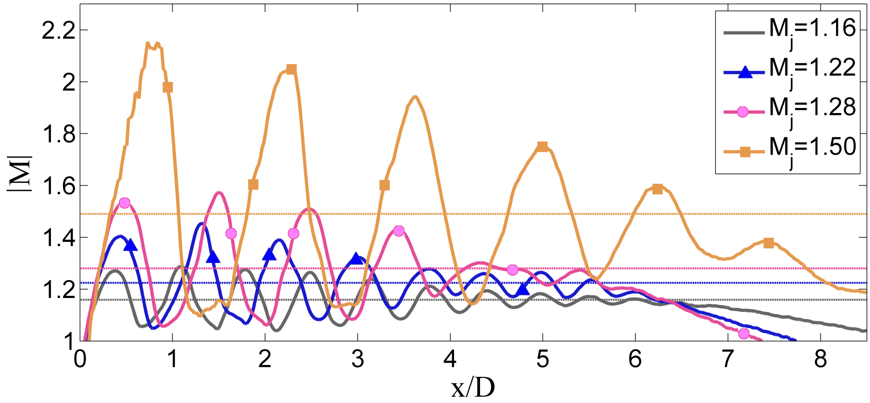

Figure 3.21: Mach number profiles in the center line of the jet. Horizontal lines mark the value of the fully expanded Mach number M_j for each case.

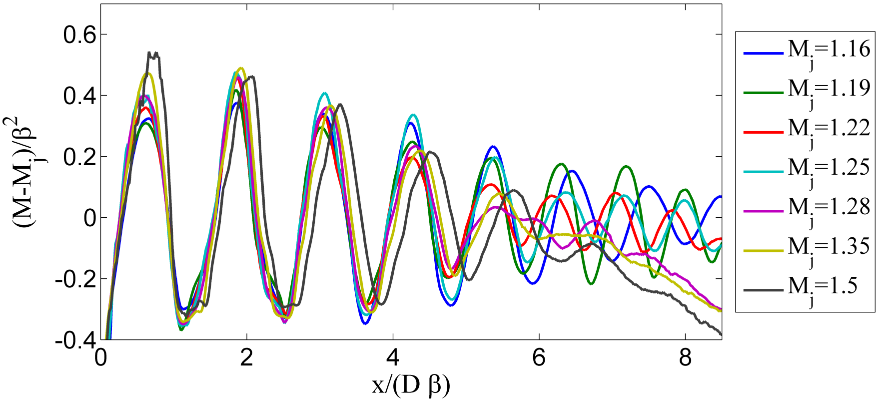

Figure 3.22: Normalisation of the Mach number profiles in the center line of the jet proposed by Savarese [79]

The results of the scaling is rather good until the 4^{th} shock-cell. After that, it is believed the screech is affecting the jet plume, destroying the shock-cell pattern, and thus the scaling is not valid anymore.

The mean shock cell length is one of the parameters that are required in the Tam's model to predict the BBSAN in the far field[90]. In order to retrieve this parameter from the flow field measurements, the location of the local minimums of the mean flow velocity on the center line of the jet have been calculated. The Mach profiles have been slightly smoothed to facilitate the peak recognition by the algorithm as shown in Fig. 3.23. The method has the drawback of slightly reducing also the amplitude of the fluctuations, but this quantity is not of interest.

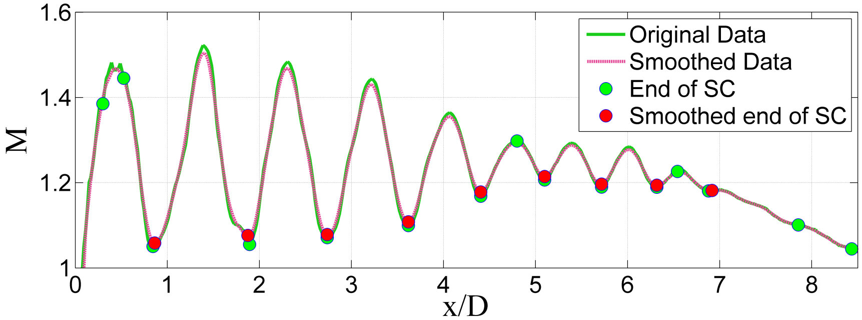

Figure 3.23: Example of shock-cell minima identification. Green points are the local minima from the original noisy signal. Red points mark the minima after smoothing the data.

The shock-cell end locations, retrieved through this method, are marked by the vertical black lines in Fig. 3.24. The averaged shock cell length has also been compared with the semi-empirical relation proposed by Harper-Bourne and Fisher [34] and expressed by Eq. 1.12. The mean value for every case is plotted in Fig. 3.25, together with the tendency line retrieved from the equation. The measured data followed the proposed trend for all the cases. The behavior is overall acceptable for $x/(\mathrm{D}\beta) < 4$. Above this point, the curves lose coherence. The hypothesis is that the heavy occurring screech is altering the shock-cells sequence, also in virtue of the fact that three different screech modes are affecting the measurements.

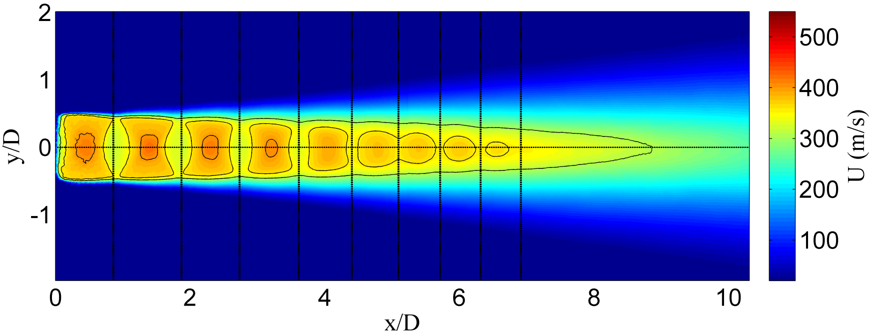

Figure 3.24: Velocity contour for $M_j = 1.25$. Solid black contour marks Mach number from 1 to 1.4. Exterior line indicates sonic line. Vertical lines denote the end of the shock cells using the method proposed.

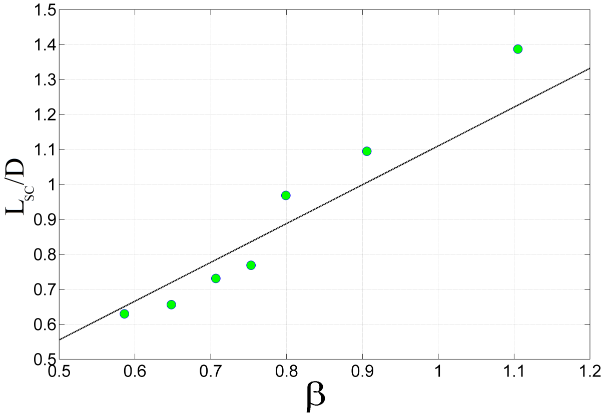

Figure 3.25: Evolution of the mean shock cell length L_{sc} with the of design parameter β. Black solid line denotes the semiempirical correlation proposed by Harper Bourne and Fisher [34]

3.5.3 Jet Mixing Layer

A description of the mixing layer of the jet is carried out in this section to be compared with the literature.

3.5.3.1 Mixing Layer Thickness

The mixing layer boundaries have been computed through the method proposed by André *et al.* [5]. The boundaries are defined as the location where the axial velocity fluctuations of the mean flow have decreased to

0.1 times the difference between the minimum and the maximum of the fluctuations in the radial profiles (Fig. 3.26). For the present investigation, instead of 0.1, the factor 0.2 was chosen since it produced more robust results. The consequence of the change of the factor is that the mixing layer thickness will be underestimated with respect to the one found in the aforementioned investigation.

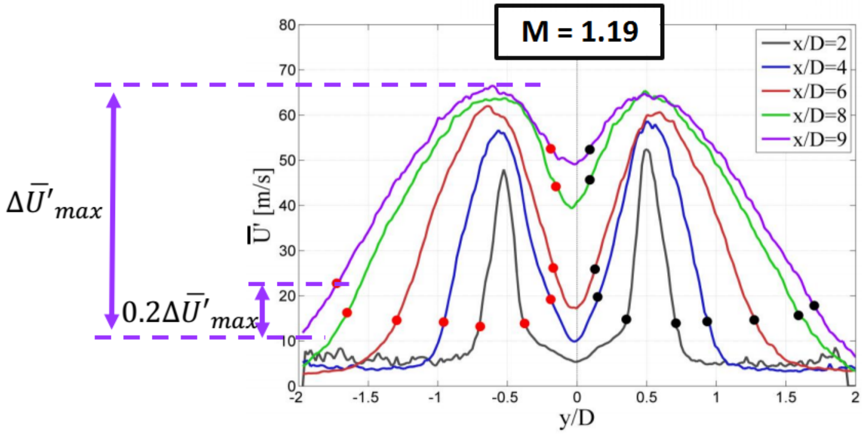

Figure 3.26: Explanation of the method used to determine the boundary of the shear layer.

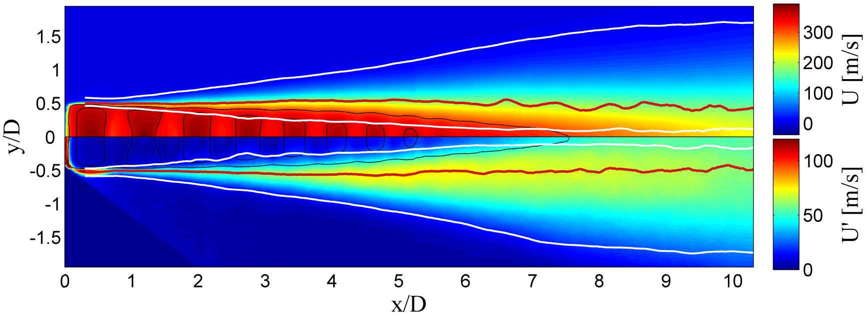

Figure 3.27: Combined contour plot of mean axial velocity component (top) and mean axial velocity component fluctuations (bottom) for the case $M_j = 1.19$. Solid white line points out the limits of the mixing layer. Solid red line identify the maximum velocity fluctuations. Solid black line is a contour of the absolute Mach number, where the outer line indicates the sonic line ($M = 1$).

A map of the jet plume merging axial velocity component (top) and axial velocity component fluctuations (bottom) for the case $M_j = 1.19$ is presented in figure 3.27.

A first result that should be noticed is that although most of the mixing layer is at subsonic conditions, a part of the mixing layer is in the supersonic region of the jet plume. The maximum fluctuations, however lay always outside of this zone. For this Mach number, the mixing layer growth does not seem to be affected by the shock cell pattern except for small undulations around x/D = 3, for the internal boundaries.

For $M_j = 1.5$, on the other hand, the inner part of the boundaries are oscillating periodically with the series of expansions and compressions taking place in the potential core.

On the basis of similar results André *et al.* [5] concluded that the mixing layer of the jet is only affected by the shock cell pattern at high under expansion degrees.

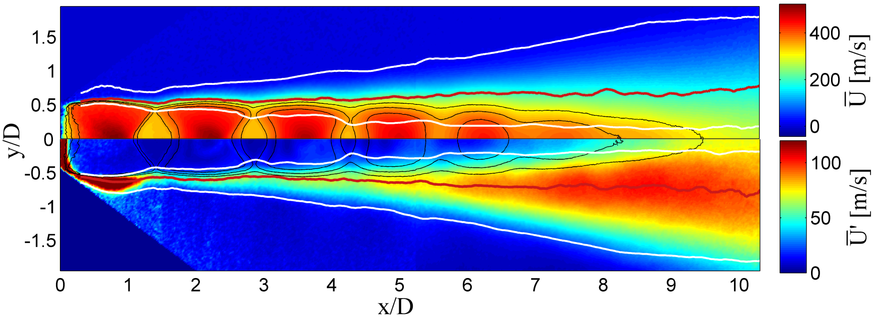

Figure 3.28: Combined contour plot of mean axial velocity component (top) and mean axial velocity component fluctuations (bottom) for the case $M_j = 1.5$. Solid white line points out the limits of the mixing layer. Solid red line identify the maximum velocity fluctuations. Solid black line is a contour of the absolute Mach number, where the outer line indicates the sonic line ($|M| = 1$).

The mixing layer thickness was computed as the distance between the inner and the outer part of the mixing layer $\delta = y_o - y_i$. A more robust quantity is the momentum thickness, which is defined as [5]:

$$\delta_\theta = \int_{y=0}^{\infty} \frac{\overline{\rho U}}{(\overline{\rho U})_0} \left[1 - \frac{\overline{U}}{(\overline{U})_0}\right] dy \tag{3.6}$$

Since only the velocity field is retrieved from the PIV measurements, an incompressible version of the momentum thickness is used here:

$$\delta_\theta = \frac{1}{[\overline{U}(y_i) - \overline{U}(y_o)]^2} \int_{y_i}^{y_o} \left[\overline{U}(y) - \overline{U}(y_o)\right] \left[\overline{U}(y_i) - \overline{U}(y)\right] dy \tag{3.7}$$

Both definitions of the mixing layer proposed before, for the case $M_j = 1.50$, are shown in Fig. 3.29, with the mixing layer thickness δ scaled by a factor

7.5, as already found in [5]. The difference in the mixing layer growth, for the upper and lower part of the image, appears to be negligible.

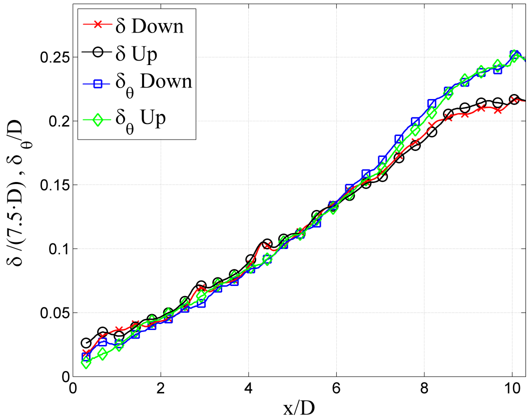

Figure 3.29: Comparison between different computations for the mixing layer thickness for the case of $M_j = 1.50$. "Down" stands for the lower part of the image ($y < 0$) and "Up" stand for the upper part image ($y > 0$).

Due to the 2D character of the PIV measurements, to quantify the fluctuations in both directions, the following quantities are introduced:

$$TI_U = \frac{\sigma(u')}{U_j} \qquad TI_V = \frac{\sigma(v')}{U_j} \tag{3.8}$$

where $\sigma(u'), \sigma(v')$ are the standard deviation of the instantaneous fluctuations of the PIV velocity fields for axial and radial direction, respectively. A

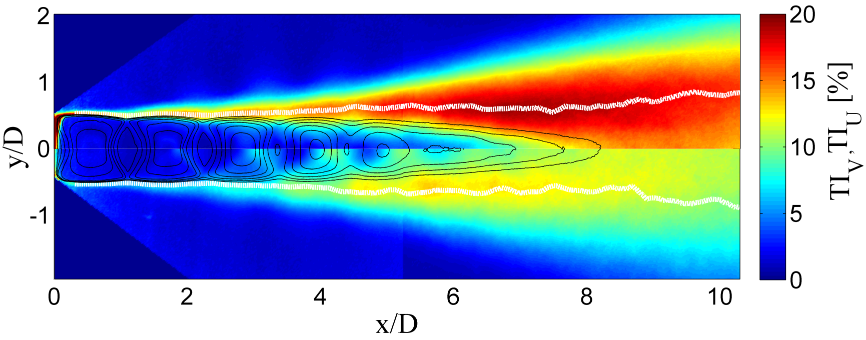

Figure 3.30: Contour plot of the axial (top) and radial (bottom) turbulence intensity for $M_j = 1.35$. Solid white line indicates the line of maximum axial velocity fluctuations.

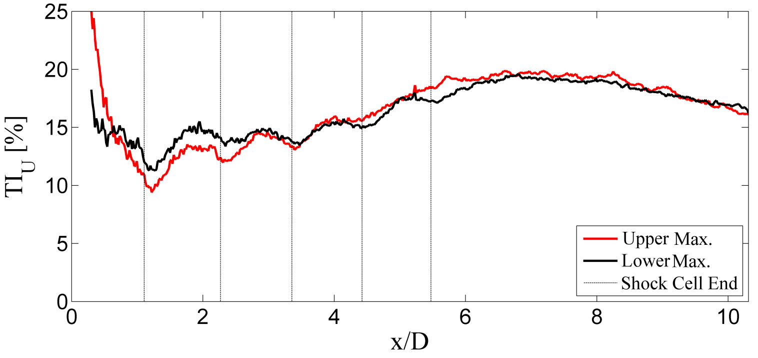

Figure 3.31: Axial turbulence intensity profiles along the lines of maximum velocity fluctuations for $M_j = 1.35$. Upper means $y > 0$ and lower $y < 0$

cartography of the turbulence intensity for both components is shown in figure 3.30. As it can be seen, the turbulence intensity in the axial direction is generally higher. Fig. 3.31 show the turbulence intensity related to the maximum axial velocity fluctuations, for the case $M_j = 1.35$.

The behavior is similar in both sides of the mixing layer. However the plot show a discrepancy closer to the jet, where the value of the fluctuations in the upper mixing layer is much higher. The reason of this feature seems to be an error of the PIV post-processing algorithm during the deformation of the interrogation window. The error perturbs the measured data till the second reflection point, where both curves collapse again. In this figure, the turbulence intensity growths approximately until x/D=7, where it reaches a maximum at 20 %, and then decays. A local modulation of the turbulence intensity level produced by the shock cell pattern is also. These modulations show minima near the end of the shock cells. These features were also noted in their data by Bridges & Vernet [15], Panda & Seaholtz [63] and Seiner & Yu [83]. Bridges & Vernet measured the turbulence characteristics of jets by means of time resolved PIV. The measurement of an underexpanded screeching jet at $M_j = 1.40$ reported that the axial turbulence intensity grew until 24 % before decaying. On the other hand, André *et al.* found in their experiments on a non screeching jet that, at small degrees of under expansion, the longitudinal turbulence intensity levels had a constant value of 16 % along the line of maximum axial fluctuations. At higher degrees of under expansion, the axial turbulence intensity was modulated, but it is also tending to the same value. Nevertheless, they pointed out that probably the presence screech tones induced an increase of the fluctuations in the downstream direction.

The turbulence intensity related to the axial velocity fluctuations for all the measured test cases is presented in Fig. 3.32. In this study, the modulation

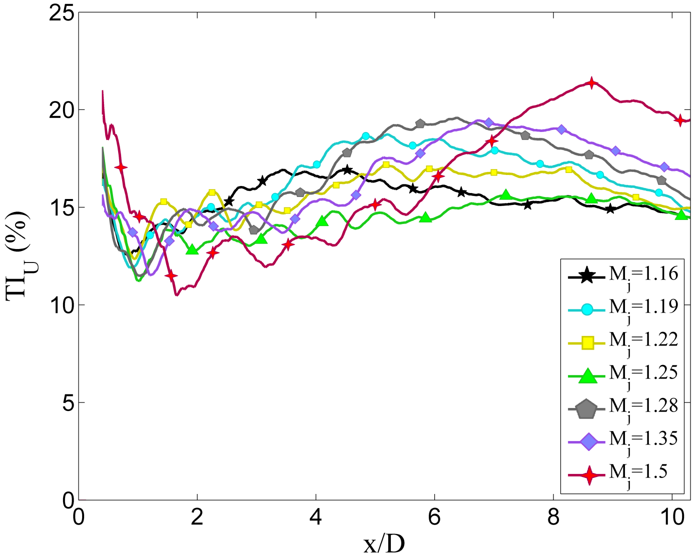

Figure 3.32: Axial turbulence intensity for the different test cases. Data have been smoothed for better readability.

of the velocity fluctuations are present in all cases, being more evident as the grade of underexpansion increases. For the test cases $M_j = 1.16$ and $M_j = 1.25$ the turbulence intensity tends to 15% after reaching the maximum. For the rest of the test cases, except $M_j = 1.5$ the axial turbulence intensity values reach a maximum and then decrease to a value ranging between 15% and 17%. For $M_j = 1.5$ the maximum value is of 21% and then it decrease to a value of 19.5%. For the latter case, the field of view limits the investigation.

It is worthy to note how the maximum of the turbulent intensity does not increase monotonically with the Mach number, as well as the distance of the maxima and the nozzle exit. This could be due to the changes of the screech modes, which seems to induce a sudden increment of the maximum turbulence intensity, followed a reduction od the maximum, until another screech mode and another sudden increment is encountered.

The trend is very similar also for the turbulence intensity of the radial velocity fluctuations, shown in Fig. 3.33 The growth and decay of the fluctuations is again found, together with the aforementioned modulation. In all cases, the values of the radial turbulence intensity are lower than the axial analogue curves. André *et al.* [5] reported a value of 10% along the maximum axial fluctuations line in their measurements. The radial turbulence intensity for the cases $M_j = 1.16$ tends to 9.5% after the maximum. For the rest of the test cases, the radial turbulence intensity decays after the maximum to values comprised between 10 and 13%. To conclude, the behavior of the

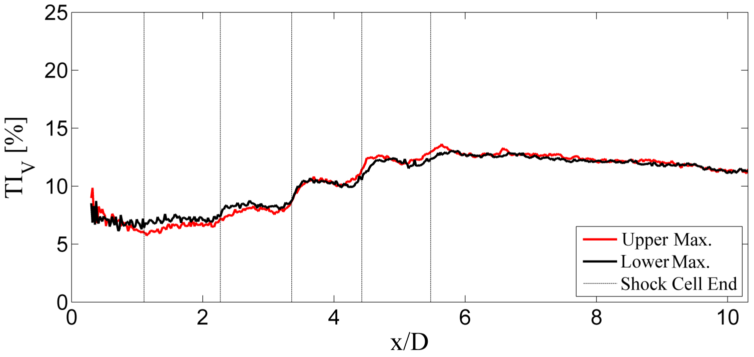

Figure 3.33: Radial turbulence intensity profiles along the lines of maximum velocity fluctuations for $M_j = 1.35$. Upper means y¿0 and lower y¡0

turbulence intensity related to both the radial and axial velocity fluctuations found in the measurements is consistent with the literature. The measured values agree with the ones reported for screeching jets. Furthermore, the measured values are also agree with the data from non screeching jets for some of the cases.

M_j	1.16	1.19	1.22	1.25	1.28	1.35	1.50
$x_{u'_{max}}/D$	3.43	5.211	5.192	7.16	6.317	6.748	8.622

Table 3.7: Location of the maximum axial velocity fluctuation for all test cases.

Finally, a trace of the standing wave associated with the screech has been found in the Reynolds shear stress field $u'v'$. Fig. 3.35 shows the presence of lobes outside the jet shear layer. Those lobes are recurrent in every test cases, also for the coaxial jet, except in the cases where the screech is not present (Fig. 4.40). The phenomenon of the standing wave was confirmed firstly by Panda in [61]. He demonstrated how the interaction between the acoustic pressure waves, moving in the upstream direction, and the pressure waves caused by the hydrodynamic fluctuations, being convected downstream, creates a pressure wavy pattern in the near field. The pressure standing wave must have a correspondent velocity standing wave, which is what has been captured by PIV. Velocity correlation maps show the presence of lobes in the shear layer, which could be the areas subjected to the moving hydrodynamics structures (Sec. 5). Nevertheless, a two-point time resolved investigation is necessary to confirm the former assumptions.

4

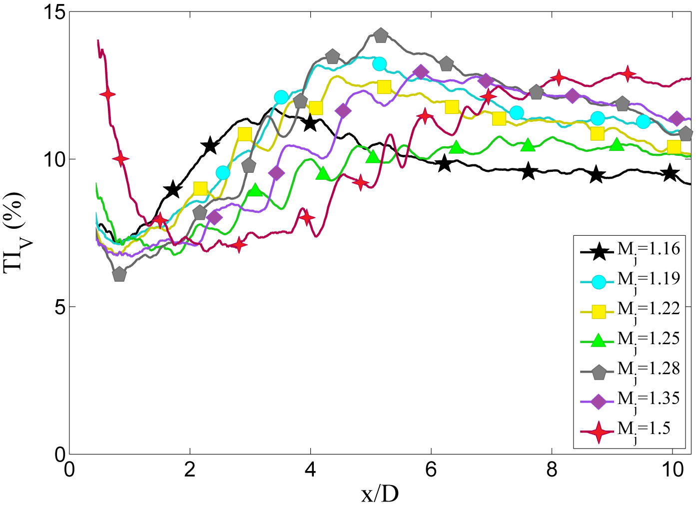

Figure 3.34: Radial turbulence intensity for the different test cases. Data have been smoothed for better readability.

3.5.3.2 Integral Length Scales

Spatial correlations are computed from the instantaneous velocity fields in order to achieve information on the size and shape of the turbulent structures in the mixing layer.

A two point spatial correlation was applied in the upper lip line of the jet $y/D = 0.5$. The correlation has also been applied in the lower lip line $y/D = -0.5$,in the outer lines $y/D = 0.55$ and $y/D = 0.6$ and in the lip line of the fully expanded diameter $y/D_j = 0.5$. The results found were similar to the ones reported here. The coefficient of spatial correlation is calculated as:

$$R_{ij}(x, y, \zeta_1, \zeta_2) = \frac{\overline{u'_i(x, y)\, u'_j(x + \zeta_1, y + \zeta_2)}}{\sigma_i(x, y)\, \sigma u'_j(x + \zeta_1, y + \zeta_2)} \tag{3.9}$$

where the indexes i and j represent the velocity component so $u'_1 \equiv u'$ and $u'_2 \equiv v'$, x and y are the coordinates of the reference point, ζ_1 and ζ_2 are the axial and radial components of the separation vector respectively, $\sigma_{i,j}$ is the standard deviation in the relative direction. The correlation function is an indicator of repetitive spatial schemes between the two variables correlated. Therefore, higher correlation values mean that the same fluctuation pattern (although with different intensity level) is present in most of the snapshots, while lower correlation is symptom of randomness between the fluctuations in the two points. Two contour plots of the autocorrelation functions R_{11} and R_{22} are shown in Figs. 3.36(a) and 3.37(a) respectively. Thanks to the

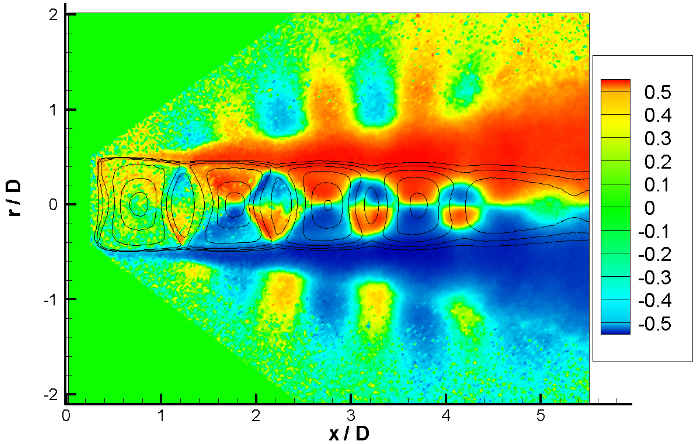

Figure 3.35: Normalized Reynolds shear stress $u'v'/\sqrt{|u'v'| \cdot \sigma(u)\sigma(v)}$ for NPR = 2.70, M$_j$ = 1.28. Black lines are Mach isocontours for M = [1:0.1:1.5].

correlation function R_{ij}, it is possible to calculate the integral length scales of the velocity fluctuations in the direction k, with k $\in (1, 2)$ as follows:

$$L_{ii}^{(k)}(x, y) = \frac{1}{2} \int_{-\infty}^{\infty} R_{ii}(x, y, \zeta_k) d\zeta_k \tag{3.10}$$

where ζ_k is the separation distance. Although the integration should be done in an infinite interval, for obvious reasons in practice a finite interval is set. Specifically, the integration was performed between the interval where the correlation value has decreased to 0.2, to avoid noise appearing in the lower part of the correlation domain. Therefore, the integral length scales is underestimated but the computation is more robust. The axial ($\zeta_2 = 0$) and radial ($\zeta_1 = 0$) cuts of the autocorrelation function R_{11} are presented in Figs, 3.36(b) and (c), where the integration domain was shadowed. The same plots for the autocorrelation function R_{22} are shown in figure 3.37. It was observed that the axial and radial velocity fluctuations u' and v' inside the jet plume are linked on the ones happening in the lip line. In the case of the radial velocity fluctuation v' this dependency goes far beyond the center line of the jet. The shape of the correlation contours suggest that the turbulent structures have an elliptical shape, which is the shape also found by Bailly *et al.* [5].

In Fig. 3.38 are shown the length scales related with the axial velocity fluctuations in the case $M_j = 1.22$. They seem to grow linearly with downstream distance, as it is the case for subsonic jets [29] and also supersonic [5] [101], but a modulation is present. This modulation starts at the first reflection point and it coincides with the rest of shock reflection points. Fig.

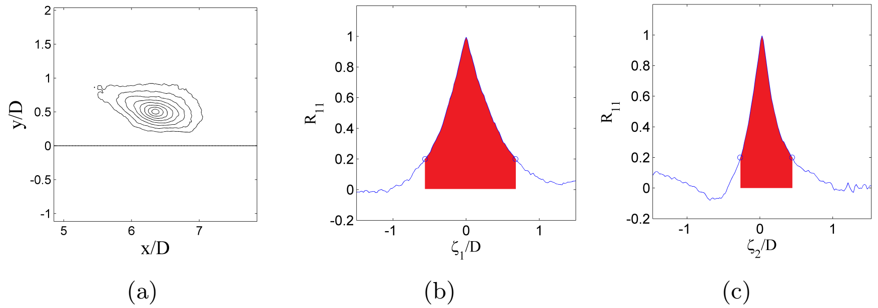

(a) (b) (c)

Figure 3.36: Autocorrelation of the axial velocity fluctuations u'. (a) Contour plot of the R_{11} function. Outer line indicates $R_{11} = 0.2$. Black horizontal line points out the center line of the jet. (b) Axial profile of the correlation function R_{11} shown in (a). Shadowed area indicates the area integrated to calculate $L_{11}^{(1)}$. (c) Radial profile of the correlation function R_{11} shown in (a). Shadowed area indicates the area integrated to calculate $L_{11}^{(2)}$.

3.39 shows the length scales related with the radial velocity fluctuations. Again, the growth of the length scales is seems linear, and the modulation in the reflection points is also retrieved. Estimates of L_{22}^{2} present a more accentuated modulation and the growth is not linear. After reached a maximum, it stabilizes to a constant level.

The ratio of the length scale to mixing layer thickness have been calculated in order to compare with the literature. In spite of the modulated behavior, the integral length scales exhibit a generally linear trend [5], as well as the rate of growth of the momentum thickness. Therefore, the ratio must tend to a constant value [101]. The ratios between the length scale of the axial

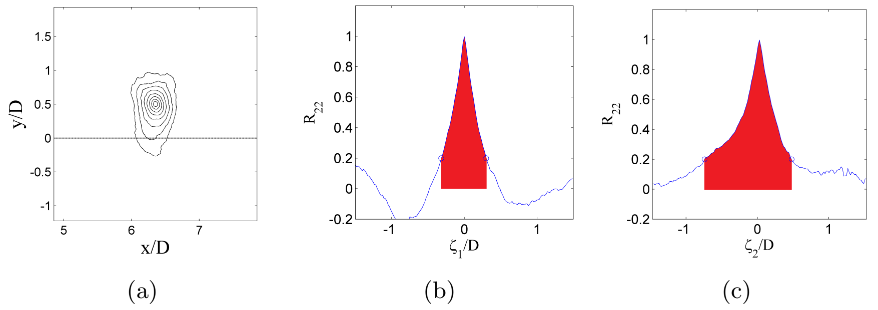

(a) (b) (c)

Figure 3.37: Autocorrelation of the axial velocity fluctuations v'. Same legend than in figure 3.36.

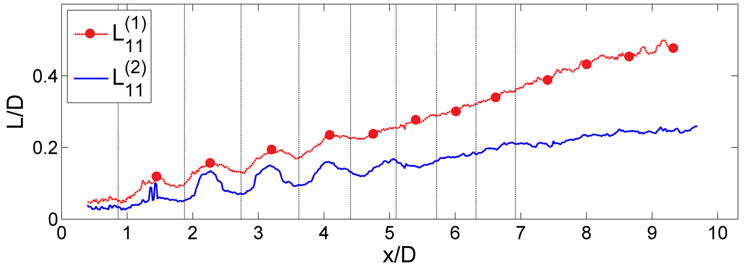

Figure 3.38: Integral length scales associated with the axial velocity fluctuations u' for the case $M_j = 1.22$. Red line indicates integral length scale in the axial direction. Blue line indicates the radial one. Black vertical lines indicates the shock cell ends.

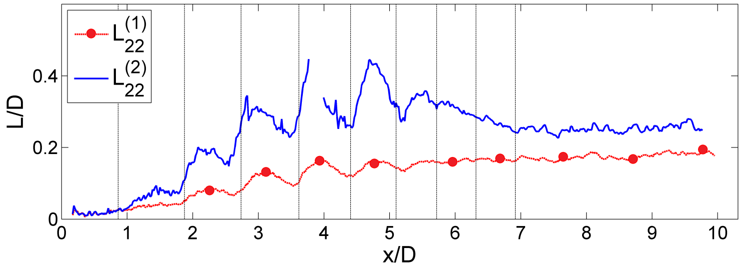

Figure 3.39: Integral length scales associated with the radial velocity fluctuations v' for the case $M_j = 1.22$. Red line indicates integral length scale in the axial direction. Blue line indicates the radial one. Black vertical lines indicates the shock cell ends.

velocity fluctuations are shown in Figs. 3.40(a) and (b). The values are plotted until x/D=8.5 because at approximately that distance the mixing layer thickness calculation starts to be affected by the limits of the FOV producing an underestimation on the calculation of this quantity. Data from the test case $M_j = 1.5$ was removed from the $L_{11}^{(1)}/\delta_\theta$ because the integral length scale exceeded the axial component of the separation vector ζ_1, so it could not be calculated from the current data.

The ratio between the axial length scale of the radial velocity fluctuations is shown in Fig 3.41 for all test cases.

In order to establish a comparison with the data from Tan *et al.* [101], the value of the ratio was taken in x/D=8. Data from André *et al.* [5] has been also compared. The values of the ratio for the different test cases, retrieved by Rubio Carpio [77], is presented in Tab. 3.8 and 3.9. Tan's research have been carried out in similar conditions than in the present study, with a

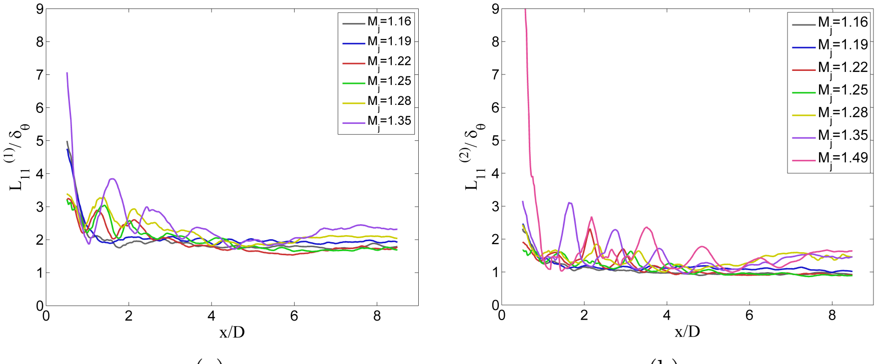

(a) (b)

Figure 3.40: Length scales of the axial fluctuating velocities along the lip line.

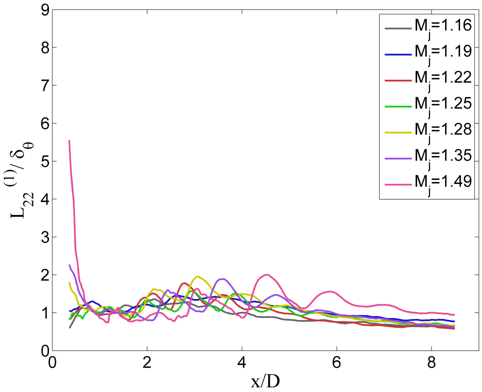

Figure 3.41: Length scales of the radial fluctuating velocities along the lip line.

screeching jet. On the other hand, the experimental set-up of Bailly was slightly different since the screech tone was suppressed cutting some notches in the nozzle lip and adding some co-flow. Therefore, the periodic coherent fluctuations associated to the tonal noise are not present in that study. Tan *et al.* already noted that the results of their experiments overestimated the results of André. They attributed these differences to the presence of the coherent periodic structures driving the acoustic mechanism. In the case of the present study, the values of the integral lengths at higher under expanded conditions also overestimate the results of Bailly, being closer to the values given by Tan. Nevertheless, at low under expansion conditions the data agrees better with the parameters retrieved by André.

	L^1_{11}/δ_θ			L^2_{11}/δ_θ		
M_j	Rubio Carpio	André	Tan	Rubio Carpio	André	Tan
1.10	-	1.76	-	-	0.83	-
1.16	1.87	1.95	-	0.97	0.89	-
1.19	1.92	-	-	0.99	-	-
1.22	1.73	-	-	0.91	-	-
1.25	1.68	-	-	0.89	-	-
1.28	2.11	-	-	1.31	-	-
1.35	2.36	2.06	-	1.33	0.97	-
1.50	-	2.15	2.39	1.42	1.03	1.28
1.60	-	-	2.39	-	-	1.28

Table 3.8: Ratios of the length scales to the momentum thickness at x/D = 8. The approximated values of André *et al* [5] and *et al* [101] are reproduced.

	L^1_{22}/δ_θ		
M_j	Rubio	André	Tan
1.10	-	1.76	-
1.16	1.87	1.95	-
1.19	1.92	-	-
1.22	1.73	-	-
1.25	1.68	-	-
1.28	2.11	-	-
1.35	2.36	2.06	-
1.50	-	2.15	2.39
1.60	-	-	2.39

Table 3.9: Ratios of the length scales to the momentum thickness at x/D = 8. The approximated values of André *et al* [5] and *et al* [101] are reproduced.

Therefore, the statistical quantities of the flow field of the jet are in concordance with the data presented in previous research, both at higher and lower degrees of under expansion, and the jet rig can be considered qualified from the flow point of view.

3.6 Acoustic Results

The objective of this section is to present the acoustic results retrieved from the successive test campaigns and compare them with literature to check that the typical acoustic characteristics of the shock associated noise are present in the measurements. For sake of brevity, only the results conducted on the third test campaign on the scaled single stream jet will be presented. First, an analysis of the evolution of the shock cell noise with the M_j is performed. From Fig. 3.42 to Fig. 3.46 an overall view of the Sound Pressure Level (SPL) measured by the eleven microphones, for several Mach numbers, is displayed. In the upper plots, the spectra at all the angles are superimposed, for an immediate view of the BBSAN peak frequency shift, and of the screech intensity. In the bottom plots, instead, the SPL, for each angle, is staggered for better readability. The SPL is defined as:

$$SPL[dB] = 20\, log_{10}\left(\frac{p'}{p_{ref}}\right) \tag{3.11}$$

where $p_{ref} = 20 \cdot 10^{-6}$ Pa. While the Strouhal number is defined as:

$$St = \frac{f \cdot D_j}{V_j} \tag{3.12}$$

where f is the frequency, D_j is the fully expanded jet diameter, and V_j is the fully expanded jet velocity.

At small under expansion degree, the shock cell pattern is weak, and the interaction between the turbulence structures in the mixing layer and the shock cell pattern is not an efficient noise source. Although the characteristic hump of the BBSAN is present in the high frequency content of the upstream microphones, the sound peak reached with this mechanism is relatively low (around 70 dB). In fact, the most intense sound is radiated downstream by means of the jet mixing noise mechanism. Furthermore, the feedback loop involving the generation of the screech tone has not been triggered at this condition, so the tonal noise is not present (Fig. 3.42 left).

On the other hand, the analysis of the spectra measured at higher under expanded conditions, shows all the typical acoustic features of the shock cell noise. The hump of broadband shock cell noise is present at the high frequency part of the spectra, except for the microphones located in the very downstream positions. Furthermore, the shock cell noise peak is now clearly visible. In the case of the microphones located downstream the peak is not so evident, except for high CNPR. The frequency of the broadband spectral peak increases as the listener moves to downstream positions, as it was already indicated by Tam [90]. In the aforementioned cases, the feedback loop involving the generation of the screech was triggered, so, the tonal noise and its harmonics are present. One can infer from these plots that the screech frequency decreases as the degree of under expansion is increased. This behavior has already been noticed in different publications

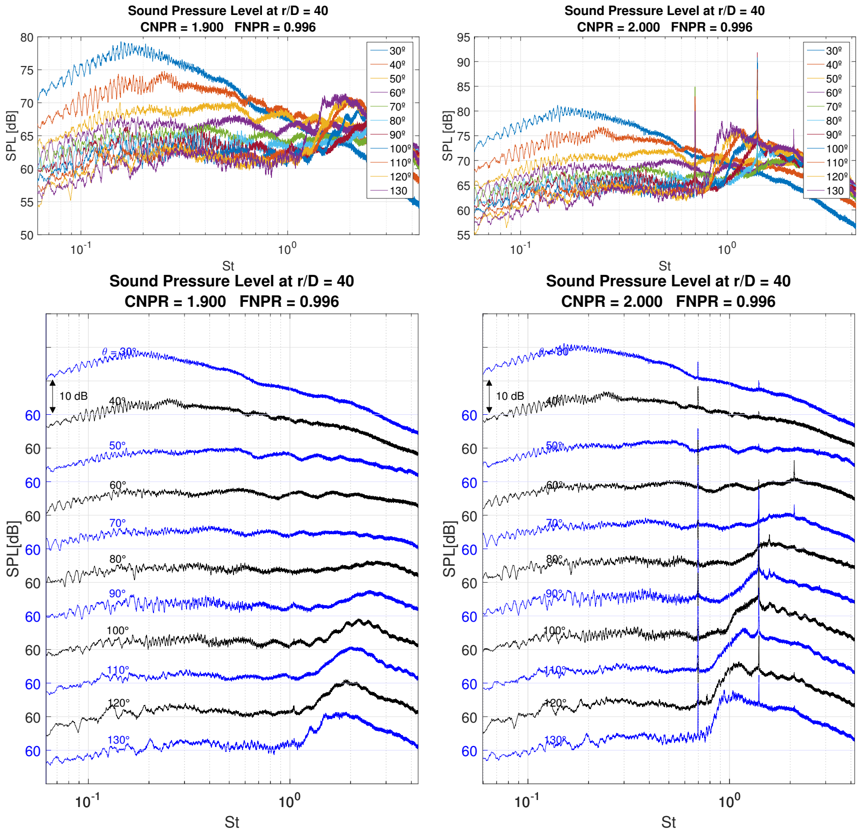

Sound Pressure Level at r/D = 40
CNPR = 1.900 FNPR = 0.996

Sound Pressure Level at r/D = 40
CNPR = 2.000 FNPR = 0.996

Sound Pressure Level at r/D = 40
CNPR = 1.900 FNPR = 0.996

Sound Pressure Level at r/D = 40
CNPR = 2.000 FNPR = 0.996

Figure 3.42: SPL (ref. $2 \cdot 10^{-5}$ Pa) for CNPR = 1.90 $M_j = 1.005$ (left) and CNPR = 2.00 $M_j = 1.05$ (right) at all the measured angles, nozzle diameter D = 0.019 m. The same curves, but staggered, are presented in the lower pictures. All curves have the same base level, which is reported on the left scale, matching the color (blue/black) of the curve whom it is referred. Despite the jets are barely supersonic, the BBSAN is clearly visible, and in the higher condition also the screech tone.

[51] [93] [95]. Interestingly, many harmonics have been identified, in some cases up to the 10^{th} one. The screech harmonics show a directivity pattern, as pointed out already by Tam [100]. However, little research has been conducted on this topic, due to the difficulties in finding screeching jets with many harmonics. It is thus recommended a further analysis and comparison with Tam's results. Furthermore, in some cases, the presence of screech subharmonics, and harmonics of the subharmonics, have been recorded. These events correspond mainly to cases when the screech was swapping

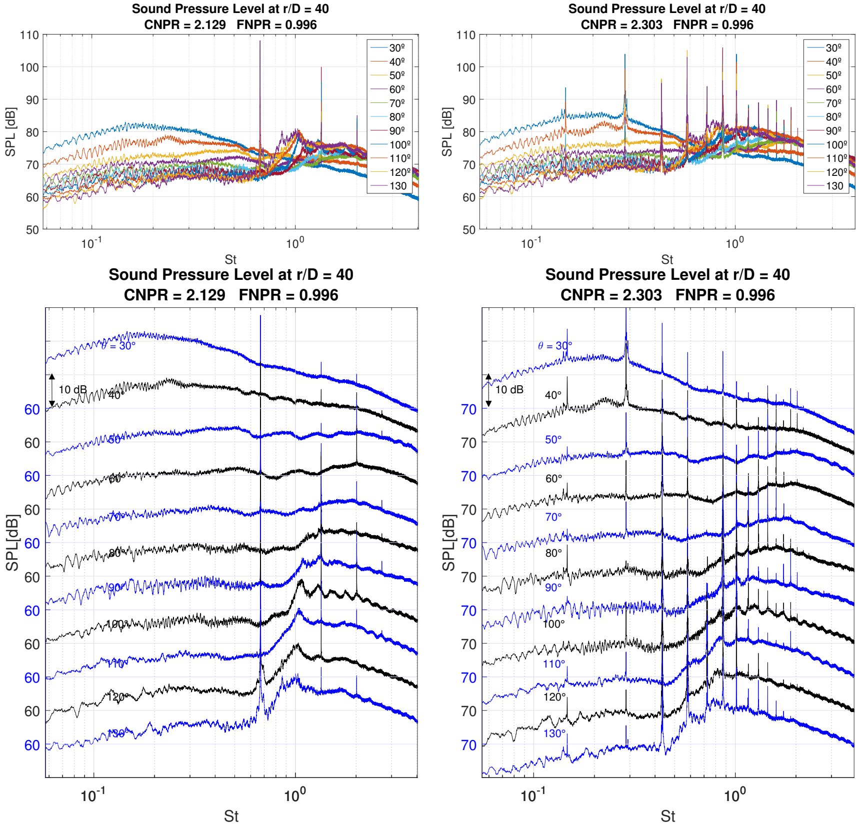

Figure 3.43: SPL (ref. $2 \cdot 10^{-5}$ Pa) for CNPR = 2.13 $M_j = 1.10$ (left) and CNPR = 2.30 $M_j = 1.16$ (right) at all the measured angles, nozzle diameter D = 0.019 m. The right images show the swapping between two screech modes, from the axisymmetric to the flapping one. Many harmonics, subharmonics, and harmonics of the subharmonics of both screech tones are visible.

from one mode to another. In Fig. 3.43, the subharmonics of both the screech tones are present, and the jet is moving from the axisymmetric to the flapping mode. Another case is for NPR = 2.70, immediately after the swap from the flapping to the helical mode 3.45. From the hydrodynamic point of view, it happens that the shock-cell structure collapses, and therefore the jet passes from a ordered configuration to a more chaotic one. Normally the presence of harmonics is indicative of a saturation mechanism. It is not known, at this point, if subharmonics could also be associated to the same saturation mechanism, or to a different feature. When the the pressure ratio is sufficiently high to lead to the Mach disk formation, no screech is further

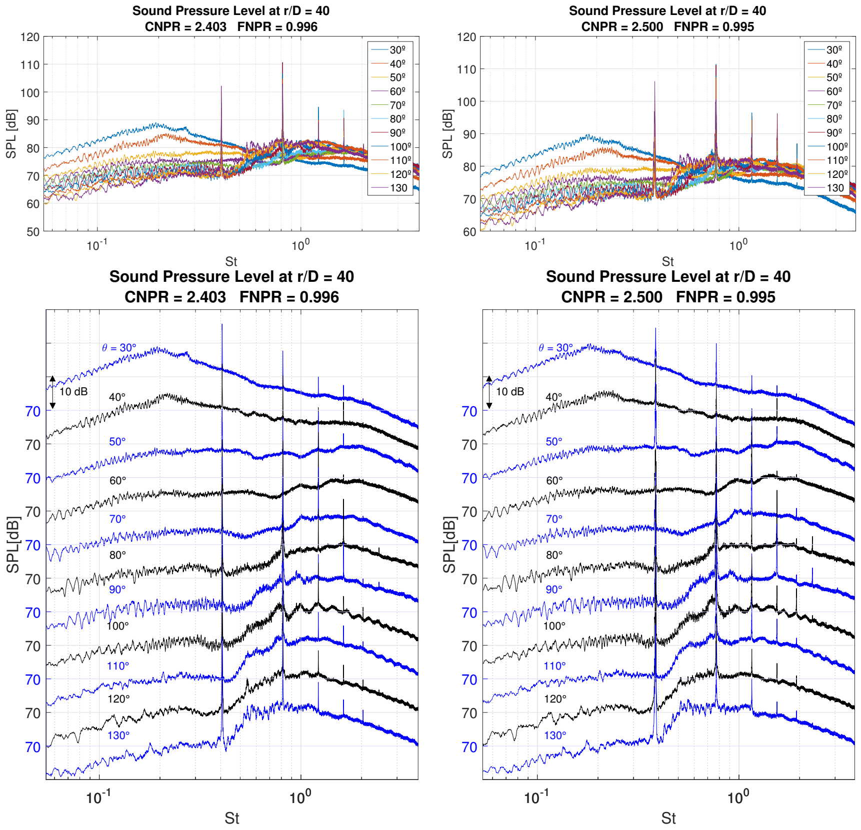

Figure 3.44: ref. $2 \cdot 10^{-5}$ Pa) for CNPR = 2.4 $M_j = 1.19$ (left) and CNPR = 2.50 $M_j = 1.22$ (right) at all the measured angles, nozzle diameter D = 0.019 m.

encountered (Fig. 3.46).

Although in these cases the shock associated noise is the main contributor to the overall noise emitted by the jet , the jet mixing noise is still present . The increase of the sound pressure level in the low frequency part of the spectra for the microphones located downstream (mainly $\theta = 30^o$ and $\theta = 40^o$) is due to this sound generation mechanism.

3.6.1 Sound Intensity Level

The Sound Intensity Level is a power flux, defined as:

$$I = \frac{p'^2}{\rho_\infty \, c_\infty} \tag{3.13}$$

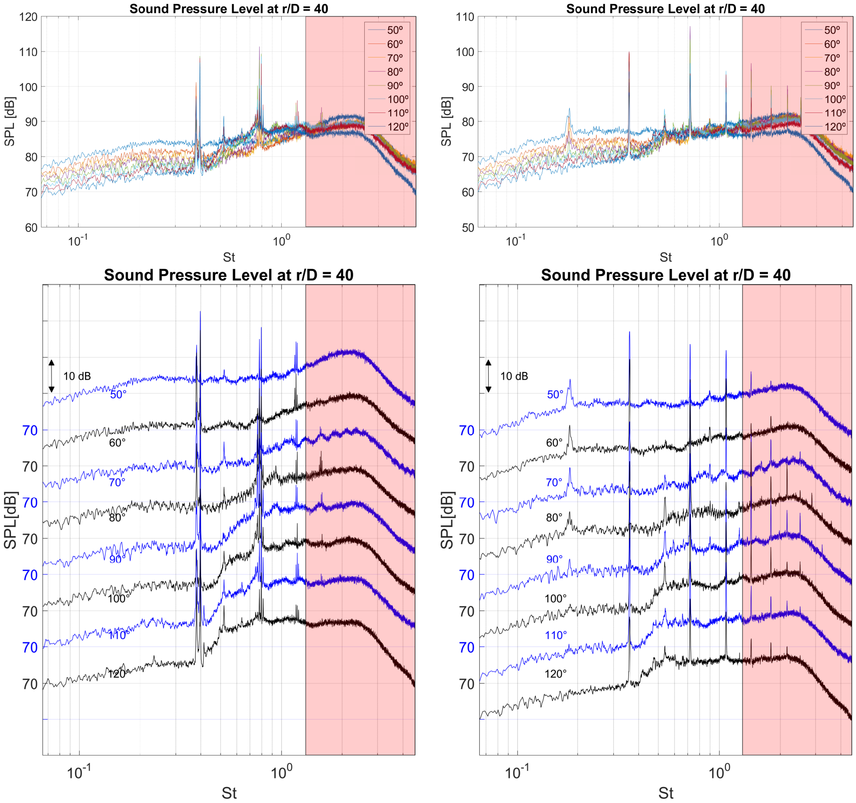

Figure 3.45: SPL (ref. $2 \cdot 10^{-5}$ Pa) for CNPR = 2.60 $M_j = 1.25$ (left) and CNPR 2.70 $M_j = 1.28$ (right) at all the measured angles, nozzle diameter D = 0.024 m, during the PIV campaign. The red area is the frequency region polluted by spurious noise due to the microphone caps. The jet is swapping from the flapping to the helical mode. For CNPR = 2.60 the two screech tones are both present, while for NPR = 2.70 subharmonics are present.

and it is expressed in decibels as $I[dB] = 10 \cdot log_{10}(I/I_{ref})$, where $I_{ref} = 10^{-12} W/m^2$ is the reference intensity. The integration of the sound intensity level on a closed surface volume lead to the Sound Power Level, which is sometime found in the literature as SWL. Harper-Bourne and Fisher [34] found out that the shock cell noise intensity is proportional to the fourth power of the off design parameter β^4. Fig. 3.47 illustrates the variation of the measured sound intensity level vs the off-design parameter β for the microphones located at $\theta = 30^o$ and $\theta = 90^o$. Measured data laying in the range $\beta > 0.4$, where shock cell noise is the main mechanism of noise generation, follows the aforementioned trend. Below this range the shock cell

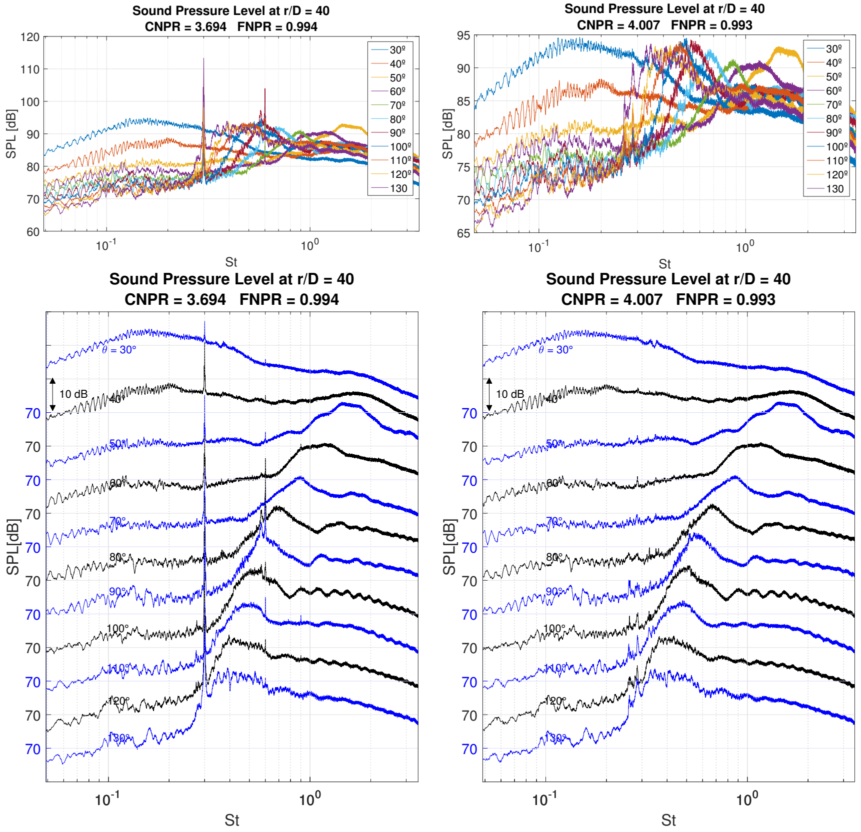

Figure 3.46: SPL (ref. $2 \cdot 10^{-5}$ Pa) for CNPR $=$ 3.67 $M_j = 1.50$ (left) and CNPR 4.00 $M_j = 1.56$ (right) at all the measured angles, nozzle diameter D $=$ 0.019 m. The presence of the Mach disk is followed by the screech tones suppression.

pattern is weak and jet mixing noise becomes dominant so the Lighthill's M^8 law is retrieved. This result agrees with the analysis of the acoustic spectra presented in Fig. 3.47a.

The screech wavelength $\lambda_{sc} = c_\infty / f_{sc}$ obtained in the measurements was compared with the literature for all the test cases. In Fig. 3.48(a), the results of the measurements are plotted together with the data gathered by Raman [72]. It was observed that measured wavelengths lay all in the point cloud retrieved in other researches. This fact seems to validate the measurements. The majority of points are located in the zones where axisymmetric (A2), sinuous (B), helical (C) or unclassified (D) modes take place.

Measured data has also been compared with the correlations proposed by Ahuja [51] for the stable axisymmetric (A2) and helical (C) modes that

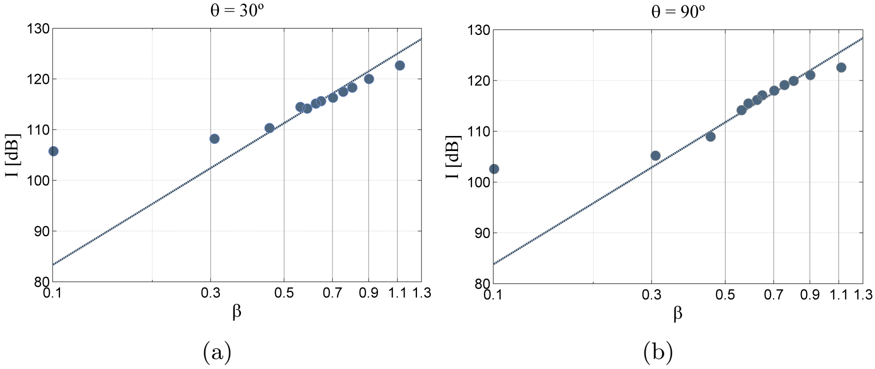

Figure 3.47: Variation of the sound intensity with the off design parameter. Solid line indicates the β^4 trend (a) Microphone located at $\theta = 30^o$ (b) Microphone located at $\theta = 90^o$.

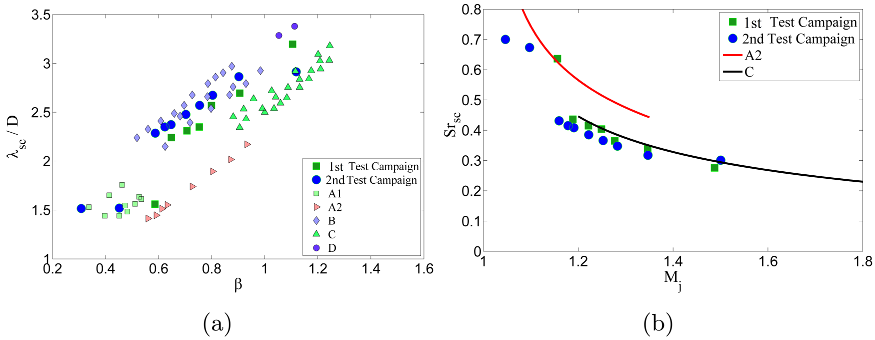

Figure 3.48: Screech frequency analysis. (a) Comparative of measured data with data gathered by Raman [72]. (b) Comparative with screech frequency prediction by Ahuja [51]. Green squares represent the PIV test campaign, while blue dots the acoustic test campaign.

were presented in Sec. 1.2.2 (equations 1.19 and 1.20). The results are presented in figure3.48(b), where the screech Strouhal number was calculated as $Sr_{sc} = f_{sc}D_j/U_j$. It was observed that most of the measured data lay near the helical mode (C) correlation. One of the points corresponding to the first test campaign lay in the stable axisymmetric mode (A2) and other two, which are supposed to belong to the unstable mode (A1) according to the data of Raman, remain far from any correlation curve.

To sum up, the measurements performed in different test campaigns showed that the noise emitted by the supersonic jet in the FAST facility contains all the acoustic features of the shock associated noise that have been previously reported in the literature. Therefore, the jet rig could be considered commissioned also from the acoustic point of view.

3.6.2 Nozzles Comparison

The acoustics results for the 2^{nd} and 3^{rd} test campaigns, involving nozzles of two different diameters, are compared. Spectra are non-dimensionalized by the Strouhal number and scaled as for distance r/D = 40. Fig. 3.49 shows very good agreement among the two test campaigns, for both the BBSAN and the screech tones, in frequency and SPL. Only for CNPR = 2.00 the mismatch in intensity is greater, the reason is unknown. Curiously, the pressure conditions for which the there is the swap between the axisymmetric and flapping screech modes is not the same for the two nozzle. For the larger nozzle, it occurs around CNPR = 2.26, while for the smaller nozzle at CNPR = 2.30.

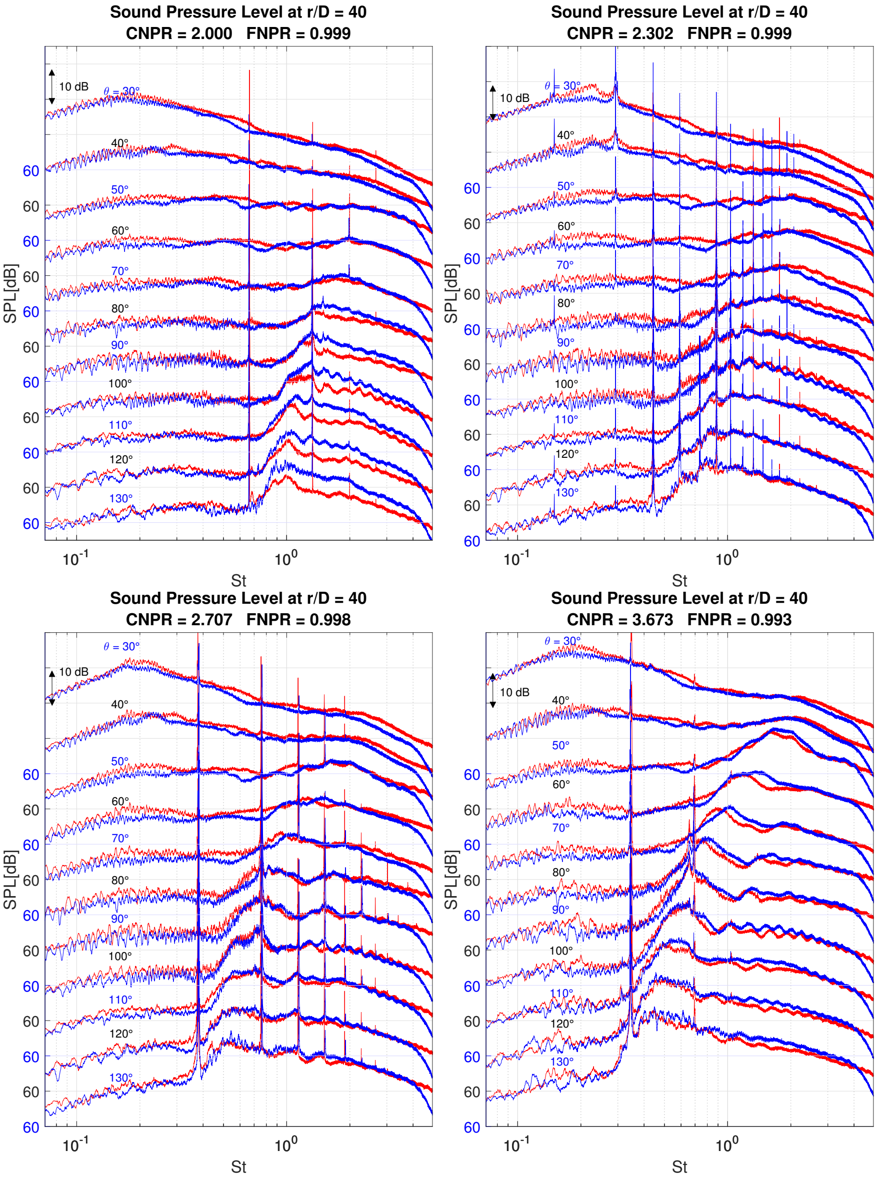

Sound Pressure Level at r/D = 40
CNPR = 2.000 FNPR = 0.999

Sound Pressure Level at r/D = 40
CNPR = 2.302 FNPR = 0.999

Sound Pressure Level at r/D = 40
CNPR = 2.707 FNPR = 0.998

Sound Pressure Level at r/D = 40
CNPR = 3.673 FNPR = 0.993

Figure 3.49: SPL (ref. $2 \cdot 10^{-5}$ Pa) for several CNPR at all the measured angles.The red and blue lines are for nozzle diameter D = 0.024 m and D = 0.019 m respectively. The drop of the SPL at higher St for the smaller nozzle is due to the limit of the microphones' dynamic range (70 kHz).

3.7 Conclusions

The FAST facility was commissioned using the results of an experimental campaign on a supersonic single stream jet in underexpanded conditions. Several NPR conditions have been investigated using PIV synchronized with microphones mounted on a polar antenna.

The velocity fields show the classical shock-cells pattern, with the shock-cell length increasing with the NPR. The evolution of the mean shock cell length L_{sc} with the of design parameter β is in agreement with the semi-empirical correlation proposed by Harper Bourne and Fisher (Fig. 3.25). It was found that the number of the shock-cells is dependent by the screech mode which is occurring, with abrupt reduction when, increasing the NPR, a successive mode is encountered (Fig. 3.20). Mean velocity profiles as well as turbulence intensities profiles have been extracted and compared with analogous examples in the literature with good agreement.

The averaged Reynolds stress field shows the presence of lobes outside the shear layer. These lobes are the trace of the standing wave fluctuations induced by the screech, as confirmed by the analysis with the usage of correlation functions.

Acoustic measurements have been compared with the literature, finding good agreement both in amplitude and Strouhal number. Screech peaks frequency have been compared with analogous research made by Ahuja *et al*, Andr *et al* and Mercier *et al*, showing also good agreement. Screech harmonics (sometimes up to the 10^th one) have been found in different conditions, plus the presence of subharmonics of the main screech frequency, and harmonics of the subharmonics. It was evidenced how such subharmonics are present only in cases of very energetic events, such when the screech mode is switching, and the shock-cells pattern is collapsing. Both harmonics and subharmonics exhibit a directivity pattern. Although for screech harmonics directivity a recent theory has been derived by Tam[100], there is no knowledge on the subharmonics, and thus further studies are highly desirable.

A second test campaign was carried out using a scaled nozzle with the aim of comparing the acoustic spectra. Results show how, in all but one condition, the broadband shock-cell noise produced by the two nozzles at $d = 40D_n$ is exactly the same both in amplitude and Strouhal number (Fig.3.49), confirming the hypothesis of self-similarity of circular jets working in underexpanded conditions. Screech main tones and harmonics also coincide in Strouhal number for all but one case, when two modes are presents, with the onset of subharmonics too. The screech harmonics amplitudes and directivity patterns also maintain reasonably good agreement in all but one test conditions.

Chapter 4

Dual stream jet

In this chapter, the results achieved for the supersonic dual stream jet are presented. For sake of clarity, the experimental setup, PIV results and acoustics results are discussed in separated sections. An attempt to use the velocity correlation maps to understand the screech dynamics, using the same methods described in Sec. 5 is proposed. The experimental setup and the acquisition phases were done in collaboration with Elena Miguel and Alejandro Rubio Carpio, who are gratefully acknowledged.

The experimental setup used is very similar to the one for the single stream jet. The reader is thus addressed to Sec. 3.3 and 3.4.2 for more details, except for what discussed in the following. PIV and acoustic measurements were performed simultaneously. The light source was kept outside the room to not pollute the microphones' signal, and also to protect the laser head from the acoustic radiation. The optical bench and the antenna with 8 microphones, ranging from 50° to 120° of polar angle (with 0° the downstream direction), were placed inside the semi-anechoic room (Fig. 4.1a). This time, an improvement to the acquisition chain made possible to record the laser pulses together with the microphone signals for all the test duration. However, also for the coaxial jet, the microphones' cap was not removed, causing a spectra pollution above 20 kHz, as already shown in Fig. 3.11. For this reason, two further test campaigns were performed, this time without the protective grid and with 11 microphones, ranging from from 30° to 130°. In the first test campaign the same test conditions used for PIV were recorded, while, for the last one, the test matrix was enlarged, and a map of Overall Sound Pressure Level was obtained.

The nozzle used is the second one described in section 2.2.2, with $D_{s2} = 44$ mm and $D_{p2} = 19.2$ m, and protrusion length h $= 16.8$ mm. Both the nozzles were painted in black matte to reduce spurious reflections.

All the test conditions (pressures, temperatures, primary mass flow rate) were recorded using the sensors described in Sec. 2.6.

4.1 Test conditions

The test conditions were established at the beginning of the project in cooperation with Airbus and already introduced in Sec. 2.1, and simulated with CFD using COMSOL® in Sec. 2.4. The detailed list of the pressure settings, together with the PIV parameters used is provided in Tab. 4.1. As stated previously, a second test campaign with only the microphones array was performed with the same test condition, and a third one with an extended test matrix. For brevity, the test conditions for this last test campaign are presented in Sec. 4.3.5, where also the acoustic results are shown.

Name	**CNPR**	**FNPR**	**M$_{jp}$**	**M$_{js}$**	**PIV Δt Lower** [μs]	**PIV Δt Upper** [μs]
Cond.01	1.675	2.450	0.891	1.207	0.4	
Cond.01	1.675	2.450	0.891	1.207	1.0	1.0
Cond.01	1.675	2.450	0.891	1.207	2.0	2.0
Cond.02	1.720	2.500	0.915	1.223	1.0	1.5
Cond.03	1.645	2.425	0.874	1.200	1.0	1.5
Cond.04	1.626	2.400	0.863	1.192	1.0	1.5
Cond.05	1.590	2.350	0.841	1.176	1.0	1.5
Cond.06	1.520	2.250	0.796	1.142	1.0	1.5
Cond.07	1.450	2.150	0.748	1.105	1.0	1.5
Cond.08	1.385	2.050	0.698	1.067	1.0	1.5
Cond.09	1.353	2.00	0.671	1.046	1.0	1.5

Table 4.1: Overview of the test conditions investigated with the PIV for the dual stream jet. M$_{jp}$ and M$_{js}$ are the fully expanded Mach number for the primary and secondary nozzle, respectively. PIV Δt Lower and Upper are the separation times used for the test campaigns where the lower and upper part of the jet plume were recorded.

4.1.1 PIV Setup

Given the larger dimensions, almost the double of the single stream jet, to record the entire jet plume with the two PIV cameras would have been possible at cost of spatial resolution. Given the limited time at disposal to perform the test, it was decided, instead, go directly for higher resolution acquisition. This was done with two different test campaign, one recording the lower part of the plume, and the second one the upper part. To achieve this efficiently, the optical setup was modified in order slide up and down, thanks to a couple of optical prisms. Another modification to the original bench consented to use a single spherical lens with focal length f = 1.0 m, instead of a combination of two (Fig. 4.1b).

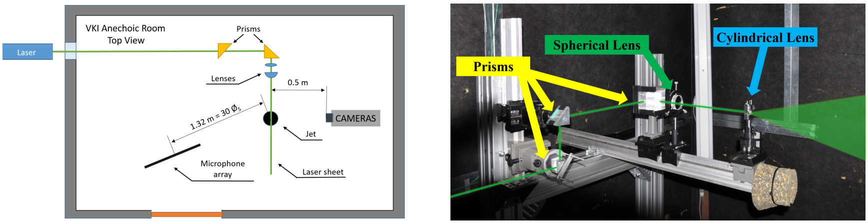

(a)

(b)

Figure 4.1: a) Sketch of the experimental setup. The laser equipment, usually source of unwanted noise, was located outside the anechoic room. Two spherical lenses and one cylindrical lens was used to create the laser sheet. b)Picture of the optical bench. Differently from the one shown in Fig. 3.3, the lens system can translate vertically to displace the laser sheet.

A third campaign was done with higher magnification, to record the jet region close to the nozzle, and between the second and the fifth shock-cell. A sketch of the different field of views is shown in Fig. 4.2.

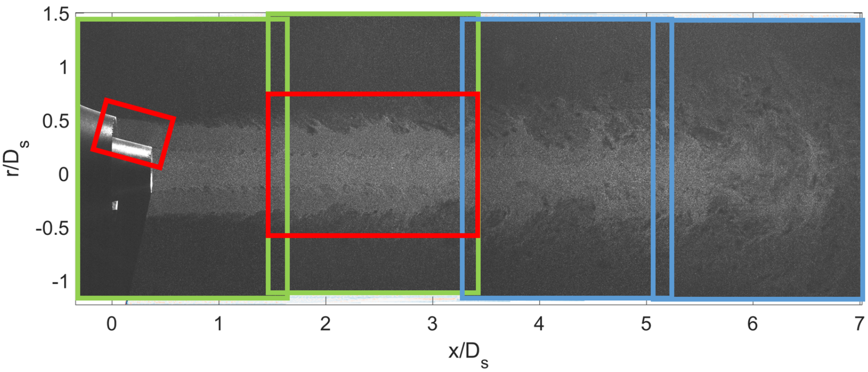

Figure 4.2: Sketch of the field of views considered to investigate the coaxial jet. The frames color identifies the couple of images acquired at the same instant.

The laser source, PIV cameras and calibration procedure, are the same for the single stream jet. The double frame acquisition was performed in three runs of 600 images each, as for the single stream jet. Between each acquisition, 4 minutes were needed to store the data, and the mass flow rate was reduced to the minimum to save compressed air, the seeding was not interrupted. Therefore small discrepancies ($< \pm 0.5\%$) in the NPR between the three runs could be present.

4.1.2 Nozzle displacement during the tests

From the comparison with the numerical database, a geometrical difference between the designed geometry and the effective one during the tests. Images from the PIV cameras, at facility off, confirmed the nozzles were set correctly in position before the test using the centering tool described in Fig. 2.6. When the jet are turned on, instead, a positive vertical shift of the secondary nozzle was observed. From the comparison of the two images, the shift was measured to be Δh = 1.9 mm, equal to a relative variation of the protrusion length -Δh / h = -11.3 % (Fig. 4.3).

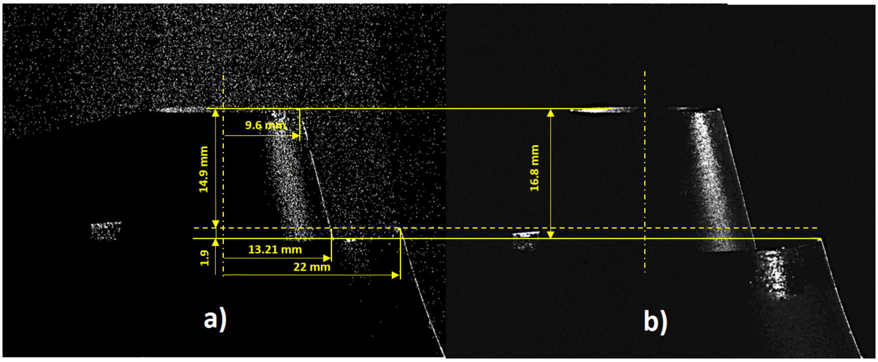

Figure 4.3: PIV image of the nozzle exit for Cond.01 a) and with facility turned off b). The dashed line shows the advancement of the secondary nozzle lip compared to the original position.

It was found the displacement to be smaller for lower pressure conditions. For Cond.09 Δh = 0.84 mm and -Δh / h = -5.0 %. The preliminary impression is thus that the pressurization of the secondary duct is the cause of this displacement. However, the displacement does not scale linearly with the pressure in the secondary flow, being $\Delta ps, Cond.01 = 147.0$ KPa and $\Delta ps, Cond.09 = 101.0$ KPa, assuming standard atmospheric condition. It has to be said, however, that a complete analysis including the nozzle thrust, nozzle specific deformation, silencer pressurization and primary circuit pressurization, was not done. The effects of the displacement are not negligible, especially in terms of shock-cells length and mass flow rate. Given the clearance section of the coaxial nozzle r_{sp} as the radial distance between the secondary nozzle lip and the primary nozzle wall, the increment is Δr_{sp}

= 1.00 mm ($\Delta r_{sp}/\ r_{sp} = 6.12\%$). This parameter would logically influence the length of the shock-cells, including the interaction between the first one before the conical shock-wave at the primary nozzle lip, which has a key role, as explained in the next section. The secondary area and secondary to primary area ratio change is, instead, $\Delta A_s/\ A_s = 4.63\%$. This is linearly translated also to the mass flow rate, and the by-pass ratio. For Cond.09 the relative variations are limited to $\Delta r_{sp}/\ r_{sp} = 1.03\%$ and $\Delta A_s/\ A_s = 2.07\%$. For the future, it is strongly recommended to fix the secondary duct to the anechoic room floor to counteract this effect. Finally, it must be stated that the nozzles are oscillating in the image plane within a range of ±2 pixels in the radial direction. It is not known is the oscillations are caused by the nozzles or the cameras themselves. For the future, a more systematic investigation, using edge identification algorithms, is recommended.

4.1.3 Acquisition Parameters

Given an initial window of 48x48 pixels^2, for a particle velocity V = 400 m/s, and a magnification factor of 0.0498 mm/pixel, the estimated time for a particle to traverse 12 pixel is $\Delta t \approx 1.5\ \mu s$.

Nevertheless, given also the highly spread velocity distribution function in the field of view, a case study was done. Three different times were tried with Cond.01: $\Delta t = 0.4$, 1.0 and 2.0 μs. The final windows size of 12x12 pixels^2, 50% overlap, is reached after a two step cross-correlation with window deformation using WIDIM. In this preliminary phase, the signal to noise ratio map, the peak locking and convergence of the turbulence were compared to choose the best settings. $\Delta t = 0.4\ \mu s$ was the shortest achievable separation time, and was also the parameter which gave the best results. This must not surprise, because it is logical that with such a small separation time, the particles are almost frozen, meaning that few of them would eventually go out of the laser sheet plane, and thus increasing the overall SNR (Fig. 4.4).

On the other side, such small Δt would cause a higher relative uncertainty at lower speed. Given a standard uncertainty around ±0.2 pixel, this would mean an uncertainty on the velocity of $0.2 Mag/\Delta t = \pm 24.7$ m/s, where Mag is the magnification factor.

On the other side, for $\Delta t = 2.0\ \mu s$, the overall signal to noise ratio decreases, and the distribution curve is more prominent to the left in Fig. 4.6, leading to higher number of discarded vector, and then the uncertainty on the low velocities is reduced to ±5 m/s.

This is especially important for the correlation techniques, which is based on identifying correctly the velocity fluctuations. For the same pressure condition, higher separation times gave a better results in terms of identification of the coherent structures.

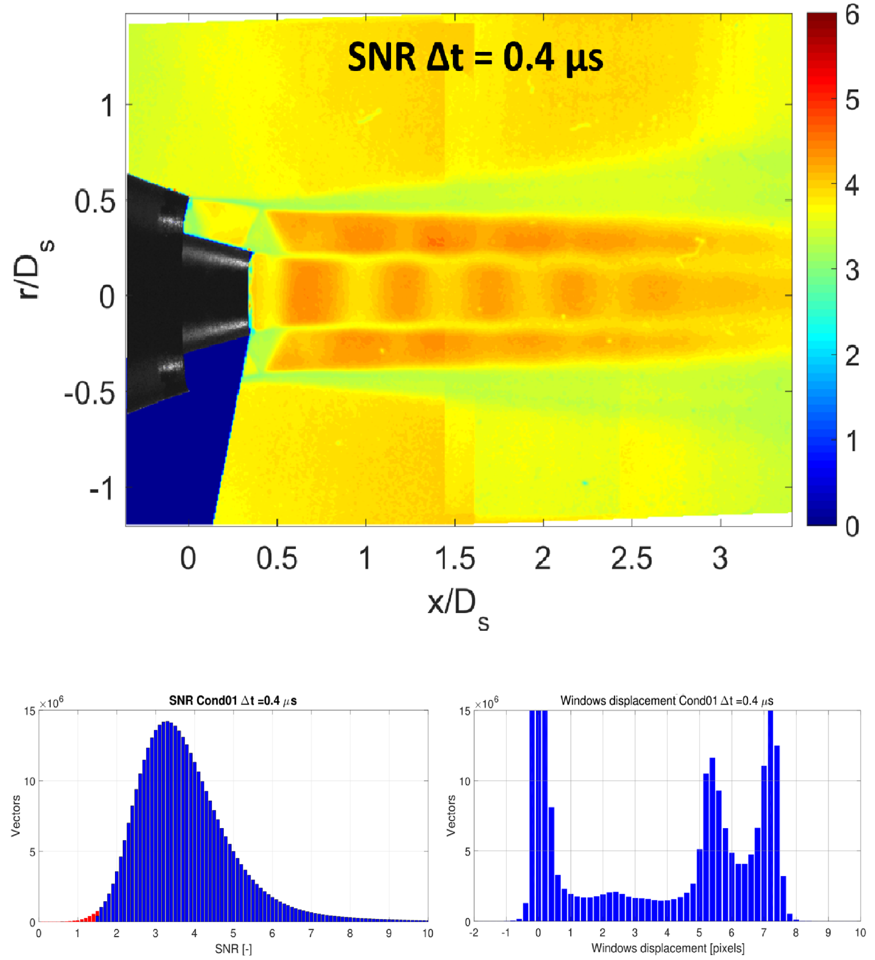

Figure 4.4: Overview of the effect of separation times $\Delta t = 0.4$ μs on the signal to noise Ratio (SNR) and on the windows displacement distribution function for Cond.01. The vectors with SNR ¡ 1.5 are discarded by WIDIM, and thus the red color in the distribution function.

Concerning the convergence of the turbulence intensity, for each test case, the point with the maximum TI was identified, and then a new mean of the TI, in that point, is computed adding the contribution of each snapshot. The results of this analysis, shown in Fig. 4.7, evidence how the convergence for $\Delta t = 1.0$ μs and $\Delta t = 2.0$ μs is slightly smoother and quicker than for $\Delta t = 0.4$ μs.

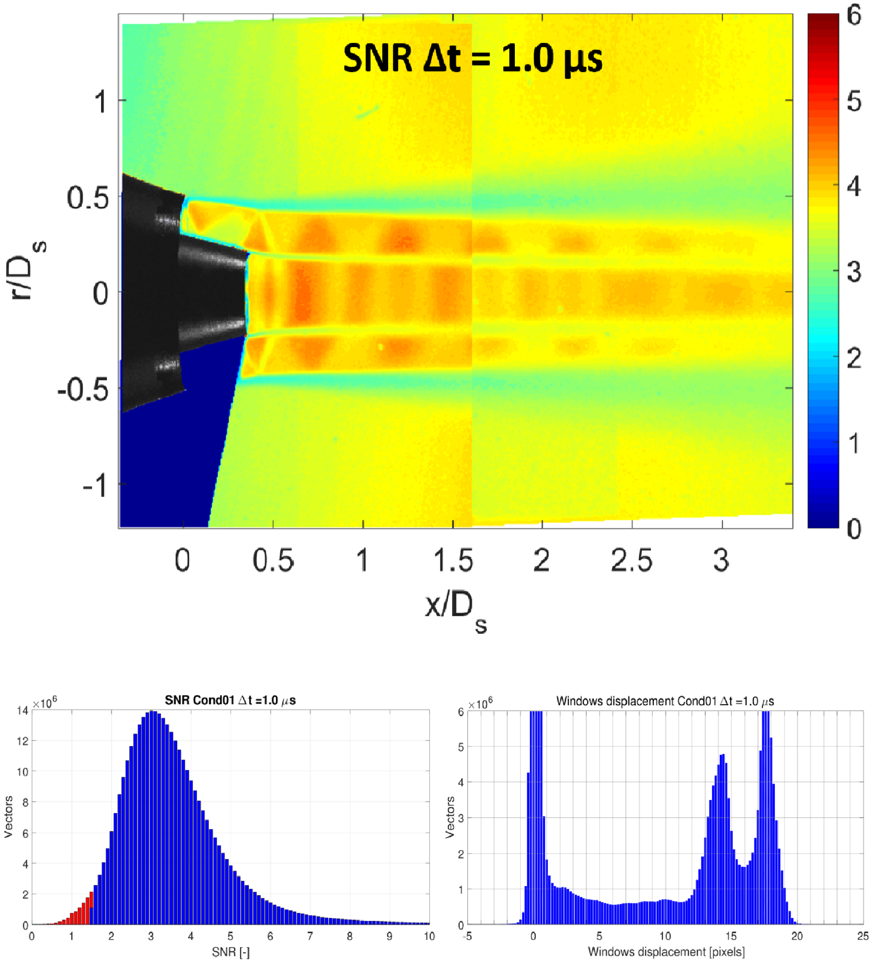

Figure 4.5: Overview of the effect of separation times Δt = 1.0 μs on the signal to noise Ratio (SNR) and on the windows displacement distribution function for Cond.01. The vectors with SNR ¡ 1.5 are discarded by WIDIM, and thus the red color in the distribution function.

For all this reasons, it was decided to use Δt = 1.0 μs for all the successive tests for the lower portion of the jet plume, and Δt = 1.5 μs for the higher portion of the jet plume.

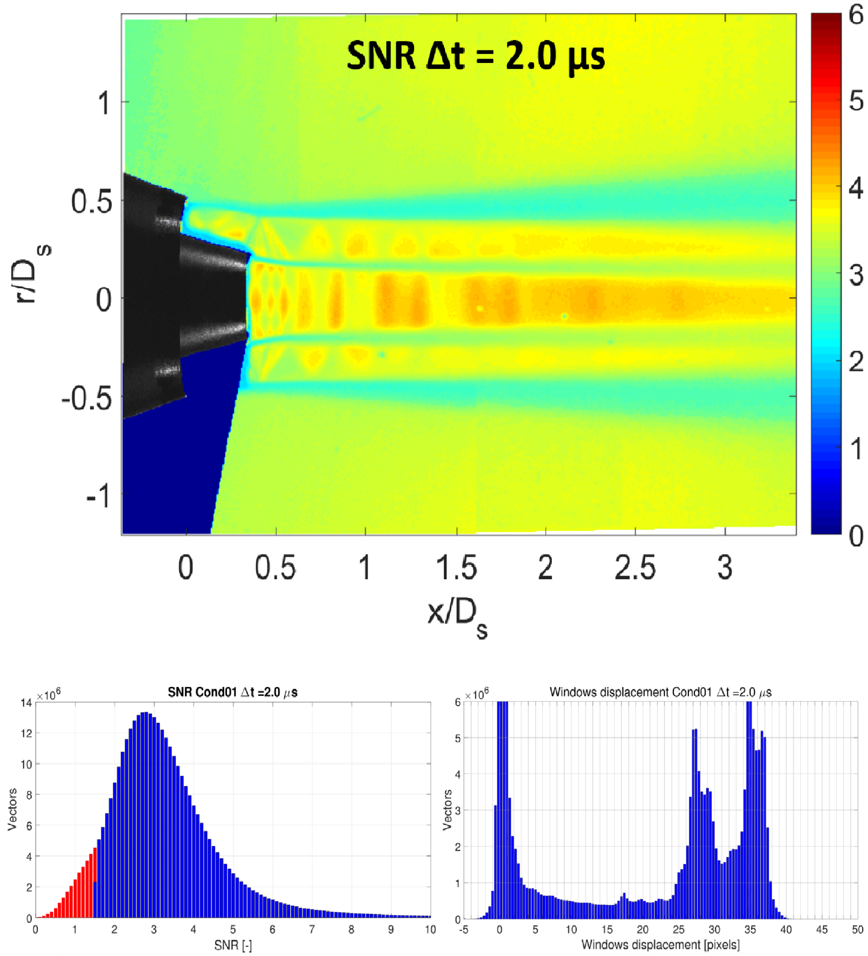

Figure 4.6: Overview of the effect of separation times $\Delta t = 2.0$ μs on the signal to noise Ratio (SNR) and on the windows displacement distribution function for Cond.01. The vectors with SNR ¡ 1.5 are discarded by WIDIM, and thus the red color in the distribution function.

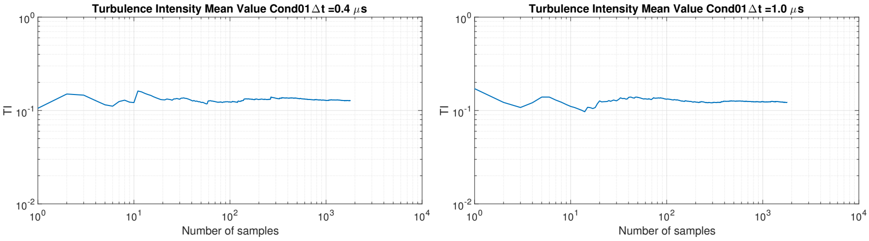

(a) Δt = 0.4 μs (b) Δt = 1.0 μs

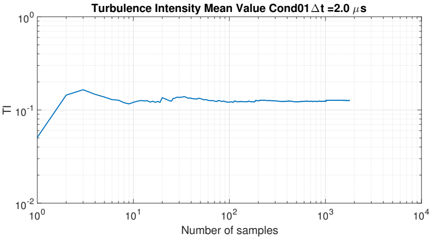

(c) Δt = 2.0 μs

Figure 4.7: Comparison of the maximum turbulence intensity convergence for three PIV separation times for Cond.01.

4.1.4 Acoustic setup

The acoustic setup is very similar to what already described for the single stream jet. The acoustic equipment (Sec. 3.4.2), the acquisition system (Sec. 3.4.3), the data processing (Sec. 3.4.4) and the calibration procedure (Sec. 3.4.5) were basically the same, except for what stated hereafter. The distance of the acoustic antenna was set to be d = 1.32 m ($d/D_{s2} = 30$). The minimum sampling frequency of the NI 5751 14-bit A/D converter together with NI PXIe-1073 was lowered from 800 kHz to 250 kHz. This made possible to record simultaneously the entire PIV acquisition phase. The signal of the laser cavity shutter was also recorded with this system. For all the tests on the coaxial jet, the acquisition parameters were: sampling time $T_s = 67.11$ s, the sampling frequency $f_s = 250$ kHz, the number of samples $N_s = 2^{24}$ and the frequency resolution $\Delta f = 0.015$ Hz (effective after PWelch $\Delta f_{PW} = 250000/32768 = 7.63$ Hz).

4.2 Particle Image Velocimetry

In this section, the results obtained with the PIV are presented. In Fig. 4.8 are shown the instantaneous velocity fields, for the downstream and upstream part of the jet plume, with Mach number M = 1 isolines, for Cond.02. Final windows size is 12x12 pixel^2 with 50 % overlap. The jet appears to maintain its annular structure for several jet diameters without losing coherence, and it seems to be mostly axisymmetric. The inner jet velocity is modulated by the external flow, locally reaching sonic speed. Due to the geometry, only half of the inner nozzle wall was illuminated by the laser sheer, while the remnant part was masked out.

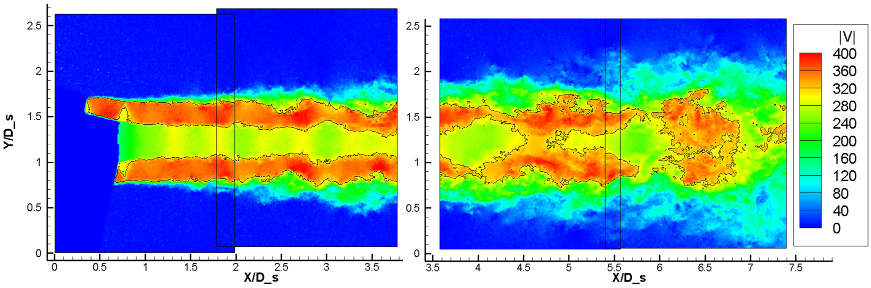

Figure 4.8: Example of instantaneous combined velocity fields with Mach number M = 1 isolines for Cond.01. Final windows size is 12x12 pixel^2 with 50 % overlap. Axis are non-dimensionalized by the secondary nozzle diameter, colormap is in m/s.

From Cond.01 to Cond.06, screech tones were recorded, while from Cond.07 to Cond.09 the microphones recorded only BBSAN. Therefore, for sake of clarity, only Cond.01 and Cond.07 will be extensively discussed in the followings, leaving the other conditions in the Appendix A. A comparison of the PIV field with the numerical LES simulation from Perez Arroyo [67] on Cond.01 will be presented. Unfortunately, no further examples of PIV on coaxial jets are present in the literature to compare with.

4.2.1 Condition 01

For Cond.01, the dataset was acquired for three different separation times (Δt = 0.4 μs, Δt = 1.0 μs and Δt = 2.0 μs), each of them accounting for 1800 images. For several reasons it was decided to use only the last 1200 images with Δt = 1.0 μs and 1800 images with Δt = 2.0 μs, for a total of 3000 images. This because of the higher uncertainty of the flow fields at Δt = 0.4 μs. Additionally, for the aforementioned cases, the acoustic spectra showed additional screech tones compared to other test cases (Fig. 4.53). These additional screech tones were eliminated from successive tests placing a foam ring around the secondary nozzle, to cover the flat nozzle portion visible in Fig. 2.5c.

In Fig.4.9 the average flow field is presented. The supersonic region extends until 6 D_s, showing a slightly asymmetry between the upper and the lower part of the image. A strong conical shock-wave starts at the lip of the primary nozzle, creating a subsonic pocket in the secondary stream. The primary flow is firstly accelerated and then its velocity appears to be modulated by the secondary flow. This must not surprise as the secondary flow completely surrounds the The jet centerline was computed with the same methodology of the single stream jet in Sec. 3.5.1.

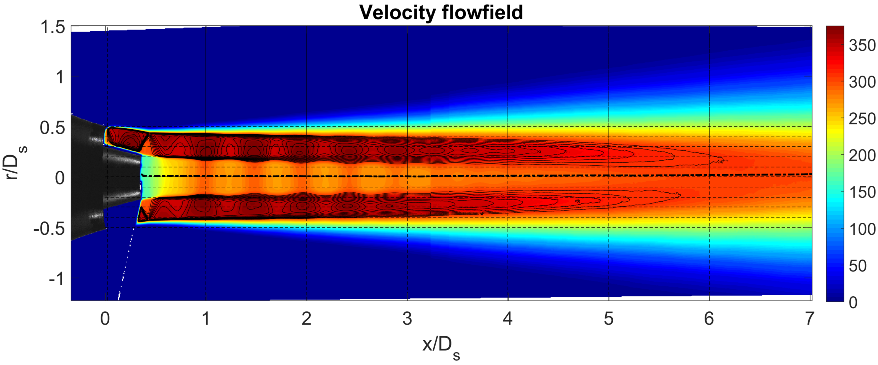

Figure 4.9: Mean velocity module flow field with M = [1:0.025:1.325] isolines at condition 01. The thicker dot-dash line is the computed jet center. Dashed lines represents the locations where radial and axial profiles for Mach number and turbulence intensity were extracted.

Fig. 4.10 shows the averaged radial velocity component. The effect of the conical inner nozzle is that both the inner and the outer flows are not ejected parallel to the nozzle axis, acting as a constraint and provoking the initial acceleration of the primary stream. Immediately after the reflection point of each shock-cell, spots are visible in the subsonic part of both the inner and outer shear layer. In the inner shear layer those spots seem to became weaker along the jet axis, while for the external shear layer the trend is opposite.

To present the results, and to check the symmetry, axial and radial profiles were extracted along some lines depicted in Fig. 4.9. Horizontal lines are equally spaced each 0.1 r/D_s, while vertical lines are placed every 1 x/S_s.

The Mach number axial profiles of the upper and lower part of the flow field are shown in Fig. 4.11. Eight shock-cells can be counted in the wake. The inner flow is accelerated and modulated by the secondary flow, reaching almost the sonic speed at $D_s = 6$. Compared to the single stream jet, the shock-cells strength (intended as the difference M_{max} - M_{min}) is not monotonically decreasing, but it reaches a maximum at the second shock-cell.

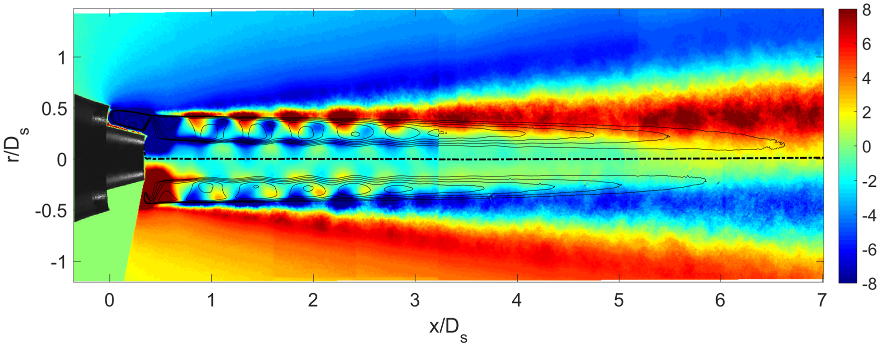

Figure 4.10: Mean radial velocity flow field with M ¿ 1 isolines.

After this point, the shock-cells strength is rapidly decreasing. However, it must be observed that the annular shock-cells system is parallel to the jet axis, but slightly converging towards the centerline. Moreover, the points of the maximum speed occur closely to the internal shear layer, with very steep variations, as visible from the Mach contour lines. In such condition it is difficult to identify univocally the location of the maxima and minima points. For this reason, it is believed the aforementioned description of the Mach profiles is affected by geometrical aspects.

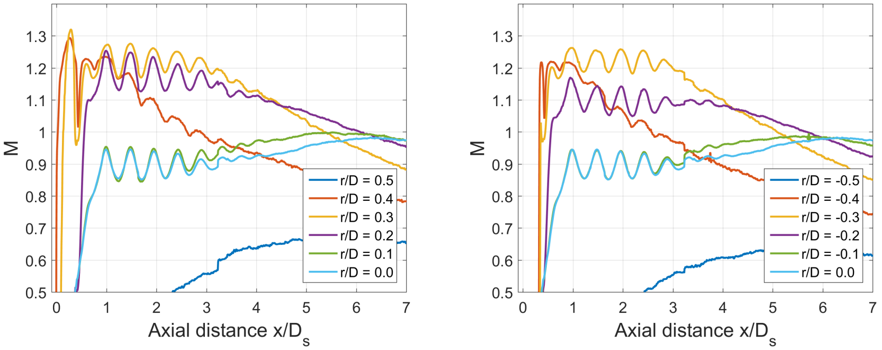

Figure 4.11: Mach number axial profiles at several radial position for the upper part (left) and lower part (right) of the image.

Nevertheless a symmetry check can be achieved. In Fig. 4.12 are plotted together the upper and lower profiles at several radial distances. The radial positions corresponds to the jet centerline (r/D = 0), the internal nozzle lip (r/D = 0.218), the ideal intersection point between the internal nozzle wall and the secondary nozzle exit area (r/D = 0.303), the secondary nozzle lip (r/D = 0.5). The profiles are fairly aligned along the measured distance, except for r/D = 0.218, where differences are more accentuated, probably also due to the strong velocity gradients.

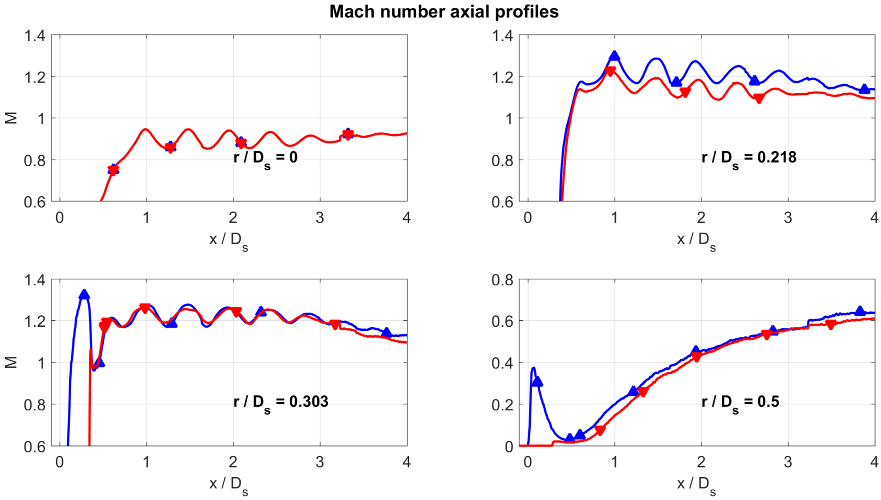

Figure 4.12: Comparison of the Mach axial profiles between the upper part (in blue, up pointing triangles) and the lower part (in red, down pointing triangles) at several radial distance.

The radial profiles are plot in Fig. 4.13. The M shape, typical for inverted velocity coaxial nozzles, is found. The side peaks progressively decrease in intensity, and the maxima location shifts towards the centerline while the plume broadens radially. The centerline, instead, does not seem to be subject to great variations, but this is a deceptive effects due to the locations where lines are extracted. As shown in Fig. 4.11, also the centerline is experiencing a variation similarly to the external flow. The right part of the graph (correspondent to the upper part of the velocity maps) seems to have higher Mach number peaks than the left side.

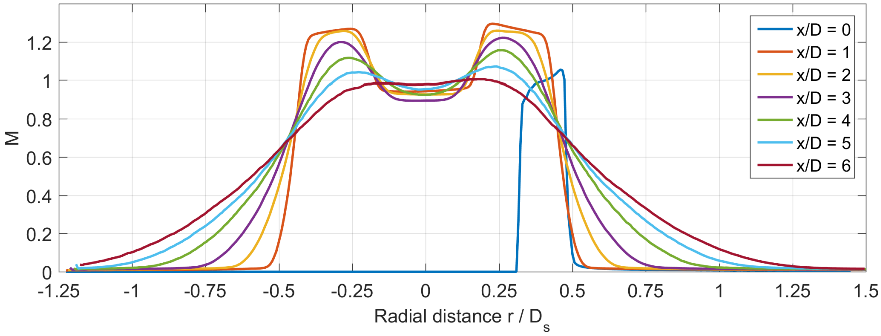

Figure 4.13: Mach number radial profiles at several axial distance.

Also for the radial profiles, the two halves are plotted together in Fig. 4.14. The external shear layer profiles appear to match perfectly until x/D = 4, while downstream we observe a small bias. The internal shear layer, instead, appears not symmetric, and thus a possibility is that it influences also external shear layer after the end of the secondary potential core, causing the aforementioned bias downstream than x/D = 4.

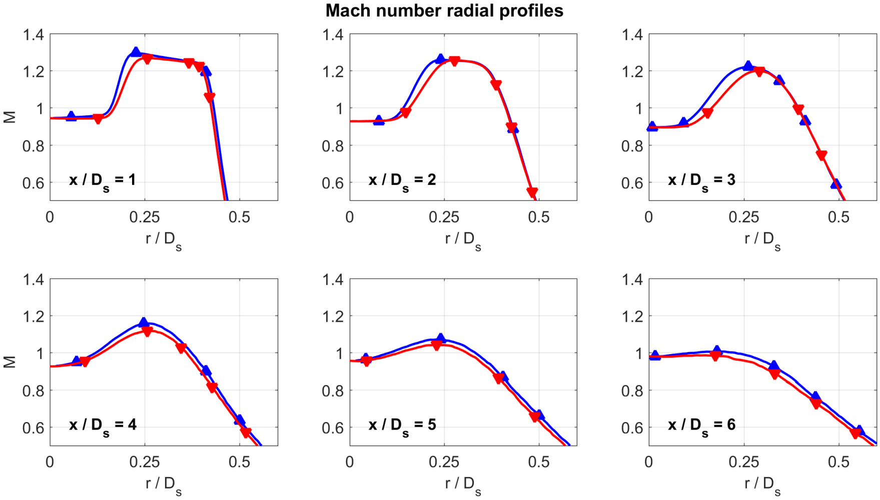

Figure 4.14: Comparison of the Mach radial profiles between the upper part (in blue, up pointing triangles) and the lower part (in red, down pointing triangles) at several axial distance

The turbulence intensity for the combined axial and radial velocity fluctuations, together with the potential cores limits, are shown in Fig. 4.15. The TI is defined in this case as:

$$TI = \sqrt{\frac{\frac{1}{2}(\overline{u'^2} + \overline{v'^2})}{V_j}} \tag{4.1}$$

The potential cores limits were estimated using the method described in Sec. 3.5.3.1. The external shear layer limit seems to grow linearly until D$_s \approx 5$, while the internal shear layers limits have different behaviors. The merging of the internal shear layers determine the ends of the primary potential core at D$_s \approx 4.2$, while the merging of the internal with the external shear layer determines the end of the secondary potential cores at D$_s \approx 3.2$. The points of maximum TI are placed on straight lines parallel to the jet axis, which are located at a radial distance near the nozzles lips, but slightly shifted towards the centerline. For the external shear layer, maxima are contained in the subsonic region, while for the internal one, in the supersonic region. These last ones are detected until the end of the primary potential core. After that, only two peaks in the radial profiles are identifiable, which are the ones in the external shear layer.

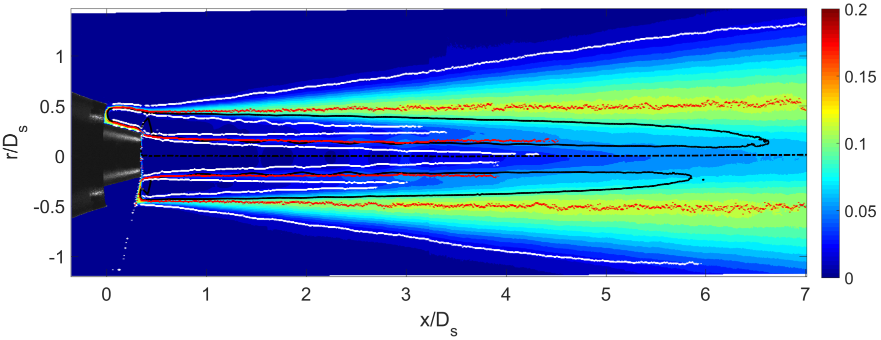

Figure 4.15: Turbulence intensity flow field. In black, the M = 1 isoline, in red, the TI maxima locations, and in white, the computed limit of the shear layer.

Axial TI profiles were extracted similarly to the Mach profiles in Fig. 4.16. For the most external line, near the shear layer maxima, the TI quickly reaches a maximum value ot TI = 0.12, and then it remains approximately constant before starting to decrease. No modulation is present. The profiles closer to the centerline, instead show a more gradual increase, with a modulation in the primary potential core occurring at the same axial distance of the end of the secondary potential cores.

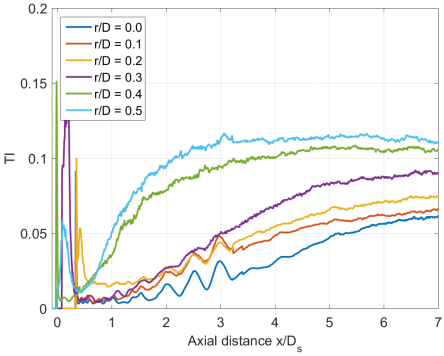

Figure 4.16: Turbulent intensity axial profiles at several radial position for the upper part of the image. The primary flow appears to be affected by the shock-cells pattern, while the secondary flow shows a weak modulation only in the internal region.

The comparison of the upper and lower profiles show fair agreement, except for a variation at r / D_s = 0.218, which can be attributed to high gradient in that radial position (Fig. 4.17). The initial spikes at r / D_s = 0 and 0.218 must be attributed to the internal nozzle lip, which is probably confusing the measurements in that point. More interesting are, instead, the peaks r / D_s = 0.303 and 0.5. Because they are broad, it is difficult to believe they are effects of spurious contribution. Looking at the radial profiles in Fig. 4.18, the two peaks at x / D = 0 can be attributed to the external shear layer and to the boundary layer. Such high turbulence intensity could be due to a systematic error in the PIV algorithm, which has a limit in the deformation of interrogation window. It is not possible to give a further description at this level of resolution. Further details may arise from the zoomed flow field which will be analyzed at a later date. Finally, it must be also stated that the nozzle vibrations may also induce a false TI increment, especially in places where the gradients are very strong, such for the initial shear layer and the boundary layer.

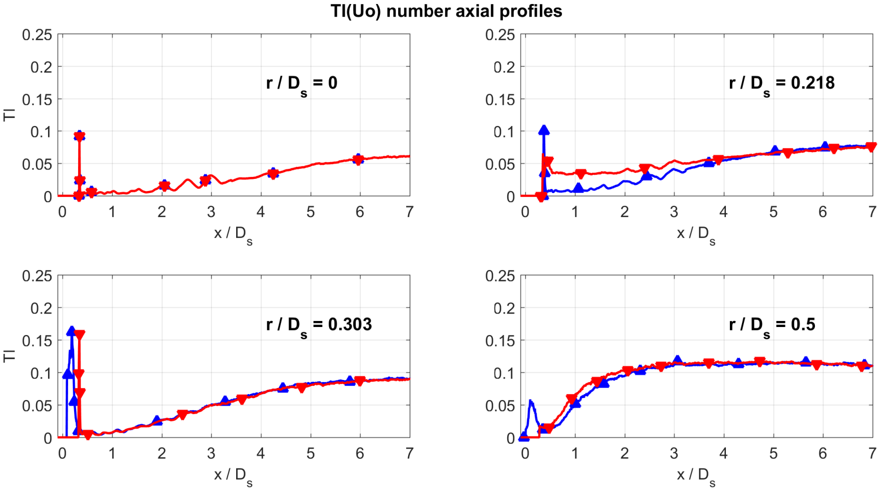

Figure 4.17: Comparison of the TI axial profiles between the upper part (in blue, up pointing triangles) and the lower part (in red, down pointing triangles) at several radial distance. The radial positions corresponds to the jet centerline (r/D = 0), the internal nozzle lip (r/D = 0.218), the ideal intersection point between the internal nozzle wall and the secondary nozzle exit area (r/D = 0.303) , the secondary nozzle lip (r/D = 0.5).

The radial turbulence intensity profiles show, initially, the presence of four peaks, two for the internal, and two for the external shear layer. The internal peaks disappears after the end of the secondary potential core, and at r/D = 6 the profile has only two broad peaks.

The comparison of upper and lower part, in Fig. 4.19 show a very good agreement, also here with a some differences in the internal shear layer.

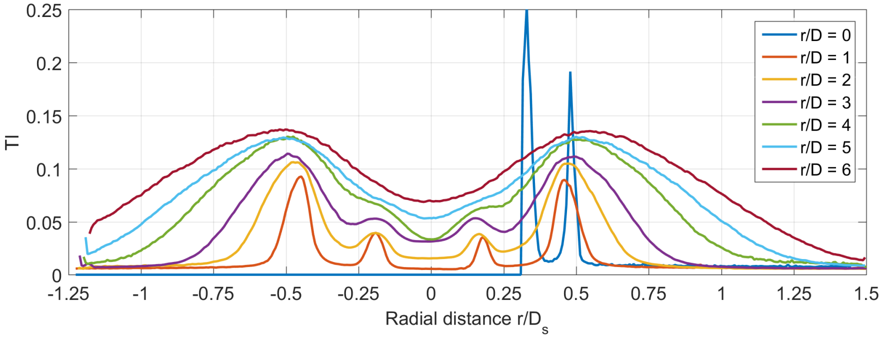

Figure 4.18: Turbulence intensity radial profiles at several axial distances.

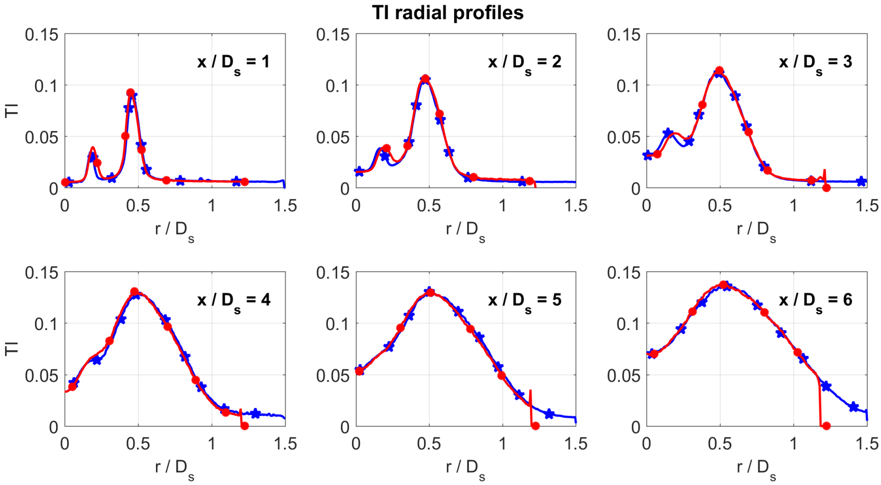

Figure 4.19: Comparison of the TI radial profiles between the upper part (in blue, stars) and the lower part (in red, circles) at several axial distance.

The divergence of the averaged velocity field map was computed. To improve visibility, the square root of the divergence is proposed in Fig. 4.20. Negative divergence means the flow is compressing, while for positive the flow is expanding, and is thus directly related to the density, and indirectly to the pressure field. From the figure, it is possible to see how the succession of shock-cells, caused by a sequence of compression and expansion waves, is transmitted radially without any reduction, and it is leading the velocity modulation in the primary flow.

From the comparison of the velocity field and the divergence of the velocity field in Fig. 4.21 it is visible how the zeros of the divergence occurs in the point of maximum or minimum speed. Looking at the Mach isolines, when

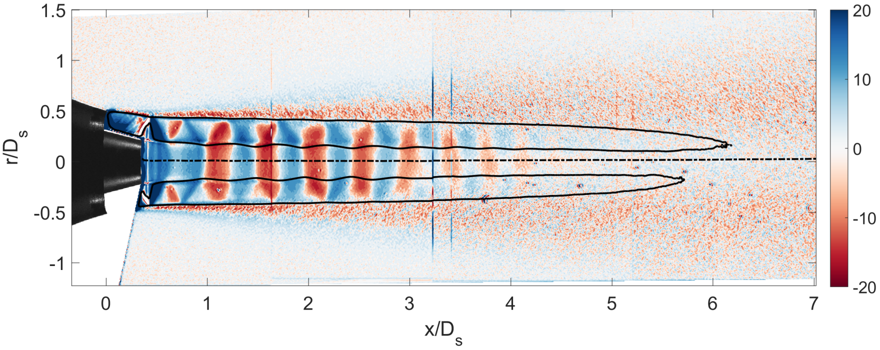

Figure 4.20: Square root of the mean velocity divergence flow field $\nabla \cdot V/\sqrt{|\nabla \cdot V|}$. The image shows how the primary and secondary flows are expanding (in blue) and compressing (in red) with the shock-cells.

the supersonic section is expanding, the subsonic one is contracting, and in both the flow is accelerating, in agreement with the Navier-Stokes equations. From these pictures it is also possible to see some asymmetry between the upper and lower part.

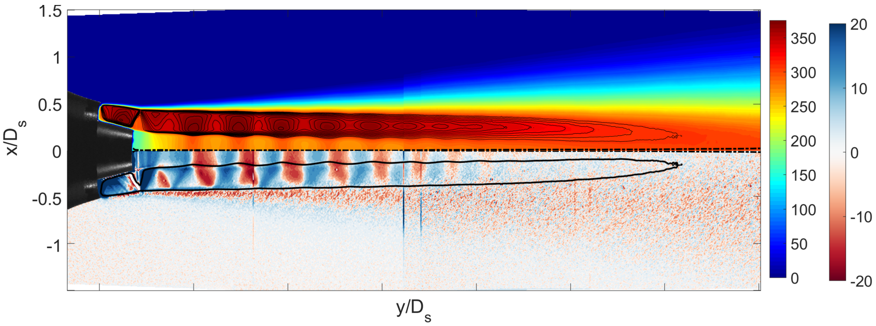

Figure 4.21: Comparison of the velocity and divergence flow field.

Finally, a zoom of the nozzle lip region is plotted in Fig. 4.22. The apparent thick boundary layer is an effect of the superimposed nozzle image. The first shock-cell is almost complete when the flow is incurring into an conical strong shock-wave starting from the lip of the secondary nozzle. A flow re-compression occurs, extending also inside the primary flow. If the velocity field does not give much more information, the divergence of the velocity is more interesting. Expansion and compression waves are visible in the averaged field, as well as the shock wave and the expansion fan.

An attempt to give a physical interpretation to this field is given in Fig. 4.23.

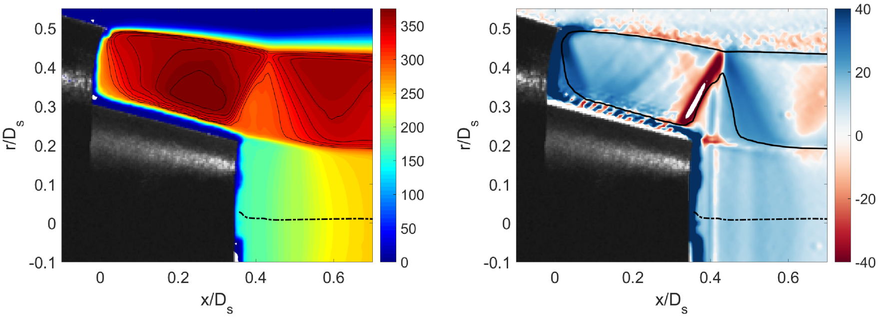

Figure 4.22: Detail of the nozzle region. Velocity flow field with M ¿ 1 isolines (left) and velocity divergence flow field (right).

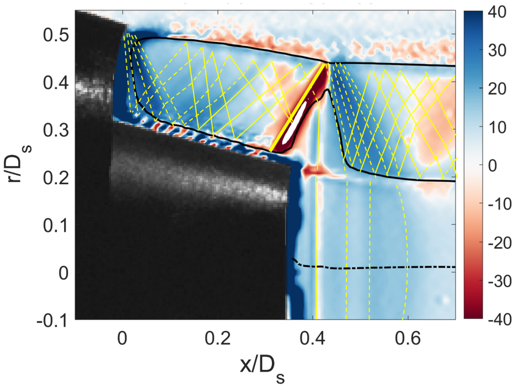

Figure 4.23: Attempt of reconstruction of the expansion (dashed line) and compression (continuous line) Mach waves in the nozzle region. It is interesting to note how in the subsonic region (low speed), the Mach waves propagate in the radial direction undeflected. When the primary flow accelerates, instead, the last expansion wave is curved (x/D$_s$ = 0.6).

In agreement with the theory of supersonic underexpanded flows, an expansion fan is forming from the lip of the secondary nozzle. The expansion waves deviate the flow, which by consequence is bending up. Of course, the nozzle wall constitutes a physical boundary, meaning that the velocity has to be parallel to it. This establishes the condition for the reflected waves: to avoid vacuum, an expansion wave must reflects as expansion waves, and vice-versa for a compression wave. The expansion fan is thus refracted as expansion waves when they impinge on the boundary layer. Interestingly, the impingement of the wave on the BL is followed by strong local re-compression, visible as red dots in the boundary layer. At this level of detail, however, it is not possible to retrieve additional information. When the refracted expansion wave impinges on the external shear layer, it is refracted back, instead, as a compression wave. This because when a wave impinges on a free surface (it must be a vortical surface), it is the pressure jump among the two regions, which establishes the kind of refracted wave. The flow, after the expansion fan, is in equilibrium with the atmospheric pressure. Then, the first refracted expansion wave impinges on the shear layer, causing a further, not necessary, small expansion. The expansion wave is, then, refracted back as a compression wave, re-establishing locally the pressure equilibrium. The compression waves refracted from the top and the bottom start to re-compress flow, meaning the first shock-cell end is approaching. Before it happens, however, the wall ends, and the flow must align with the jet axis. This is done thanks to a strong conical shock-wave, that slows the flow down to subsonic speed. The pressure wave is transmitted even inside the primary flow, where a vertical compression wave is present just in front of the primary nozzle. It is worthy to note that the strength of the conical shock-wave is not constant, being the Mach number upstream not uniform. From the shock tables, the Mach number after the shock-wave may be lower down to M = 0.79, with a correspondent total pressure loss around $\Delta \mathrm{p}_0 = -2\%$. Across the shock, therefore, there is a non-uniform entropy and vorticity production. From the point where the shock-wave impinges the external shear layer, another expansion fan departs, to counteract the sudden pressurization. This time, the expansion fan does not meet a wall but the inner shear layer, therefore pressure condition would determine the type of refracted wave. Because of the conical shock-wave, the inner jet is surely at higher pressure than the surrounding flow, and thus the expansion fan is refracted as a compression fan. Also from the velocity point of view, the streamlines are bending up, and a succession of expansion waves would make them straight, instead. The image evidence also that the expansion fan is leading the acceleration of the primary stream. Initially, visible expansion waves are propagating radially as vertical line, but when the flow accelerates at nearly sonic speeds, they became curved. The superposition of compression waves causes the red spot at the end of the picture. Successively, the trail of compression waves are converted to expansion ones, and the classical shock-cell pattern may finally establish, although further strong shock waves are not encountered.

Finally, the average of the product of the fluctuations $u'v'$ was computed and presented in Fig. 4.24 and normalized in Fig. 4.25. In case of incompressible flow, this is directly related to the Reynolds shear stress, defined as $Re_{ss} = \rho u'v'$, and thus this label is strictly valid only outside of the shear layer, where M ¡ 0.3 and the ambient density is constant. This is very important because in the Lighthill tensor, which includes all the possible sound sources, it is possible to neglect the other sound sources except the Re_{ss}. From the picture, it is possible to recognize the same lobes present also in the single stream jet (Fig. 3.35). Such lobes are present only in Cond.01-06, where screech tones were recorded. In Cond.07-09, instead, they disappear, and screech is also not present.

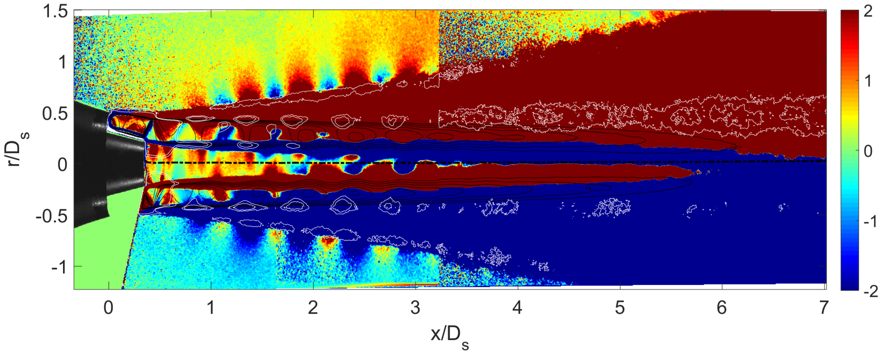

Figure 4.24: Flow field of the averaged velocity fluctuations product $u'v'$. The black lines are M = [1:0.05:1.325] isocontour lines. In white, the isocontour lines of the mean radial velocity field (Fig. 4.10). The scale enhances the lobes outside the jet shear layer. In that region, the flow is incompressible, and therefore $u'v'$ is directly related to the Reynolds shear stress.

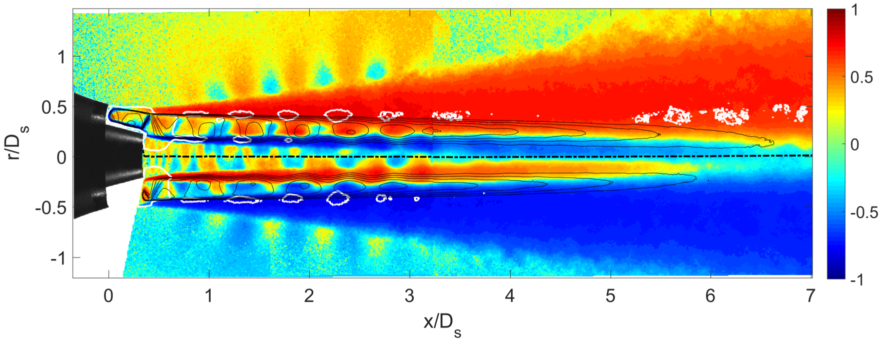

Figure 4.25: Normalized Reynolds shear stress $u'v'/\sqrt{|u'v'| \cdot \sigma(u)\sigma(v)}$. The black lines are M = [1:0.05:1.325] isocontour lines. In white, the isocontour lines of the mean radial velocity field (Fig. 4.10).

4.2.2 Condition 07

This condition is characterized by the absent of screech tones, and by the presence of important asymmetries in the jet plume (Fig. 4.26). The supersonic region extends until 5 D_s for the upper part and 4.1 D_s for the lower one. A complex shock-waves interaction is occurring in the upper image at the lip of the primary nozzle, while in the lower part a simple conical shock-wave is present, like for the condition 01. A stronger shock-cells pattern is present in the upper part of the image, while in the lower one is weaker and not aligned. The primary stream accelerates, but the velocity is not modulated as in the other test cases.

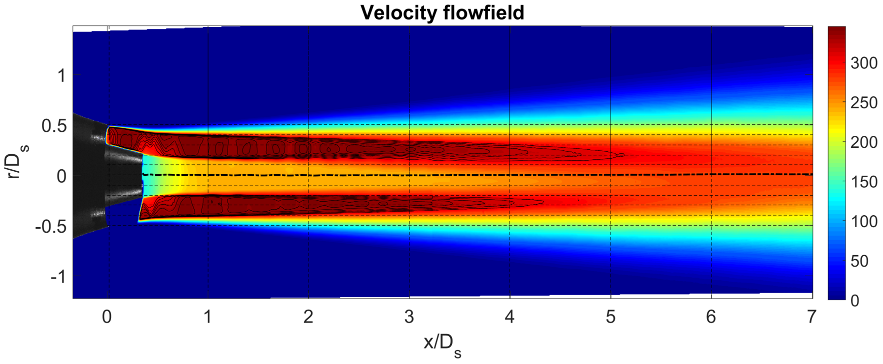

Figure 4.26: Mean velocity module flow field with M ¿ 1 isolines at condition 07. The thicker dot-dash line is the computed jet center. Dashed lines represents the locations where radial and axial profiles for Mach number and turbulence intensity were extracted. The flow field exhibit a marked asymmetry between the upper and the lower part of the image.

From the radial velocity component, in Fig. 4.27, in the subsonic region some spots are observable in correspondence of the shock-cells, vanishing when the pattern became weaker. In the supersonic region those spots are more pronounced, but only in the upper part of the image.

Similarly for Cond.01, profiles were extracted along horizontal and vertical straight lines plotted in Fig. 4.26.

In Fig. 4.28, the axial Mach number profiles show a shock-cells pattern irregular and quite different between the two halves of the image. In the upper part, for r / D = 0.2, the Mach number initially decreases and then it slightly increases around x / D = 3.5. Looking at the mean velocity map, the upper secondary flow is not monotonically converging through the centerline. However, in this region the velocity gradient is intense, and thus the interpretation is uncertain. The Mach number profile in the centerline is initially flat, with a small modulation, and it start to increase after x / D =

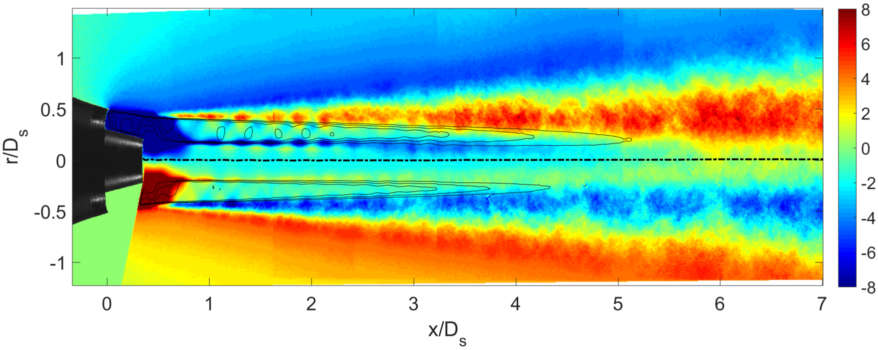

Figure 4.27: Mean radial velocity flow field with M ¿ 1 isolines.

3, reaching a plateau at x / D = 6. The number of identifiable shock-cells is 11 for both upper and lower part.

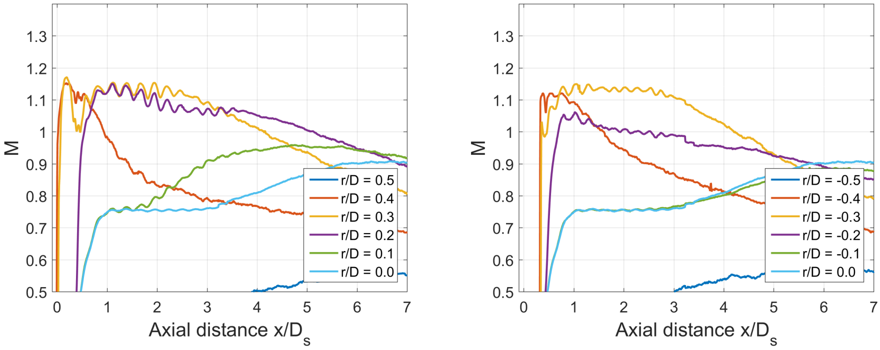

Figure 4.28: Mach number axial profiles at several radial position for the upper part (left) and lower part (right) of the image.

The comparison between the upper and lower profiles, in Fig. 4.29, show the shock-cell system is completely different both in shock-cells strength and spacing. It is worthy to note, at r / D_s = 0.303, that the lower secondary flow does not recover from the conical shock-wave in the same way than the upper one. Given that the total pressure before the sonic throat is the same, it is clear that there was a different loss of total pressure between the two parts. This can be explained looking at velocity field, the two shock-wave are not equal. For the lower part, a single shock is present, but for the upper one a sequence of smaller shocks is slowing the flow. It is well known from the literature that a sequence of shock-waves is less dissipative than a single one. Hence, although the difference at such low Mach number may be small, the effects are important. Unfortunately it is not possible to determine what is causing this asymmetry from the PIV images, because of the shadowed area.

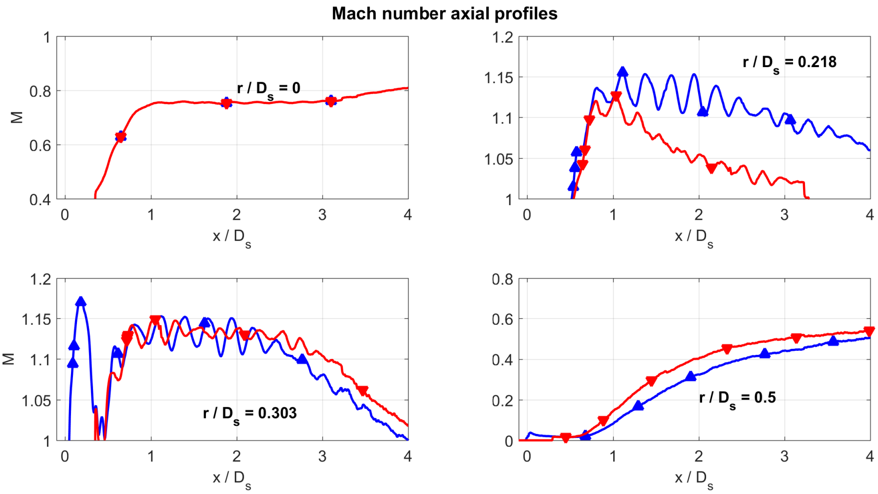

Figure 4.29: Comparison of the Mach radial profiles between the upper part (in blue, up pointing triangles) and the lower part (in red, down pointing triangles) at several axial distance

The radial Mach profiles are depicted in Figs. 4.30) and 4.31. However, from the axial profiles comparison, it is evident that the upper and lower part are not directly comparable, since the shock cells are not aligned.

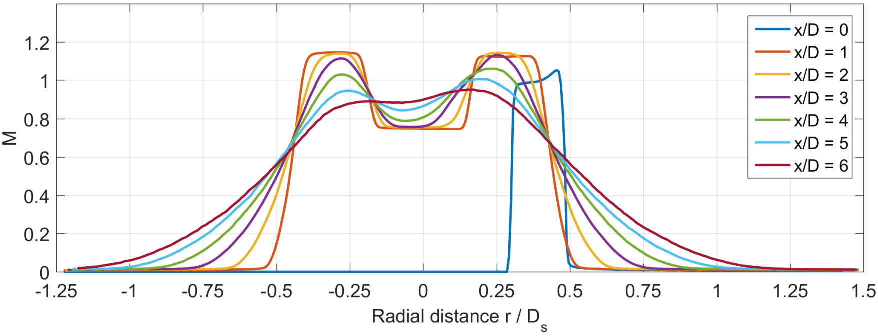

Figure 4.30: Mach number radial profiles at several axial distance.

Only above x / D = 4 the Mach axial profiles are not oscillating anymore, and thus the radial profiles are more meaningful. It is found that the asymmetry decays far from the nozzle, and, especially for the external shear layer, good agreement is found between the upper and lower profiles.

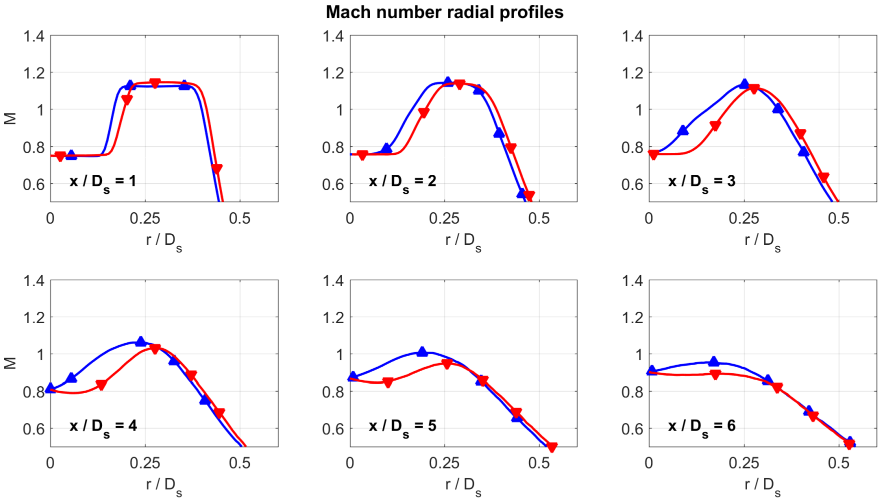

Figure 4.31: Comparison of the Mach radial profiles between the upper part (in blue, up pointing triangles) and the lower part (in red, down pointing triangles) at several axial distance. Some agreement is found only in the external shear layer of the secondary stream.

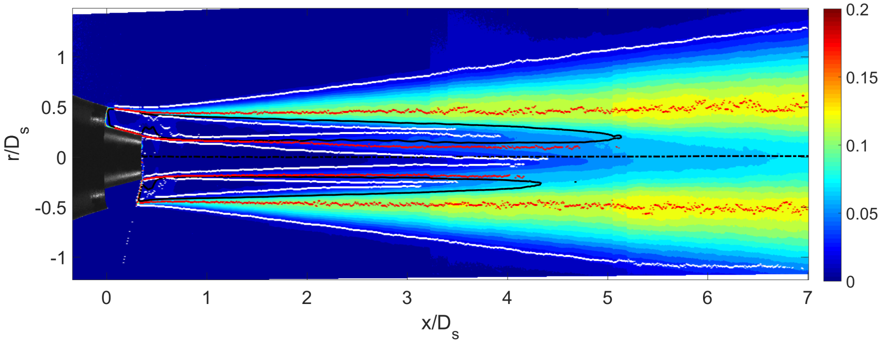

Figure 4.32: Turbulence intensity flow field. In black, the M = 1 isoline, in red, the TI maxima locations, and in white, the computed limit of the shear layer. The external shear layer limit grows linearly until the end of the FOV, while the internal shear layers limits have different behaviors for the upper and lower parts of the image. The merging of the internal shear layers determine the ends of the potential cores.

Similarly to the previous case, the TI map, including maxima and shear layers limits, is shown in Fig. 4.32. Despite the different pressure condition, the flow topology is analogous. The points of maximum are placed horizon-

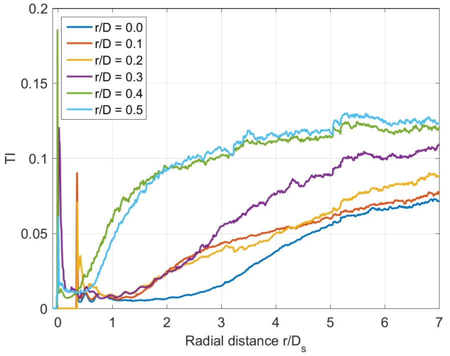

Figure 4.33: Turbulent intensity axial profiles at several radial position for the upper part of the image. The primary flow appears to be affected by the shock-cells pattern in a little measure, and only near the nozzle exit.

tally, with the internal shear layer maxima being detectable until x / D ≈ 4.5 . Also the length of the potential cores are comparable with Cond.01, although they are thinner.

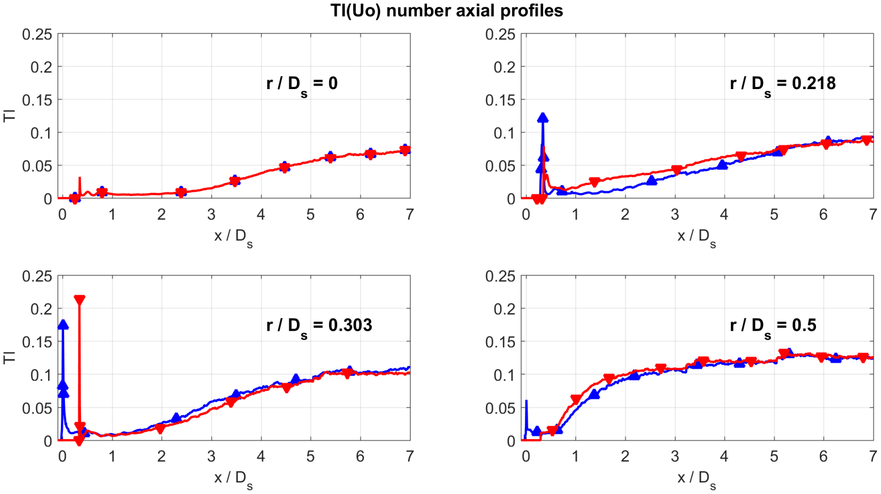

Figure 4.34: Comparison of the TI axial profiles between the upper part (in blue, up pointing triangles) and the lower part (in red, down pointing triangles) at several radial distance. The radial positions corresponds to the jet centerline (r/D = 0), the internal nozzle lip (r/D = 0.218), the ideal intersection point between the internal nozzle wall and the secondary nozzle exit area (r/D = 0.303) , the secondary nozzle lip (r/D = 0.5).

The axial cuts shown in Fig. 4.33 are also similar to Cond.01 except that the TI in the centerline is not modulated, a part for a wave immediately after the primary nozzle exit. The maximum TI approaches the value of 12 % at the end of the FOV.

The comparison of the upper and lower profiles finds quite good agreement between them. This is rather interesting, because it means that despite the mean velocities are different, the fluctuations are rather the same.

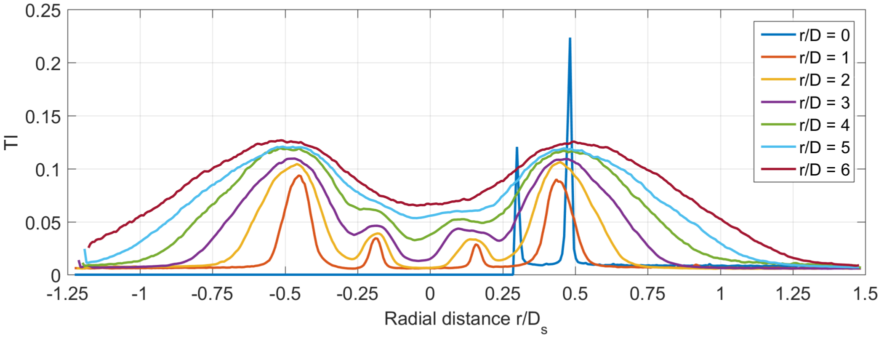

Figure 4.35: Turbulence intensity radial profiles at several axial distances.

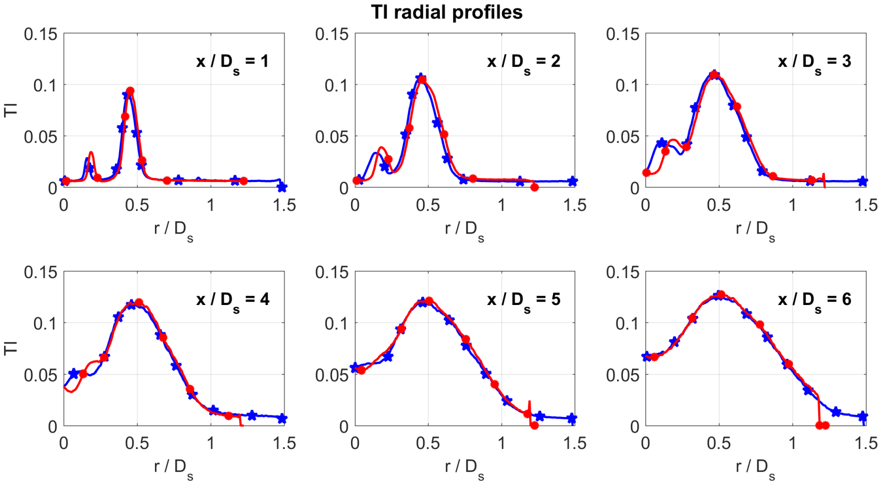

Figure 4.36: Comparison of the TI radial profiles between the upper part (in blue, stars) and the lower part (in red, circles) at several axial distance.

Also the radial TI profiles, shown in Figs. 4.35 and 4.36, show a marked asymmetry only in the internal shear layer, but the external one is symmetric. This is important to make some assumptions on the validity of the acoustic measurement. At least for the jet noise component, the asymmetry should not take an important role. Unfortunately the same cannot be said for the BBSAN.

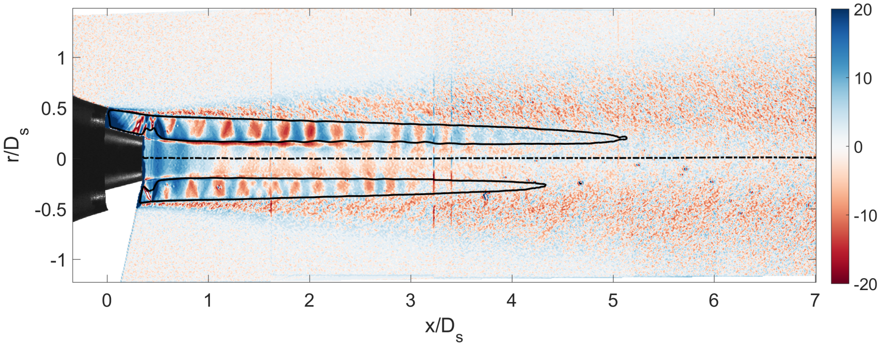

Figure 4.37: Square root of the mean velocity divergence flow field $\nabla V/\sqrt{|\nabla V|}$. The image shows how the primary and secondary flows are expanding (in blue) and compressing (in red) with the shock-cells.

Concerning the divergence of the velocity field, presented in Fig. 4.37, the upper and lower part do not show a symmetric pattern, and, more important, the internal stream is not modulated with the shock-cells anymore. This was predicted already by the COMSOL simulation in Sec. 2.4.

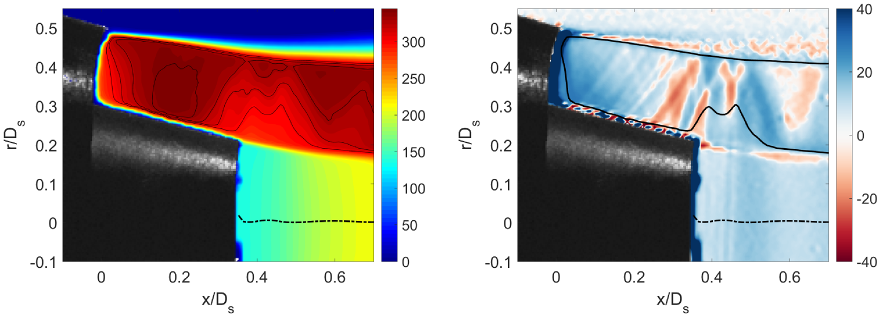

Figure 4.38: Detail of the nozzle region. Velocity flow field with M ¿ 1 isolines (left) and velocity divergence flow field (right). The shocks interactions is quite complex. A first shock-cell is complete, but immediately after a shock-wave is starting from the primary nozzle lip.

The complex shock-waves system at the end of the primary nozzle is now discussed. From Fig. 4.38 the Mach isocontour lines form a M-shape, and at least three shocks are detectable. The first one, starting from the left of the picture, is the shock associated with the end of the first shock-cell, which is completed before the end of the nozzle. A second one immediately follows, this one caused by the primary nozzle lip, and finally an upside-down λ shock is formed.

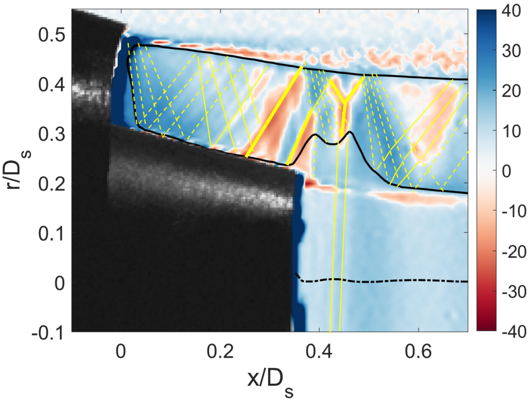

Figure 4.39: Attempt of reconstruction of the expansion (dashed line) and compression (continuous line) Mach waves in the nozzle region.

An attempt to explain these complex interactions is given in Fig. 4.39. The exit of the secondary nozzle marks the beginning of the acceleration zone. An expansion fan departs from the secondary nozzle lip. When the expansion waves encounter the boundary layer, they are refracted back, as expansion waves, similarly to Cond.01. This time, however, the lower pressure conditions content the closure of a first shock-cell before the nozzle end. The resulted weak shock wave impinges on the shear layer and it is refracted as an expansion fan. Being the flow still supersonic, a second shock-wave is needed to turn the flow horizontal at the end of the primary nozzle. This second conical shock-wave interacts with the expansion fan coming from the refraction point of the previous shock with the external shear layer. The expansion fan is strong enough to limit the extension of the subsonic pocket downstream the lip shock-wave. However, the latter is not canceled, it propagates towards the shear layer, leading to the formation of an upside-down λ shock laying on the shear layer. This shock slows the flow, causing another enlargement of the subsonic pocket by opposing to the expansion fan. This leads to the formation of a M-shaped sonic line. After the λ shock, another expansion fan is present, causing again an acceleration of the secondary stream, and to the formation of the shock-cells pattern in the wake. What is still unknown, is why only half of the flow is presenting this peculiar behavior. It must be reinforced that this information is generated from the divergence of the mean velocity field, and not from the mean of the instantaneous divergence of the velocity fields, which is a more correct representation of the flow field.

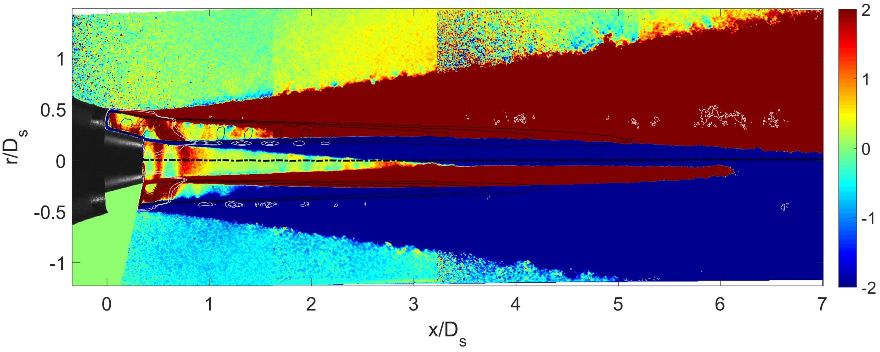

Figure 4.40: flow field of the averaged velocity fluctuations product $u'v'$. The black lines are M = [1:0.05:1.325] isocontour lines. In white, the isocontour lines of the mean radial velocity field (Fig. 4.27). The scale should enhance the lobes outside the jet shear layer shown in Fig. 4.24. Here, instead, they are not present, despite some shock-cells are occurring. For this test case, the screech is not occurring, but the BBSAN is still present in the acoustic spectrum.

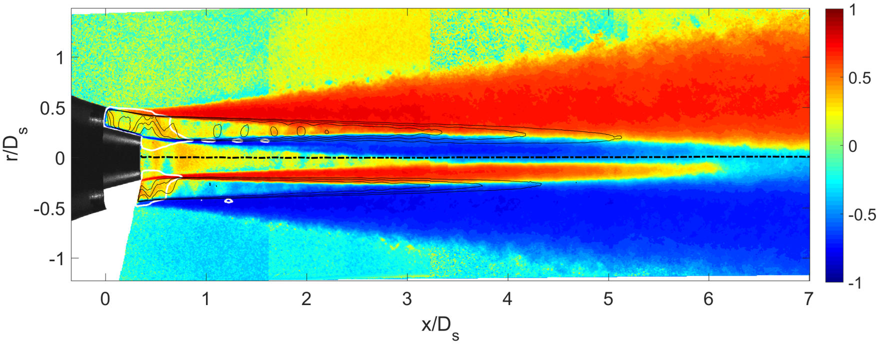

Figure 4.41: Normalized Reynolds shear stress $u'v'/\sqrt{|u'v'| \cdot \sigma(u)\sigma(v)}$. The black lines are M = [1:0.05:1.325] isocontour lines. In white, the isocontour lines of the mean radial velocity field (Fig. 4.10).

Finally, in Figs. 4.40 and 4.41 the product of the velocity fluctuations, $u'v'$, are shown. Compared to all the previous tests, where screech was present, here, for the first times, lobes are not appearing. This suggests an existing relationship between the screech phenomenon and the lobes.

4.2.3 On the jet asymmetry

Concerning the discovered jet asymmetry, it is difficult to found a definitive answer at this stage, without further tests. Analyzing the error chain, here are some possible sources:

- **Nozzle asymmetry**. The first check to be done is towards the experimental setup, and naturally to the coaxiality of the two nozzles.
  - **Nozzle coaxiality**. Concerning this point, a centering tool was used before each test with this purpose, and no error was found. The two nozzles were centered within the manufacturing tolerance (order of 20 μm).
  - **Axes misalignment**. What the calibrator cannot say, however, is that the two nozzles' axes are aligned or not. All the pieces of the inner duct, the inner nozzle, and the external nozzle were made by turning process, so with extremely small probability of axial deformation. The external duct, instead, is composed of shorter traits, with welded flanges, and bolts to join them. Here axes misalignments are possible, due to deformations during the welding process, or not uniform force applied to the screws. To check this, a digital level was used on each segment, in three different directions. All the measurements returned an angle difference between the segments falling into the interval $\Delta\alpha = \pm 0.1^o$. The inner duct is composed of separate segments screwed together. Although improbable, a check for misalignment was also conducted, rolling the jointed duct on a calibrated plane. Indeed it was found the duct was not perfectly straight, but forming an arc. However, the light of the arc was measured with calibrated thicknesses, and it was found to be below t = 20 μm, on a 1.5 m arc. Therefore, the installation or manufacturing errors were excluded as source of the jet asymmetry.
- **PIV error**. After checking the jet rig, the next source of error may come from the PIV setup.
  - **Laser sheet misalignment**. This is a typical error that may occur in PIV. The laser sheet has to pass by the jet axis, to ensure complete axisymmetry, and an aluminum rigid plate, with one of the two faces passing through the nozzle axis, was used before each test campaign to perform a correct alignment. If the laser plane is not aligned with the jet axis, it will intersect it only in one point, while it is more and more diverging going far from that point. This is source of errors in the axial velocity, and it may cause, a reduction of the signal to noise ratio in the cross-correlation, due to out-of-plane particles. Even so, it is a 'symmetric' error, because it influence both the jet halves in the same way. Therefore,

    it may not cause the velocity fields shown previously. If the laser plane is still parallel to the jet axis, but not passing through it, for the given geometry there is for sure a loss of symmetry. In particular, a half of the jet would appear more 'compressed' in the radial direction than the other half. However, this would not cause any error in the axial velocity component, because of the jet axysimmetry. Quantities such the shock-cell spacing would not be minimally affected. If the jet is totally axisymmetric, the shock-cells would be aligned also with such error, which is not the case.

  - **Optics misalignment**. In this point must enter all the possible sources such as the focal number, the particle size on the sensor, camera not aligned with laser sheet, etc... For all of these, no reason has been found so far to explain a bias in the averaged velocity field. Eventually a camera misalignment could make it, but given the angles, the error would be negligible.
  - **Pre-processing and cross-correlation**. Errors may come surely from the background determination and subtraction, or from the velocity determination, but also in this case there is no reason to privilege a half of the jet compared to another one.

- **Flow natural asymmetry**. This points accounts for all the effects not known a priori, such as the room recirculation, the influence of external structures such the PIV optical bench, cameras, acoustic foam on the nozzle, etc..., that may break the axisymmetry. Eventually, the axisymmetry itself is not a stable configuration for this jet, or not at all the pressure conditions. A stability analysis may help in answering this question

- **Nozzle pressure deformation**. Without further information, this is the most credited source of the jet asymmetry. As explained in Sec. 4.1.2, the external duct experiences a structural deformation due to the pressure. The hypothesis is that inner duct, which is centered through three screws passing through the external duct (Fig. 2.10), is moved by the screws which are fixed to the latter. The screws are not placed symmetrically in the duct, therefore depending of the vertical displacement, the central nozzle may displace differently.

4.2.4 On the effects of the shock-waves interaction on the screech

From the comparison of the results of Cond.01 and Cond.07, and also the other test conditions, it can be inferred that the shock-waves interaction has a key role in screech suppression. Cond.06 (Sec. A.5) show also a distinctive asymmetry, in the Mach profiles, symmetry in the conical shock-wave, and nevertheless it exhibits screech tones in the spectrum (Sec. 4.3.4). Also in Cond.08 (Sec. A.6) the plume is not symmetric, and the conical shock-wave is symmetric, but in this case, the shock-wave is complex, and screech is not present (Sec. B.8). An comparison of the conical shock-wave for all the tested conditions is presented in Fig. 4.42.

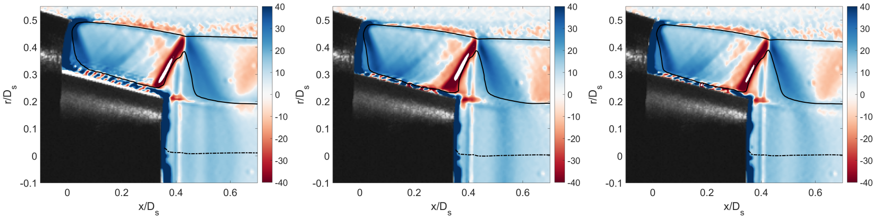

(a) Cond.01 (b) Cond.02 (c) Cond.03

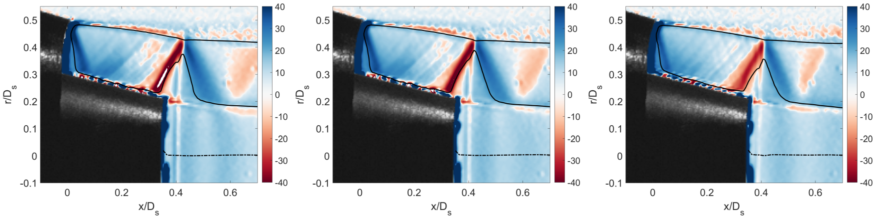

(d) Cond.04 (e) Cond.05 (f) Cond.06

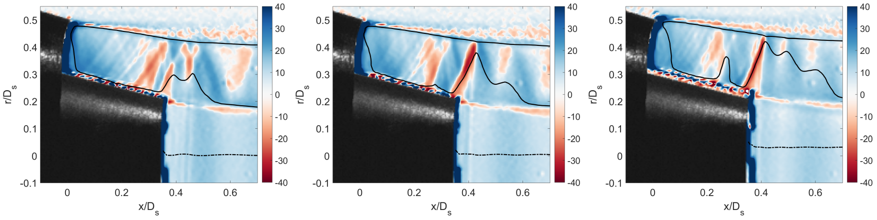

(g) Cond.07 (h) Cond.08 (i) Cond.09

Figure 4.42: Square root of the mean velocity divergence flow field $\nabla V/\sqrt{|\nabla V|}$. Zoomed view of conical shock wave region for all the tested conditions.

In the literature, screech tones are found also at such low underexpansion, and also in condition of not perfect symmetry. Although this is only a preliminary study, it is inferable that it is this complex shock-wave, and not the asymmetry, to break the acoustic feedback loop at the base of the screech. To confirm this hypothesis, it would be sufficient to test a condition with screech, modifying the nozzle geometry in order to obtain an interaction between the nozzle lip shock, and the expansion fan at the end of the first shock-cell. This could be achieved simply changing the thickness that is placed under the secondary nozzle, with a shorter one. With the help of the CFD, it is not difficult to compute the required length reduction. Different thicknesses should be tried in order to investigate the onset and the ending of the phenomenon.

4.2.5 Shock-cells length

In this section, the averaged shock-cells length will be subject of discussion. First of all, as already presented in Sec. 4.2.1, the location where to take the measurements is not obvious. The centerline would be the best option, because, for the sake of studying only the shock-cells length, the velocity modulation induced by the shock-cells would be sufficient to determine the shock-cell length, because of the spatial correspondence of the two. However, from Cond.07 to Cond.09 the primary flow is not modulated anymore, and thus a comparison would be impossible.

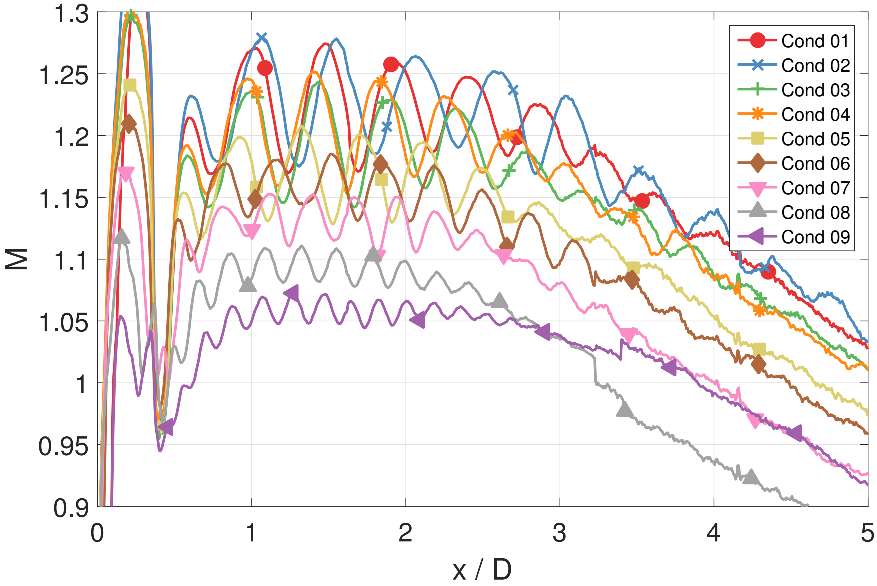

Figure 4.43: Overall comparison of the Mach axial profiles at radial distance r/D = 0.303.

Therefore, to have a fixed reference for all the test cases, the Mach profiles at r / D = ±0.303, already used in Fig. 4.12, will be compared. In Fig. 4.43 and 4.44 it is possible to observe the rapid decay of both amplitude and strength of the shock-cells. The average shock-cell lengths were retrieved using the same methodology explained in Sec. 3.5.2. The shock-cells are identified from the axial Mach profiles minima, and their length is averaged. Both upper and lower profile lengths are plotted in Fig. 4.45 together with the uncertainty bars at 95% confidence level. The uncertainty comes from the different length of the shock-cells in the Mach

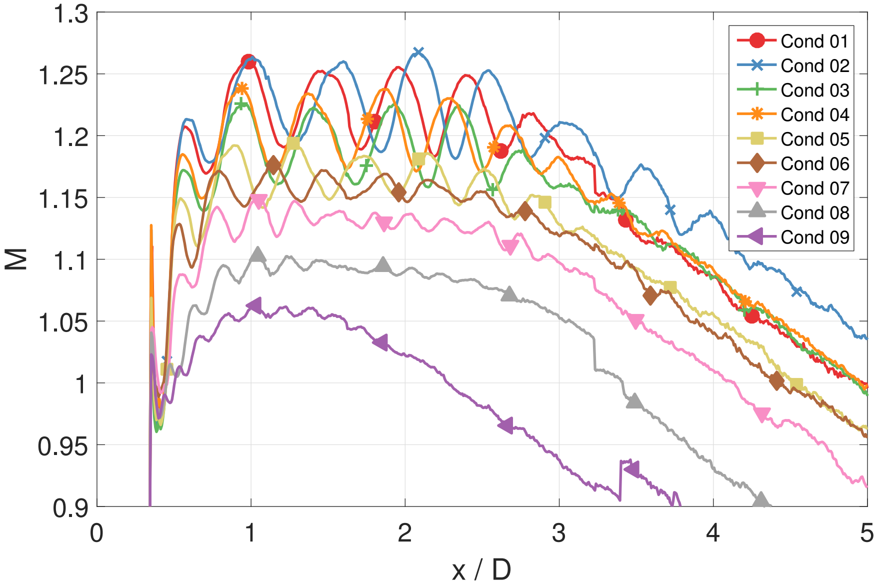

Figure 4.44: Overall comparison of the Mach axial profiles at radial distance r/D = -0.303.

profile. For higher pressure condition, a lower number of shock-cells was identified, hence the larger uncertainty. Additionally, a Fourier analysis was also performed and the peak wavelengths added to the plot. The wide uncertainty must be attributed to the small number of shock-cells, especially in the higher conditions. Furthermore, as stated previously, the supersonic plume is converging on the inner nozzle, so the profile extraction is not optimum. And finally, the shock-cells are naturally shortening along the axis direction. Another approach could be to measure the shock-cells length per each velocity field, and successively perform the average. This would lead to more accurate uncertainty quantification, because based on 1800 snapshots.

The same approach used for the single stream jet in Sec. 3.5.2 has been tried, non-dimensionalizing the axial length by the factor $D_s\beta$, and the y axis as $(M - M_j)/\beta^2$. However, this approach was not satisfactory (Fig. 4.46). Hence a modified scaling law was found to better collapse the curves. First of all, the influence of the conical shock-wave was removed shifting in the axial direction all the curves in order to match the first peak after the shock-wave, which has become the new zero. Second, instead of using the secondary jet diameter to scale the x coordinate, the clearance section h was used, because more representative of the real flow passage section. Third, for both axis it was used $\beta^{3/2}$, instead of β to scale quantities. With this approach, curves related to Cond.01 to Cond.06 find quite good agreement, but not for the last three, the ones with a complex shock-waves pattern, and no screech.

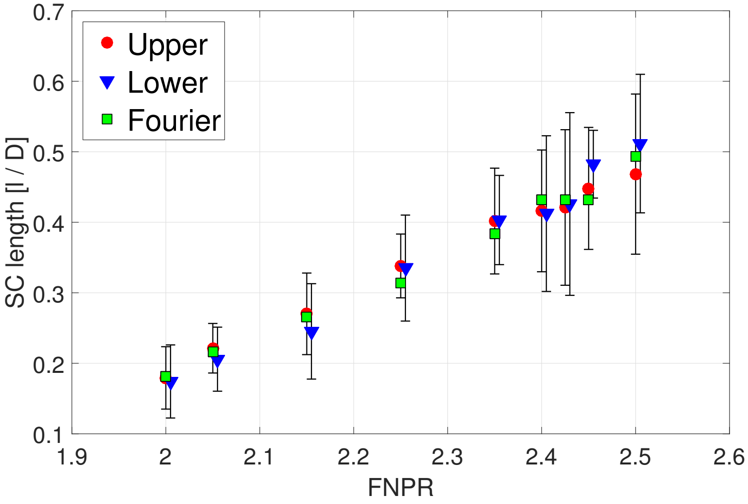

Figure 4.45: Shock-cells length, at different FNPRs, with error bars 95% confidence level, measured at r / D = 0.303, for the upper part of the image(left) and the lower part(right.). Triangles were slightly shifted for better readability. The higher uncertainty for the highest test conditions is due to a lower number of shock-cells.

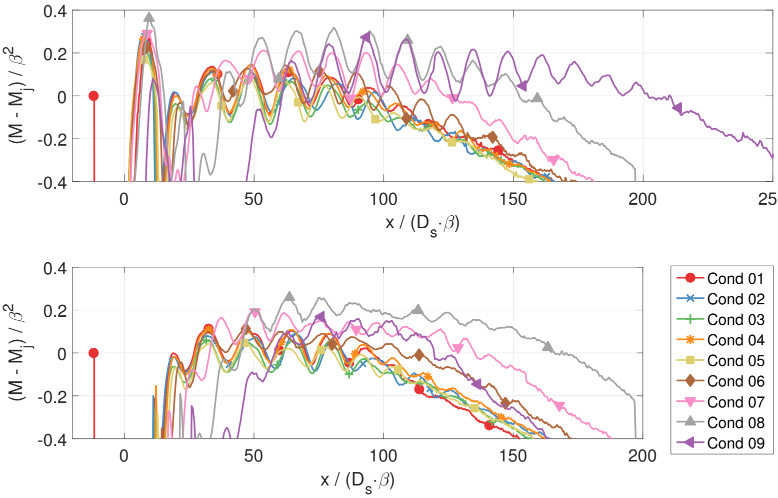

Figure 4.46: First attempt to collapse of the Mach number curves using the same non-dimensionalization of the single stream jet. M_j is the fully expanded Mach number, β is the off-design parameter

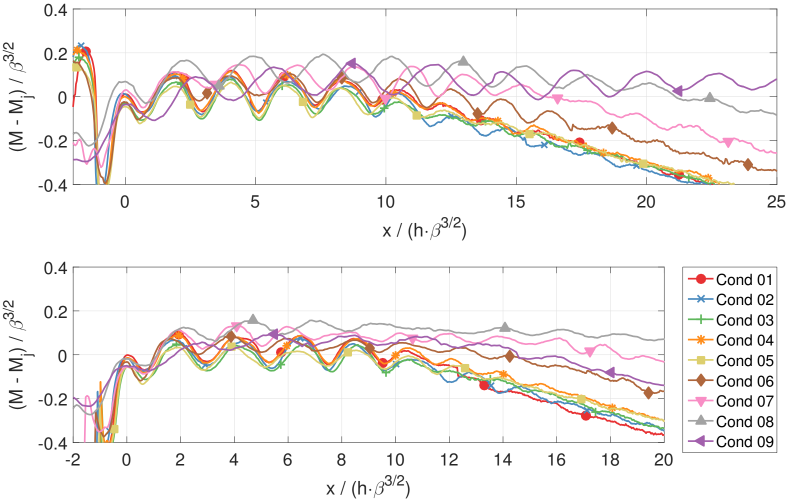

Figure 4.47: The collapse of the Mach number curves using a proper non-dimensionalization. In order to collapse, the curves were shifted in the axial direction to match the first shock-cell. M_j is the fully expanded Mach number, β is the off-design parameter, h is the clearance distance between the primary nozzle wall and the secondary nozzle lip.

The reason for this mismatch is unknown, although, it is logic to think it may come from the asymmetry or from the complex shock-waves. Indeed, the topology of the primary nozzle lip is very different. In the first six cases, the secondary flow turns through a strong, conical shock-wave, which is associated to entropy production and pressure losses. For Cond.07-09, instead, the supersonic flow turns by means of a series of weaker shocks, which are neither present in the whole secondary flow section passage. This will induce a minor loss of total pressure, hence a different behavior. And finally, the screech is not present in the last three cases, which has for sure an effect on the shock-cells, as already found by André [5]. A fitting parameter k was introduced to collapse also these curves. This parameter could be applied to β or to the clearance section. In the first case, it would mean the fully expanded Mach number needs to be modified, while for the second case it would be the clearance section. Given that a reduction of the shock-cells is needed to fit the curves, a positive k is required. In the case of relation with β, this would signify that the fully expanded Mach number to be higher, and so the total pressure, which is impossible because total pressure cannot increase. We suggest a relation with the clearance section h, which is estimated to be more realistic. Results are shown in Fig. 4.48. All the curves have been artificially shifted to match intensity and position of the third shock-cell peak. k is equal to 1 for Cond.01 to Cond.06 and it is slightly different for the upper and lower profiles: $k_{upper} = [1.06\ 1.22\ 1.35]$, $k_{lower} = [0.96\ 1.05\ 1.3]$ for Cond.07, Cond.08 and Cond.09 respectively. While the values for Cond.07 could be explained as the nozzle asymmetry, the other two cannot. Furthermore, at lower pressure condition, the secondary nozzle vertical deformation is reduced, and thus the critical area should be smaller, and not bigger. This behavior should be investigate more in future works.

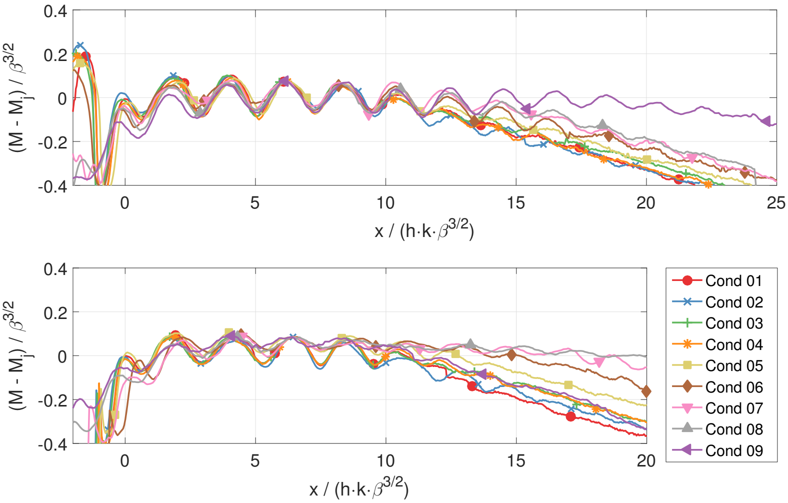

Figure 4.48: The collapse of the Mach number curves using a proper non-dimensionalization. In order to collapse, the curves were shifted in the axial direction to match the first shock-cell. M_j is the fully expanded Mach number, β is the off-design parameter, h is the clearance distance between the primary nozzle wall and the secondary nozzle lip, $k_{upper} = [1.06\ 1.22\ 1.35]$, $k_{lower} = [0.96\ 1.05\ 1.3]$ for Cond.07, Cond.08 and Cond.09 respectively

4.2.5.1 Spatial Fourier analysis

The mean Mach profiles already presented have been transformed into Fourier space in order to improve the shock-cell length assessment. Moreover, the it would be interesting to find higher harmonics that could be used in the Tam's model for BBSAN peak identification [92]. In order to remove the baseline from the profiles, a moving average with large stencil was used. This improved the analysis without altering significantly the spectral content, as shown in Fig. 4.49.

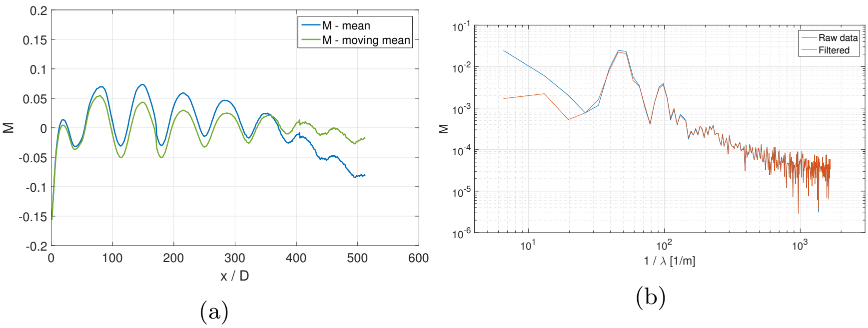

(a)

(b)

Figure 4.49: Effect of moving mean on the Fourier spatial analysis on the shock-cells system in space domain a), and Fourier domain b).

In Fig. 4.50 the spatial frequency and the spatial wavelengths are shown. A Hanning window was applied to the profiles to reduce border effects. The same color convention of the previous graphs was used, for this reason the spatial wavelength of Cond.02, which is the highest pressure tested, is also the largest. A second peak is identifiable from Cond.01 to Cond.06 in Fig. 4.50a. It is suggested, also in this case, to perform a spatial Fourier decomposition on the instantaneous field, and then to make the average. This could help in the correct peak identification.

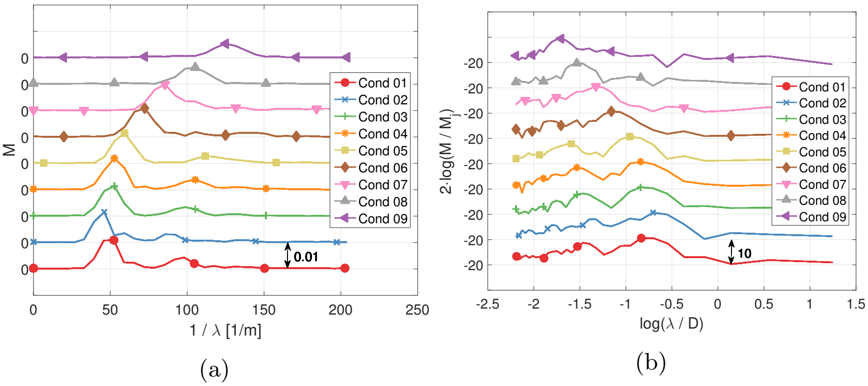

(a)

(b)

Figure 4.50: Spatial Fourier decomposition of the shock-cell system at a radial distance r/D = 0.303. the logarithmic visualization helps to visualize multiple harmonics of the main wavelength.

Finally also the wavelength profiles were non-dimensionalized in the same way of the shock-cell Mach profiles, finding a very good agreement in the Fourier domain for both intensity and wavelength.

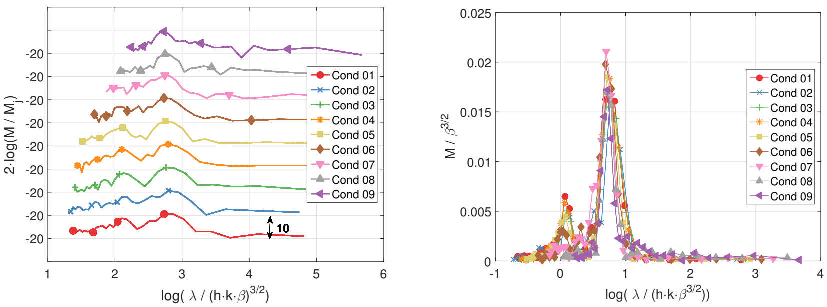

Figure 4.51: Non-dimensionalization and collapse of the Fourier spatial decomposition for all the test cases.

4.3 Acoustic Measurements

In this section the acoustic results of the test campaigns will be presented. For brevity, only selected case will be shown, leaving all the rest in the Appendix B. As already anticipated at the beginning of this chapter, the acoustic recordings performed in synchronous with PIV were polluted in high frequencies by the presence of the protective grid on the microphones. Therefore a second test campaign was conducted without the protective grid. For the PIV test campaign, Cond.01, Cond.06 and Cond. 07 will be presented. The first and the second show two different screech tones, while the latter has no screech at all. Afterward, the results of an acoustic campaign based on an extended test matrix will be presented in form of OASPL map.

4.3.1 Comparison with other experiments

In order to validate the acoustic results, the spectra obtained from the single stream jet, both from numerical simulation (Pérez Arroyo *et al* [68]) and experiments (André *et al* [4], results of Sec. 3.6), and with numerical simulation of the dual stream jet (Pérez Arroyo *et al* [67]. The spectra for the single stream jet in Fig. 4.52 are taken at $\theta = 120^o$ and CNPR = 2.30, while for the dual jet Cond.01 is compared (FNPR = 2.45, CNPR = 1.675). Spectra were non-dimensionalized and set to the same distance of r/D = 30.

Although the conditions are not directly comparable because of the different underexpansion, it is worthy to note that the experiments of the dual stream showed a noise level lower by 10 dB compared with a single nozzle of the same diameter, and at smaller underexpansion. This is rather bizarre, also considering that the dual stream has two shear layers, and thus two sources of sound. Also the numerical simulation of the dual stream show higher noise levels, similar to the single stream ones.

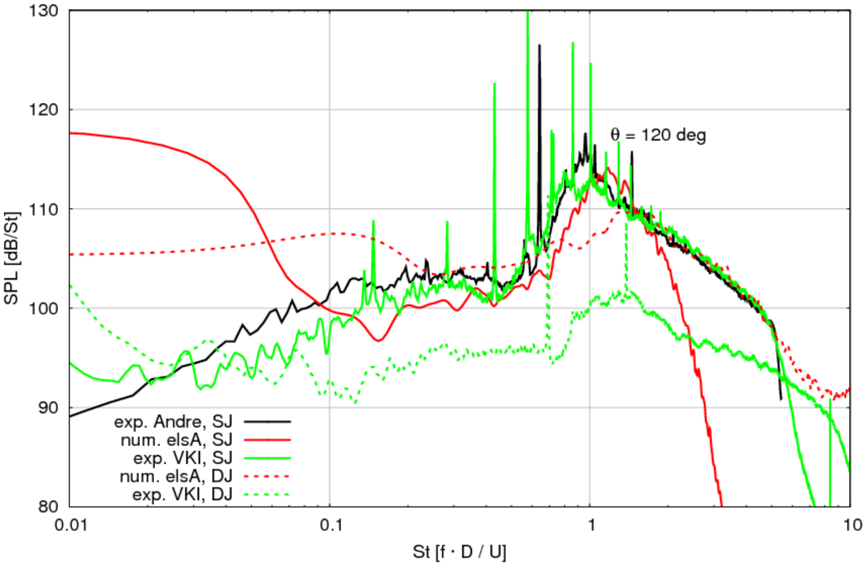

Figure 4.52: Comparison of the acoustic spectra at $\theta = 120^o$, for different test cases. The non-dimensional distance from the nozzle exit is equal to r/D = 30 for all the curves. The experimental measurement from André of a single underexpanded jet at CNPR = 2.30 (—), is compared with VKI experiment (—)(also presented in Fig. 3.43), and with numerical LES simulation from Pérez Arroyo (—). On the same graph, in dashed lines, are also compared the dual stream jet results obtained from LES simulations made by Pérez Arroyo (- -) and the VKI results for (- -) for FNPR = 2.45 and CNPR = 1.675. This comparison shows how the dual stream jet is on overall 10 dB quieter than the single stream one. Courtesy of C. Pérez Arroyo.

This discrepancy was subject of many investigations, including the repetition of the tests, and an acquisition error was excluded. Experiments were repeated for both the single and coaxial jet on the same day, without moving the antenna array. In all cases the spectra matched the previous ones. The cause of this sound reduction must be searched in the flow.

4.3.2 Condition 01: FNPR = 2.45, CNPR = 1.67

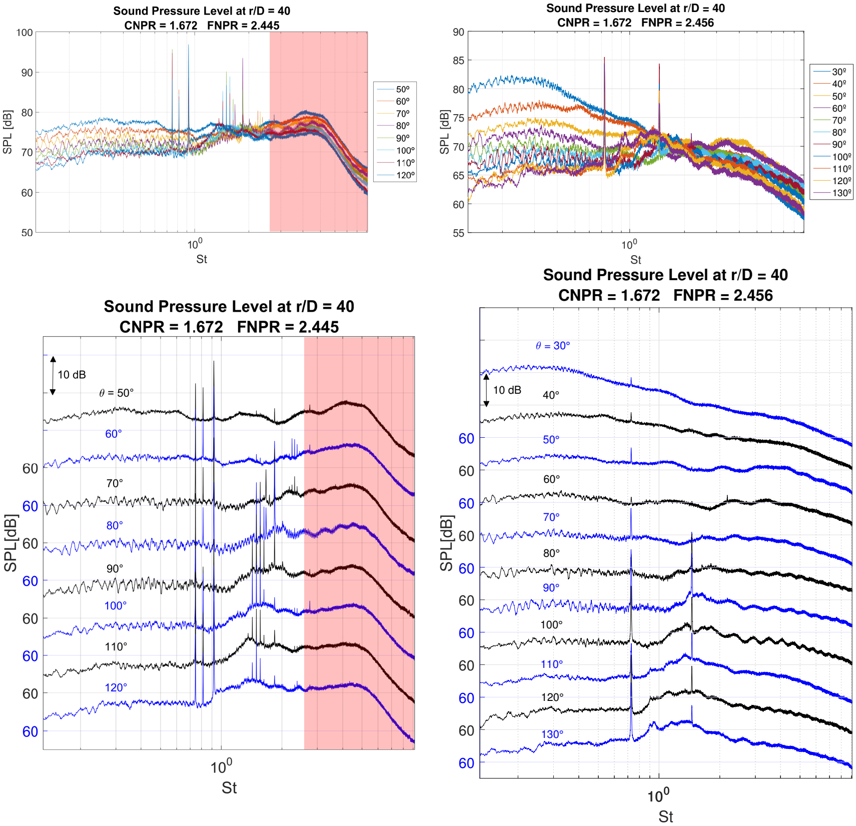
Sound Pressure Level at r/D = 40
CNPR = 1.672 FNPR = 2.445

Sound Pressure Level at r/D = 40
CNPR = 1.672 FNPR = 2.456

Sound Pressure Level at r/D = 40
CNPR = 1.672 FNPR = 2.445

Sound Pressure Level at r/D = 40
CNPR = 1.672 FNPR = 2.456

Figure 4.53: SPL (ref. $2 \cdot 10^{-5}$ Pa) for condition 01 at all the measured angles vs St. In the left column, the results of the first PIV acquisition are shown, while on the right the results of successive tests, conducted with a foam ring placed around the nozzle to damp acoustic reflections. Plots are vertically spaced for better readability. In the title are reported the real test conditions measured by the instruments.

Hereafter are shown the results obtained for both the test campaigns with and without the microphones' cap. For the PIV tests, in the very first acquisitions, it was recorded a triple screech tone at all the angles (Fig. 4.53 on the left). This behavior was caused by the flat portion of the secondary nozzle, which was acting as a reflective surface. It was already found in the literature that reflecting surfaces can alter the feedback loop. In any case, covering the initial part of the nozzle with an acoustic foam ring, 5 cm thick, eliminated the spurious tones, and so it was kept for all the successive tests.

An example of 'clean' spectra for Cond.01 is shown in Fig. 4.53 on the right. From the analysis, several differences can be found compared to the single stream jet. The screech tones are not exceeding 20 dB from the broadband noise level, and show directivity. The main peak loses intensity for $\theta = 70^o$, while the first harmonics disappear for $\theta < 80^o$. A very tiny second harmonic is visible only for $\theta = 60^o$. The BBSAN is not very pronounced, and this makes difficult to track a directivity pattern. Known the average shock cell length from the PIV, the BBSAN frequency peaks were computed using Eq. 1.17. The resulting pattern was, despite all the efforts, not satisfactory. Even trying several convective speed, or shock-cell lengths, it was not possible to fit the peaks at all angles. A comparison of the far field noise of the single and coaxial in the form of contour plot is shown in Fig. 4.54. The single stream jet had NPR = 2.46, and for both plots intensities were scaled as to be at distance r / D = 40.

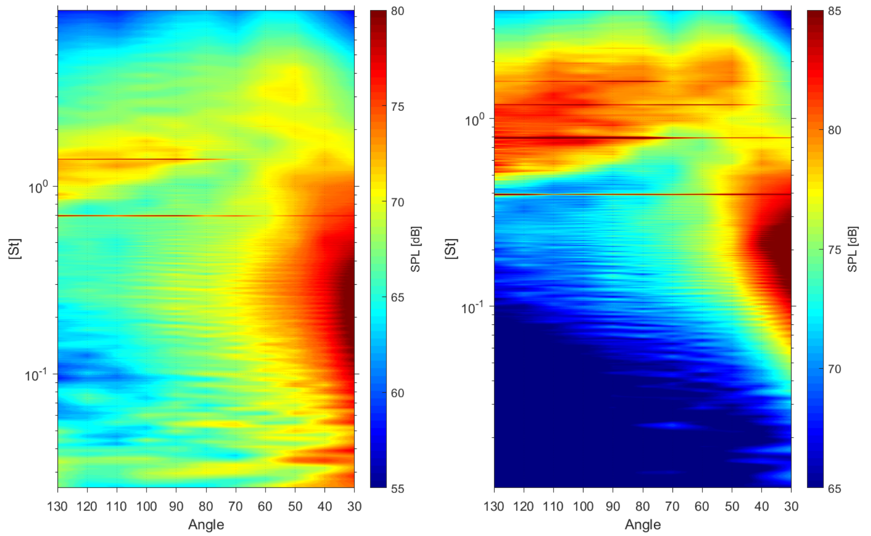

Figure 4.54: SPL (ref. $2 \cdot 10^{-5}$ Pa) for the coaxial jet at Cond.01 and the single stream jet at NPR = 2.46 at all the measured angles vs St.

The horizontal red lines correspond to the screech tones and harmonics. Despite the different scales, necessary to visualize correctly the plots, similarities and differences can be identified. The subsonic jet noise component has a similar shape and intensity for both jets. The BBSAN, on the contrary, it begins in a similar frequency range, but it is much weaker for the coaxial jet. In particular, its frequency and angular extension is reduced. A 'hole' in the BBSAN between $60^o < \theta < 90^o$ is visible for the dual stream jet. These low sound levels may explain the difficulties in finding a directivity pattern at all angles.

4.3.3 Condition 06: FNPR = 2.25, CNPR = 1.52

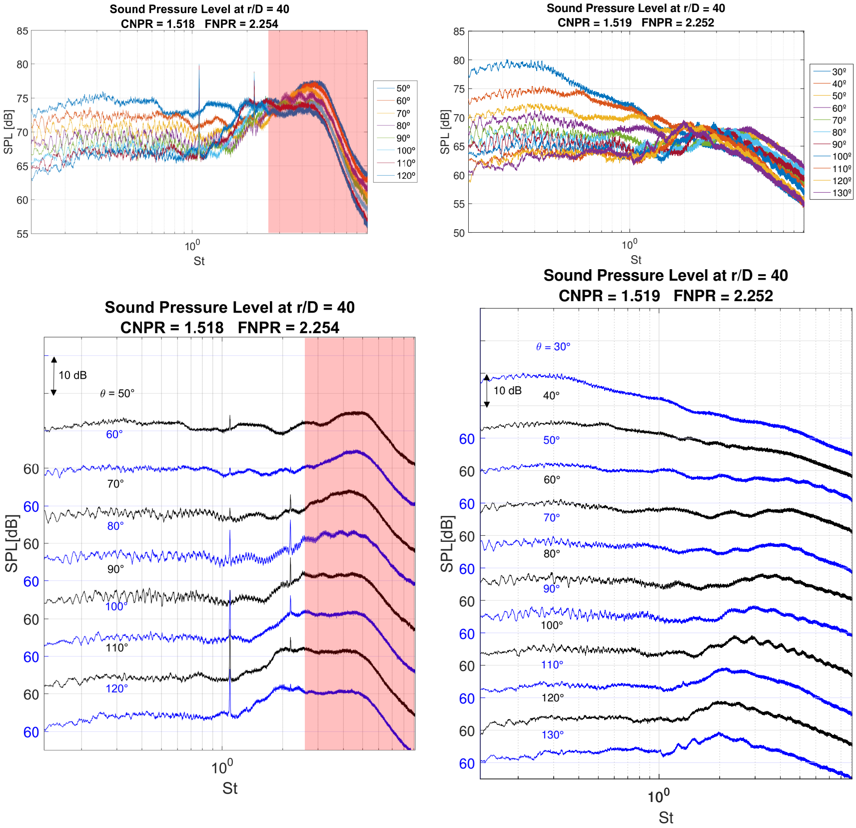
Sound Pressure Level at r/D = 40
CNPR = 1.518 FNPR = 2.254

Sound Pressure Level at r/D = 40
CNPR = 1.519 FNPR = 2.252

Sound Pressure Level at r/D = 40
CNPR = 1.518 FNPR = 2.254

Sound Pressure Level at r/D = 40
CNPR = 1.519 FNPR = 2.252

Figure 4.55: SPL (ref. $2\cdot10^{-5}$ Pa) for condition 06 at all the measured angles vs St. In the left column, the results of the first PIV acquisition are shown, while on the right the results of successive tests, conducted without the microphones' protective grid. Plots are vertically spaced for better readability. In the title are reported the real test conditions measured by the instruments.

Cond.06 spectra are depicted in Fig. 4.55. During the PIV campaign a screech tone was present, while in the successive campaign it disappeared. Without any image, it is not possible to know if the screech disappearance was caused by a nozzle asymmetry, different from the previous case, or by the missing PIV setup, which was introducing some reflective surfaces. In any case, the screech present in the PIV was successively identified as flapping or helical mode (see Sec. 5), the same kind present also in Cond.05. This kind of screech presents a characteristic directivity pattern, with low level at $\theta = 90^o$ and $50^o < \theta < 70^o$, while the first harmonic is present for $70^o < \theta < 110^o$. Unfortunately it is not possible to follow the BBSAN directivity due to the spectra pollution. For the non-screeching case, instead, it is possible to observe a directivity pattern of the BBSAN. In the contour plot, shown in Fig. 4.56, Cond.06 is compared with a single stream jet at NPR = 2.30. Again, the frequency extension of the BBSAN is much smaller than the single case, as well as the intensity level. This time, there is no gap in the BBSAN across the angles, although the shape appears linear, and not curved towards up like for the single stream jet.

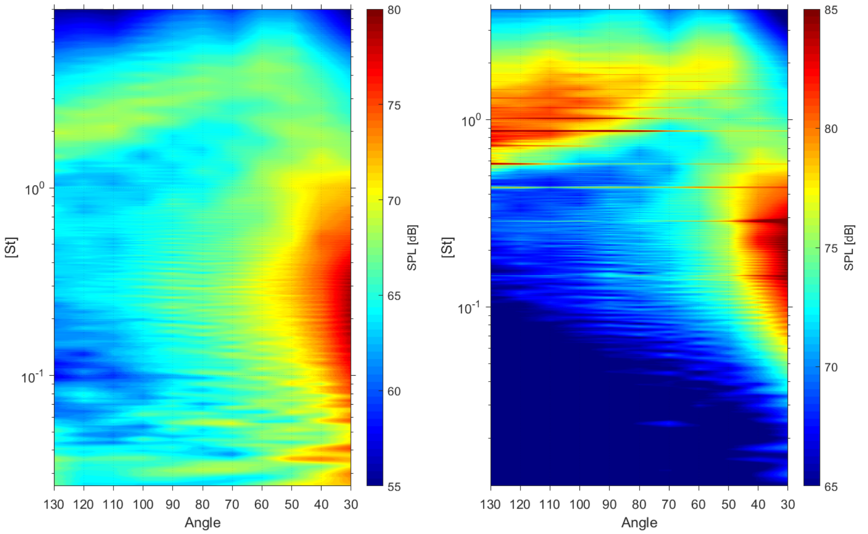

Figure 4.56: SPL (ref. $2 \cdot 10^{-5}$ Pa) for the coaxial jet at Cond.06 and the single stream jet at NPR = 2.30 at all the measured angles vs St.

4.3.4 Condition 07: FNPR = 2.15, CNPR = 1.46

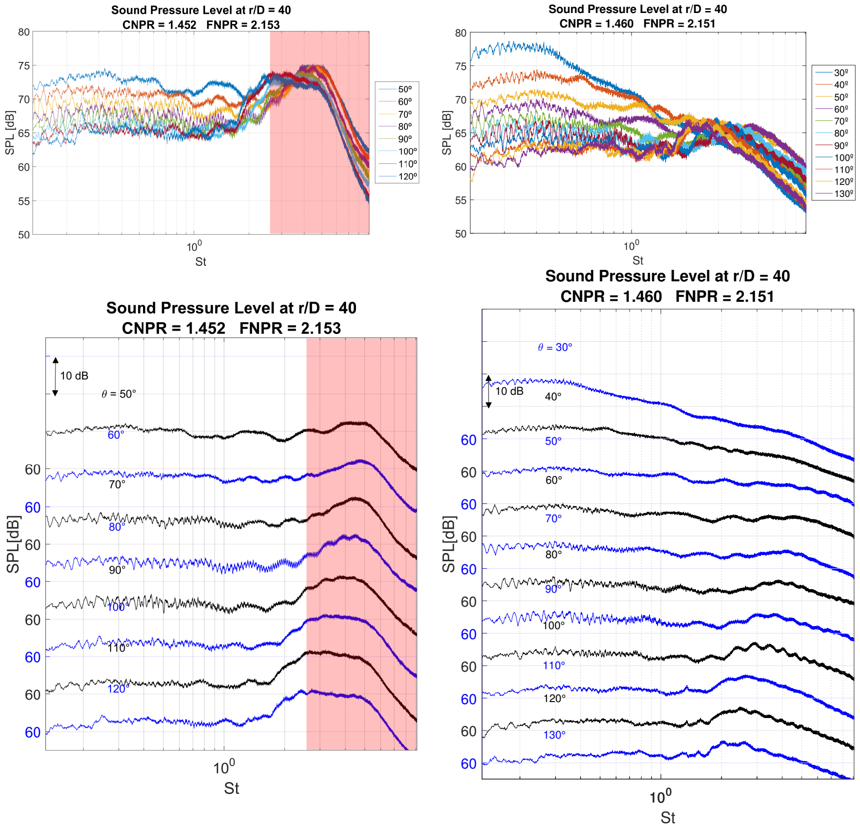

Figure 4.57: SPL (ref. $2 \cdot 10^{(} - 5)$ Pa) for condition 07 at all the measured angles in Hz and St. In the left column, the results of the first PIV acquisition are shown, while on the right the results of successive tests, conducted without the microphones' protective grid. Plots are vertically spaced for better readability. In the title are reported the real test conditions measured by the instruments.

Finally, Cond.07 is shown in Fig. 4.57. For this one and the subsequents, screech was not found. As explained in Sec. 4.2.4, it is not certain if it was due to the asymmetry or to the shock-waves interaction.

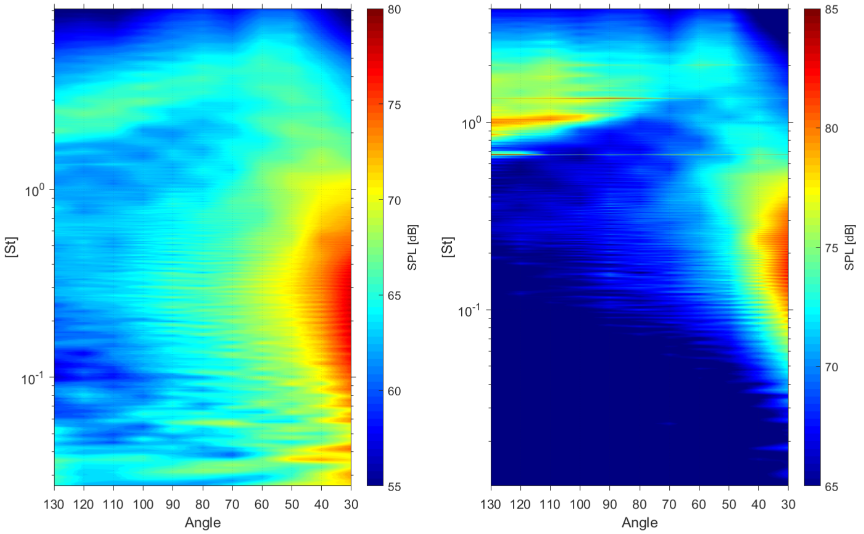

Figure 4.58: SPL (ref. $2 \cdot 10^{-5}$ Pa) for the coaxial jet at Cond.06 and the single stream jet at NPR = 2.30 at all the measured angles vs St.

4.3.5 Extended Test Matrix

An exploratory test campaign was conducted to investigate the sound generated by the coaxial jet for other combinations of CNPR and FNPR. With the aim to perform a sensitivity analysis on the conditions already tested (red marks in Fig. 4.59), more points were added keeping constant the FNPR and changing the CNPR (blue marks).

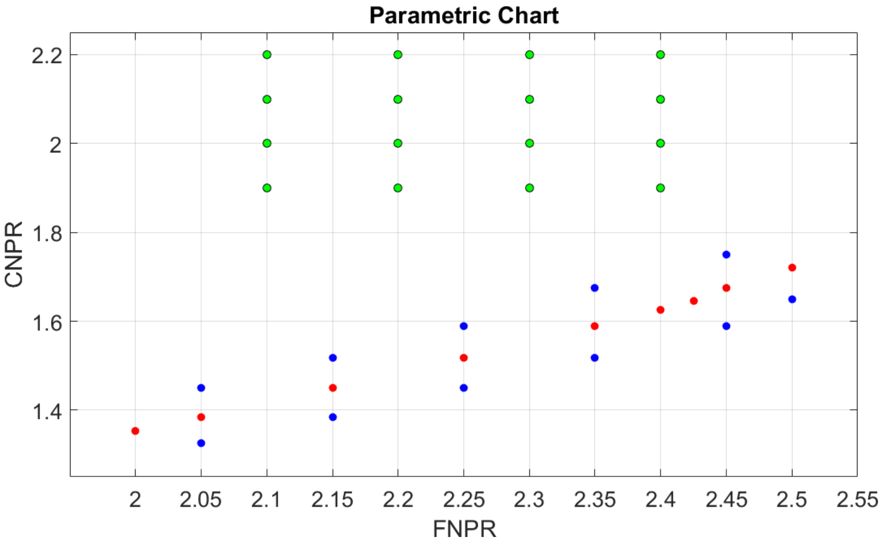

Figure 4.59: Parametric investigation chart for the acoustic experiments. In red, the conditions from 01 to 09 investigated also with PIV. In blue, additional points investigated only with microphones to perform a sound sensitivity analysis. In green, additional points investigated to assess the influence of the supersonic primary stream.

Finally, Tanna *et al* [104][103] and Tam *et al* [96][97] experienced an overall shock-cell noise reduction caused by the almost complete destruction of the shock-cell system when the primary nozzle runs slightly supersonic. This motivated the investigation of the region where the primary nozzle should be slightly supersonic (green marks in Fig. 4.59). The conditional is obligatory, in this case, always due to the conical shock wave present at the secondary nozzle lip, which increases in an unpredictable way the pressure at the primary nozzle exit. The CNPR conditions are, instead, related only to the ambient pressure. It is thus expected that a higher total pressure is required in order to have also the primary nozzle supersonic. All the test condition parameters are contained in Tab. 4.2.

Name	**CNPR**	**FNPR**	$\mathbf{M}_{jp}$	$\mathbf{M}_{js}$
Cond.10	1.65	2.500	0.877	1.223
Cond.11	1.589	2.450	0.841	1.208
Cond.12	1.518	2.350	0.796	1.176
Cond.13	1.450	2.250	0.748	1.142
Cond.14	1.385	2.150	0.698	1.106
Cond.15	1.325	2.050	0.647	1.067
Cond.16	1.750	2.450	0.931	1.208
Cond.17	1.675	2.350	0.891	1.176
Cond.18	1.589	2.250	0.841	1.472
Cond.19	1.518	2.150	0.796	1.106
Cond.20	1.450	2.050	0.748	1.067
Cond.21	1.900	2.100	1.003	1.087
Cond.22	2.000	2.100	1.046	1.087
Cond.23	2.100	2.100	1.087	1.087
Cond.24	2.200	2.100	1.124	1.087
Cond.25	1.900	2.200	1.003	1.124
Cond.26	2.000	2.200	1.046	1.124
Cond.27	2.100	2.200	1.087	1.124
Cond.28	2.200	2.200	1.124	1.124
Cond.29	1.900	2.300	1.003	1.159
Cond.30	2.000	2.300	1.046	1.159
Cond.31	2.100	2.300	1.087	1.159
Cond.32	2.200	2.300	1.124	1.159
Cond.33	1.900	2.400	1.003	1.192
Cond.34	2.000	2.400	1.046	1.192
Cond.35	2.100	2.400	1.087	1.192
Cond.36	2.200	2.400	1.124	1.192

Table 4.2: Overview of the acoustic extended test campaign. M_{jp} and M_{js} are the fully expanded Mach number for the primary and secondary nozzle, respectively.

4.3.5.1 Band Limited Overall Sound Power Level

To verify effective sound power level while changing the FNPR and CNPR, the Sound Power Level (SWL) of the jet should be measured. By definition, the SWL is the logarithm of the total sound power emitted by a source in all direction divided by a reference power. It is therefore defined as:

$$SWL = 10\, log_{10} \left(\frac{\int_A I\, \mathrm{d}A}{W_{ref}} \right) \tag{4.2}$$

where I is the sound impulse (W/m^2), A is an arbitrary area surrounding the source and W$_{ref}$ $= 10^{-12}$ W is the reference power. Being:

$$I = \frac{p^2}{\rho\, c} \tag{4.3}$$

hence,

$$SWL = 10\, log_{10} \left(\frac{\int_A p^2\, \mathrm{d}A}{\rho_\infty\, c_\infty\, W_{ref}} \right) \tag{4.4}$$

If we consider also that:

$$\rho_\infty\, c_\infty = \frac{p_\infty\, \gamma}{c_\infty} \tag{4.5}$$

and that for a sphere with radius r:

$$\int_A p^2\, \mathrm{d}A = \int_0^\pi 2\pi\, r^2\, p^2\, sin\theta\, \mathrm{d}\theta \tag{4.6}$$

it is straightforward to derive

$$SWL = 10\, log_{10} \left(\frac{2\pi\, r^2\, c_\infty\, p_{ref}^2}{p_\infty\, \gamma\, W_{ref}} \int_0^\pi \int_0^\infty 10^{PSD/10}\, \mathrm{d}f\, \mathrm{d}\theta \right) \tag{4.7}$$

where PSD is the power spectral density, p$_{ref}$ $= 2 \cdot 10^-5$ Pa is the sound pressure reference and f is the frequency. The previous formula is valid under the hypothesis of axisymmetric of the radiated sound (at least one axis of symmetry). In real life, of course, simplifications must be done, and the integrals have to be replaced by a sum:

$$BLOPWL = 10\, log_{10} \left(\frac{2\pi\, r^2\, c_\infty\, p_{ref}^2}{p_\infty\, \gamma\, W_{ref}} \sum_{\theta_1}^{\theta_2} \sum_{f_1}^{f_2} 10^{PSD/10}\, \Delta f\, \Delta\theta \right) \tag{4.8}$$

which is the definition of the Band Limited Overall Sound Power Level [12]. It is band limited because modern acquisition system records on digital supports, and thus the signal is always discretized, and the microphones have limits in their dynamic range. The major limitation in using this definition for jet noise is constituted by the fact that jet noise is axisymmetric with good approximation, but the sound has a directivity pattern within the polar angle. So this quantity will change depending the initial and final polar angle, as well as the microphones polar distribution. This aspect must be considered in order to compare the BLOPWL from different authors in the literature. On the other side, it is also a flexible tool to determine the noise power emitted in a specific direction, nor in a specific frequency range, i.e. to isolate the shock-cell noise. Using this method, Bhat *et al* [12] were able to find a region in their parametric study where the noise level was not monotonically increasing with the pressure condition. From the SPL contour plot (Fig. 4.60a) he identified the region responsible for the shock-cell noise, and computed the BLOPWL map relative only to that component (Fig. 4.60b).

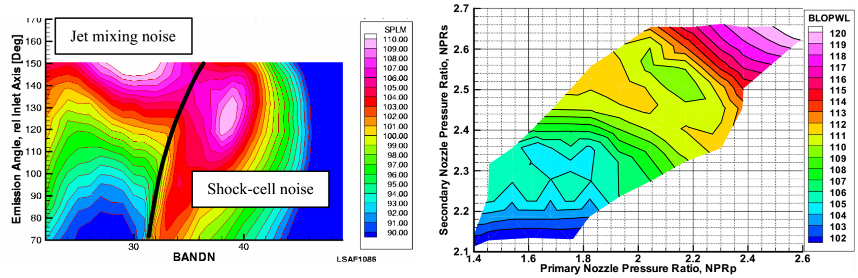

(a)

(b)

Figure 4.60: a) SPL of a coaxial jet from where the jet mixing noise region and shock-cell noise are identified. b) BLOPWL computed using only the shock-cell noise component for many CNPR and FNPR condition. Bhat *et al*[12]

It is important to note that the results of Bhat *et al* come from a very different jet rig. A central plug was present, and the primary nozzle was heated, leading to a conventional velocity profile in the plume. It is not straightforward to apply the same conclusion to our coaxial jet. From the results of all the measured conditions, a map of the BLOPWL was created in function of the CNPR and FNPR. The spectra were integrated in the whole angle and frequency range, and result is depicted in Fig. 4.61. Unfortunately Cond.17 was not recorded due to technical problem, and thus that important point is missing. However, the map contour map, especially in the 3D visualization, suggest that in the surrounding of CNPR = 1.7 and FNPR = 2.4 there is a local minimum. This is in agreement with the experiments of Bath, although the overall sound was considered, not only the shock-cell noise.

The next step would be to isolate the shock-cell noise only, and redraw the map. If the reduction of the sound level would be confirmed, this would mean that temperature effects does not are not affecting this sound

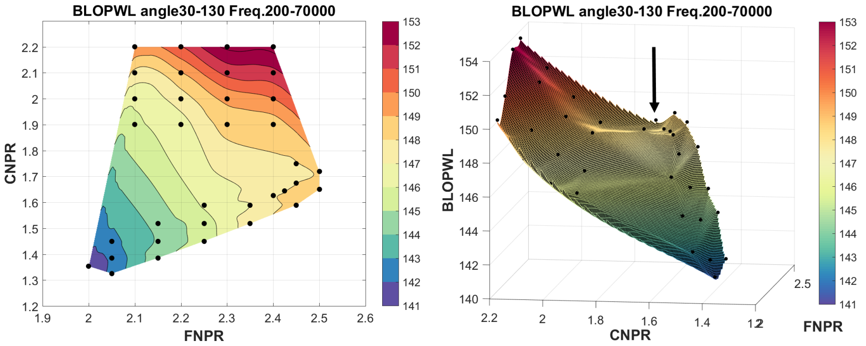

(a) (b)

Figure 4.61: Band Limited Overall Power Level computed integrating the acoustic spectra from 30 to 130 degrees, and from 200 to 70000 Hz (a), and its 3D representation (b). Curiously, the main points under investigations (Condition from 01 to 09) lay on a small 'valley', where the sound power level is smaller.

reduction, and thus the phenomenon could be studied also in a non-heated facility such FAST. Concerning the noise reduction postulated and verified in experiments by Tanna *et al* [104][103] and Tam *et al* [96][97], this feature was not encountered for the tested range of pressures, or at least, not as overall on all the angles. It must be also stated that in their experiments they used a coaxial nozzle with area ration $\mathrm{A}_s/\mathrm{A}_p = 0.86$ only, the internal nozzle was cylindrical (meaning no conical shock-wave due to change of secondary flow direction), the FNPR was ranging from 3.0 to 4.3 and the CNPR from 1.0 to 4.0, and the total temperature ratio was also not equal to 1. For all these reasons, the two results cannot be directly compared. However, effects on the high frequency noise when the primary flow is supersonic were recorded, but in the downstream direction.

Fig. 4.62 shows the BLOPWL integrated on a frequency range between 4000 and 70000 Hz (equivalent Strouhal depending on test condition). These boundaries make sure to capture the shock-cell noise, included the screech, at all the angles. This is even more crude approximation compared to Bath, because no attempt is made to separate shock-cell noise from jet mixing noise. Anyway, from the collected spectra, it is observable how the BBSAN hump is several dB higher than the jet mixing noise, at least in the rear arc, and therefore it is assumed, with an approximation, that performing the integration the result is representative of the shock-cell noise SWL. For the forward arc, instead, it is rather valid the opposite, the contribution of the jet mixing noise overcomes the shock-cell noise.

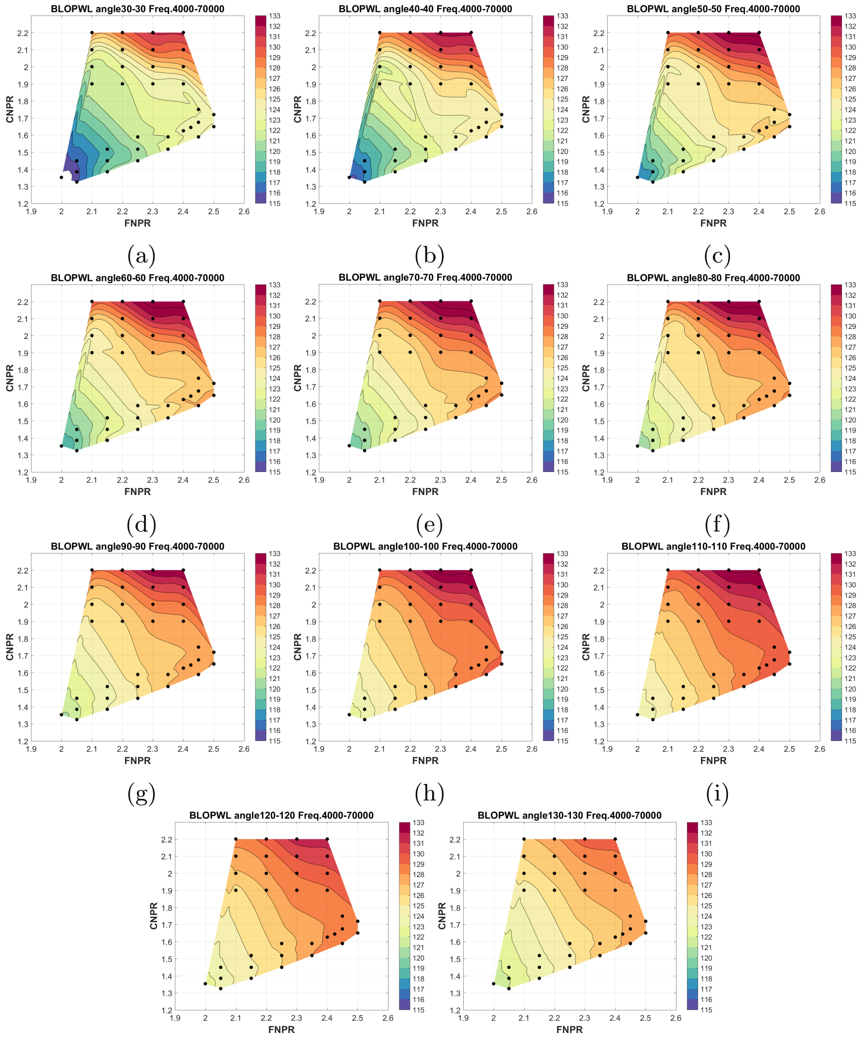

(a) (b) (c)

(d) (e) (f)

(g) (h) (i)

(j) (k)

Figure 4.62: Band Limited Overall Power Level computed integrating the acoustic from 4000 to 70000 Hz, ranging from $\theta = 30^o$ (a) to $\theta = 130^o$ (k).

Therefore the reader is invite to read the maps as high frequency shock-cell noise from $\theta = 60^o$ to $\theta = 130^o$ and as high frequency jet mixing noise from $\theta = 30^o$ to $\theta = 40^o$. For $\theta = 50^o$ the discrimination is more difficult, depending on the test condition. After stated the limitation of this approach, it is possible to evidence how the contours for $\theta = 60^o$ to $\theta = 130^o$ are rather similar, without any change in the trend with the primary stream becoming supersonic. On the other hand, for the remaining angles, $\theta = 30^o$ to $\theta = 50^o$, the maps exhibit a noise reduction around FNPR = 2.1 and CNPR = 2.0, and also for FNPR = 2.45 and CNPR = 1.7 the pattern is more complex. Remembering what said before, the conclusion is that the high frequency jet mixing noise is affected by the changes in the primary stream conditions, even when the high frequency shock-cell noise is not. The next analysis should pass by a more rigorous separation of the shock-cell noise from the jet mixing noise. The method used by Viswanathan *et al* [113] seems very promising for this scope, despite its complete applicability for supersonic coaxial jets must be assessed.

4.4 Conclusions

A PIV experimental investigation on a supersonic coaxial jet was done for the first time. The measurements were performed synchronously with microphones mounted on a polar antenna in the far field. Nine test conditions were analyzed with PIV and thirty six in total with microphones.

PIV mean flow fields were presented, showing a complex wake. Immediately after the secondary nozzle exit, the flow is accelerating supersonically, until a strong conical shock-wave is encountered at the lip of the primary nozzle. This confirms the CFD prediction, and it was found to be an important factor affecting both the primary and secondary streams, as well as the acoustics of the jet. In particular, the strong re-compression affects the primary mass flow rate and exit speed considerably, and it is thus a design factor for the engine manufacturers. The interaction between the conical shock-wave and the secondary stream is different while varying the FNPR. In particular starting from Cond.06, the length of the first shock-cell, the one bounded by the primary nozzle wall, is decreasing. When the length of this shock-cell is equal to the primary nozzle protrusion length, the conical shock-wave interacts with the expansion fan of the second shock-cell. This is the origin of a complex shocks pattern where expansion fans and shock-waves intersect in the secondary streams, leading to the acoustical effect to cancel the screech. Further investigation are advisable in order to assure if the screech suppression is occurring also at higher FNPR by simply changing the primary nozzle protrusion length.

The primary flow velocity appears to be modulated in space following the shock-cell pattern, becoming even supersonic in some instantaneous field. This modulation occurs until screech is onset. Afterwards, the influence of the secondary flow on the primary one is not visible anymore.

Turbulence axial and radial profiles for the different conditions were extracted, and nozzles core regions, and shear layer limits identified. Similarly to the single stream jet, the averaged Reynolds stress field shows the presence of lobes outside the shear layer. However, such lobes are disappearing when also screech disappears. Although this is not a definitive proof, it constitutes a strong evidence that these lobes are the trace of a standing wave caused by the jet modes exited by the screech.

The average shock-cell length were retrieved, and a new scaling law was deduced to make them collapse. Spatial Fourier transform was applied to the averaged profiles, finding the main peak wavelength to match the shock-cell length. Also in the Fourier space, the new scaling law was found appropriate to make all the curves collapse, and thus finding a characteristic non-dimensional wavelength, and a harmonic.

Acoustic results presents similarities with the classical single stream jet, like the screech and the directivity pattern of the BBSAN but also new features. The jet appears surprisingly quieter in comparison of a single stream jet with the same secondary nozzle diameter. The screech directivity pattern is also different from the single stream jet. Only the first harmonic is clearly visible, while a second one is present only at certain angles. Furthermore, depending on the test condition, also the main tone shows a peculiar directivity pattern, and at least in one case the presence of two screech tones was detected, showing the swap between the two. Screech tones may disappear completely in certain conditions. It is believed that this interaction of the shock-waves disrupt the feedback loop, thus it still unknown how. Eventually, this may also be caused by jet asymmetry, which is not negligible at lower pressure conditions.

An exploratory acoustic campaign with an extended test matrix was performed. The contour map of the Band Limited Overall Sound Power Level show a region where the noise is not monotonically increasing with the pressure, in agreement with previous literature. Analyzing the contribution to the BLOPWL of each angular direction, at high frequencies, it suggests certain combinations of parameters may cause a reduction of the jet mixing noise in the downstream direction. A more precise approach should pass by the separation of the shock-cell noise contribution from the jet mixing noise, using methods already present in the literature.

Chapter 5

Inference of Screech-Induced Fluctuations from the Correlation Maps

The correlation maps presented in Sec. 3.5.3.2, have been already used in the literature to compare the integral length scales among different experiments. A new methodology is proposed here to interpret these graphs and infer the jet screech dynamics. Normally, this would be not trivial, or even impossible, because the source information is not time resolved, and therefore doubts on its reliability as investigation method, may arise. However, hypothesis can be made to support the methodology, which are:

- The dynamics is periodic over the sampling time;

- The periodic fluctuations must contain the majority of the turbulence kinetic energy;

The first condition is necessary and sufficient. It is necessary because if there is no periodicity, it makes no sense to talk about jet random dynamics, if not to describe statistical quantities. It is sufficient because, despite the acquisition is not time-resolved, a periodic fluctuation would always lead to high level of correlation among two points affected by the same periodic fluctuation. Furthermore, for wave-kind fluctuations, zones of positive and negative correlation must be present. In this light, all the non-periodic fluctuations would then reduce the correlation level. Hence, the second hypothesis: having most part of the energy in the periodic fluctuation would help in maintaining high the correlation level. This simply because the decrease of correlation due to the random fluctuations contribution would be limited.

Finally, it would be helpful, of course, to have large correlation zones it could be possible to infer the overall motion of the flow. All such conditions could be found in a screeching jet, which have been extensively studied in the past, and therefore, results can be compared to validate the methodology. A simple approach would then be discussed here, which aims to extend the screech knowledge for the coaxial jet case, where, instead, there are no examples in the literature.

5.1 Single Stream Jet

The case of a jet at CNPR = 2.70, M_j = 1.28 is studied. The evolution of the correlation functions along the lip line for R_{11} and R_{22} are shown in Figs. 5.1 and 5.2. The red X represent the point where the correlation refers to, belonging to the shear layer at r/D = 0.5. Black lines and white lines correspond to positive and negative correlation respectively. Negative correlation means that when in the point on the red X there is a positive fluctuation in the considered direction, in the correlated point the fluctuation is negative.

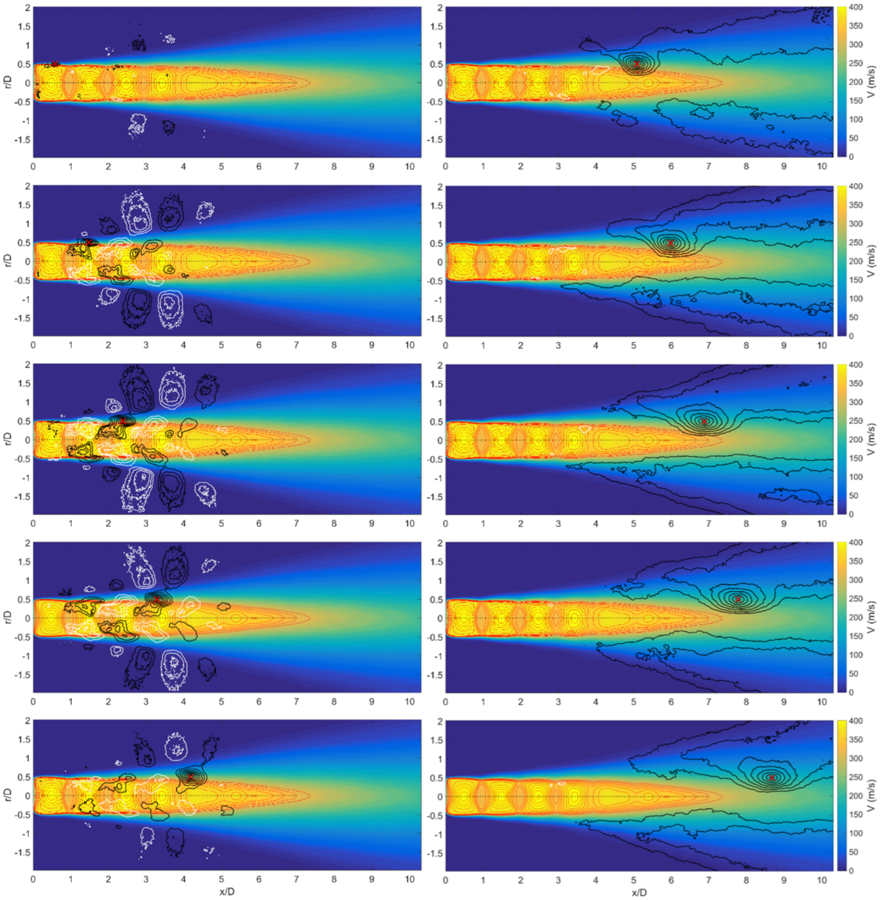

Figure 5.1: Image sequence showing the contours of the correlation function R_{11} along the horizontal line r/D = 0.5 for CNPR = 2.70. Black lines and white lines correspond to positive and negative correlation respectively, ranging from $0.2 \leq |R_{11}| \leq 1$.

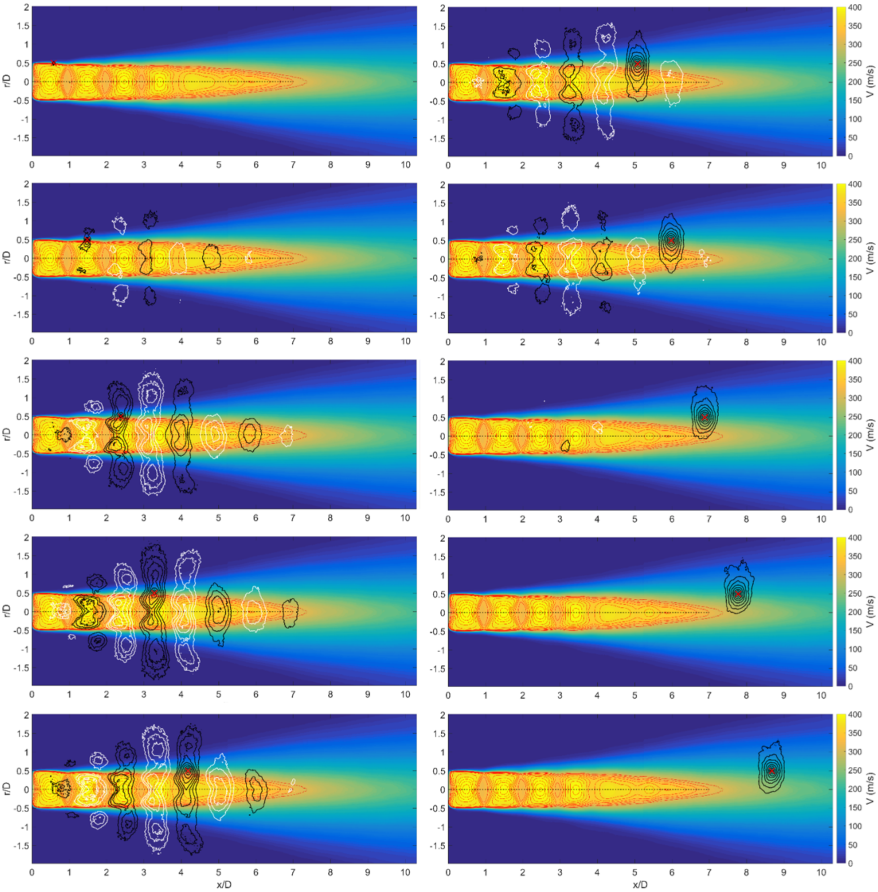

Figure 5.2: Image sequence showing the contours of the correlation function R_{22} along the horizontal line $r/D = 0.5$ for CNPR = 2.70. Black lines and white lines correspond to positive and negative correlation respectively, ranging from $0.2 \leq |R_{22}| \leq 1$.

This does not mean that in a specific zone there are only negative or positive fluctuations, but simply that, most of the time, they have opposite signs. The contour values range between $0.2 \leq |R| \leq 1$. Red lines represent $M \geq 1$ isocontours. We can observe the existence of pattern for both the axial and radial component autocorrelation. Initially, positive and negative correlations coexist, and lobes are visible outside the shear layer, until the end of the supersonic region. After that point, the pattern become more confused. For R_{11} extended regions with low correlation values are present, and smaller high correlated areas. For R_{22}, on the contrary, only circumscribed zones are present in the wake.

Following the concept of positive and negative fluctuations, a sample

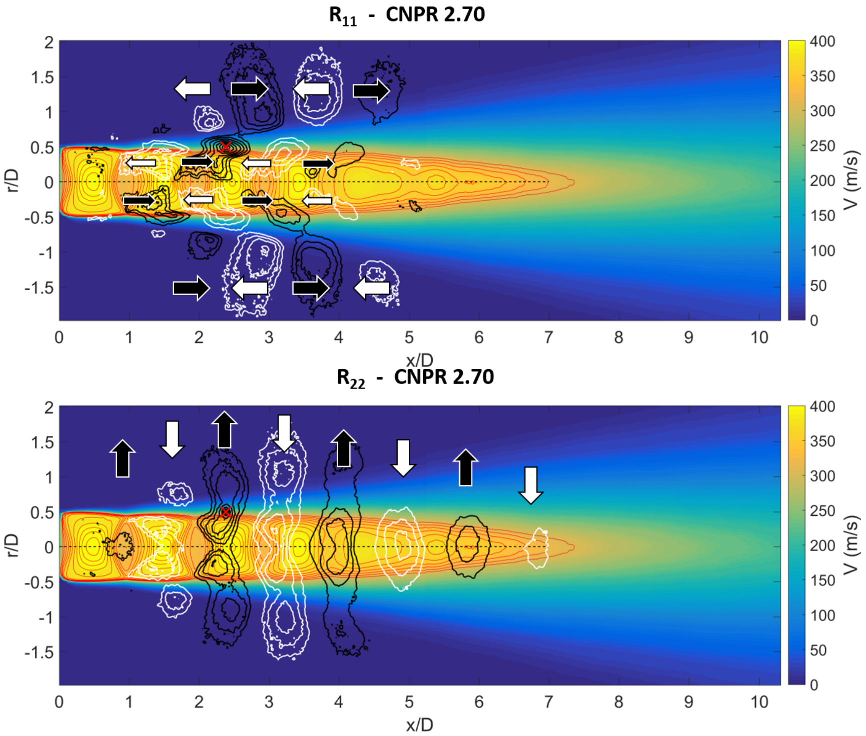

Figure 5.3: Contours of the correlation function R_{11} (top) and R_{22} for the point located in the red X for $M_j = 1.28$. Black lines and white lines correspond to positive and negative correlation respectively, ranging from $0.2 \leq |R| \leq 1$. Red lines represent $M \geq 1$ isocontours. Black and white arrows represent positive and negative velocity fluctuations respectively.

image has been chosen, and black and white arrows were superimposed to highlight the overall motion (Fig. 5.3). As stated previously, higher correlation value means that a fluctuation in not random, but is repetitive and periodic among the instantaneous flow fields, which are decorrelated one from each other, because of low acquisition rate (compared to the screech dynamics). High correlation values coupled with extensive region can be interpreted as a macroscopic movement, or a scheme. For both the R_{11} and R_{22} cases, it is evident how a very large region of the flow is correlated with the point marked with the red X. Starting with the radial direction, we can infer a sinusoidal motion of the jet, because when in X there is a positive fluctuation, a large jet zone follows it, while contiguous zones have negative fluctuations. This motion is correlated also with velocity fluctuation outside the shear layer, shaped as alternated lobes. It is not known at this time

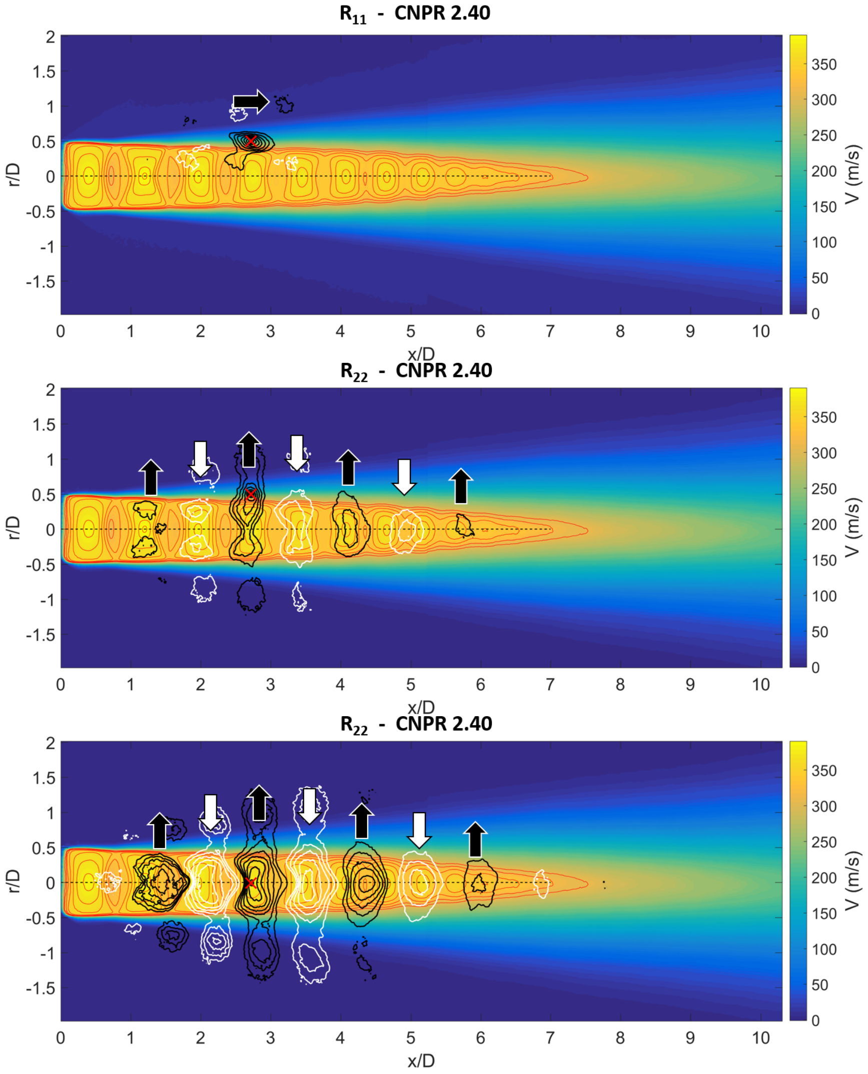

Figure 5.4: Contours of the correlation function R_{11} and R_{22} for the point located in the red X for $M_j = 1.19$. Black lines and white lines correspond to positive and negative correlation respectively, ranging from $0.2 \leq |R| \leq 1$. Red lines represent $M \geq 1$ isocontours. Red lines represent $M \geq 1$ isocontours. Black and white arrows represent positive and negative velocity fluctuations respectively.

if these lobes are related to the screech standing waves or to the traveling hydrodynamic fluctuations. Further studies are necessary to answer to this

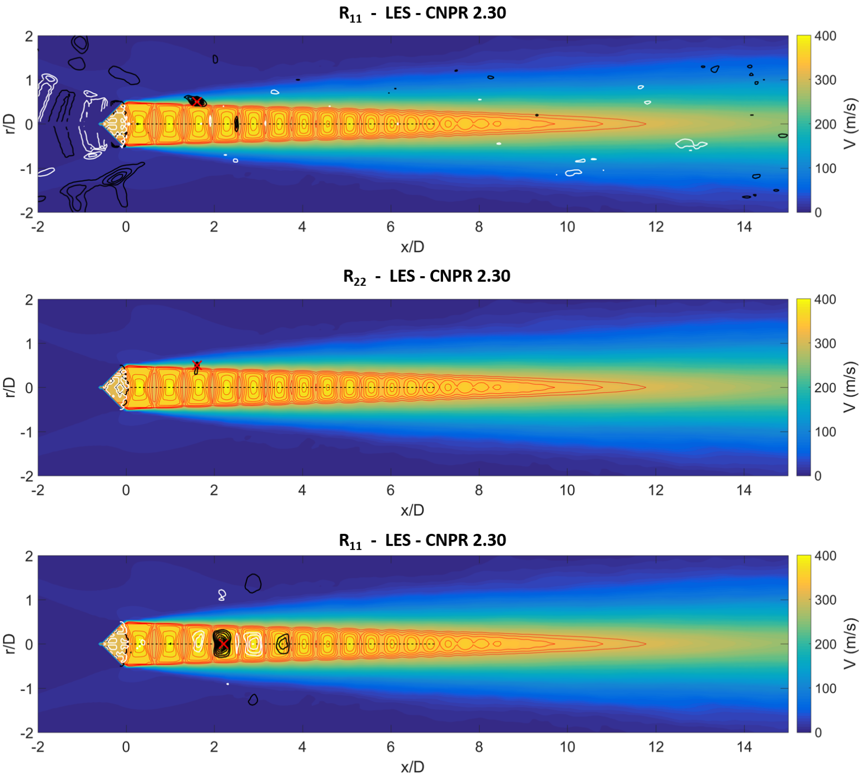
R_{11} - LES - CNPR 2.30

R_{22} - LES - CNPR 2.30

R_{11} - LES - CNPR 2.30

Figure 5.5: Contours of the correlation function R_{11} and $R_{22}$for the point located in the red X for $M_j = 1.16$. Black lines and white lines correspond to positive and negative correlation respectively, ranging from $0.2 \leq |R| \leq 1$. Red lines represent $M \geq 1$ isocontours. Black and white arrows represent positive and negative velocity fluctuations respectively.

question. For the axial direction, it is also possible to infer a sinusoidal or flapping motion due to the combination of positive and negative fluctuations. It is interesting to note that the lobes outside the shear layer are not aligned with the correlated supersonic regions, which show an elongated shape in the axial direction. From the recorded acoustic measurements, the screech mode lays on the boundary between the sinusoidal mode (B) and the helical mode (C). Unfortunately, the standard PIV technique does not consent to know the azimuthal velocity component, which would definitely solve the ambiguity.

If the dynamics is helical, both for the radial and axial fluctuations the motion would be periodic, and thus would lead to higher autocorrelation for both velocity components. A particular case is the sinusoidal dynamics, laying in a fixed plane, which is the superposition of two helical modes with opposite sign wavenumbers. Also in this case, the autocorrelation of both axial and radial velocity component between two points, belonging to the same wave, would be high. For sinusoidal oscillations in a random plane, instead, it is expected the velocity autocorrelation to drop due to the randomness of the flapping plane.

For $M_j = 1.19$, the correlation maps are shown in Fig. 5.4. The axial component shows a pattern typical for random fluctuations, which have indeed a certain extension in space, but does not represent any jet dynamics. For the radial component, instead, we could still visualize large correlated zones with alternated sign, especially in the centerline. Knowing from the literature that this screech mode is pure flapping (aka sinusoidal mode (B)), it is possible to find confirmation of the aforementioned assumptions.

It is important to remind, however, that until this point, there are no proof that the oscillation schemes retrieved so far are associated with the screech, or with the BBSAN, for instance. To verify this, the same analysis on a non-screeching jet was done. It has been decided to chose a numerical database coming from LES simulations carried out by Pérez Arroyo *et al*[68], with CNPR = 2.3 and $M_j = 1.16$. A comparison of the far field acoustic spectra for the numerical database and two experimental databases (from VKI and André), is presented in Fig. 5.5, showing good agreement for the BBSAN, but no screech. Fig. 5.5 shows the correlation maps for the LES simulation. There are no clearly visible patterns or schemes, but only the extension of the coherent turbulence structures around the correlated point. Fig. 5.6, instead, depicts the correlation maps for the PIV experiments. From the literature, the screech should correspond to the axisymmetric mode (A2), and the images seem to confirm this result.

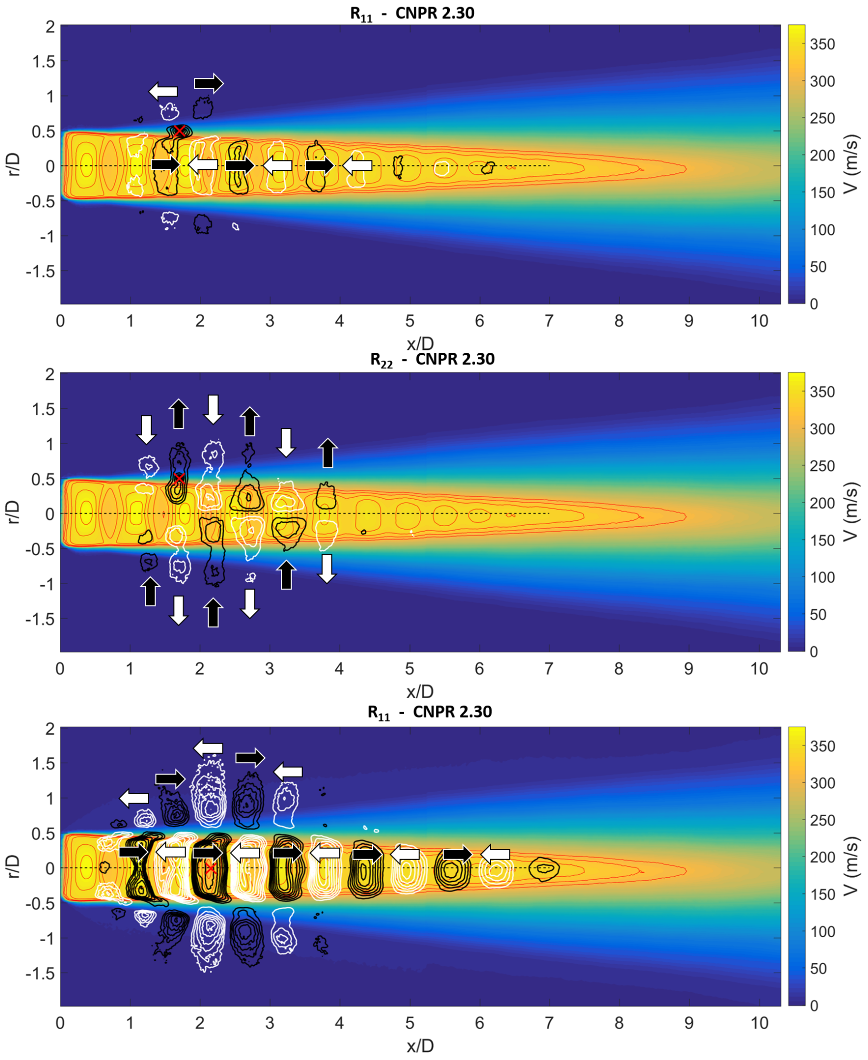

Figure 5.6: Contours of the correlation function R_{11} and R_{22} for the point located in the red X for $M_j = 1.16$. Black lines and white lines correspond to positive and negative correlation respectively, ranging from $0.2 \leq |R| \leq 1$. Red lines represent $M \geq 1$ isocontours.. Black and white arrows represent positive and negative velocity fluctuations respectively.

5.2 Dual Stream Jet

The same approach was used to identify screech modes for the coaxial flow. Because of the decorrelated set of images, the initial and final part of the plume were studied separately. For the coaxial flow, two shear layers are present, and thus the correlation was computed along four lines, corresponding to the upper and lower half of the jet, plus the centerline. If one considers all the possible different correlations, two autocorrelations: R_{11} and R_{22} and two cross-correlations: R_{12} and R_{21}, one may obtain 20 different correlation map evolutions for each test condition. To evidence the very particular behavior of the coaxial jet, compared to the single stream jet, all those map evolutions for Cond.01 are shown in Sec. 5.2.1. Concerning the screech analysis, for brevity, only few significant correlation maps will be shown to evidence the jet behavior.

From the acoustic data, three distinct behaviors were observed (Fig. 5.7). From Cond.01 to Cond.04 the screech frequency showed a very small change in frequency. This is due to the shortening of the shock-cells, similarly to the single stream jet. Cond.05 exhibits two screech tones, one similar to the previous cases, and a second, stronger, tone at higher frequency. From Cond.07 no screech tone is observed anymore. The relative correlation maps do not present any recognizable pattern, and they will not be shown.

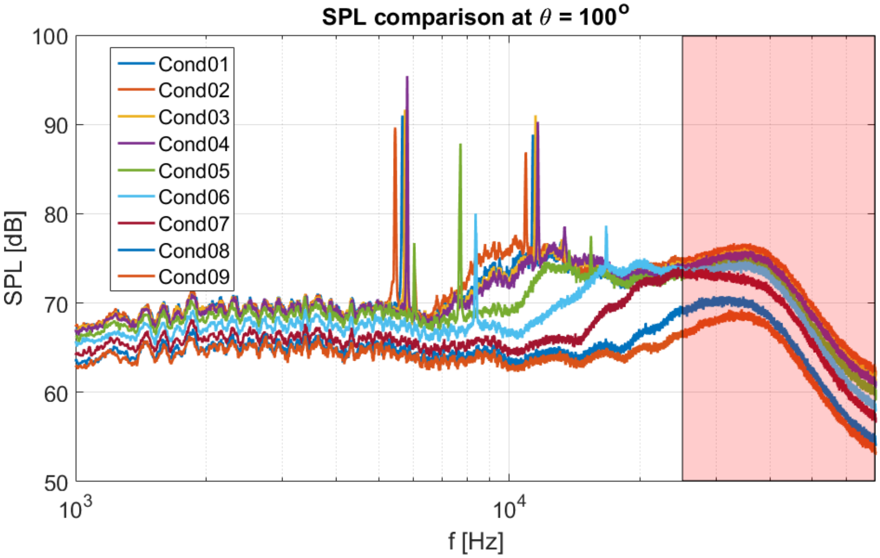

Figure 5.7: Spectra comparison at $\theta = 100^o$ for all the tested conditions with PIV. The area evidenced in red is polluted by the presence of the microphone protective grid.

5.2.1 Correlation Maps for Cond.01: : FNPR = 2.45, CNPR = 1.67.

In this section, it is shown the evolution of the correlation maps, in function of the position of the reference point. As reminder, the subscript 1 refers to the axial velocity component, and the subscript 2 to the radial velocity component. R_{11} and R_{22} are thus the two autocorrelation functions, and R_{12} and R_{21} are the cross correlation functions. Each correlation evolution accounts for 10 maps evaluated along lines parallel to the jet axis direction. The reference point is indicated with a red X on the map. Black lines and white lines correspond to positive and negative correlation respectively, ranging from $0.2 \leq |\mathrm{R}| \leq 1$. Red lines represent $\mathrm{M} \geq 1$ isocontours. Black and white arrows represent positive and negative velocity fluctuations respectively. The maps are ordered in columns, following a top-down sequence in the figure.

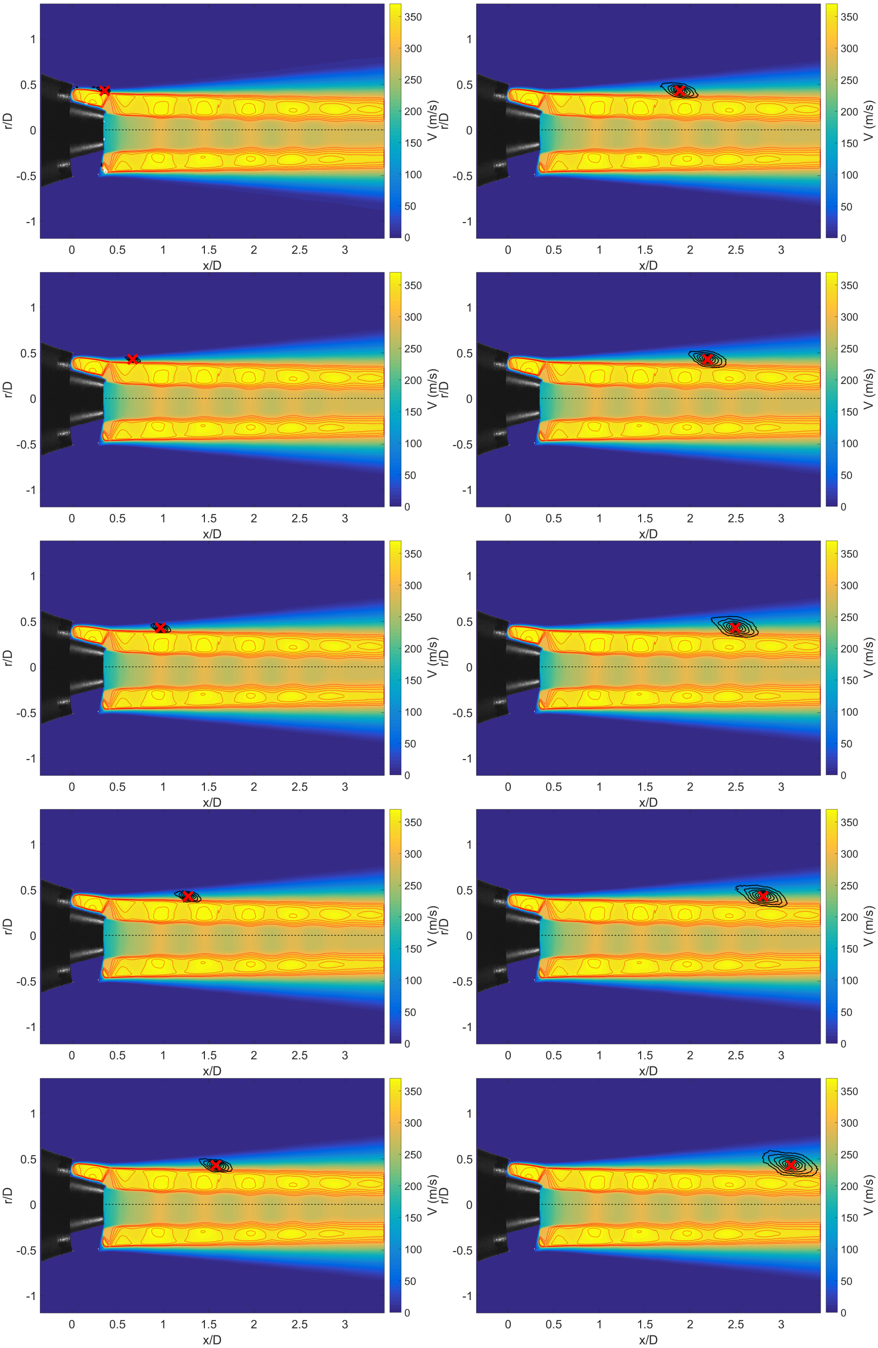

Figure 5.8: Image sequence showing the contours of the correlation function R_{11} along the horizontal line r/D = 0.427 for condition 01.

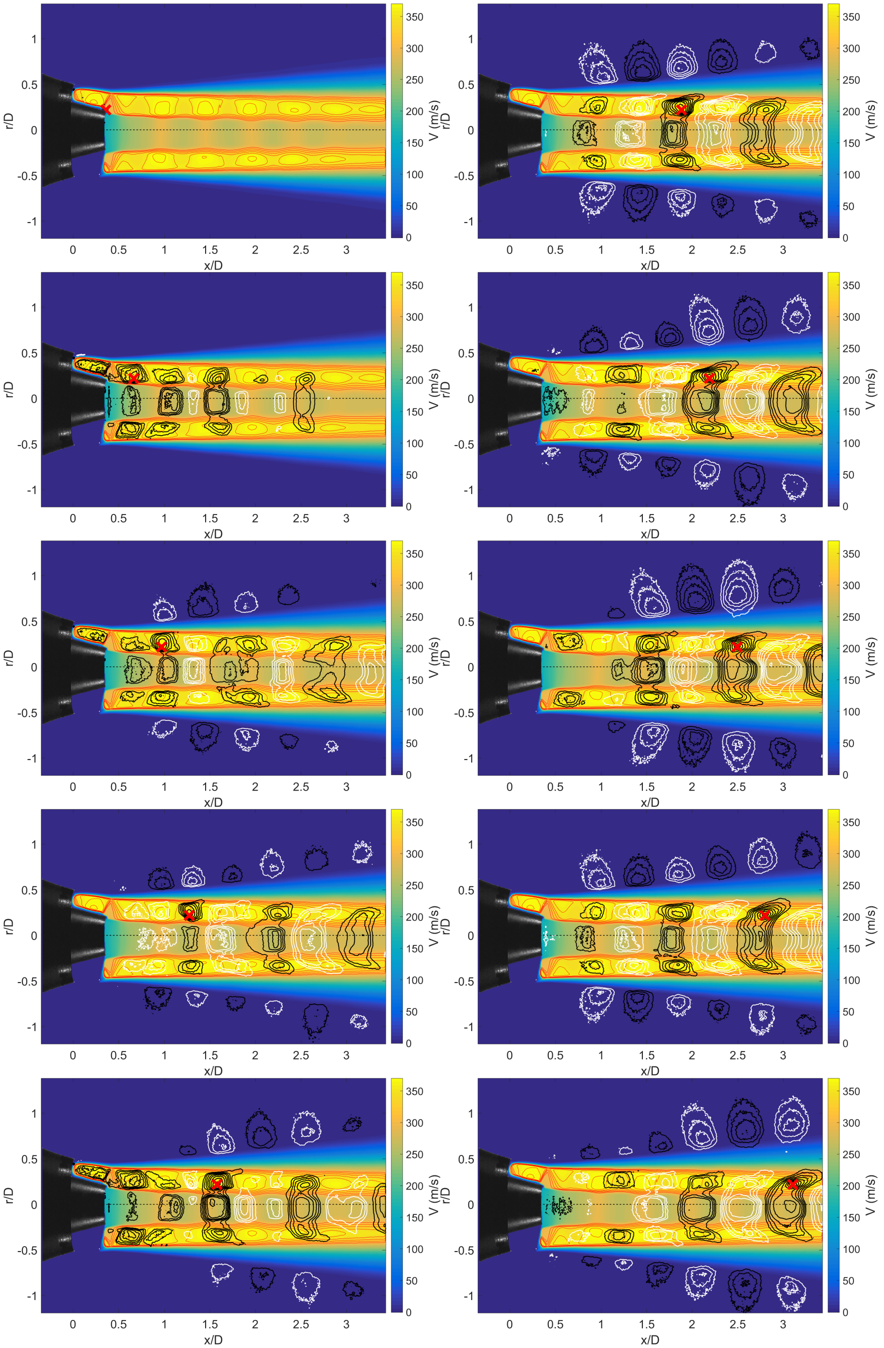

Figure 5.9: Image sequence showing the contours of the correlation function R_{11} along the horizontal line $r/D = 0.218$ for condition 01.

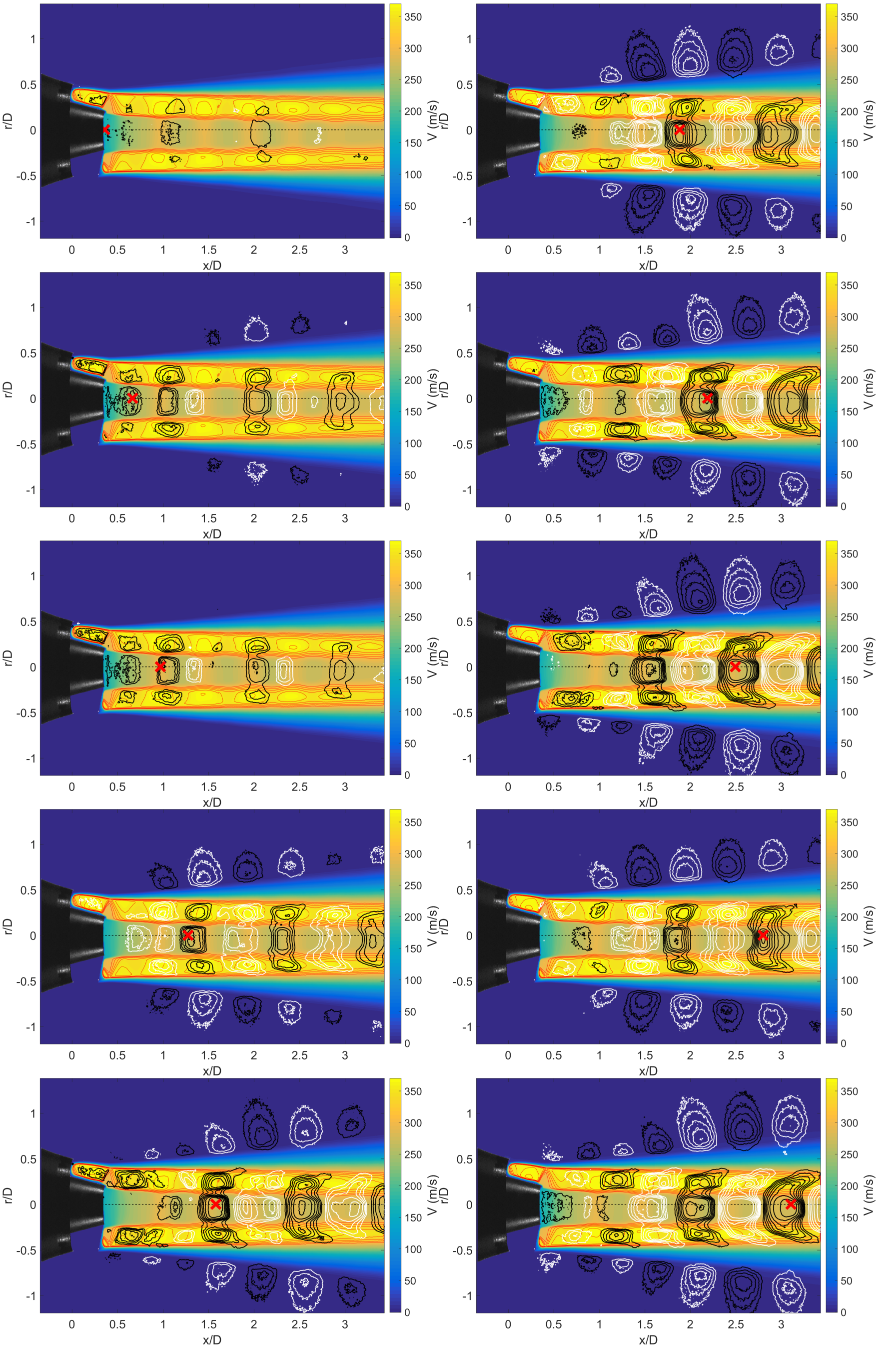

Figure 5.10: Image sequence showing the contours of the correlation function R_{11} along the horizontal line r/D = 0 for condition 01.

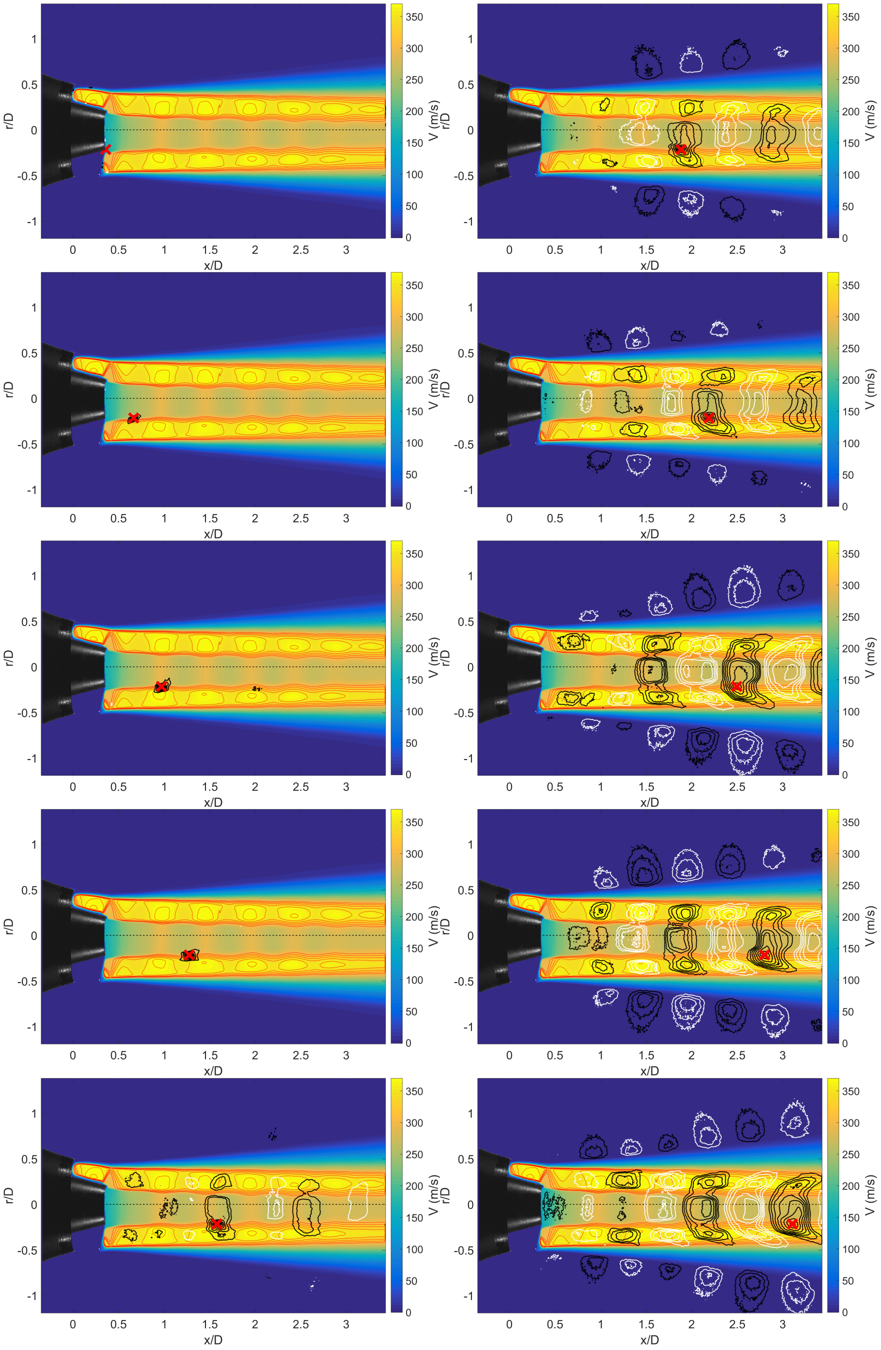

Figure 5.11: Image sequence showing the contours of the correlation function R_{11} along the horizontal line r/D = -0.218 for condition 01.

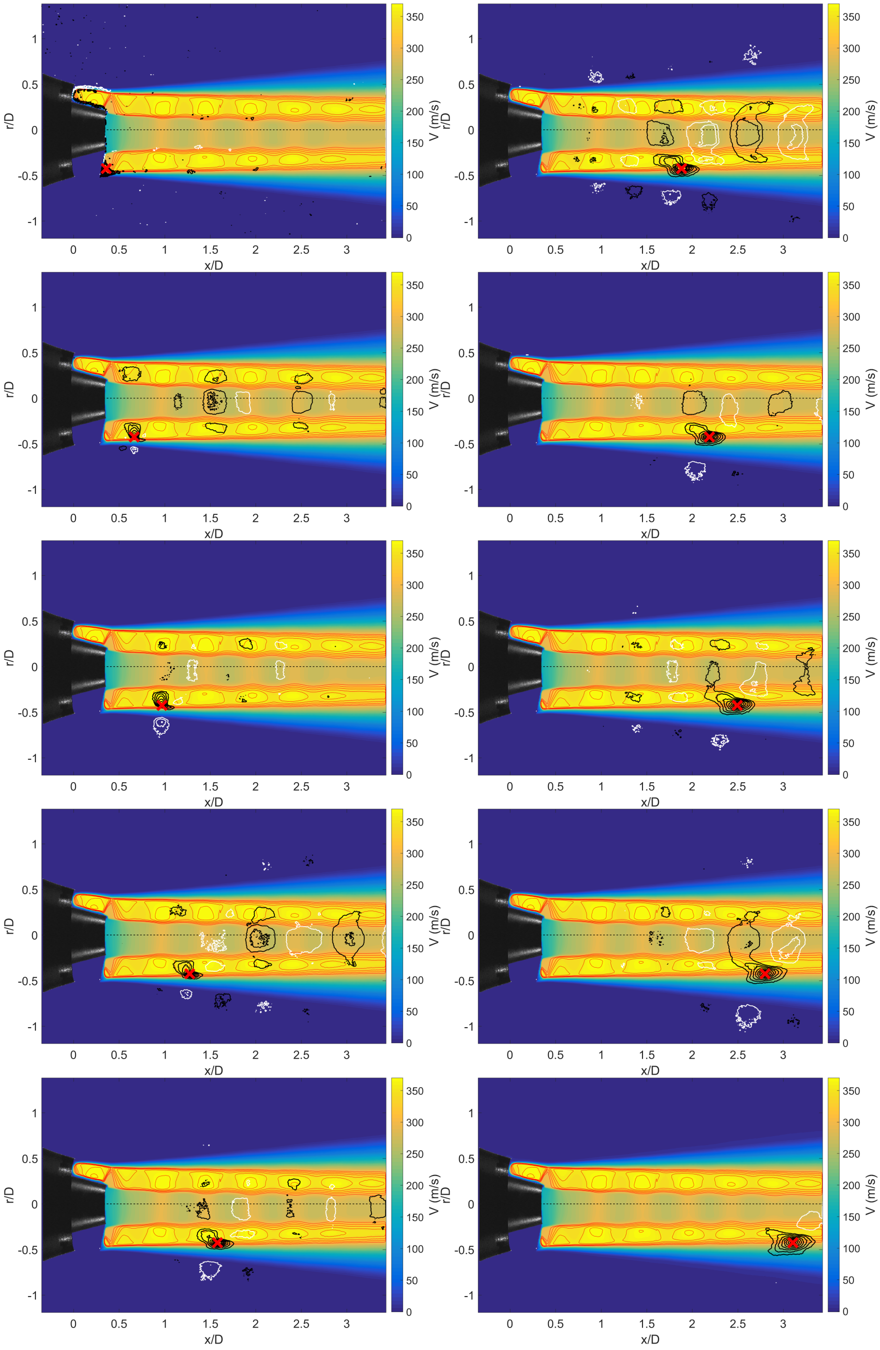

Figure 5.12: Image sequence showing the contours of the correlation function R_{11} along the horizontal line r/D = -0.427 for condition 01.

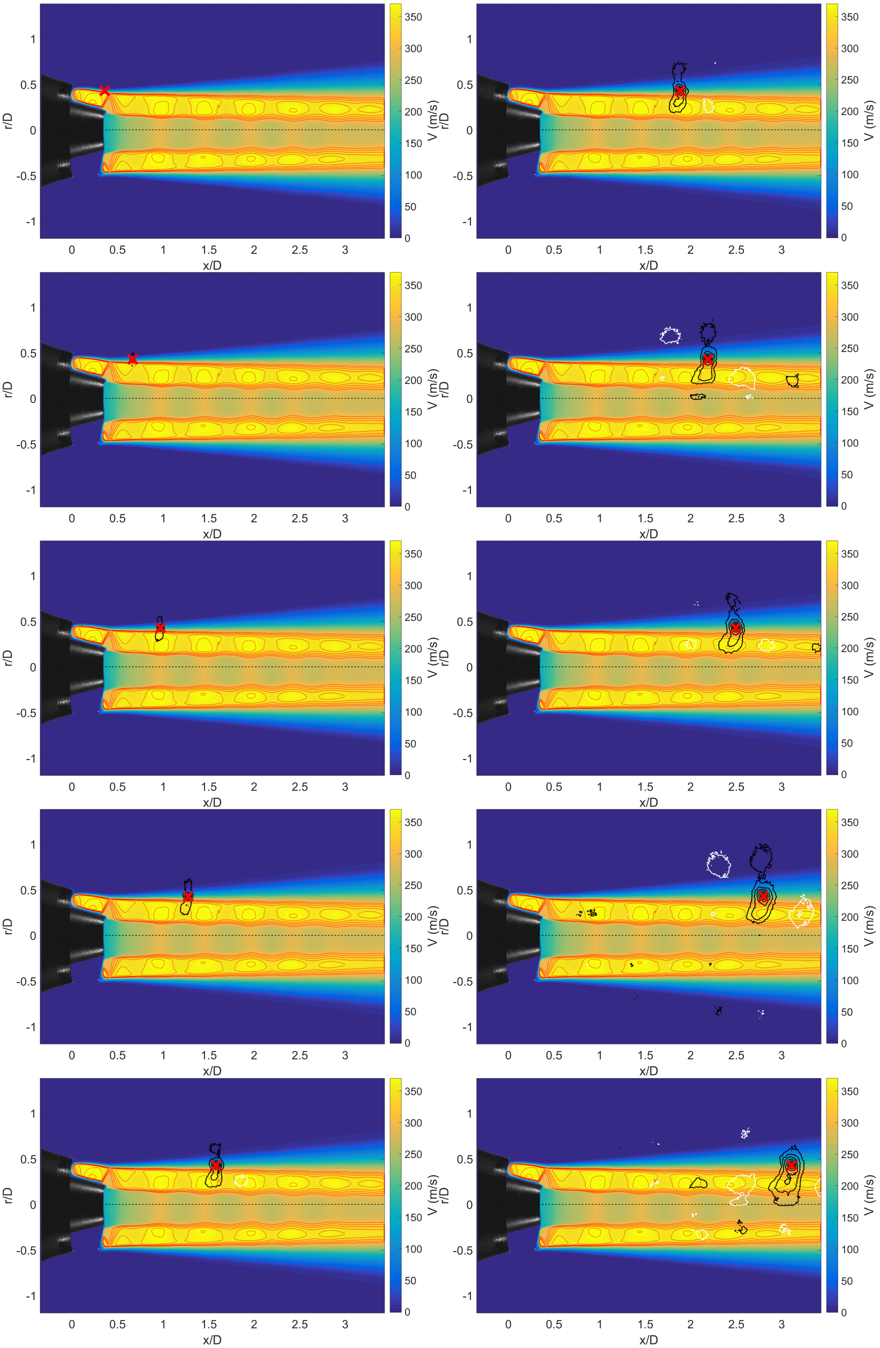

Figure 5.13: Image sequence showing the contours of the correlation function R_{22} along the horizontal line $r/D = 0.427$ for condition 01.

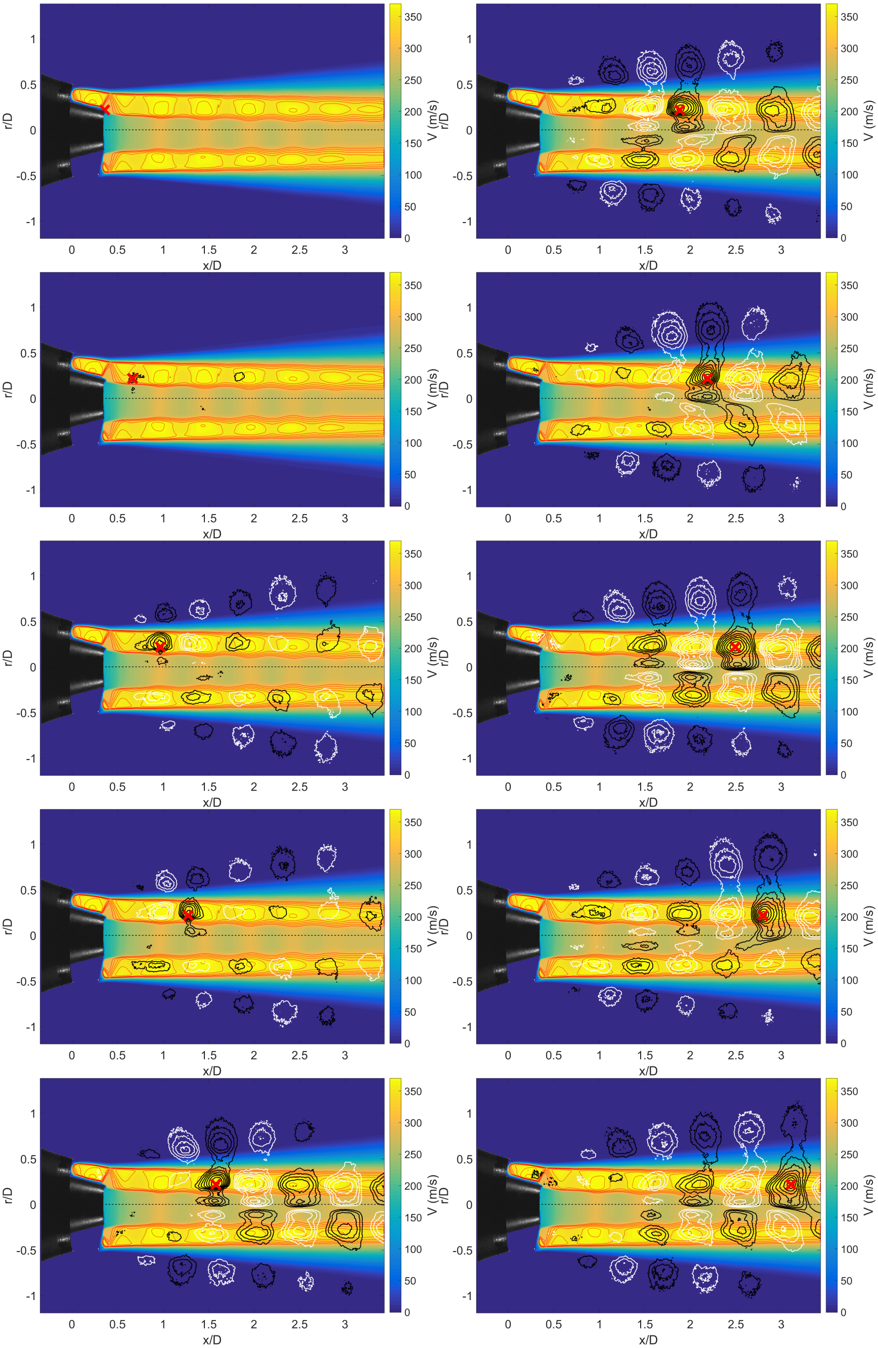

Figure 5.14: Image sequence showing the contours of the correlation function R_{22} along the horizontal line r/D = 0.218 for condition 01.

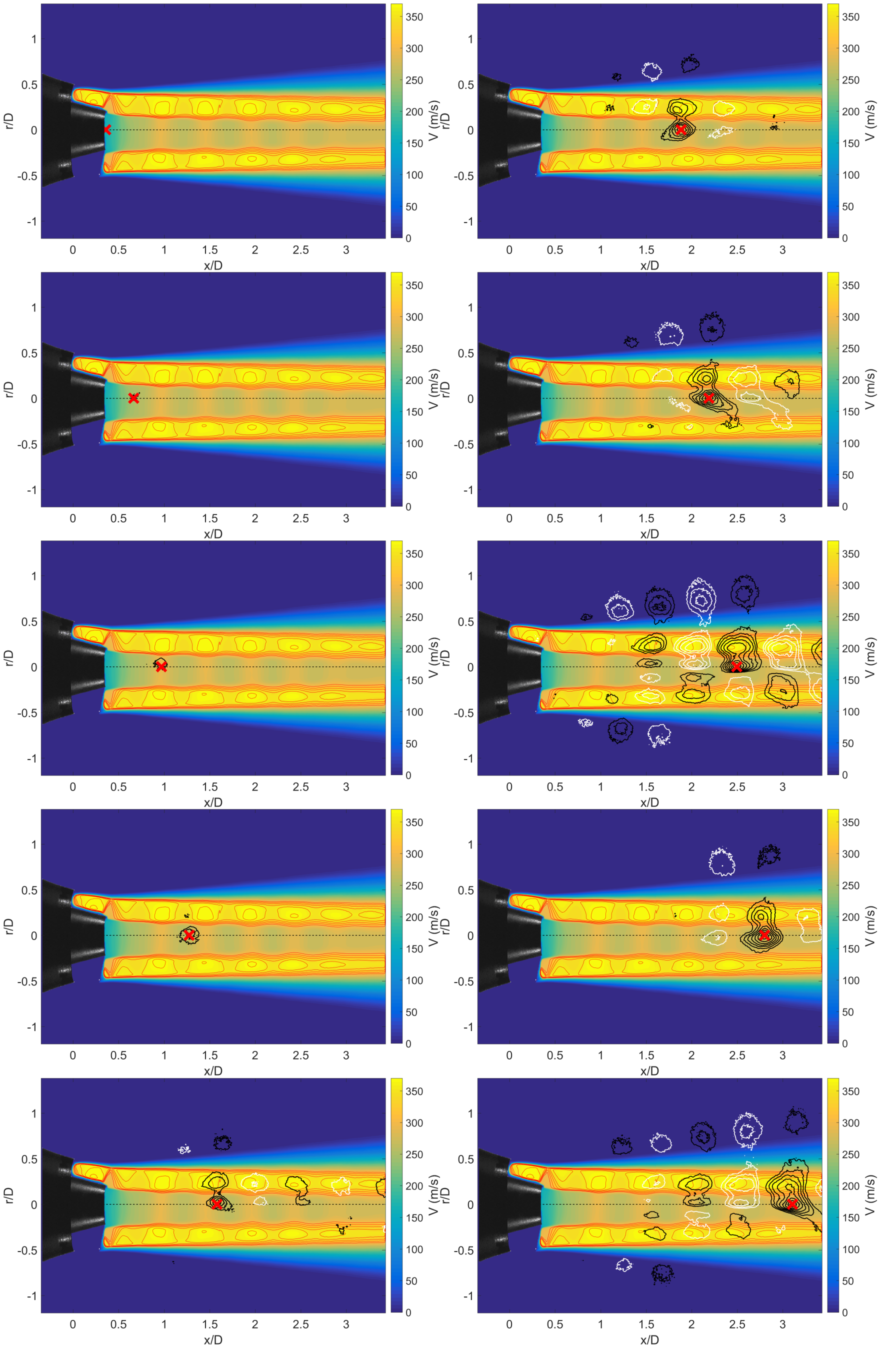

Figure 5.15: Image sequence showing the contours of the correlation function R_{22} along the horizontal line $r/D = 0$ for condition 01.

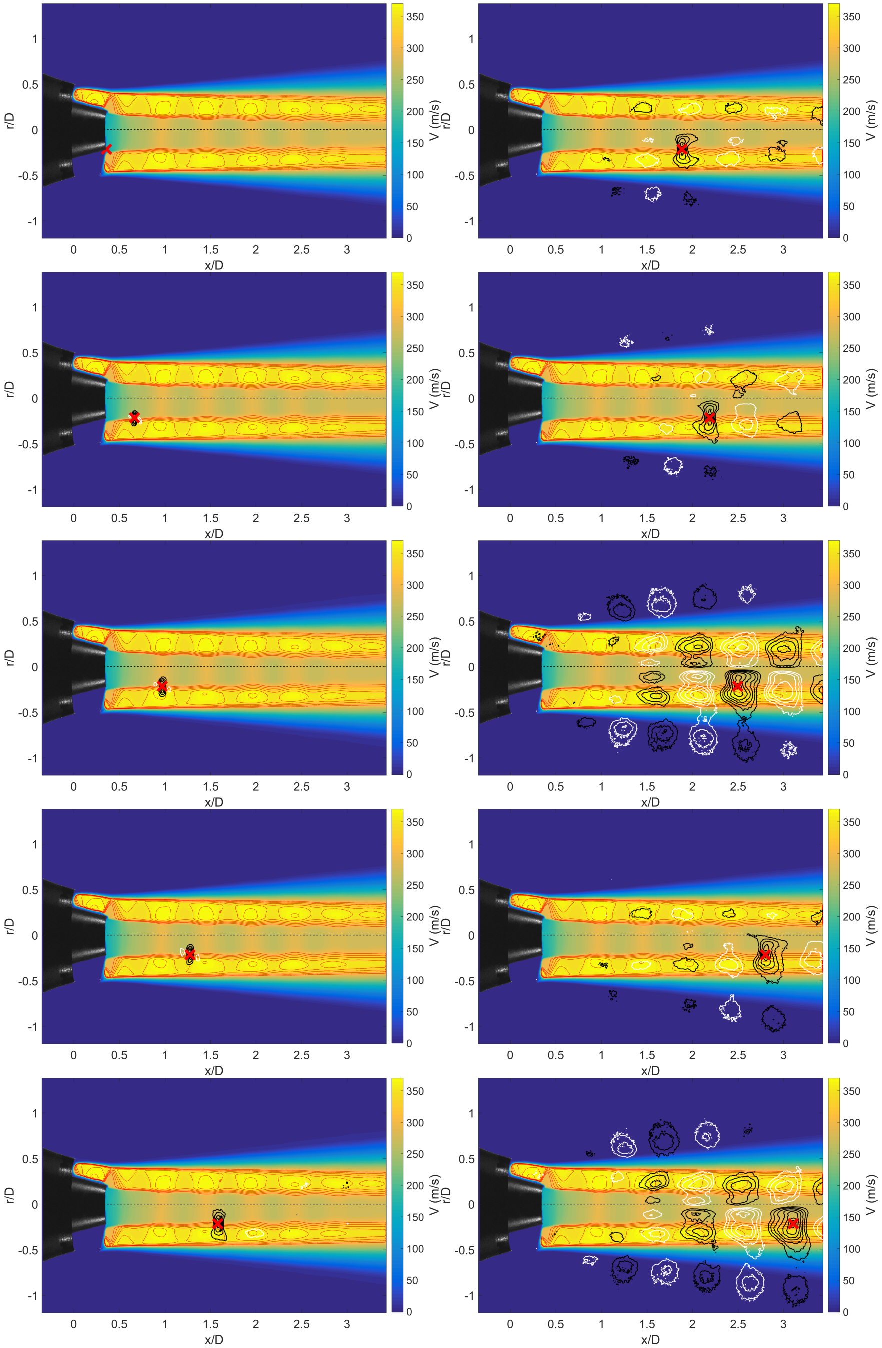

Figure 5.16: Image sequence showing the contours of the correlation function R_{22} along the horizontal line r/D = -0.218 for condition 01.

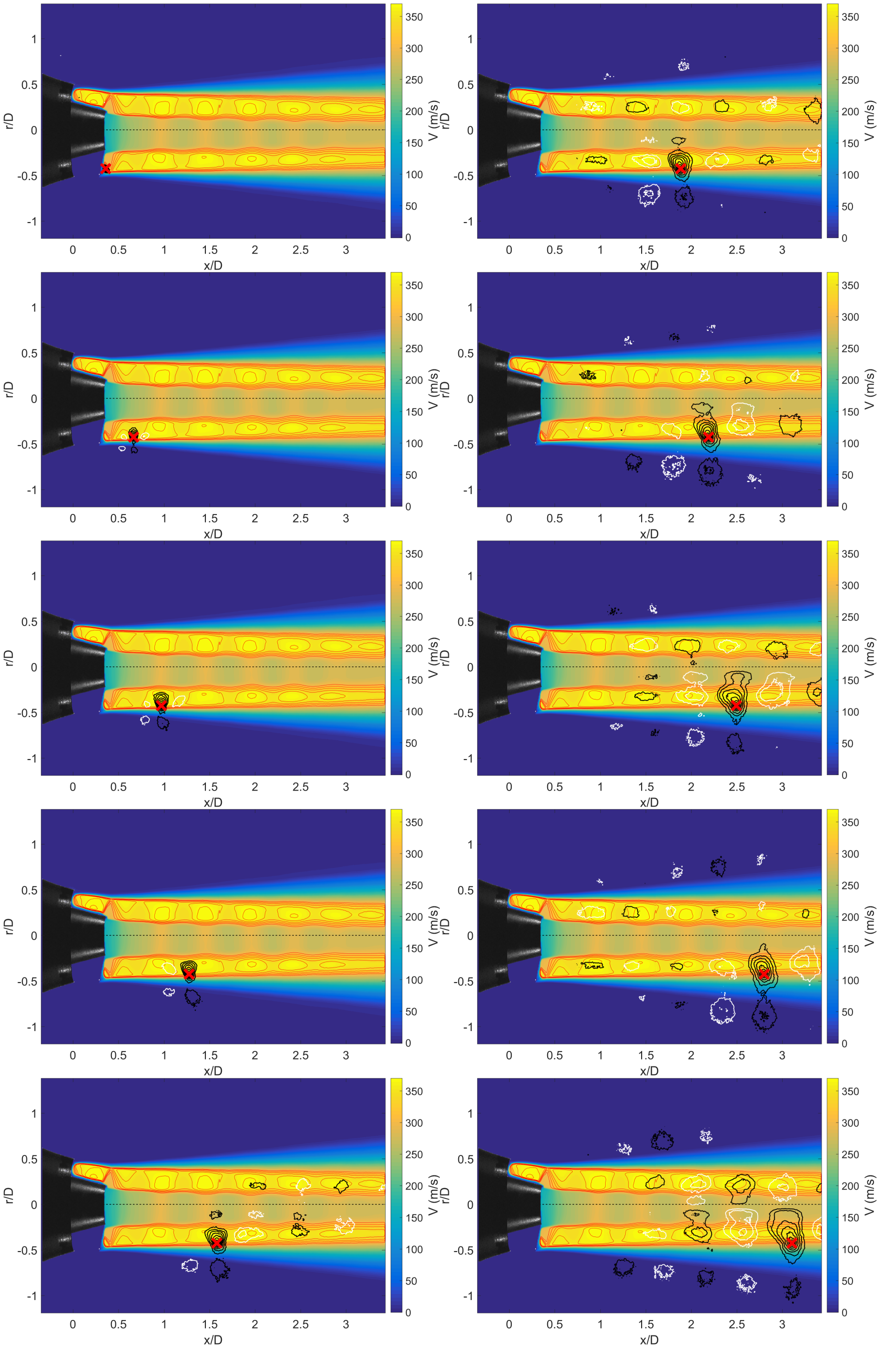

Figure 5.17: Image sequence showing the contours of the correlation function R_{22} along the horizontal line r/D = -0.427 for condition 01.

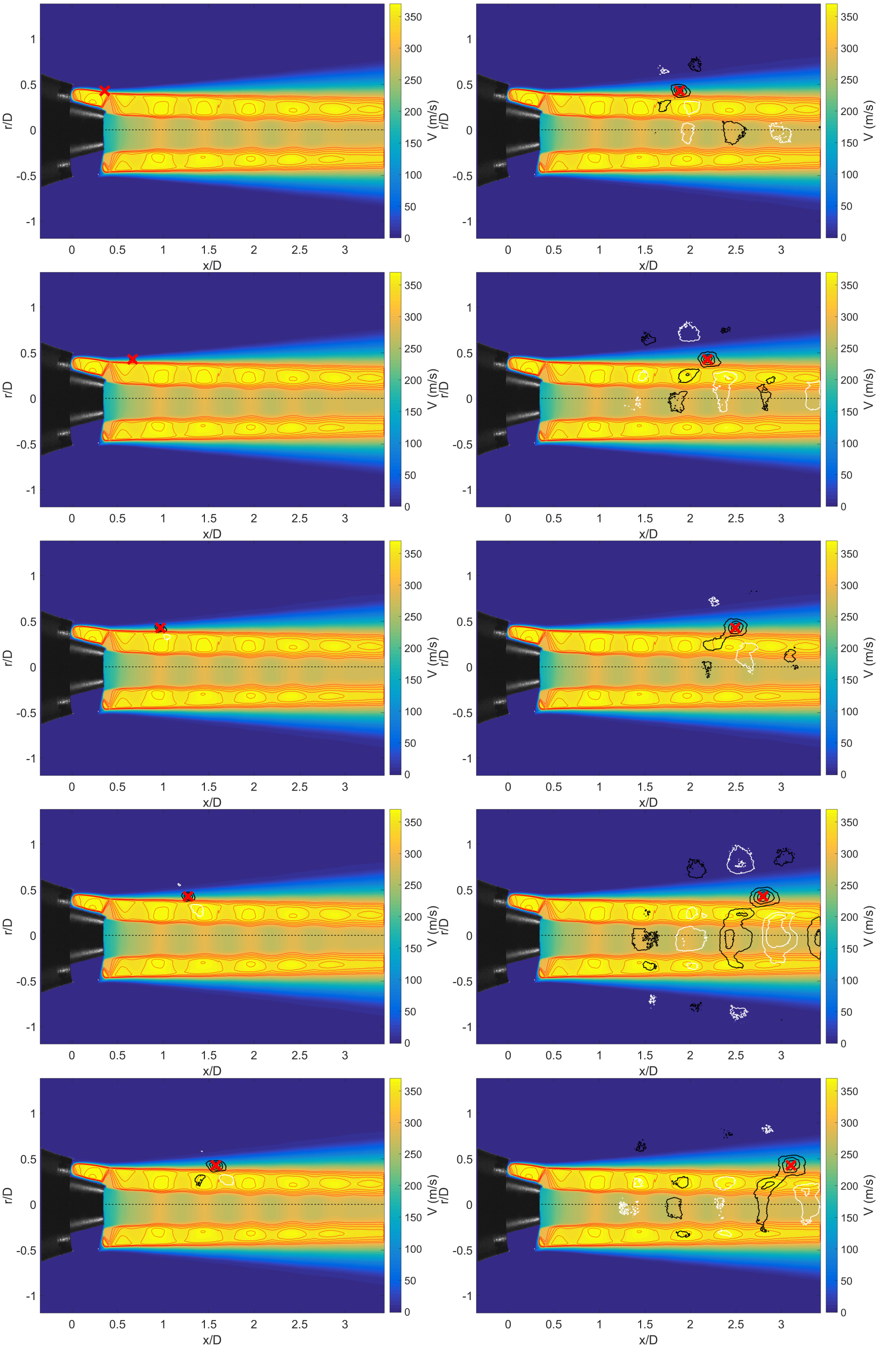

Figure 5.18: Image sequence showing the contours of the correlation function R_{21} along the horizontal line $r/D = 0.427$ for condition 01.

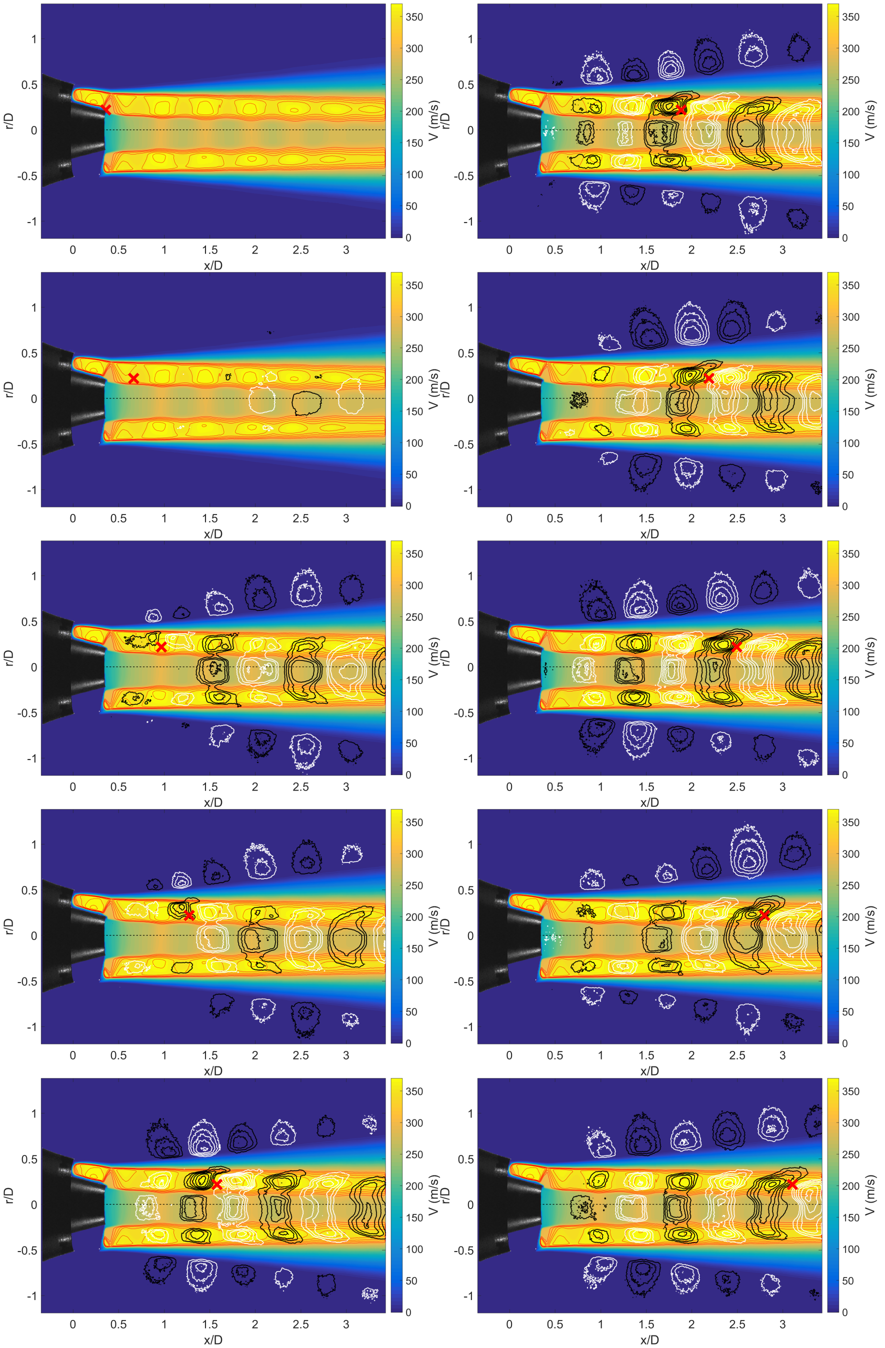

Figure 5.19: Image sequence showing the contours of the correlation function R_{21} along the horizontal line $r/D = 0.218$ for condition 01.

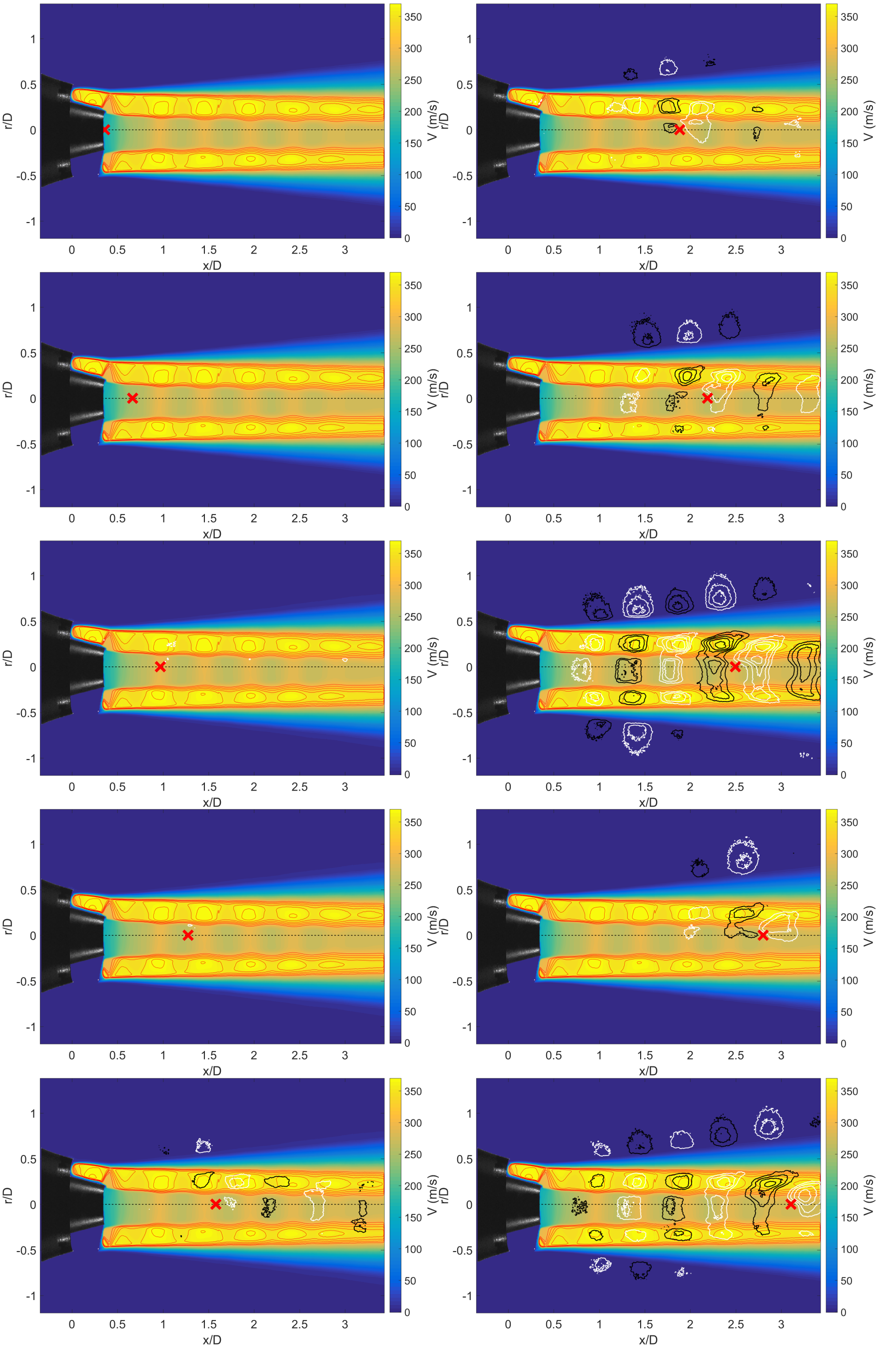

Figure 5.20: Image sequence showing the contours of the correlation function R_{21} along the horizontal line $r/D = 0$ for condition 01.

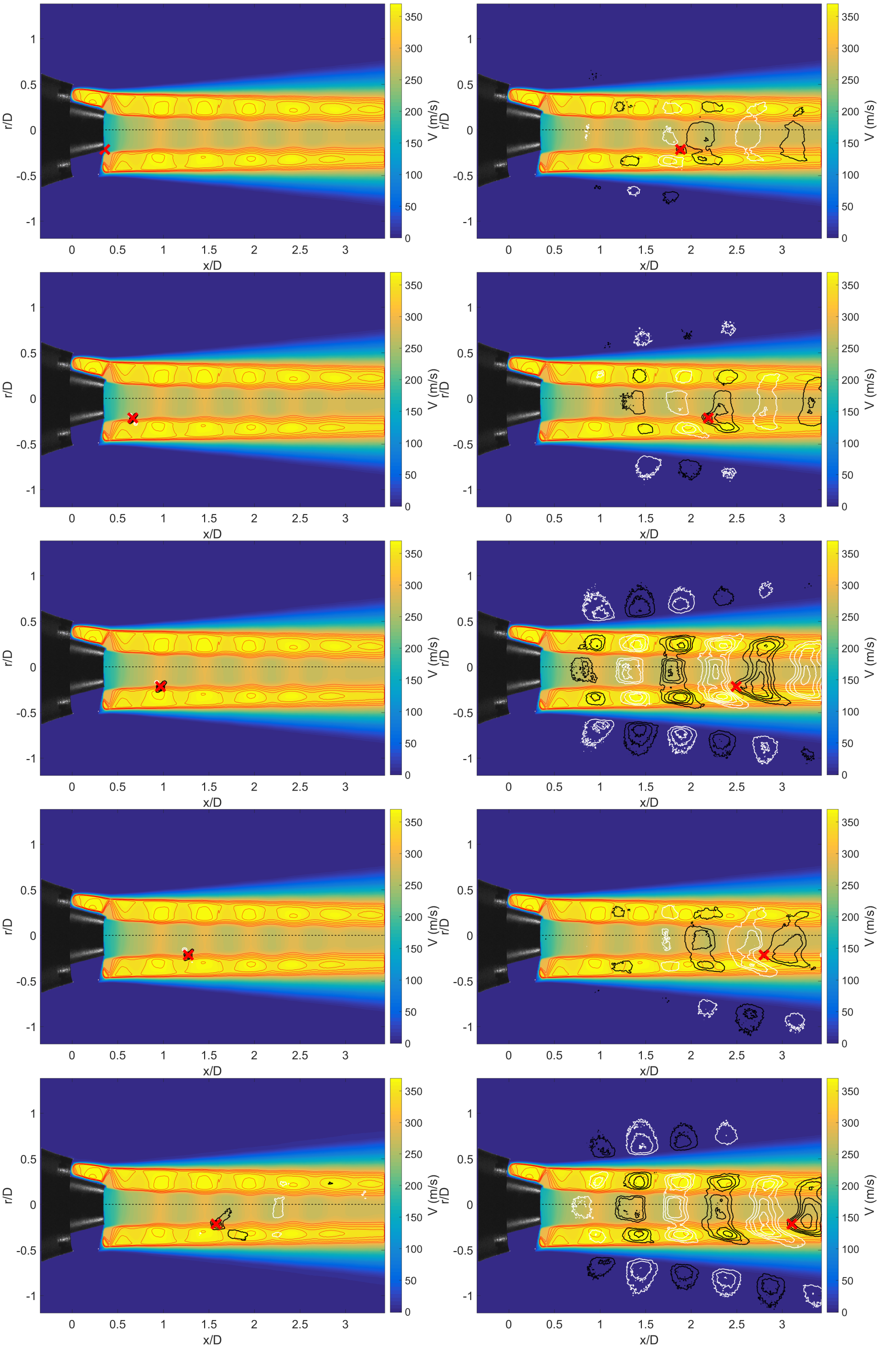

Figure 5.21: Image sequence showing the contours of the correlation function R_{21} along the horizontal line r/D = -0.218 for condition 01.

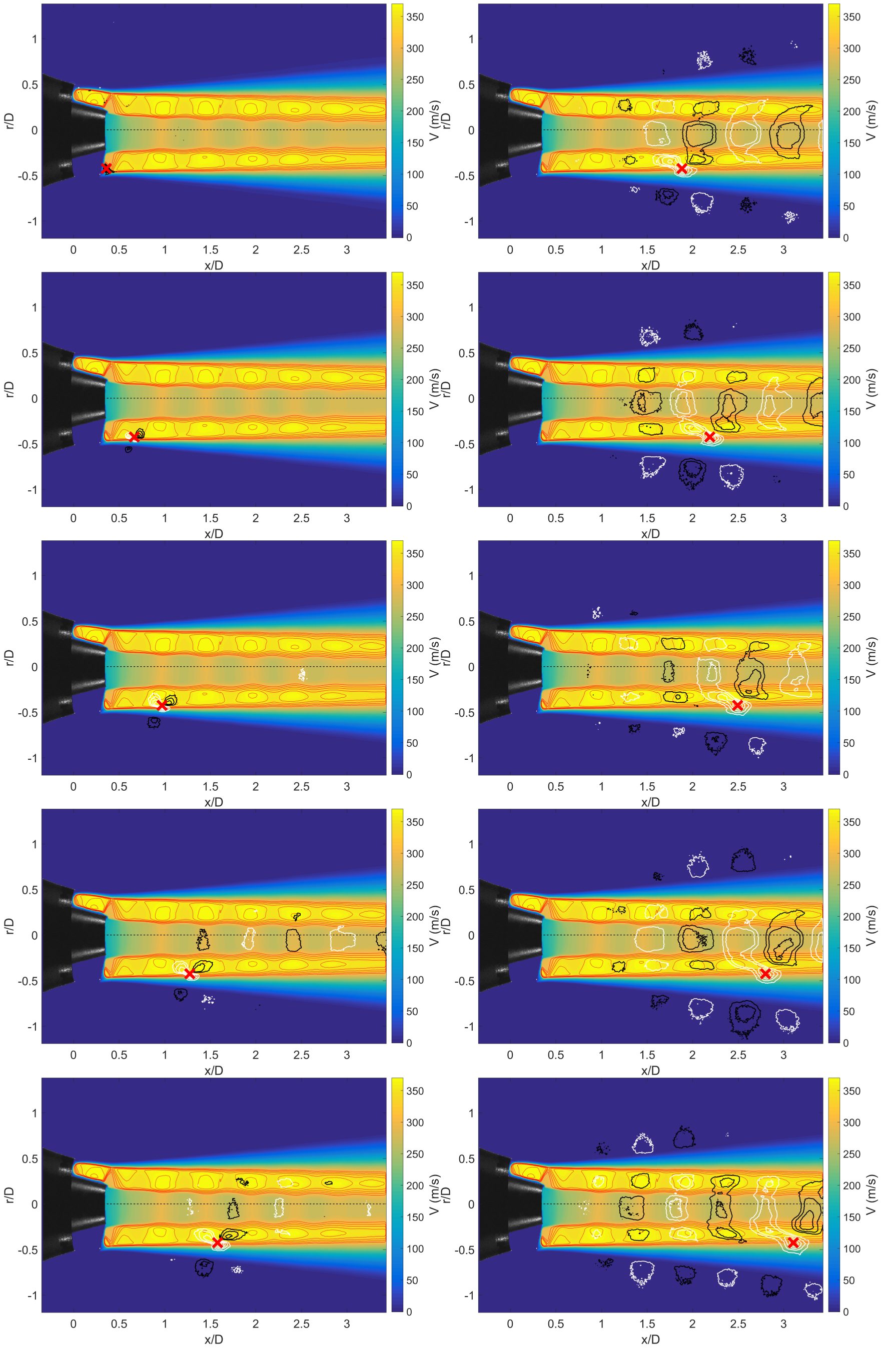

Figure 5.22: Image sequence showing the contours of the correlation function R_{21} along the horizontal line r/D = -0.427 for condition 01.

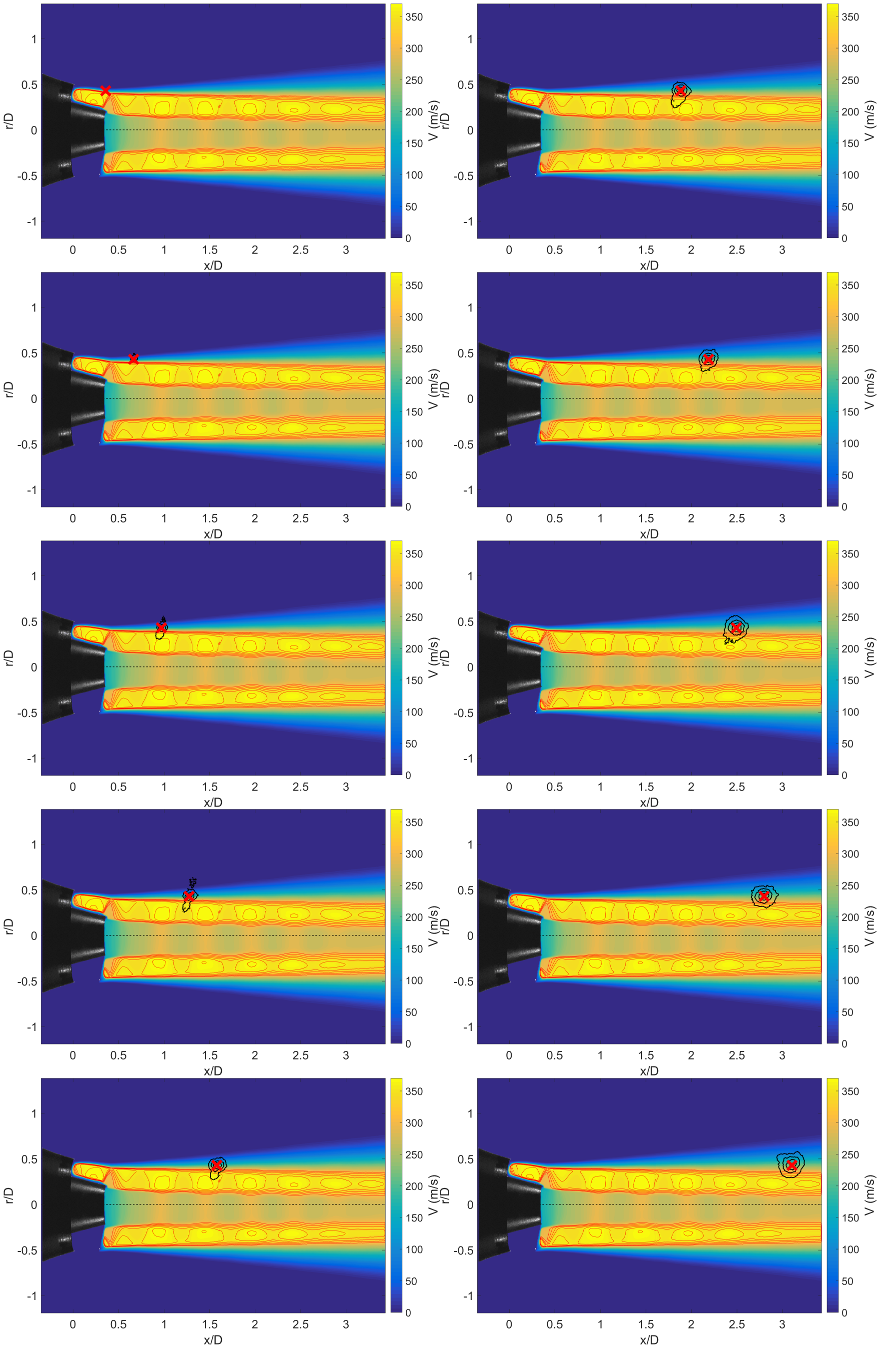

Figure 5.23: Image sequence showing the contours of the correlation function R_{12} along the horizontal line $r/D = 0.427$ for condition 01.

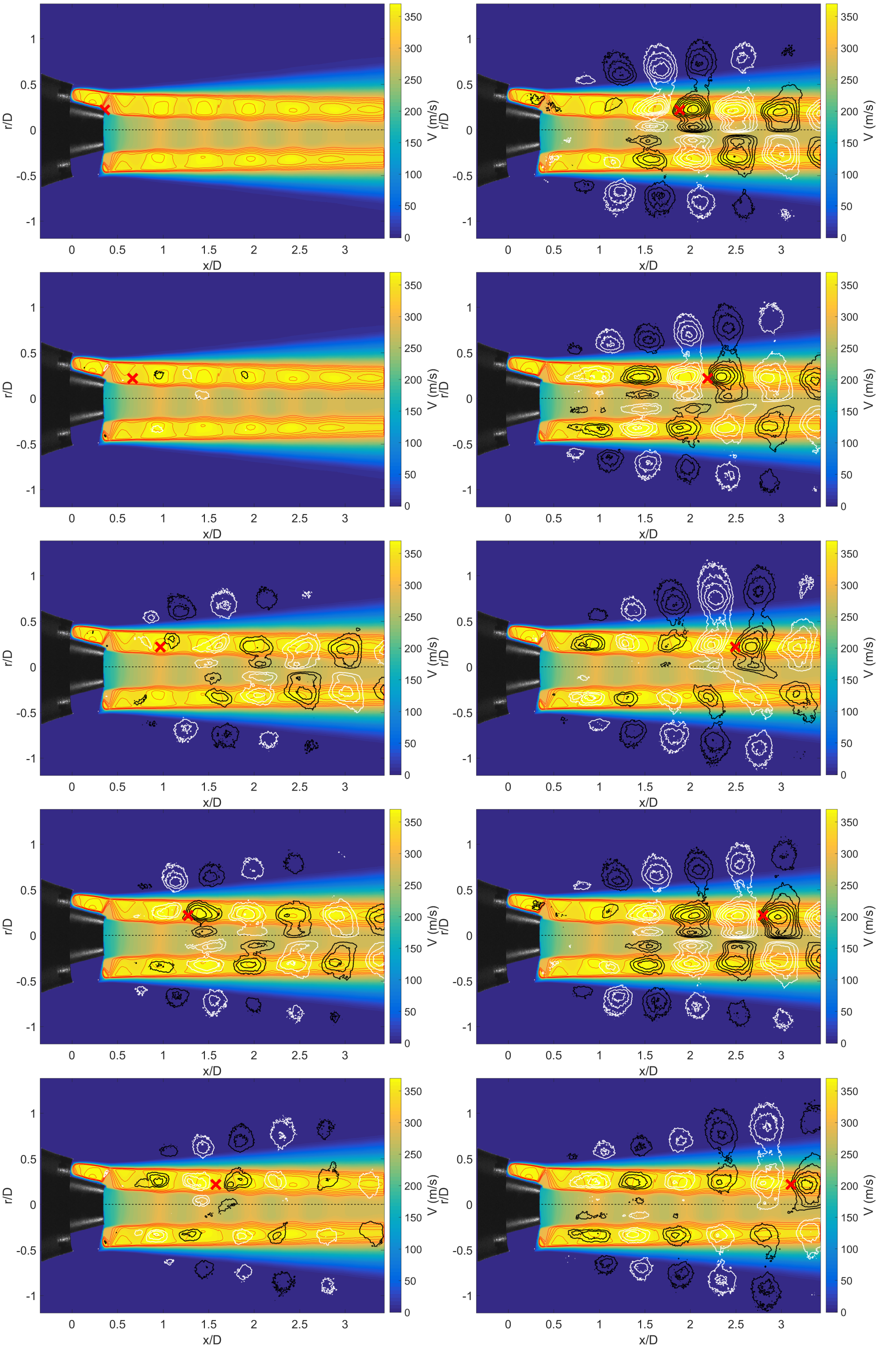

Figure 5.24: Image sequence showing the contours of the correlation function R_{12} along the horizontal line r/D = 0.218 for condition 01.

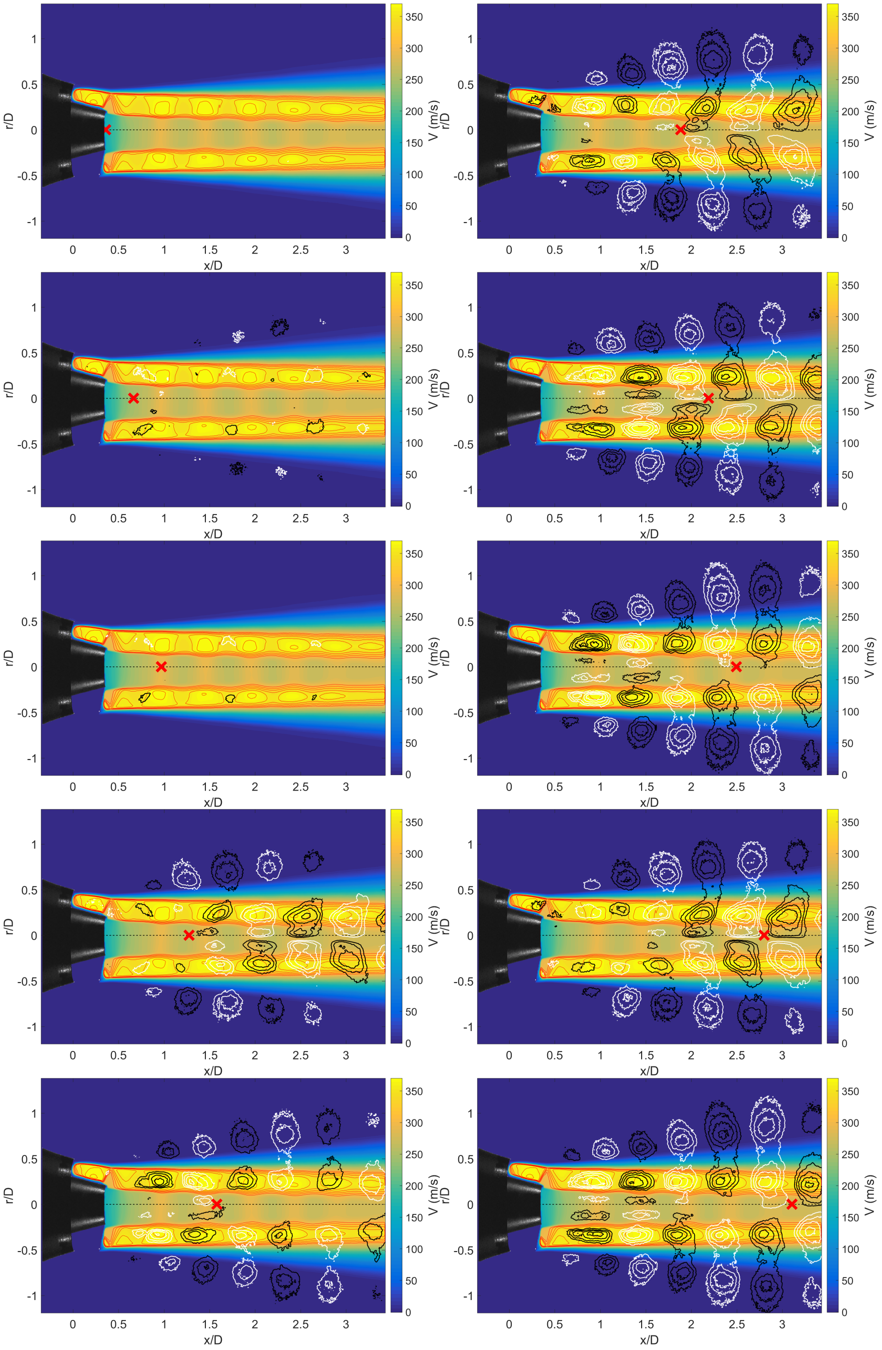

Figure 5.25: Image sequence showing the contours of the correlation function R_{12} along the horizontal line r/D = 0 for condition 01.

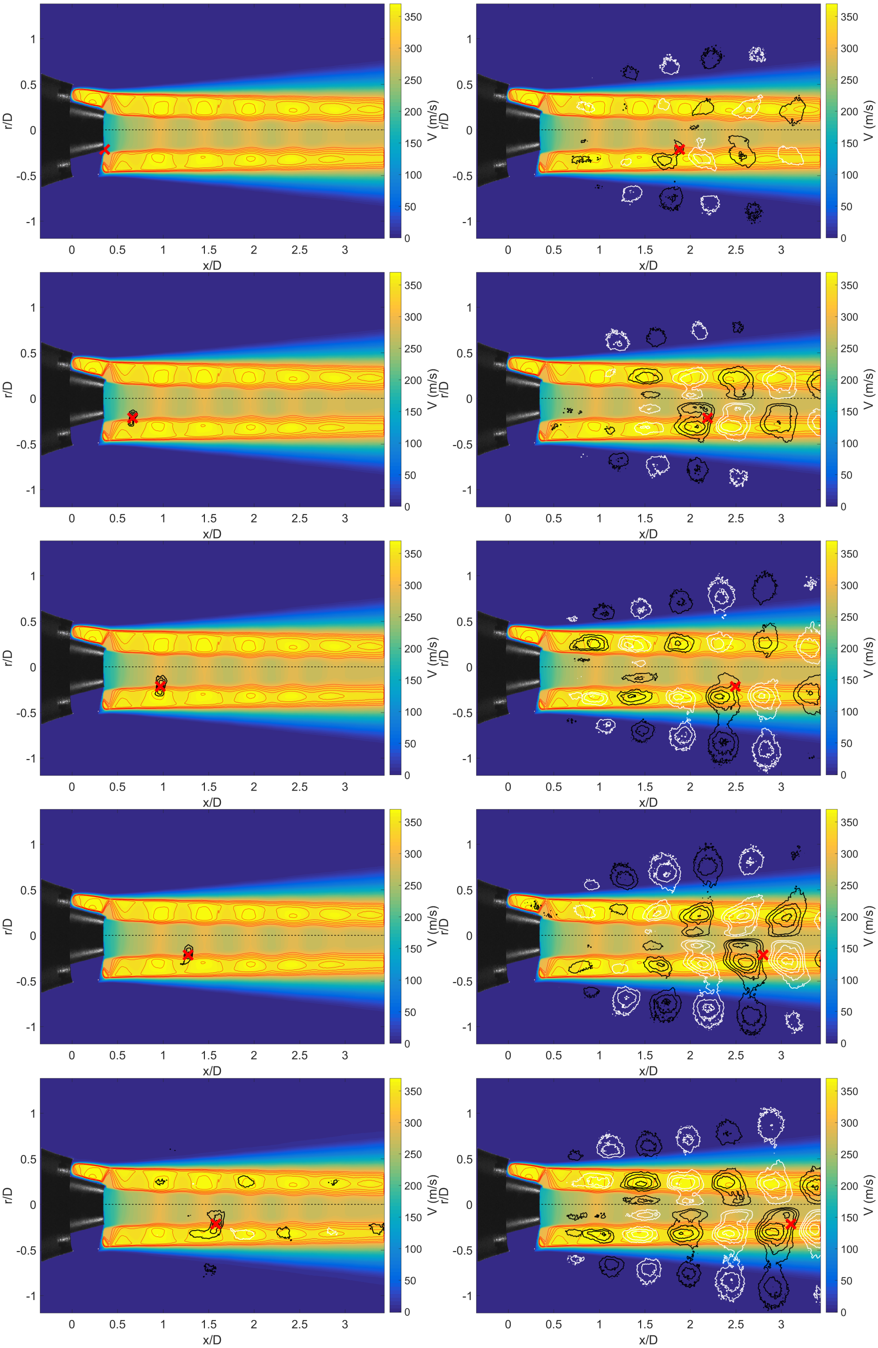

Figure 5.26: Image sequence showing the contours of the correlation function R_{12} along the horizontal line r/D = -0.218 for condition 01.

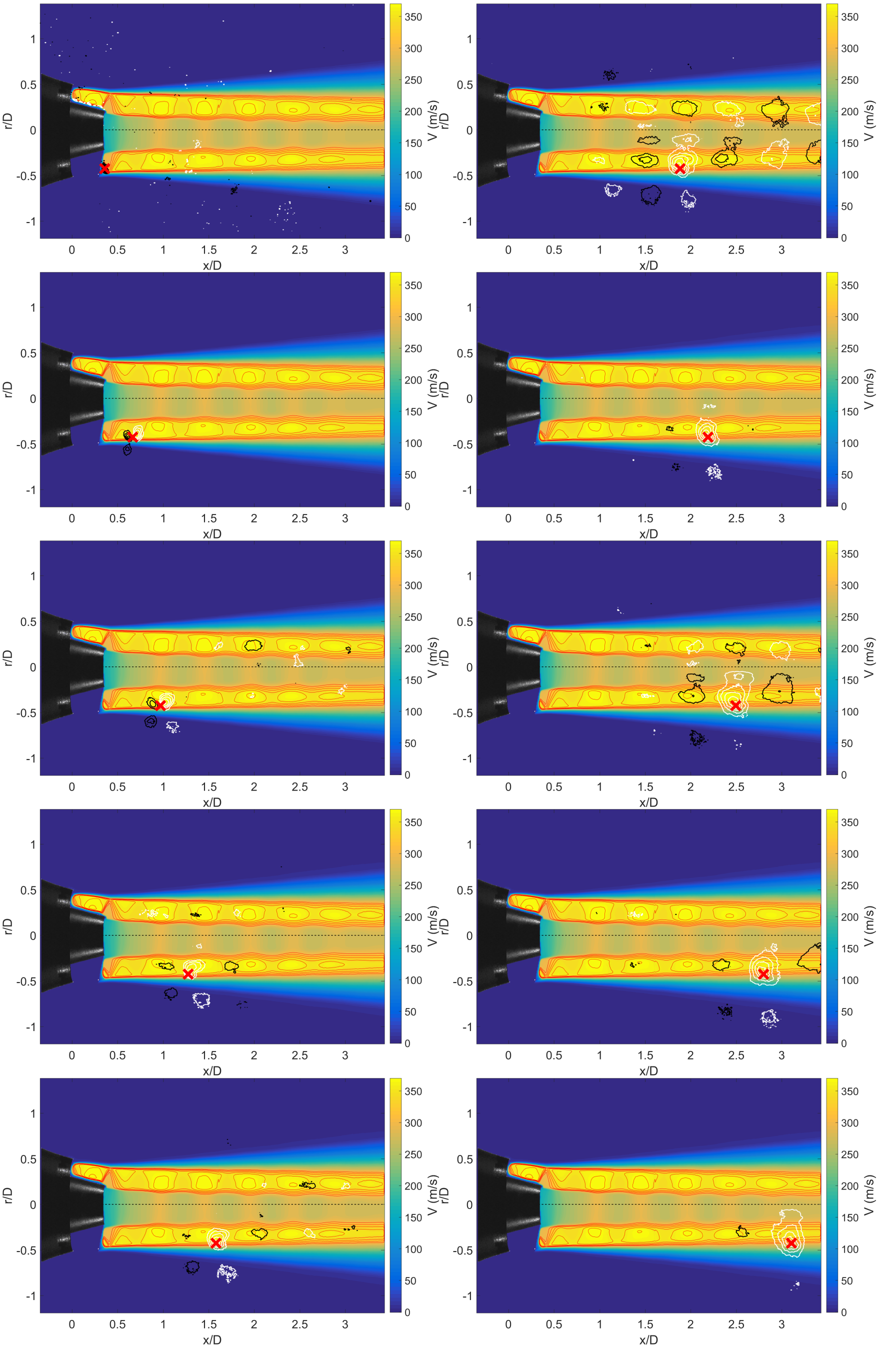

Figure 5.27: Image sequence showing the contours of the correlation function R_{12} along the horizontal line r/D = -0.427 for condition 01.

5.2.2 Cond.01 FNPR = 2.450 CNPR = 1.675

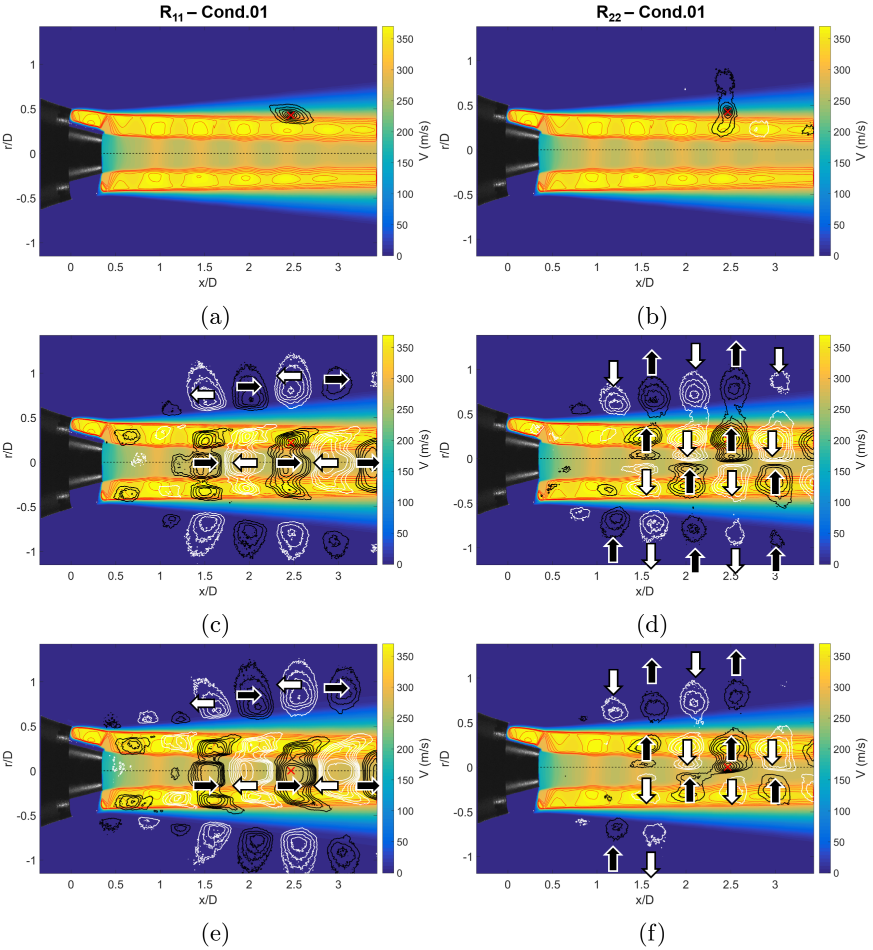

Figure 5.28: Contours of the correlation function R_{11} and R_{22}, at Cond.01, for the point located in the red X located in the external shear layer (top), internal shear layer (middle) and centerline (bottom). Black lines and white lines correspond to positive and negative correlation respectively, ranging from $0.2 \leq |R| \leq 1$. Red lines represent $M \geq 1$ isocontours. Black and white arrows represent positive and negative velocity fluctuations respectively.

The autocorrelation maps for Cond.01, for the first part of the plume, are presented in Fig. 5.28. The top row shows a typical contour pattern found in the external shear layer. The correlated region grows along the axial direction without showing any modulation for both the axial and radial component. The internal shear layer is rather more interesting. Correlation contours exhibits extended regions with high correlation values both inside and outside the jet for both the axial and the radial direction. For the axial component, the correlated area covers the entire jet section, with positive and negative values separated by approximately 1 shock-cell length. External lobes are present on both sides of the jet with opposite sign relatively to axial fluctuation. The pattern does not change significantly when the point is on the centerline. The radial correlation maps show, instead, an antisymmetric pattern. Overall, the inferable dynamics is of symmetric axial compression end expansion of the jet plume, coupled with a radial expansion and compression as well. In analogy with the single stream jet, the external lobes should be related to the screech tone, although, also and in this case, it is not known if those are related with the standing wave or with the hydrodynamic fluctuations. The downstream part of the plume shows a very similar pattern, with the correlation zones fading into a large coherent structure moving in the axial direction, in analogy with the single stream jet.

Based on these evidences, it is possible to assume that a symmetric screech mode is affecting the flow. The origin of this screech seems to be the internal shear layer, and not the external one, as the presence external lobes would demonstrate. Those are, in fact, strongly correlated with the fluctuations in the internal shear layer. However, it must be also stated that the absence of correlation in the external shear layer is not a definitive proof that the latter is not involved in the screech feedback loop. It may be that the random component of the axial turbulence overwhelms in intensity the periodic one, yielding to a drop in the correlation value. Also for the single stream jet at NPR = 2.30 and NPR = 2.40 the R_{11} was low in the shear layer.

Given the geometry of the coaxial jet, it would make sense to describe this screech mode as a "pulsation" mode. This appears evident from instantaneous velocity fields, such as in Fig. 5.29.

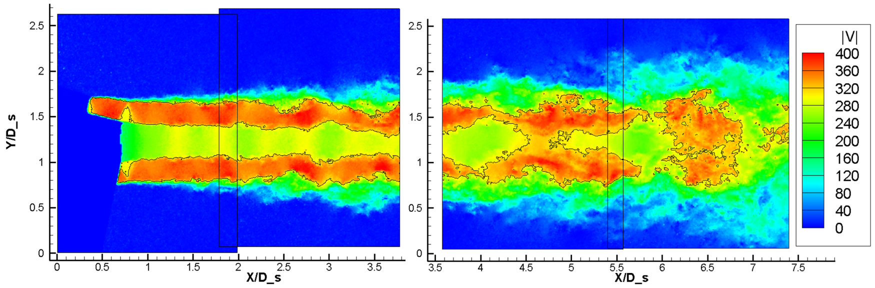

Figure 5.29: Example of instantaneous combined velocity fields with Mach number M = 1 isolines for Cond.01.

The visual effect is of a periodic overflow from the primary jet, being convected downstream such as in a rubber tube. This may be a possible explanation of the phenomenon, due to the known influence of the conical shock wave on the primary stream. A symmetric oscillation may cause a change in the primary nozzle exit pressure, and thus in the mass flow rate. Unfortunately, the installed pressure regulators are not fast enough to follow the fluctuation.

Also for the coaxial jet, the comparison with a non-screeching case was possible thanks to LES simulation done by Pérez Arroyo [67]. The results are the same for the external shear layer, with a slightly smaller extension of the correlated zones. Also for the internal shear layer, the correlated regions are small, and without negative correlation zones (Fig. 5.30). Similarly to the single stream jet, this further supports the hypothesis that the screech is the responsible of the correlated pattern from PIV images.

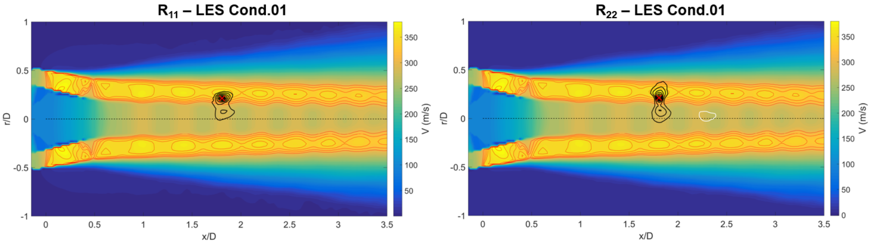

(a) (b)

Figure 5.30: Contours of the correlation function R_{11} and R_{22}, at Cond.01, for the point located in the red X located in the external shear layer (top), internal shear layer (middle) and centerline (bottom). Black lines and white lines correspond to positive and negative correlation respectively, ranging from $0.2 \leq |R| \leq 1$. Red lines represent $M \geq 1$ isocontours. Black and white arrows represent positive and negative velocity fluctuations respectively.

5.2.3 Cond.05 FNPR = 2.35 CNPR = 1.59

For this condition, as early stated, two screech tones were present during the acquisition time. However, only one of the two, different from the previous cases, was dominating the spectra at all the angles. As consequence, a different screech mode has been scooped. Fig. 5.31 shows how the external shear layer remains poorly correlated with the rest of the plume, especially for R_{11}. The fluctuations in the internal shear layer remain interestingly correlated with the rest of the plume. The axial autocorrelation shows an antisymmetric motion this time, while the radial component became symmetric along the radial direction. This is far more evident for the R_{22} in the centerline. Also in this case, lobes are present in the near field. A sinusoidal or flapping screech mode may thus be inferred. Fig. 5.32 shows an instantaneous velocity field for Cond.05 where it is more evident the plume macroscopic motion.

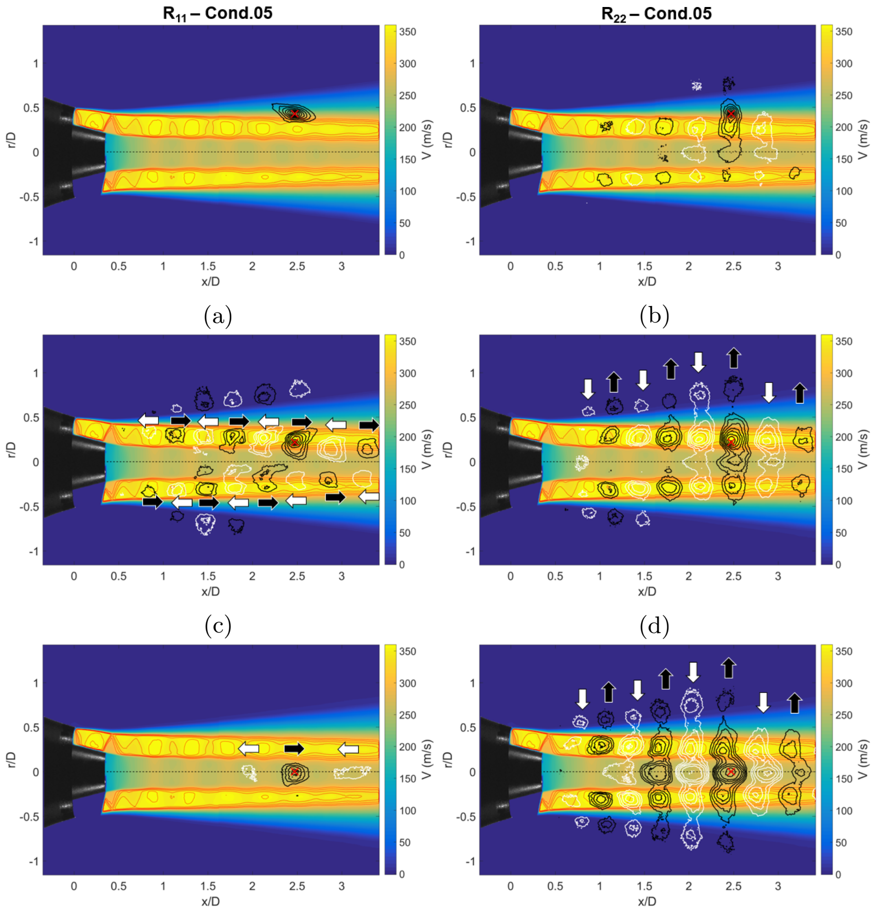

(a) (b)

(c) (d)

(e) (f)

Figure 5.31: Contours of the correlation function R_{11} and R_{22}, at Cond.01, for the point located in the red X located in the external shear layer (top), internal shear layer (middle) and centerline (bottom). Black lines and white lines correspond to positive and negative correlation respectively, ranging from $0.2 \leq |R| \leq 1$. Red lines represent $M \geq 1$ isocontours. Black and white arrows represent positive and negative velocity fluctuations respectively.

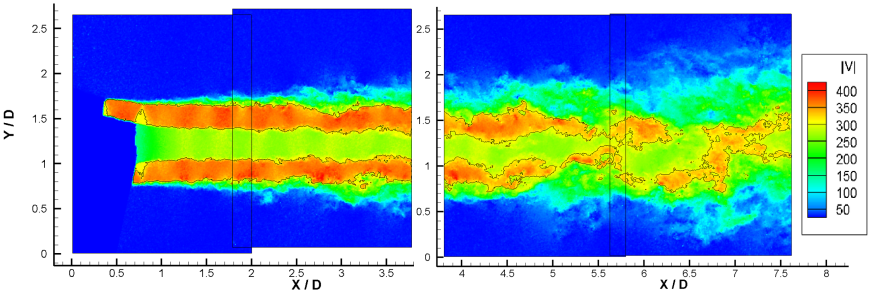

Figure 5.32: Example of instantaneous combined velocity fields with Mach number M = 1 isolines for Cond.05.

5.3 Conclusions

A new methodology to infer the jet screech dynamics was attempted based on spatial correlation function. Albeit the measurements were not time-resolved, the interpretation of the correlation maps seems robust and easier than other methods such as POD. The inferred dynamics are in agreement with the actual knowledge on screech for the single stream jet. For the coaxial flow, two screech modes have been inferred for the tested pressure conditions. At higher pressure (from Cond.01 to Cond.04), a symmetric "pulsation" mode is present. Lowering the pressure conditions (Cond.05 and Cond.06), a sinusoidal mode was found. And finally, from Cond.07 to Cond.09, no screech tone was detected at all. These results remain part of an exploratory test campaign, and their applicability are confined to this rig configuration, and these pressure conditions. Therefore others, more aimed, measurements are required for a more comprehensive and detailed characterization of the coaxial jet. Particularly, the influence of the conical shock wave on the rupture of the screech feedback loop must be investigated more in detail.

Chapter 6

Closing remarks and perspectives

An experimental facility to study shock-cell noise on a supersonic coaxial jet was designed, commissioned and tested at the von Karman Institute for Fluid Dynamics. A new coaxial silencer was realized and validated through the commercial software Multiphysics ® showing a high damping levels of the noise already at low frequencies. Two sets of nozzles have been designed and validated through RANS simulation always using COMSOL Multiphysics ®. The simulations have provided an insight of the flow that was used for the design of the experimental setup.

Several test campaigns on a supersonic single stream jet were conducted using PIV and in synchronous with microphones mounted on a polar antenna. Acoustic results show the presence of screech in each test condition, whose frequencies accord well with the literature. Multiple screech harmonics and subharmonics tones have been documented for the first time, showing a directivity pattern somehow similar to the supersonic broadband noise (BBSAN). The BBSAN show directivity pattern, which scales well with precedent experiments in the literature.

PIV results evidences different extension of the supersonic region, showing a sudden shortening when a certain NPR is reached, corresponding to the onset of a different screech mode. Statistical quantities at several NPR were documented. Mach number profiles in the centerline have been extracted, and good collapse of the curves was achieved using a scaling law from the literature. The jet potential core has also been identified and the shear layer grow rate has been measured. The Reynolds shear stress average field shows the presence of lobes in the jet near field which cannot be explained if not assuming they are the trace of a standing wave caused by the screech.

Turbulence integral length scales have been computed using correlation functions. Results show a periodic increment and decrement of the length scales in correspondence of the shock-cells, in disagreement with analogous research carried out on a supersonic jet where screech was suppressed. From the correlation maps, an evidence of large coherent structures being convected along the shear layer was found, thus supporting the hypothesis of the existence of wavepackets. A simple method to infer the screeching dynamics from the correlation maps was proposed.

The retrieved information was used by Rubio Carpio [77] to feed a wavepackets-based model to predict broadband shock-cell noise, showing good agreement in determining the position of the peaks at different angles, and thus supporting the hypothesis that wavepackets are present in the flow and are responsible for the BBSAN.

A coaxial jet with subsonic primary stream, and supersonic secondary stream, was studied experimentally. Multiple combinations of pressure conditions for the primary and secondary flows have been tested. Acoustic measurements have been performed in synchronous with the PIV, which has been used for the first time on a supersonic coaxial flow.

The presence of both screech and broadband noise was recorded in the majority of the tests, and a directivity pattern was recognized for the latter, as expected. For a certain pressure condition, the screech was suppressed. Experimental evidences suggest this may be related to a complex shock interaction occurring at the end of the primary nozzle. Two screech modes have been identified with at least one condition where two modes are present at the same time. In comparison with a single stream jet, the coaxial jet acoustic spectra show a curious quieter zone of the BBSAN for an interval angle between 60°and 90°.

Also here, Mach number profiles have been extracted and average shock cell length was measured in each test case, showing a progressive shortening while lowering the total FNPR. The jet potential cores have also been identified and the shear layer grow rate have been measured.

The influence of a conical shock-wave at the exit of the primary nozzle was studied. It was found that at lower pressures, the interaction of this shock-wave with an expansion fan leads to the formation of a complex shocks-pattern, and ultimately to the screech suppression.

Following the example of the single stream jet, correlation functions have been used, and integral length scales have been retrieved. The external shear layer presents zones of high correlation that increase in size in the downstream direction, but remain limited to the shear layer boundaries. For the internal shear layer, on the contrary, the correlation zones are covering large portion of the internal flow in both axial and radial direction, with presence of coherence lobes outside the external shear layer. The comparison with the LES of a supersonic coaxial non-screeching jet show how the correlation zones are much smaller, thus suggesting the screech is the cause of the correlation behavior. Similarly to the single stream case, the jet screeching dynamics was educed. The correlation maps suggest the presence of a pulsation (or breathing) of the internal jet, which is cause/effect of the screech. When a second screech mode is encountered, the correlation maps change, suggesting a sinusoidal oscillation of the internal jet, instead. In the cases without screech, the correlation area is greatly reduced, and a pattern similar to the LES (although not the same pressure condition), was found. All these evidences suggests that the screech feedback loop may take place in the internal shear layer, although more studies, time-resolved, are necessary to confirm this hypothesis.

6.1 Future perspectives

This project opens several scenarios for further improvements and researches. For sake of clarity, the opportunity to be exploited from the already acquired data, and the new possible experiments, will be discussed separately.

6.1.1 Exploiting the acquired data

The recorded database, from PIV and microphones, for both the single and coaxial jet, is very rich, and it would be certainly a loss to not fully exploit it.

Starting from the PIV, only the very basic pre-processing and correlation was performed. Using advanced image treatment (such as POD [52]) for an efficient removal of background noise from images, and advanced correlation techniques (adaptive windowing, different window function), may lead to higher precision, and thus reducing the uncertainty.

The zoomed field of views remained unexploited, but very useful information could be retrieved with unprecedented resolution. A detailed view of the conical shock-wave, which lead in some cases to the cancellation of the screech, is achievable.

The synchronization between microphones and PIV has not been exploited. Several trials have been done to perform phase-locked average have been done without success. Nevertheless, not all the paths have been followed, and, as personal belief, very important information may be extracted.

The acoustic database comprehends more test conditions, compared to the PIV. For the single stream jet, a study on the screech harmonics directivity and on the subharmonics is mandatory, considering the lack of knowledge about them. For the coaxial jet, as well, a study on the screech directivity is suitable, especially in light of the hypothesis that the feedback loop comes from the internal jet. When the internal flow became supersonic, the presence of two screech tones was detected, as well as an important increment of the shock-cell noise. The low BBSAN levels at certain angles, is also worthy of investigation.

A first, simple, attempt to estimate the BBSAN contribution on the sound power level was attempted. BLOPWLs at certain angles finds deeps for particular CNPR and FNPR combinations. However, other, more advanced, techniques [113] would be more suitable to separate the BBSAN from the jet mixing noise. The goal would be to establish if a certain combination of FNPR/CNPR attains a quieter shock-cell noise.

Finally, the prediction of the BBSAN through wavepackets model feed with PIV data should be improved for the single stream jet, and tried for the coaxial jet. The propagation of the sound waves in the supersonic region was formerly addressed by Tam *et al*[92], but not implemented in a complete predictive model.

6.1.2 Filling the knowledge gap with new experiments

Recent progresses of the technology make available interesting possibilities for further investigation. The best case would be a time resolved PIV campaign. High acquisition frame rate would consent to identify and follow the perturbations in space and time, leading to unprecedented detailed analysis. The existence of wavepackets, and their convection speed, would find an absolute response. However, two aspect must be considered, the FOV extension, and the frequency. Larger facilities, facilitate the second aspect, because the shock-cell noise will occur at lower frequencies, but they would require multiple lasers and cameras to investigate the flow. This because the light scattered from particles limits the maximum distance of the instruments from the jet. On the other side, a smaller jet rig would consent with a single camera to record a large portion of the flow, but then the frequencies would be too high to consent a time resolved study. The FAST facility is in a middle position between the two cases. It has the correct dimension to investigate an extended field of view, with a single camera, without sacrificing too much the resolution, and it has screech and BBSAN frequency between 5 and 7.5 kHz. To respect the Nyquist criteria, this mean an instantaneous FOV at 15 kHz, and considering that two laser pulses are requested, this means a dual cavity laser at 15 kHz, and a camera frame rate of 30 kHz. All these requirements can be fulfilled with actual technology, despite at a high price, probably.

The precedent requirements could be relaxed for LIF (Laser Induced Fluorescence) Schlieren technique. As reminder, in this technique, a laser excites a fluorescent plate, which emits incoherent light for typically 10 ns, which is then used as source for the classical Schlieren technique. The advantage consists in very sharp images, where also weak sound waves are typically visible. In comparison to the PIV, the light is not scattered by particles, but comes directly from the source. Previous experiences [76] have demonstrated the efficacy of this technique. Because the light generated by a laser is usually more than enough for a standard camera, a larger FOV can be achieved simply increasing the distance from the camera and the jet rig. This would consent also larger jets to be investigated, with the advantage of the lower shock-cell noise frequency. Furthermore, Schlieren does not require a double shot, and therefore a dual cavity laser, shooting at 7.5 kHz each cavity, may suffice. This relaxation comes at a price, obviously, which is the quantitative analysis of the velocity field. The experimentalists should therefore account to obtain only a qualitative description of the jet motion, and a visualization of the screech feedback loop. For coaxial jet, this may be, for sure, worthy the effort, given the lack of knowledge on it.

Standard Stereo-PIV may give important information on the flow tridimensionality. For the single stream jet, it is inferred that some screech modes are helicoidal because of precedent Schlieren analysis, however quantitative informations of the spinning rate, for instance, are missing. For the coaxial jet, it would be even more important, to understand if the jet has some spinning motion or not. The correlation maps retrieved from LES of the coaxial jet show the presence of coherence structures also in the azimuthal direction, which cannot be verified experimentally.

If the weak point of standard PIV is the time resolution, and also the spatial resolution, due to the correlation window size, the situation is inverted for Laser Doppler Velocimetry. This point wise measurement can guarantee very high acquisition frequency, and can be used to characterize the jet small scales of turbulence, that are invisible with PIV. The thin shear layer, and more important, the boundary layer of the nozzles leap, requires this characterization in order to understand the receptivity of the boundary layer versus the pressure perturbations. A two point correlation would also help in identifying the time scales of the wavepackets. Unfortunately, all of this in a point at time.

Intrusive techniques would fill another gap, which concerns the pressure. However, it is opinion of the author that the uncertainty related on the usage of a probe in a supersonic field, united with the time consumption and the point-wise measurement, makes the effort not interesting, especially in presence of other time resolved techniques such LDV.

Acoustic measurements in the near field, alone or synchronized with other time resolved optical measurements (Schlieren, LDV), may add other useful information on the sound generation mechanism. Examples are present in the literature [31], showing the possibility to separate the hydrodynamic from the acoustic contribution and to estimate the position of the noise source .

Finally, acoustic beamforming could be an interesting way to identify the regions of noise sources at different frequencies. Traditional beamforming and deconvolution approaches, however, may result too inaccurate, because both the sources jittering, and high frequencies. Inverse methods, such Generalized Inverse Beamforming (GIBF)[86] [109] [107] [20] [14], could me more suitable, instead. The possibility to use distribute multi-polar sources, plus the adoption of tailored Green's function for the propagation in the supersonic region, adds more physics to the problem, and thus could give more reliable estimation.

Appendix A

PIV measurements

A.1 Condition 02

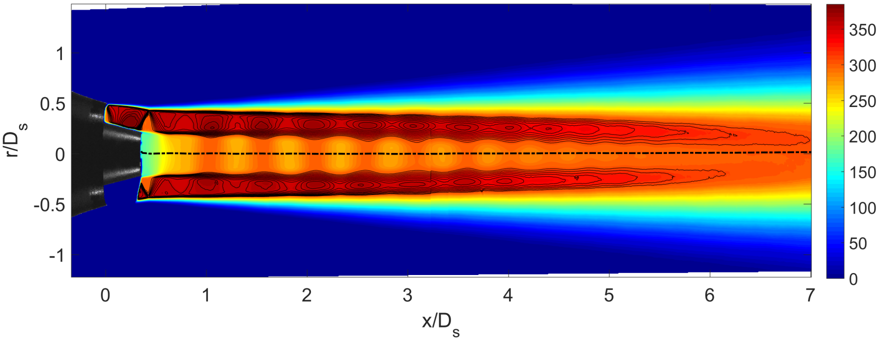

Figure A.1: Mean velocity module flow field with M > 1 isolines at condition 02.

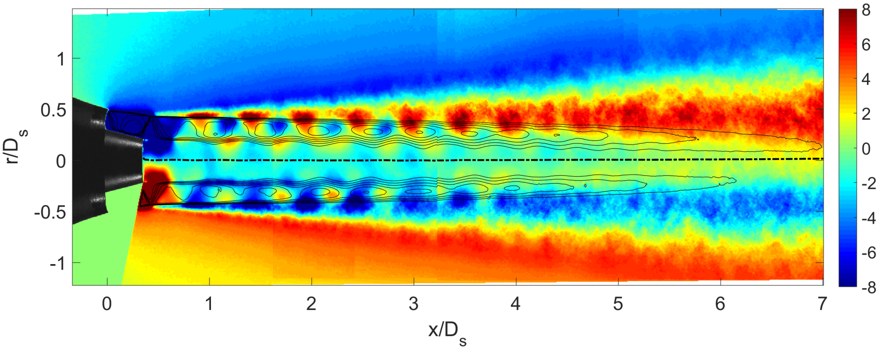

Figure A.2: Mean radial velocity flow field with M > 1 isolines.

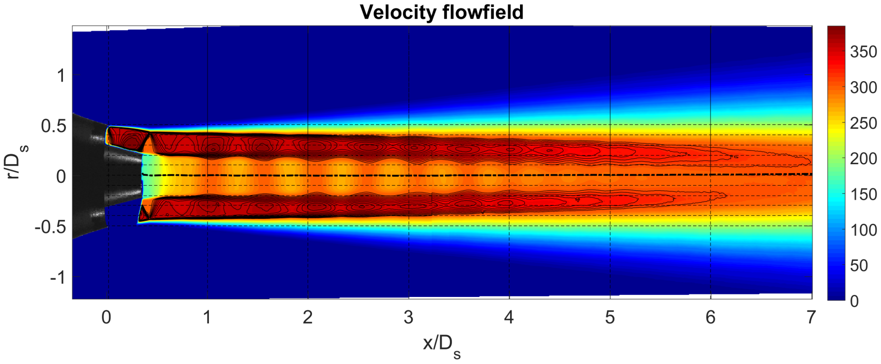

Figure A.3: Same as for Fig. A.1, the dashed lines represents the locations where radial and axial profiles for Mach number and turbulence intensity have been extracted.

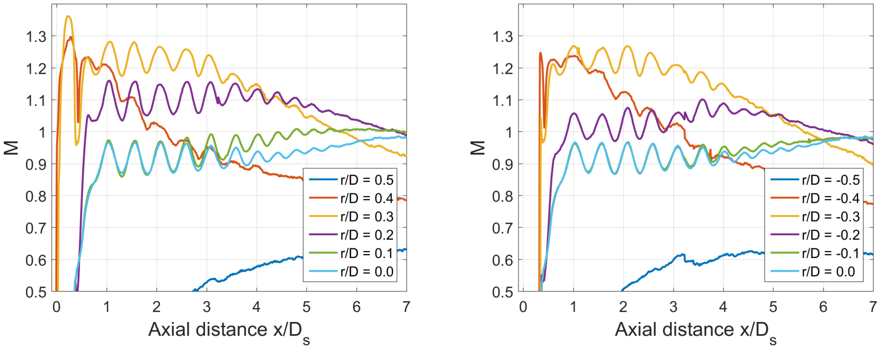

Figure A.4: Mach number axial profiles at several radial position for the upper part (left) and lower part (right) of the image.

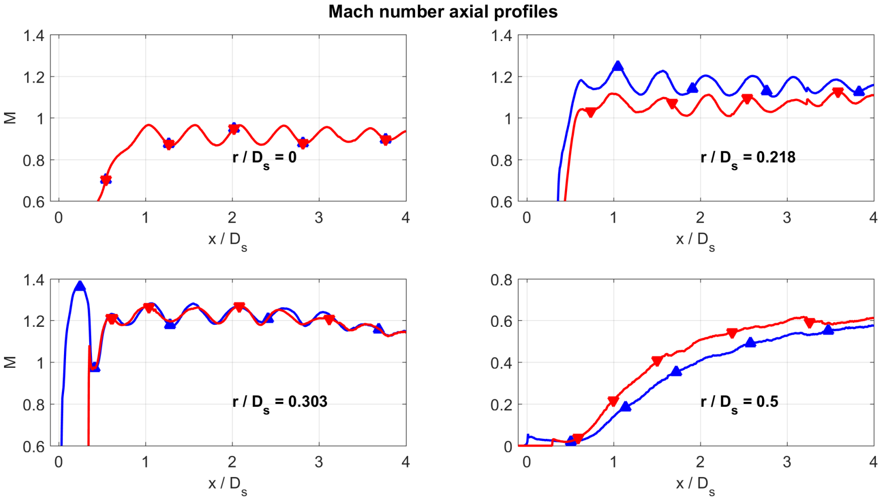

Figure A.5: Comparison of the Mach axial profiles between the upper part (in blue, up pointing triangles) and the lower part (in red, down pointing triangles) at several radial distance. The radial positions corresponds to the jet centerline (r/D = 0), the internal nozzle lip (r/D = 0.218), the ideal intersection point between the internal nozzle wall and the secondary nozzle exit area (r/D = 0.303). the secondary nozzle lip (r/D = 0.5).

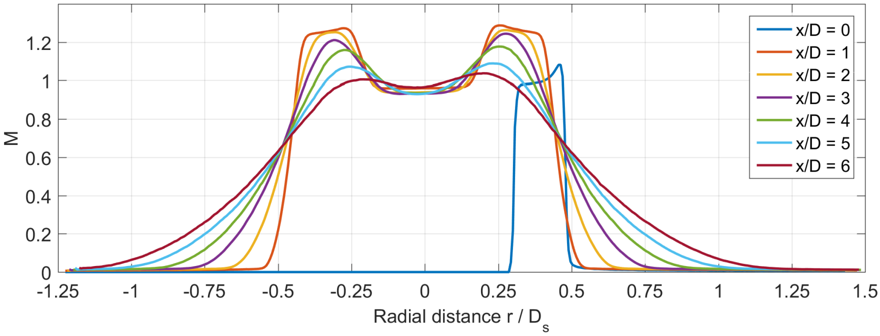

Figure A.6: Mach number radial profiles at several axial distance.

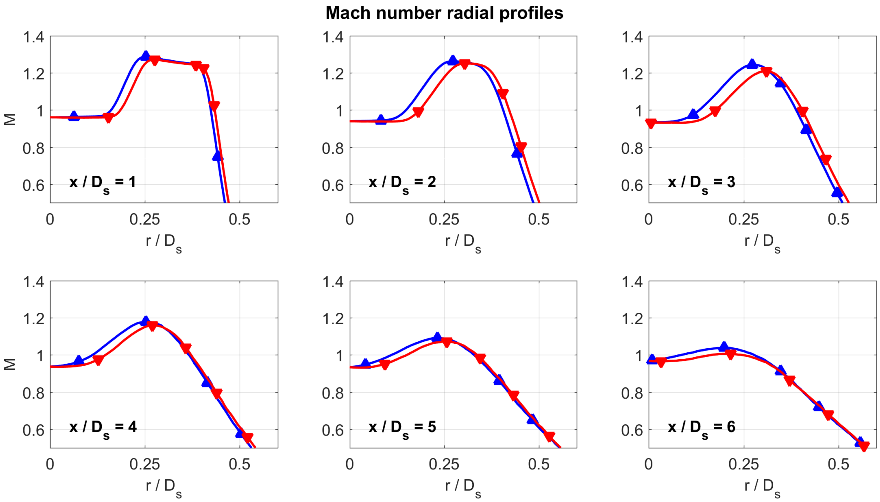

Figure A.7: Comparison of the Mach radial profiles between the upper part (in blue, up pointing triangles) and the lower part (in red, down pointing triangles) at several axial distance

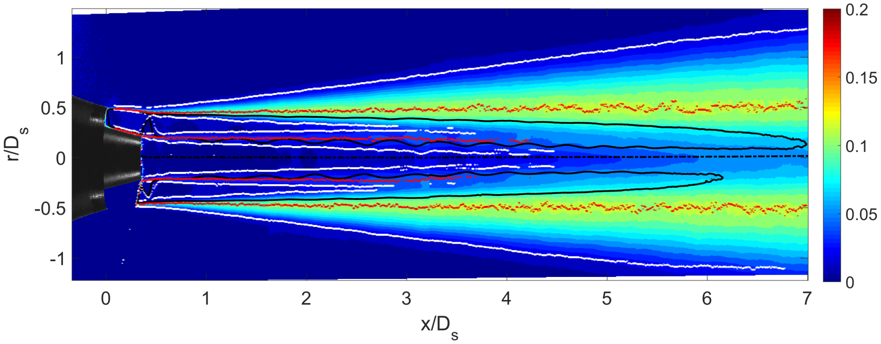

Figure A.8: Turbulence intensity flow field. In black, the M = 1 isoline, in red, the TI maxima locations, and in white, the computed limit of the shear layer.

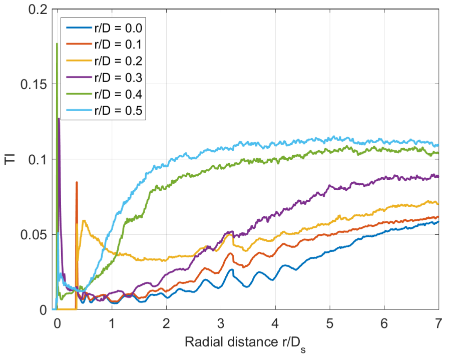

Figure A.9: Turbulent intensity axial profiles at several radial position for the upper part of the image.

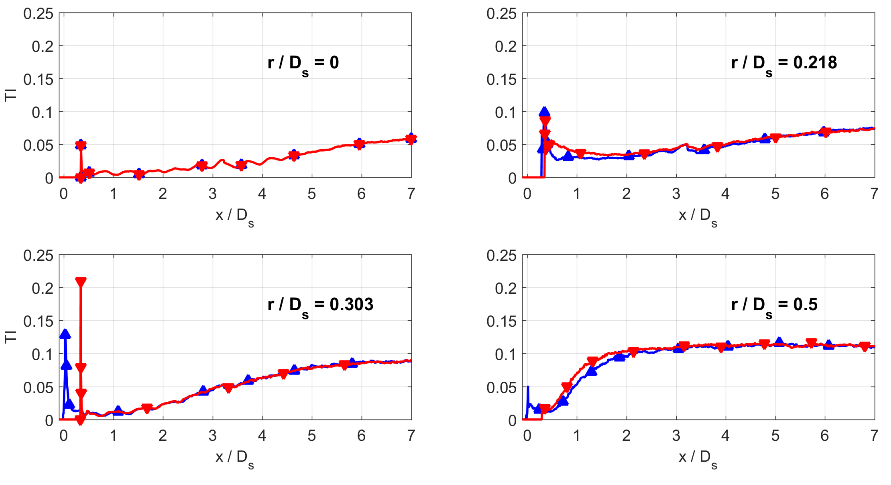

Figure A.10: Comparison of the TI axial profiles between the upper part (in blue, up pointing triangles) and the lower part (in red, down pointing triangles) at several radial distance. The radial positions corresponds to the jet centerline (r/D = 0), the internal nozzle lip (r/D = 0.218), the ideal intersection point between the internal nozzle wall and the secondary nozzle exit area (r/D = 0.303). the secondary nozzle lip (r/D = 0.5).

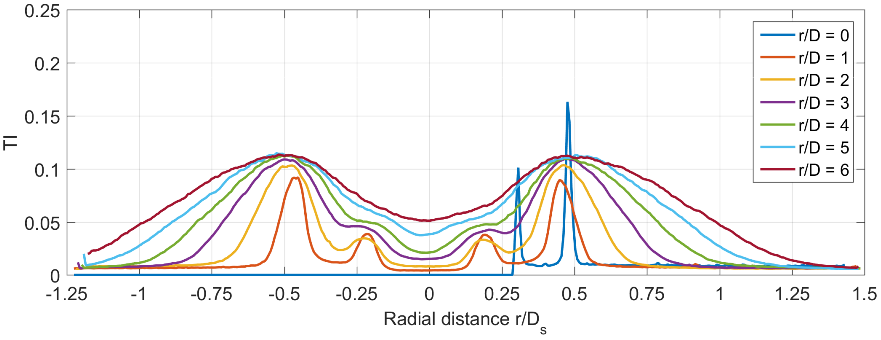

Figure A.11: Turbulence intensity radial profiles at several axial distances.

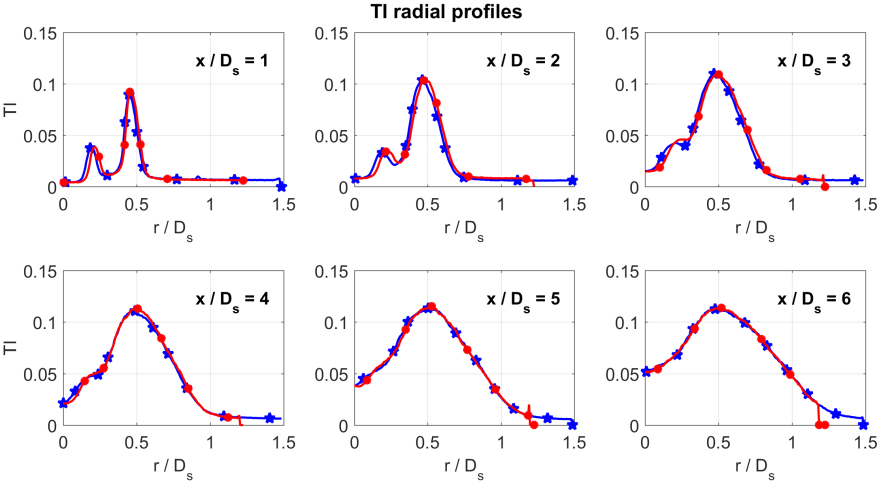

Figure A.12: Comparison of the TI radial profiles between the upper part (in blue, stars) and the lower part (in red, circles) at several axial distance.

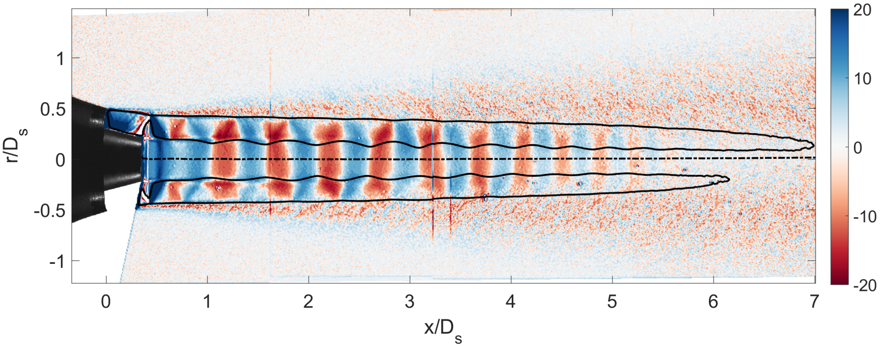

Figure A.13: Square root of the mean velocity divergence flow field $\nabla \cdot V/\sqrt{|\nabla \cdot V|}$. The image shows how the primary and secondary flows are expanding (in blue) and compressing (in red) with the shock-cells. The black line is the sonic line.

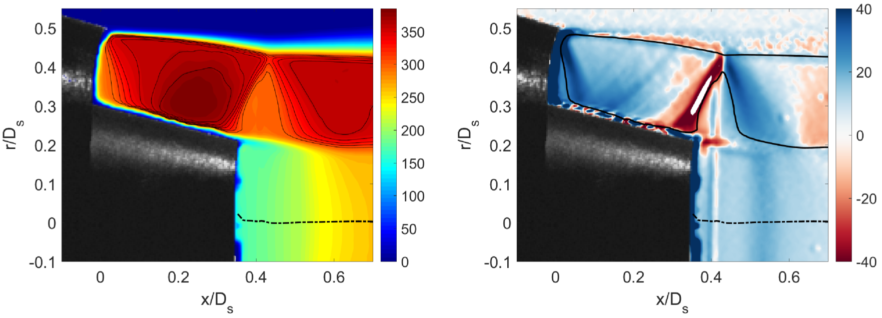

Figure A.14: Detail of the nozzle region. Velocity flow field with M > 1 isolines (left) and velocity divergence flow field (right).

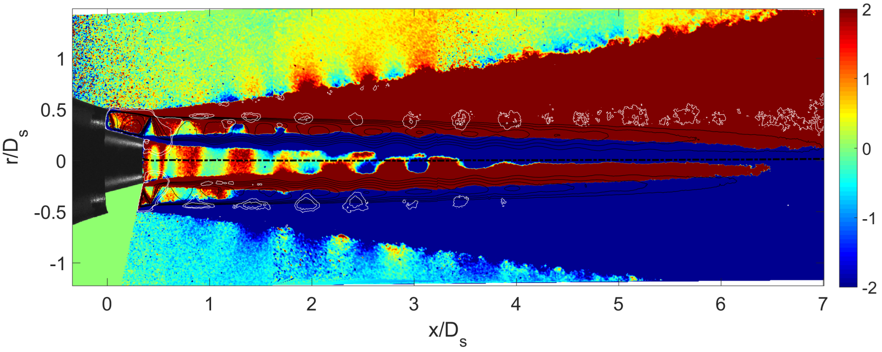

Figure A.15: Flow field of the averaged velocity fluctuations product $u'v'$. The black lines are M = [1:0.05:1.325] isocontour lines. In white, the isocontour lines of the mean radial velocity field (Fig. A.2). The scale enhances the lobes outside the jet shear layer.

A.2 Condition 03

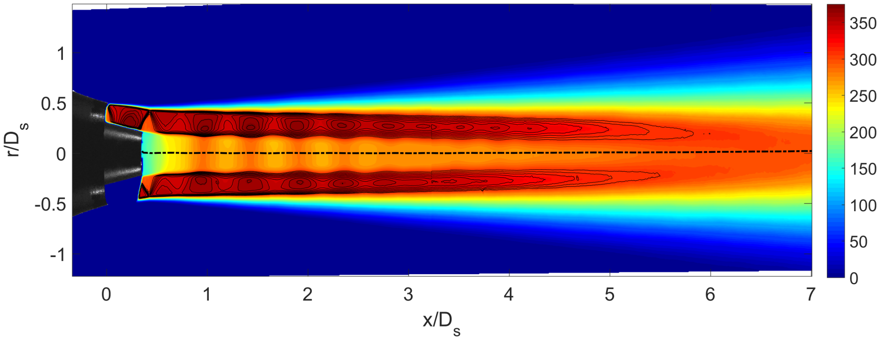

Figure A.16: Mean velocity module flow field with M > 1 isolines at condition 03.

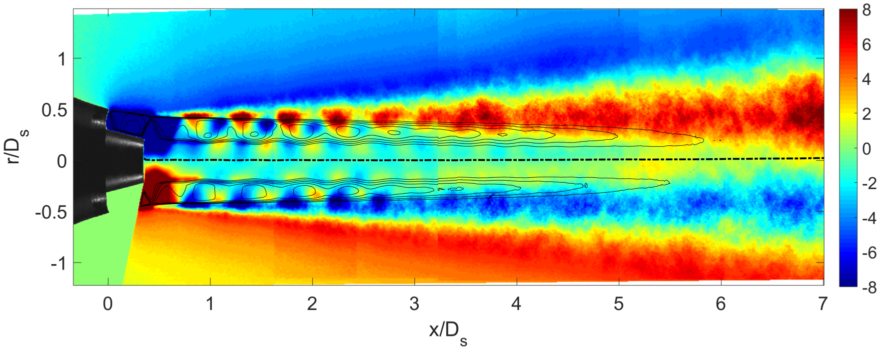

Figure A.17: Mean radial velocity flow field with M > 1 isolines.

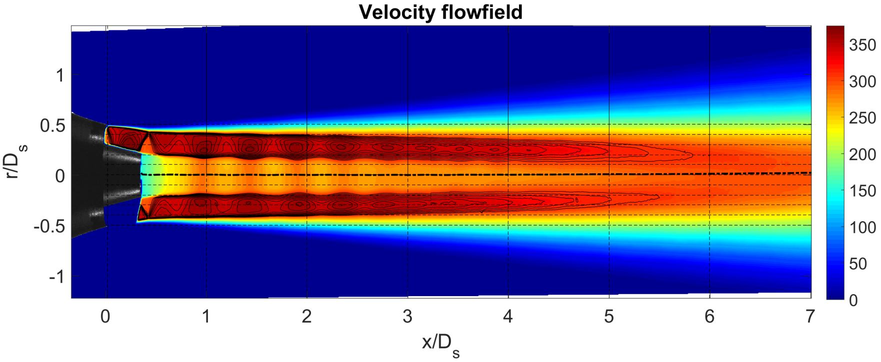

Figure A.18: Same as for Fig. A.16, the dashed lines represents the locations where radial and axial profiles for Mach number and turbulence intensity have been extracted.

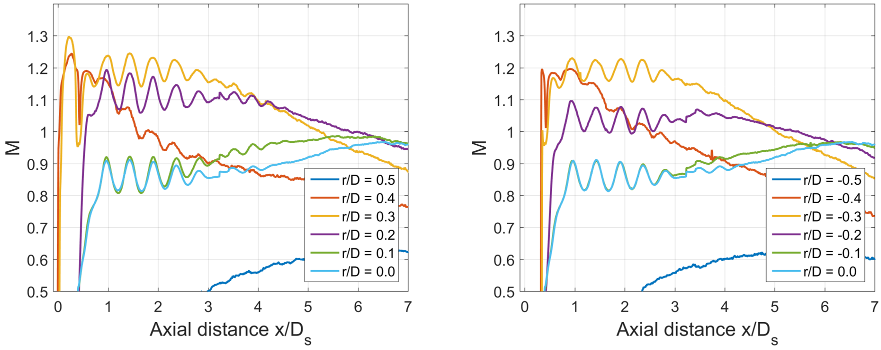

Figure A.19: Mach number axial profiles at several radial position for the upper part (left) and lower part (right) of the image.

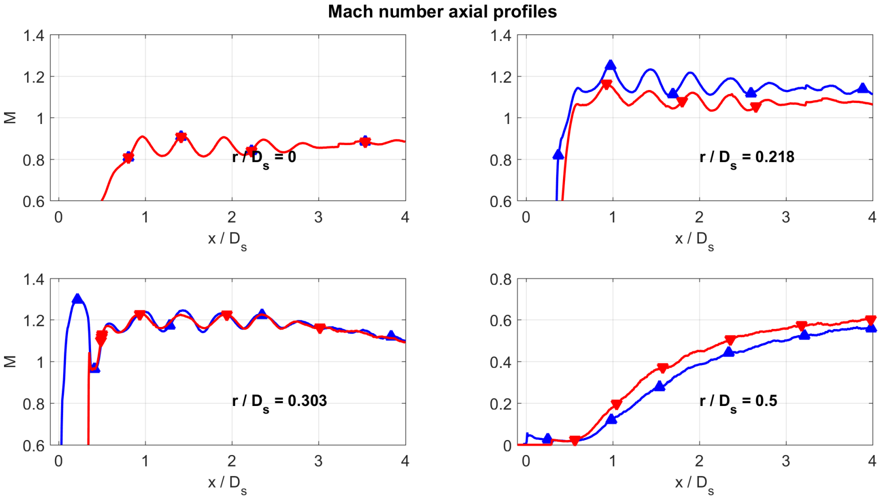

Figure A.20: Comparison of the Mach axial profiles between the upper part (in blue, up pointing triangles) and the lower part (in red, down pointing triangles) at several radial distance. The radial positions corresponds to the jet centerline (r/D = 0), the internal nozzle lip (r/D = 0.218), the ideal intersection point between the internal nozzle wall and the secondary nozzle exit area (r/D = 0.303). the secondary nozzle lip (r/D = 0.5).

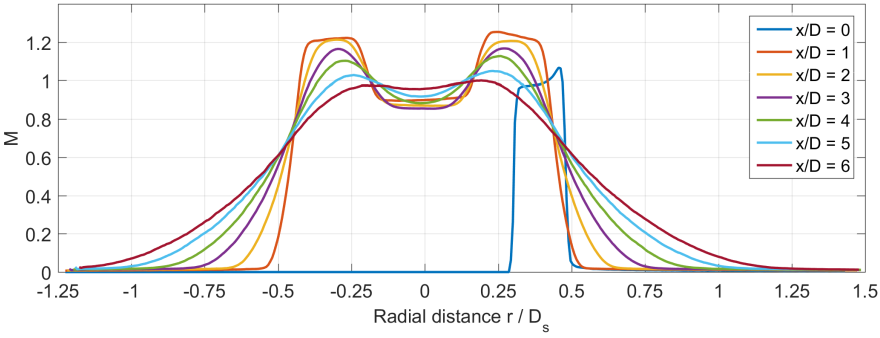

Figure A.21: Mach number radial profiles at several axial distance.

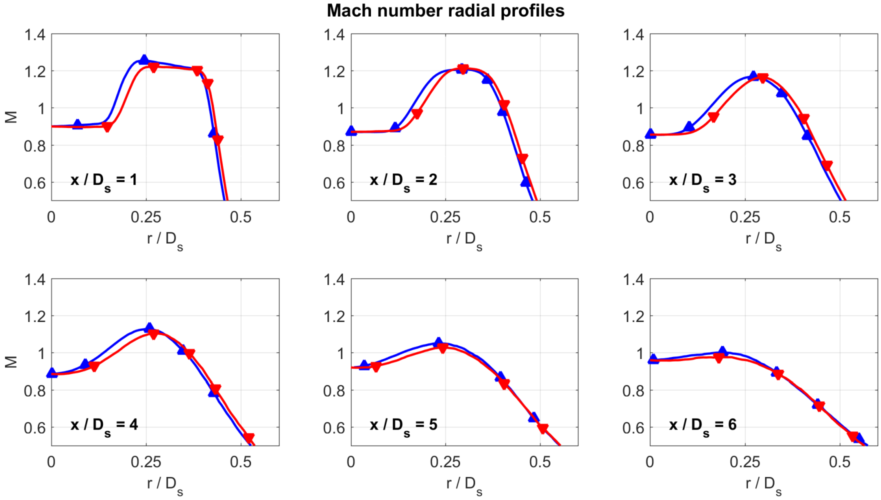

Figure A.22: Comparison of the Mach radial profiles between the upper part (in blue, up pointing triangles) and the lower part (in red, down pointing triangles) at several axial distance

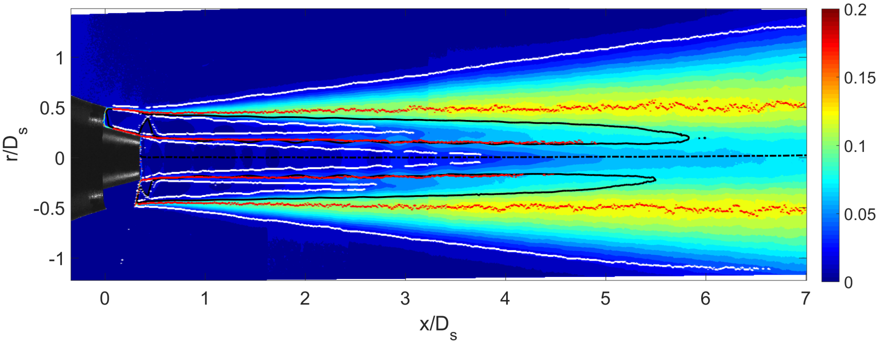

Figure A.23: Turbulence intensity flow field. In black, the $M = 1$ isoline, in red, the TI maxima locations, and in white, the computed limit of the shear layer.

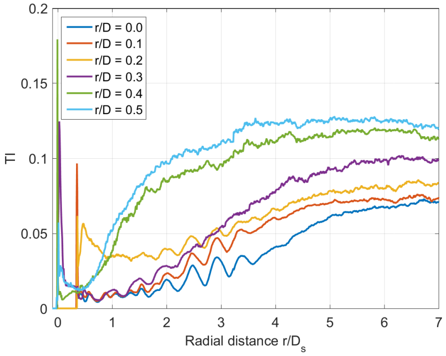

Figure A.24: Turbulent intensity axial profiles at several radial position for the upper part of the image.

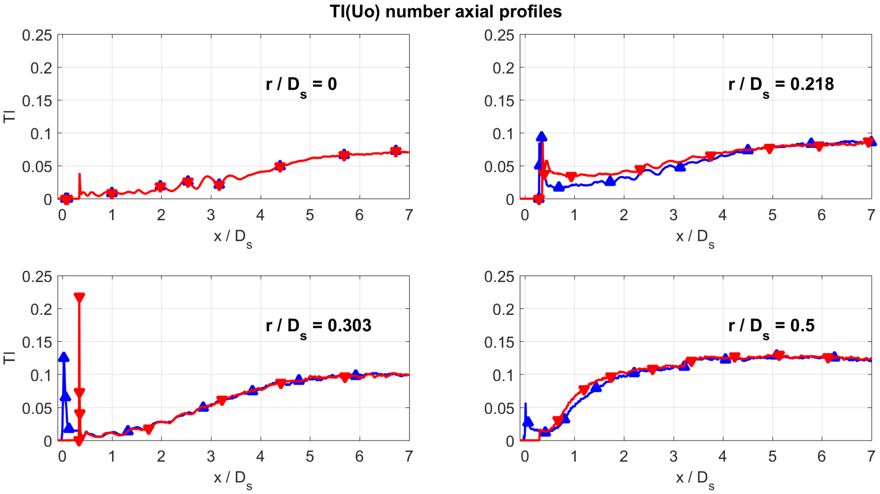

Figure A.25: Comparison of the TI axial profiles between the upper part (in blue, up pointing triangles) and the lower part (in red, down pointing triangles) at several radial distance. The radial positions corresponds to the jet centerline (r/D = 0), the internal nozzle lip (r/D = 0.218), the ideal intersection point between the internal nozzle wall and the secondary nozzle exit area (r/D = 0.303). the secondary nozzle lip (r/D = 0.5).

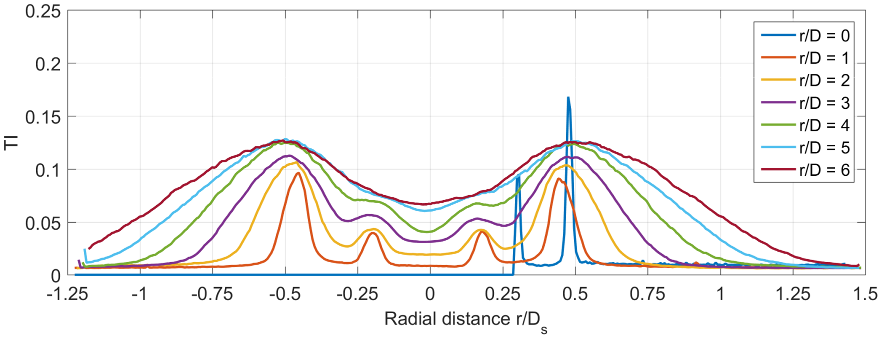

Figure A.26: Turbulence intensity radial profiles at several axial distances.

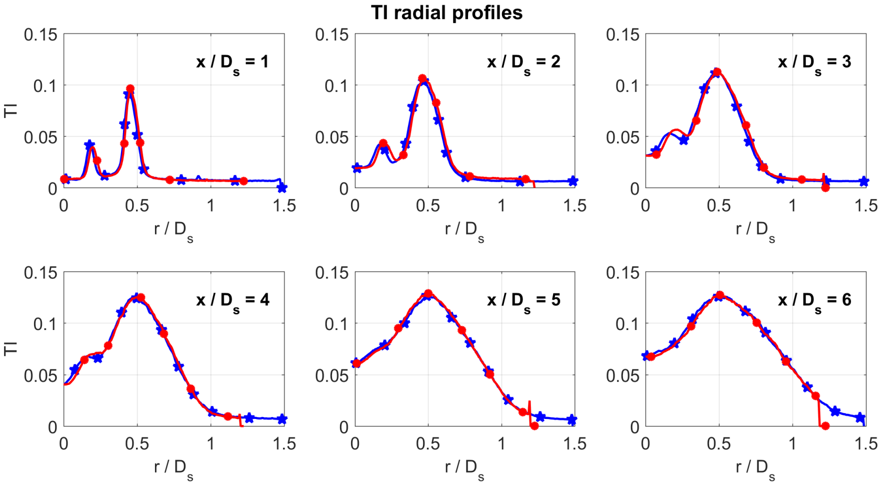

Figure A.27: Comparison of the TI radial profiles between the upper part (in blue, stars) and the lower part (in red, circles) at several axial distance.

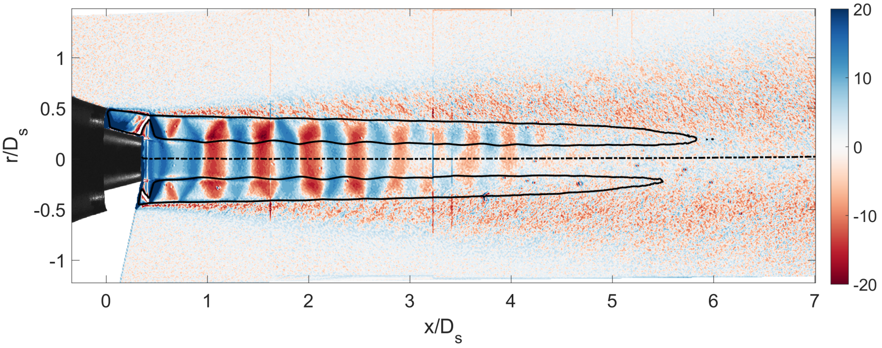

Figure A.28: Square root of the mean velocity divergence flow field $\nabla \cdot V/\sqrt{|\nabla \cdot V|}$. The image shows how the primary and secondary flows are expanding (in blue) and compressing (in red) with the shock-cells. The black line is the sonic line.

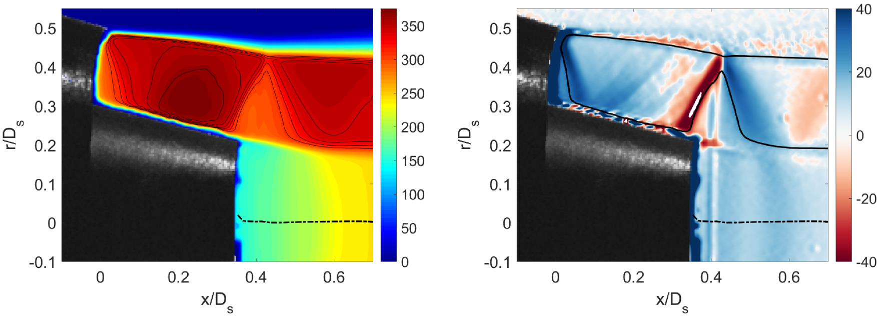

Figure A.29: Detail of the nozzle region. Velocity flow field with M > 1 isolines (left) and velocity divergence flow field (right).

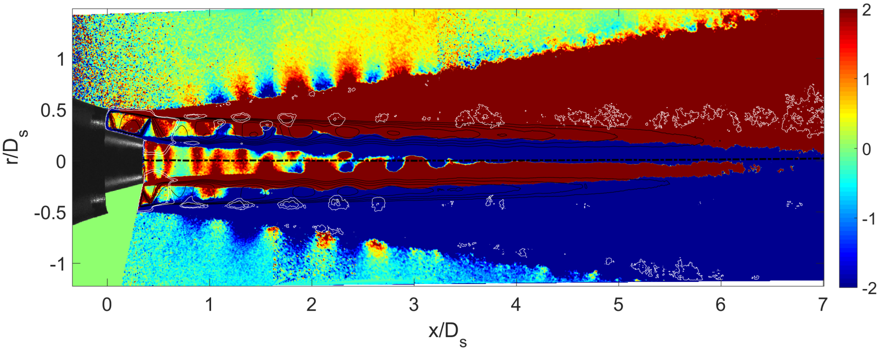

Figure A.30: Flow field of the averaged velocity fluctuations product $u'v'$. The black lines are M = [1:0.05:1.325] isocontour lines. In white, the isocontour lines of the mean radial velocity field (Fig. A.17). The scale enhances the lobes outside the jet shear layer.

A.3 Condition 04

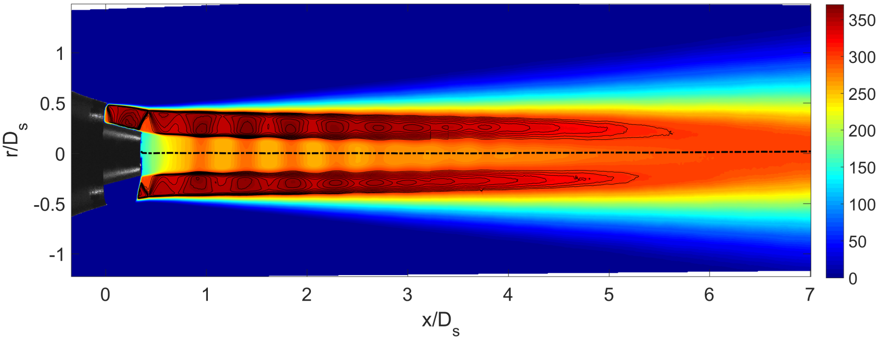

Figure A.31: Mean velocity module flow field with M > 1 isolines at condition 04.

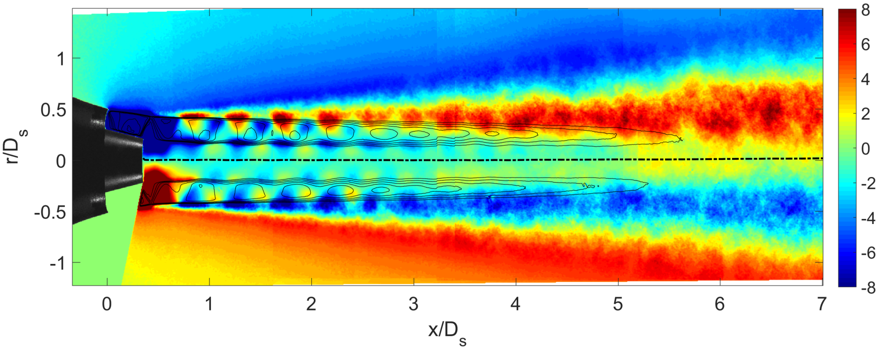

Figure A.32: Mean radial velocity flow field with M > 1 isolines.

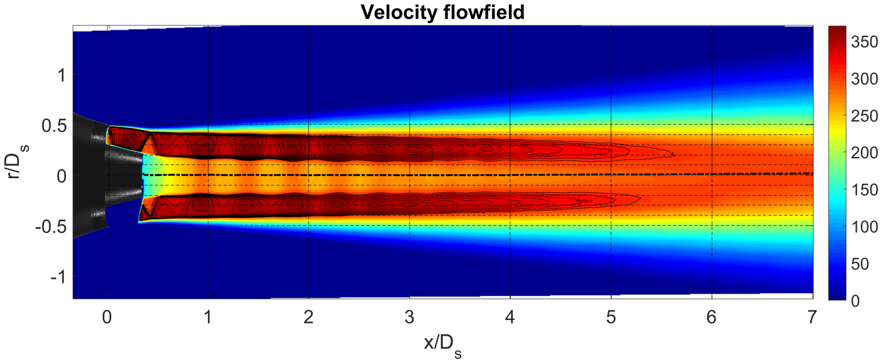

Figure A.33: Same as for Fig. A.31, the dashed lines represents the locations where radial and axial profiles for Mach number and turbulence intensity have been extracted.

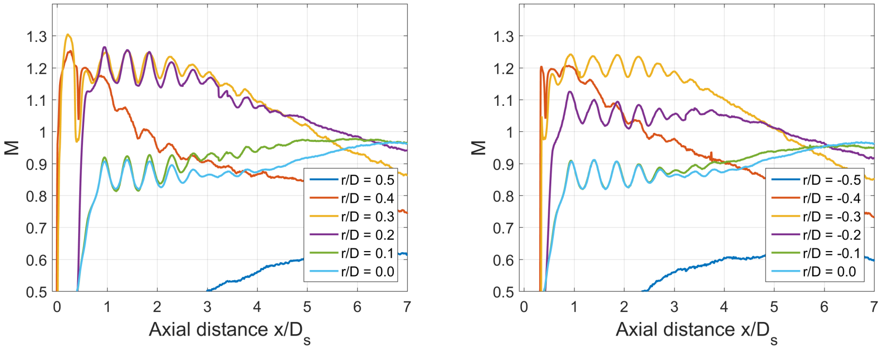

Figure A.34: Mach number axial profiles at several radial position for the upper part (left) and lower part (right) of the image.

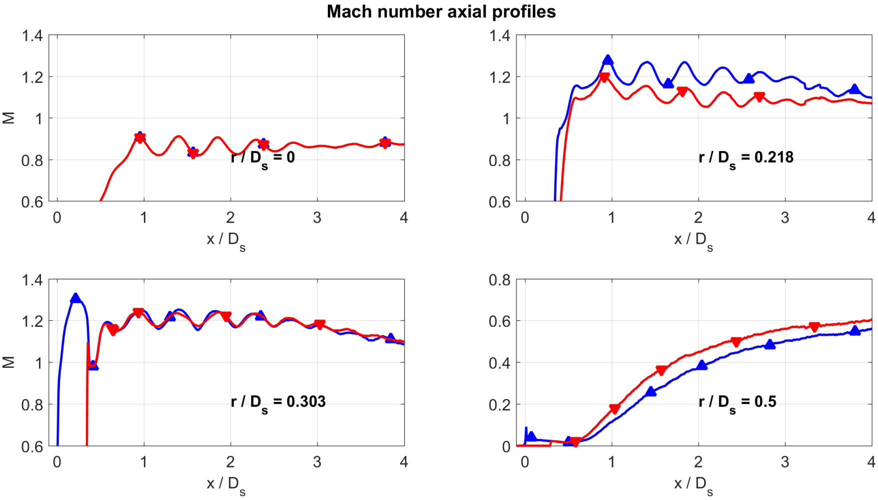

Figure A.35: Comparison of the Mach axial profiles between the upper part (in blue, up pointing triangles) and the lower part (in red, down pointing triangles) at several radial distance. The radial positions corresponds to the jet centerline (r/D = 0), the internal nozzle lip (r/D = 0.218), the ideal intersection point between the internal nozzle wall and the secondary nozzle exit area (r/D = 0.303). the secondary nozzle lip (r/D = 0.5).

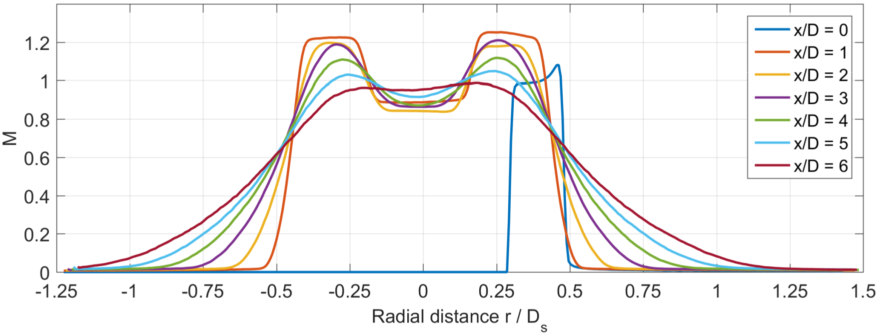

Figure A.36: Mach number radial profiles at several axial distance.

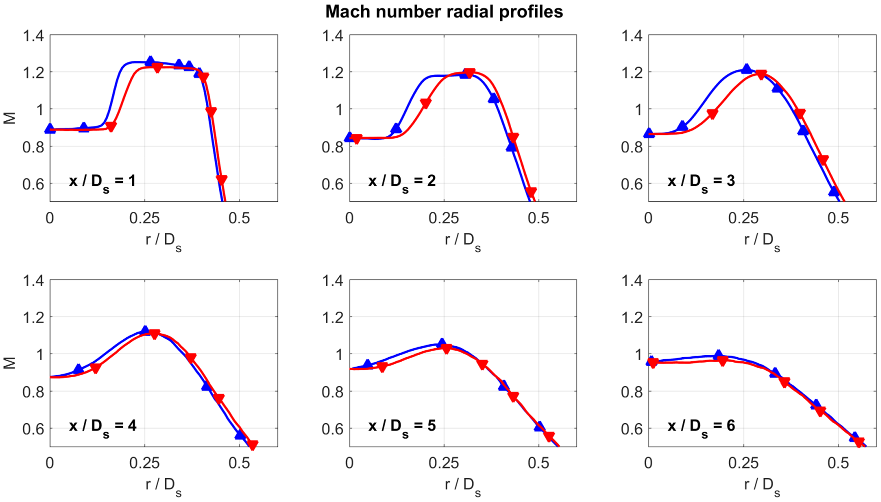

Figure A.37: Comparison of the Mach radial profiles between the upper part (in blue, up pointing triangles) and the lower part (in red, down pointing triangles) at several axial distance

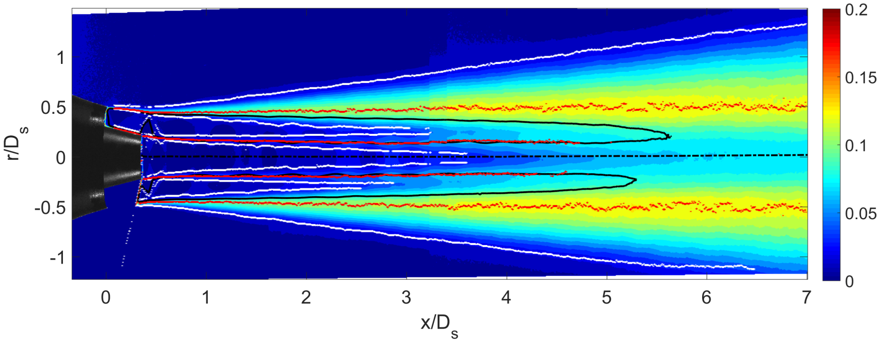

Figure A.38: Turbulence intensity flow field. In black, the M = 1 isoline, in red, the TI maxima locations, and in white, the computed limit of the shear layer.

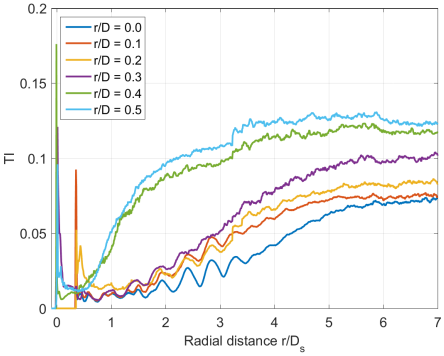

Figure A.39: Turbulent intensity axial profiles at several radial position for the upper part of the image.

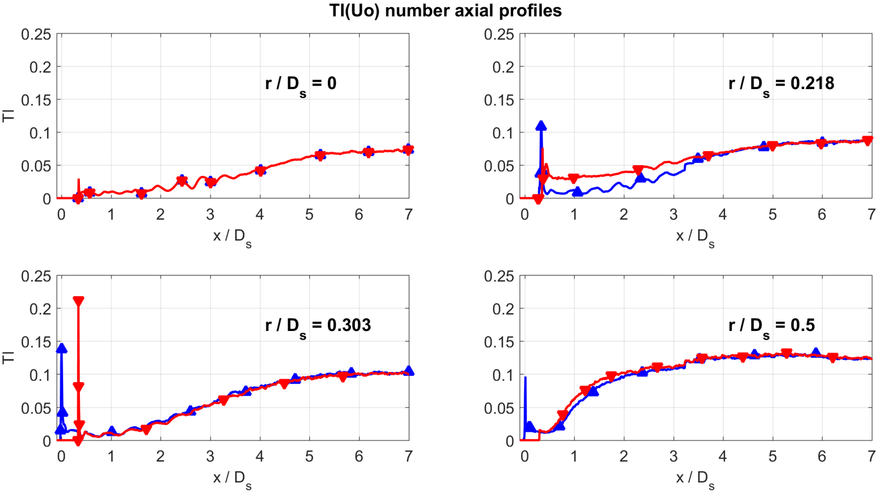

Figure A.40: Comparison of the TI axial profiles between the upper part (in blue, up pointing triangles) and the lower part (in red, down pointing triangles) at several radial distance. The radial positions corresponds to the jet centerline (r/D = 0), the internal nozzle lip (r/D = 0.218), the ideal intersection point between the internal nozzle wall and the secondary nozzle exit area (r/D = 0.303). the secondary nozzle lip (r/D = 0.5).

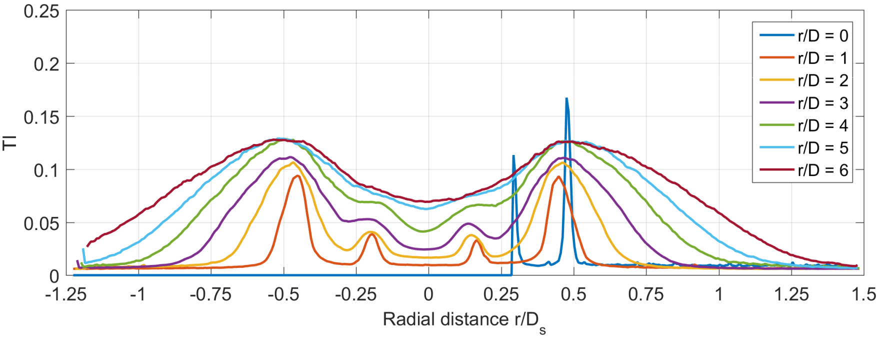

Figure A.41: Turbulence intensity radial profiles at several axial distances.

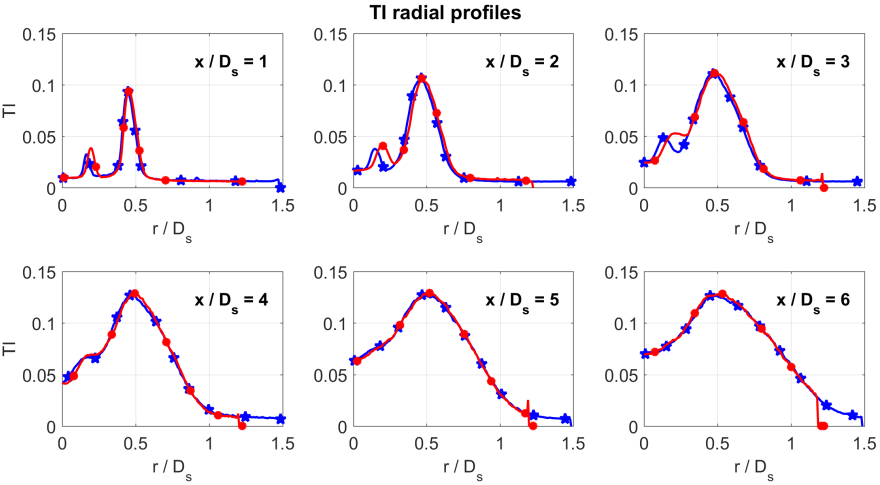

Figure A.42: Comparison of the TI radial profiles between the upper part (in blue, stars) and the lower part (in red, circles) at several axial distance.

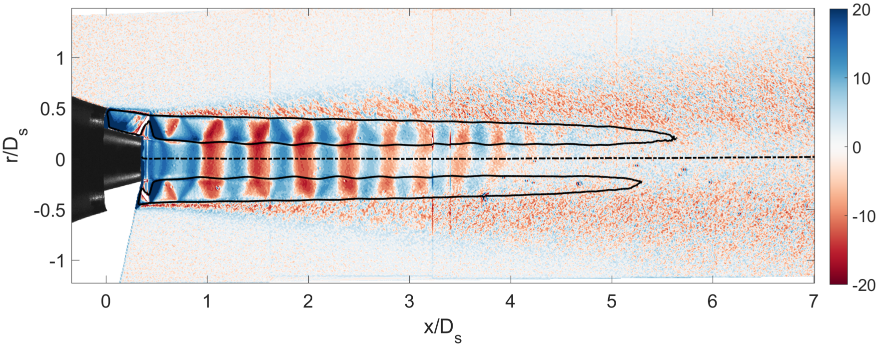

Figure A.43: Square root of the mean velocity divergence flow field $\nabla \cdot V/\sqrt{|\nabla \cdot V|}$. The image shows how the primary and secondary flows are expanding (in blue) and compressing (in red) with the shock-cells. The black line is the sonic line.

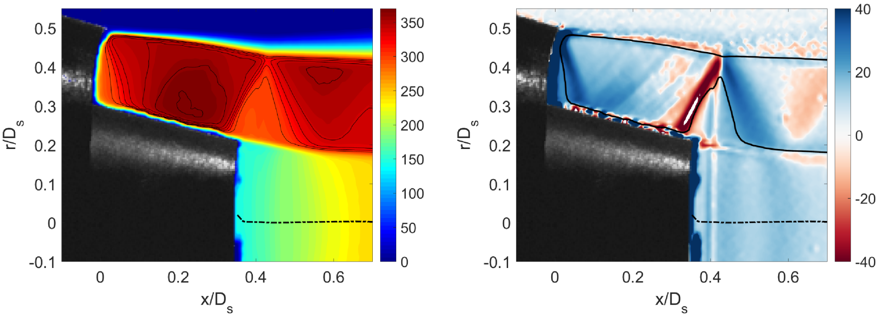

Figure A.44: Detail of the nozzle region. Velocity flow field with M > 1 isolines (left) and velocity divergence flow field (right).

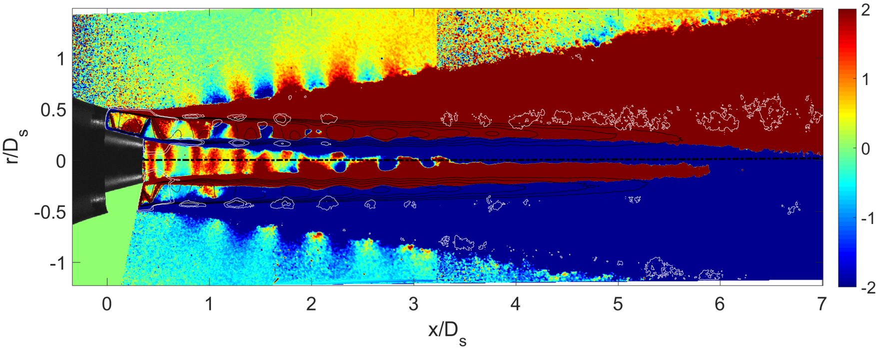

Figure A.45: Flow field of the averaged velocity fluctuations product $u'v'$. The black lines are M = [1:0.05:1.325] isocontour lines. In white, the isocontour lines of the mean radial velocity field (Fig. A.32). The scale enhances the lobes outside the jet shear layer.

A.4 Condition 05

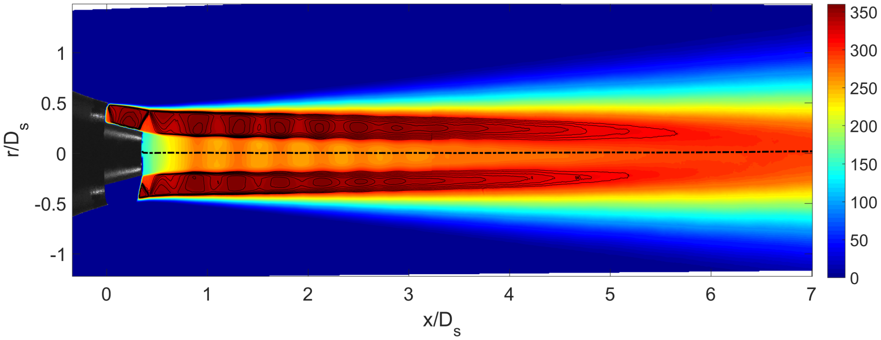

Figure A.46: Mean velocity module flow field with M > 1 isolines at condition 05.

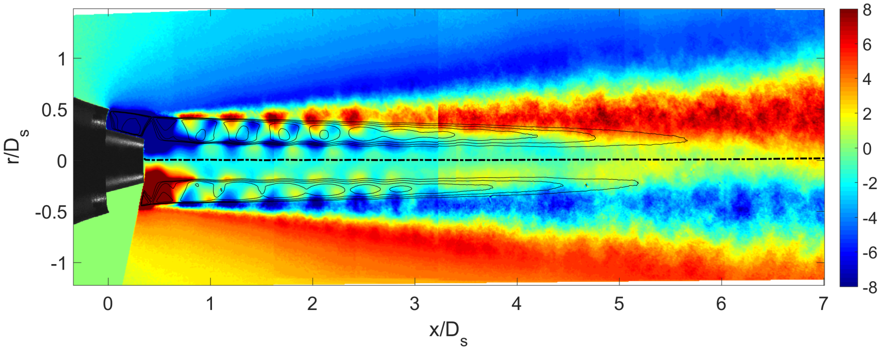

Figure A.47: Mean radial velocity flow field with M > 1 isolines.

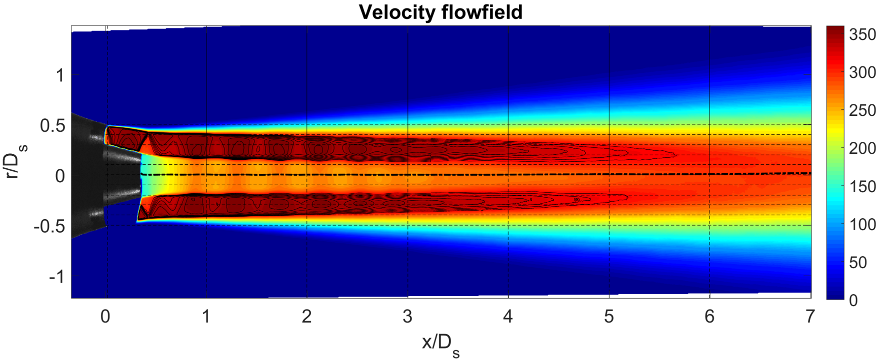

Figure A.48: Same as for Fig. A.46, the dashed lines represents the locations where radial and axial profiles for Mach number and turbulence intensity have been extracted.

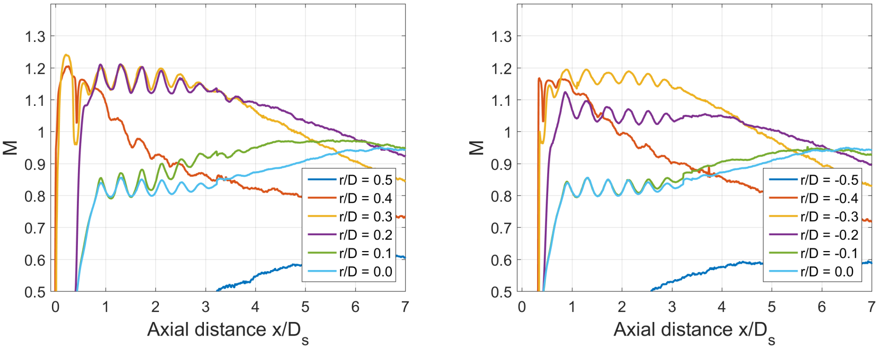

Figure A.49: Mach number axial profiles at several radial position for the upper part (left) and lower part (right) of the image.

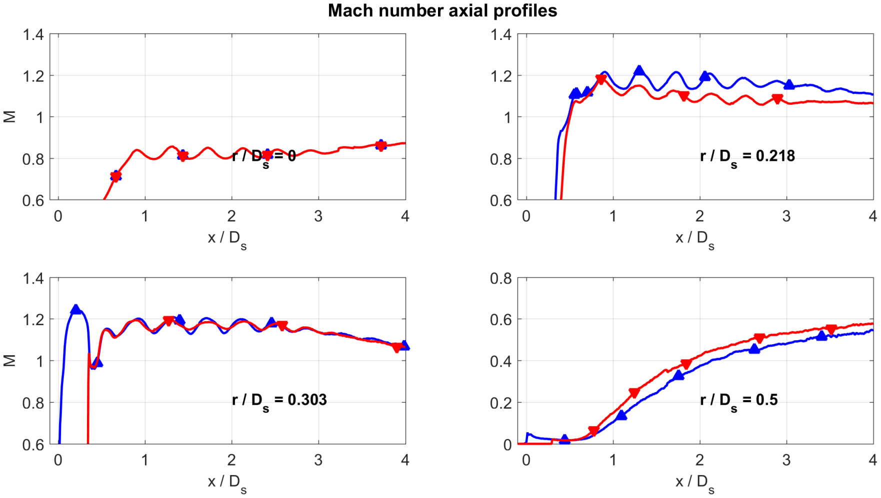

Figure A.50: Comparison of the Mach axial profiles between the upper part (in blue, up pointing triangles) and the lower part (in red, down pointing triangles) at several radial distance. The radial positions corresponds to the jet centerline (r/D = 0), the internal nozzle lip (r/D = 0.218), the ideal intersection point between the internal nozzle wall and the secondary nozzle exit area (r/D = 0.303). the secondary nozzle lip (r/D = 0.5).

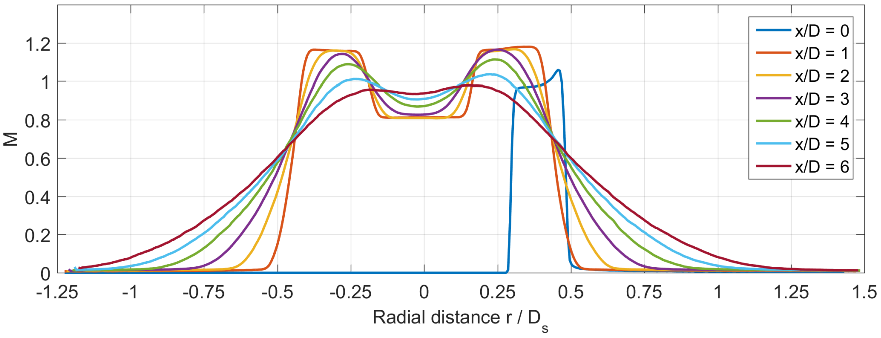

Figure A.51: Mach number radial profiles at several axial distance.

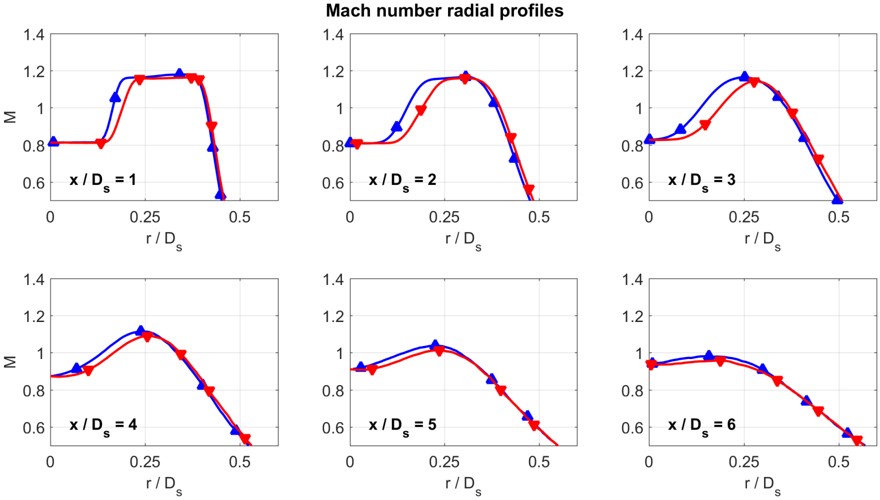

Figure A.52: Comparison of the Mach radial profiles between the upper part (in blue, up pointing triangles) and the lower part (in red, down pointing triangles) at several axial distance

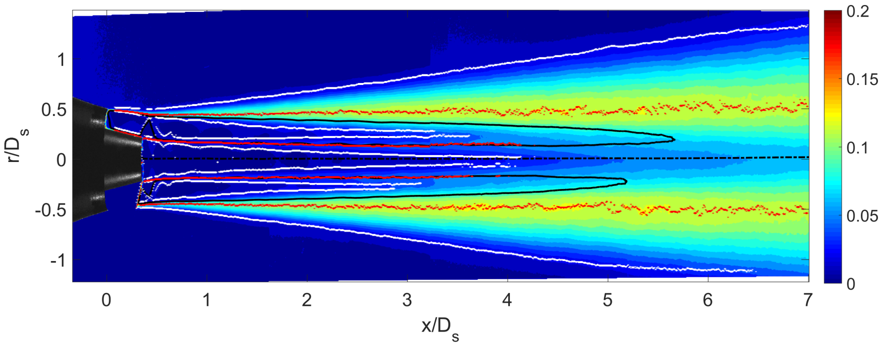

Figure A.53: Turbulence intensity flow field. In black, the M = 1 isoline, in red, the TI maxima locations, and in white, the computed limit of the shear layer.

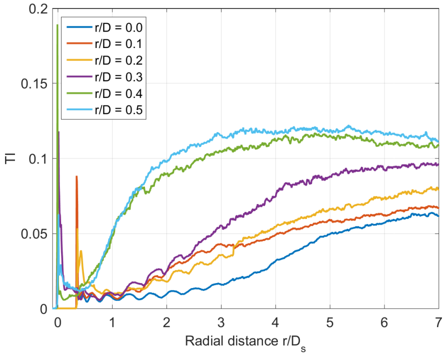

Figure A.54: Turbulent intensity axial profiles at several radial position for the upper part of the image.

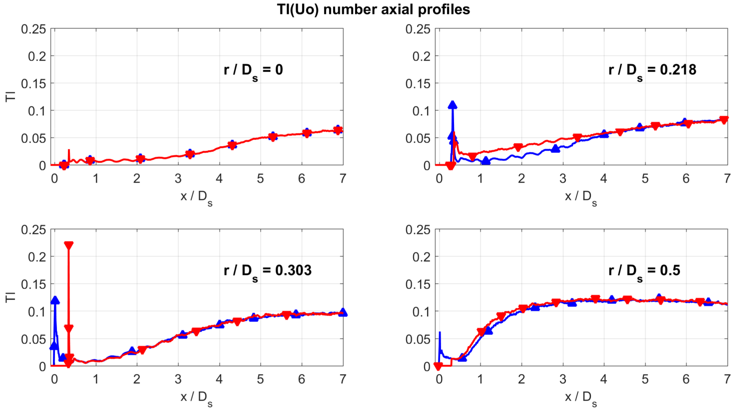

Figure A.55: Comparison of the TI axial profiles between the upper part (in blue, up pointing triangles) and the lower part (in red, down pointing triangles) at several radial distance. The radial positions corresponds to the jet centerline (r/D = 0), the internal nozzle lip (r/D = 0.218), the ideal intersection point between the internal nozzle wall and the secondary nozzle exit area (r/D = 0.303). the secondary nozzle lip (r/D = 0.5).

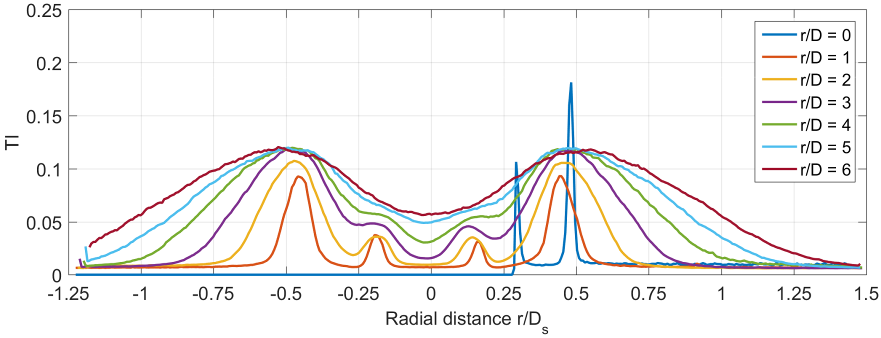

Figure A.56: Turbulence intensity radial profiles at several axial distances.

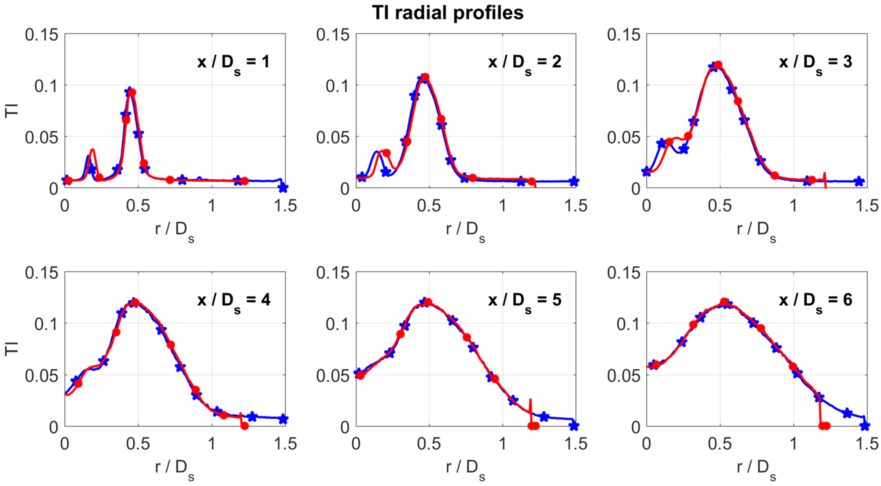

Figure A.57: Comparison of the TI radial profiles between the upper part (in blue, stars) and the lower part (in red, circles) at several axial distance.

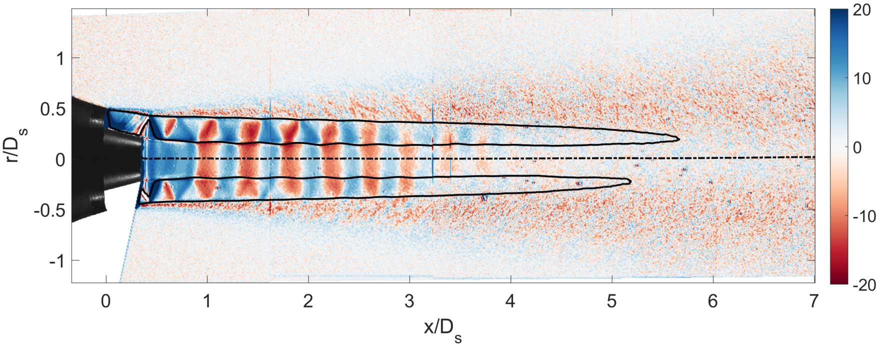

Figure A.58: Square root of the mean velocity divergence flow field $\nabla \cdot V/\sqrt{|\nabla \cdot V|}$. The image shows how the primary and secondary flows are expanding (in blue) and compressing (in red) with the shock-cells. The black line is the sonic line.

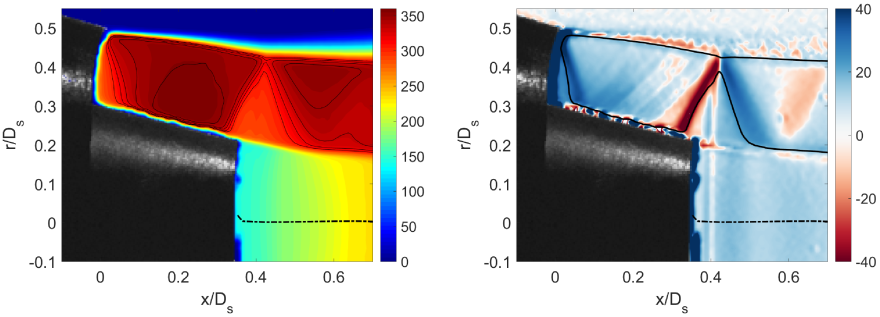

Figure A.59: Detail of the nozzle region. Velocity flow field with M > 1 isolines (left) and velocity divergence flow field (right).

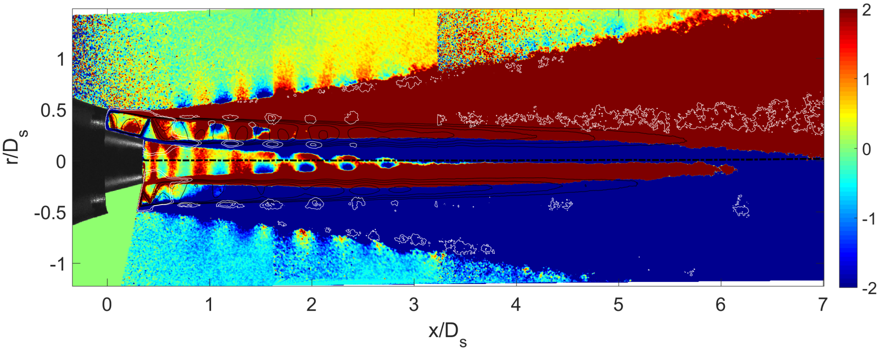

Figure A.60: Flow field of the averaged velocity fluctuations product $u'v'$. The black lines are M = [1:0.05:1.325] isocontour lines. In white, the isocontour lines of the mean radial velocity field (Fig. A.47). The scale enhances the lobes outside the jet shear layer.

A.5 Condition 06

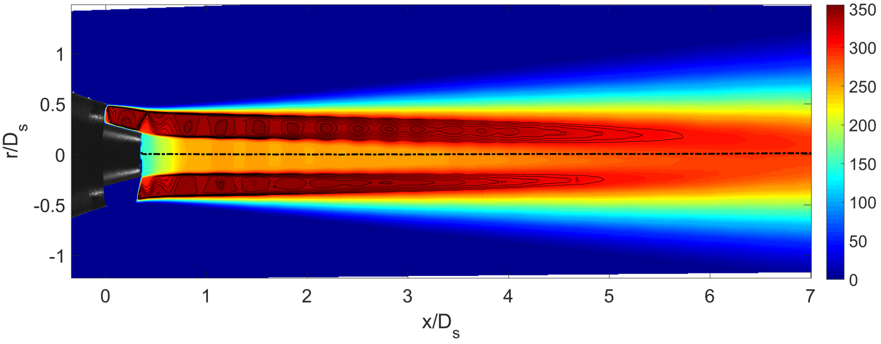

Figure A.61: Mean velocity module flow field with M > 1 isolines at condition 06.

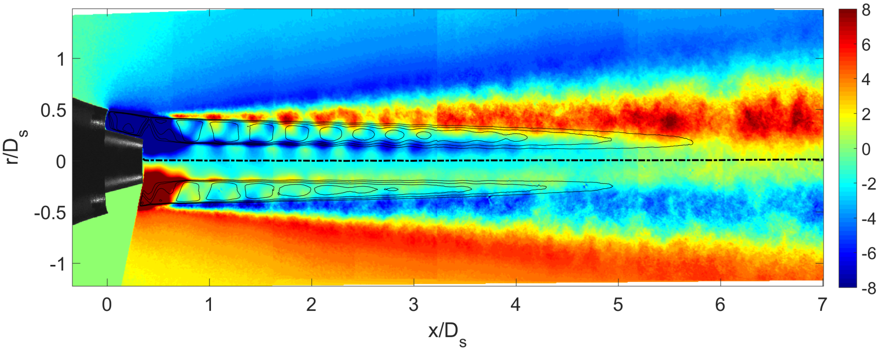

Figure A.62: Mean radial velocity flow field with M > 1 isolines.

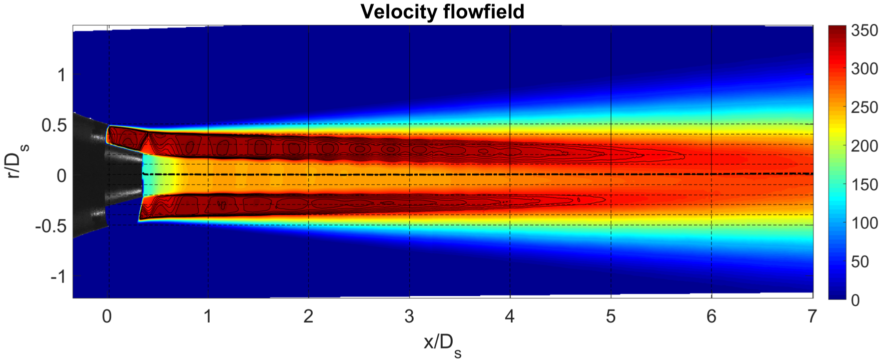

Figure A.63: Same as for Fig. A.61, the dashed lines represents the locations where radial and axial profiles for Mach number and turbulence intensity have been extracted.

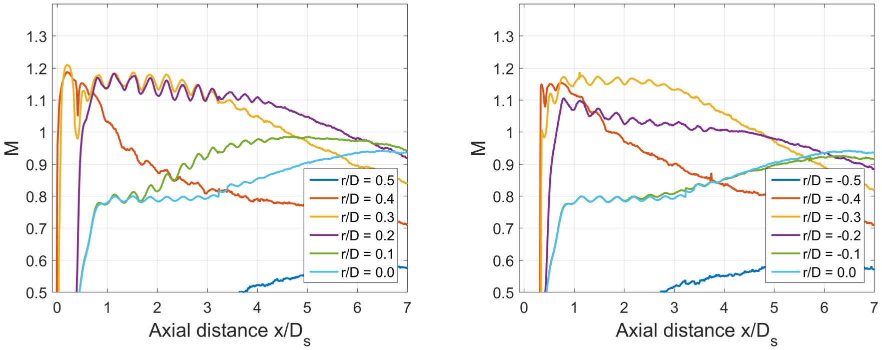

Figure A.64: Mach number axial profiles at several radial position for the upper part (left) and lower part (right) of the image.

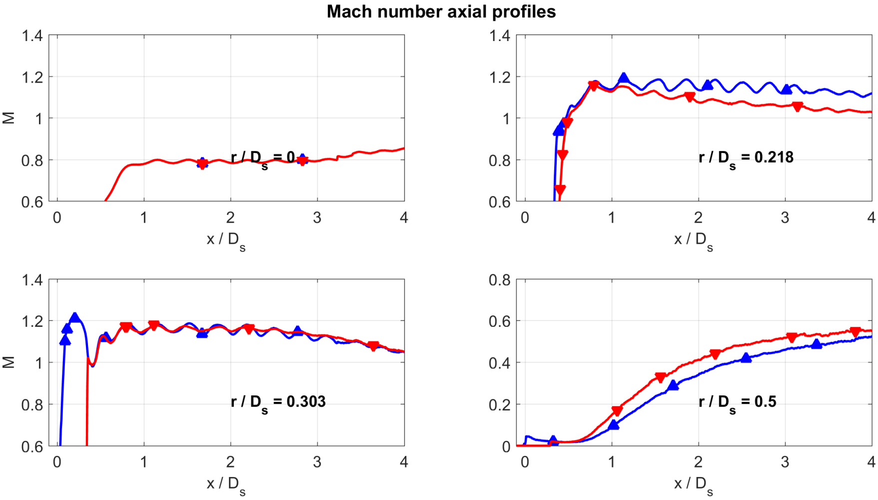

Figure A.65: Comparison of the Mach axial profiles between the upper part (in blue, up pointing triangles) and the lower part (in red, down pointing triangles) at several radial distance. The radial positions corresponds to the jet centerline (r/D = 0), the internal nozzle lip (r/D = 0.218), the ideal intersection point between the internal nozzle wall and the secondary nozzle exit area (r/D = 0.303). the secondary nozzle lip (r/D = 0.5).

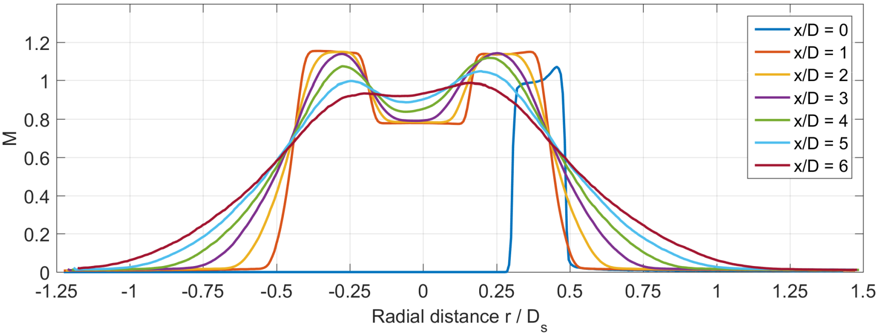

Figure A.66: Mach number radial profiles at several axial distance.

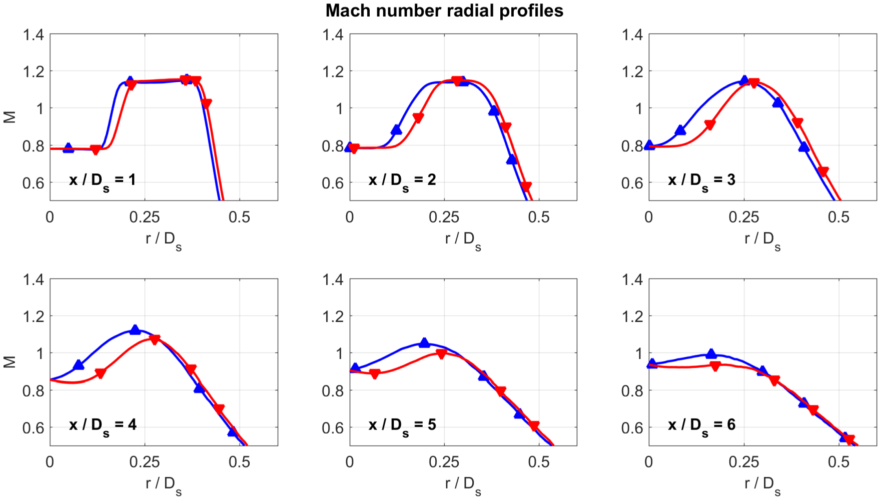

Figure A.67: Comparison of the Mach radial profiles between the upper part (in blue, up pointing triangles) and the lower part (in red, down pointing triangles) at several axial distance

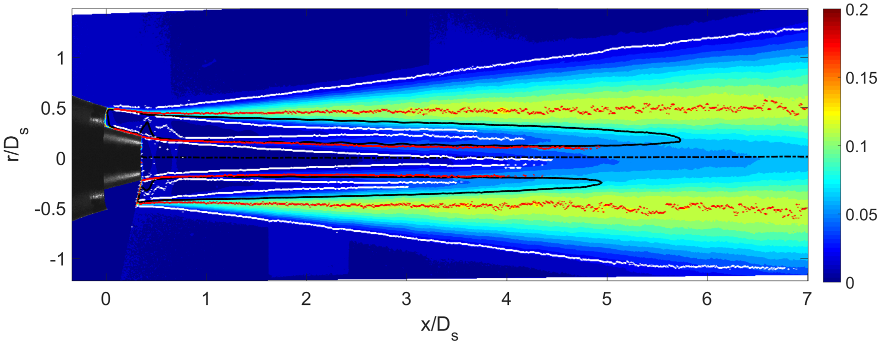

Figure A.68: Turbulence intensity flow field. In black, the M = 1 isoline, in red, the TI maxima locations, and in white, the computed limit of the shear layer.

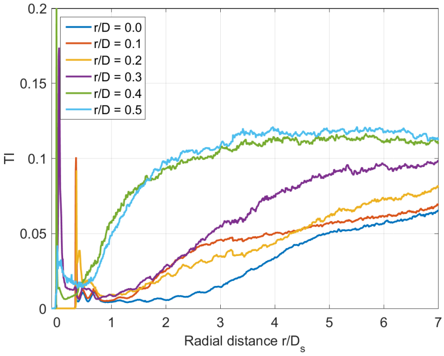

Figure A.69: Turbulent intensity axial profiles at several radial position for the upper part of the image.

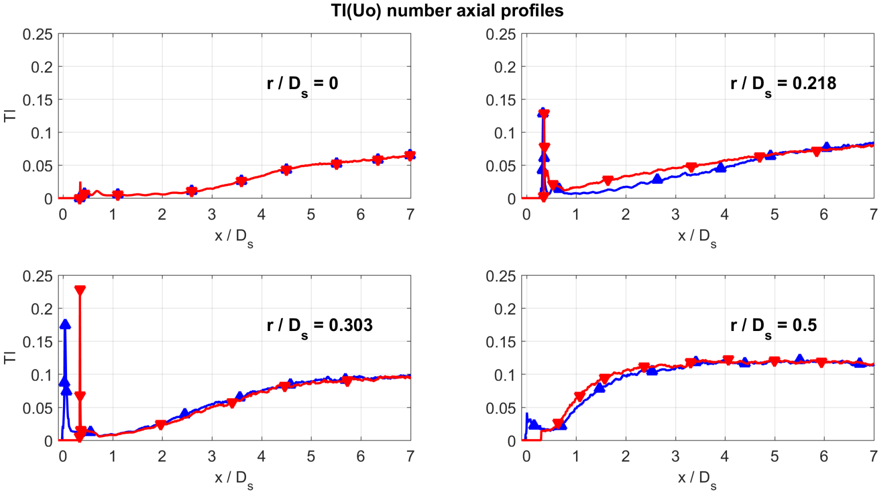

Figure A.70: Comparison of the TI axial profiles between the upper part (in blue, up pointing triangles) and the lower part (in red, down pointing triangles) at several radial distance. The radial positions corresponds to the jet centerline (r/D = 0), the internal nozzle lip (r/D = 0.218), the ideal intersection point between the internal nozzle wall and the secondary nozzle exit area (r/D = 0.303). the secondary nozzle lip (r/D = 0.5).

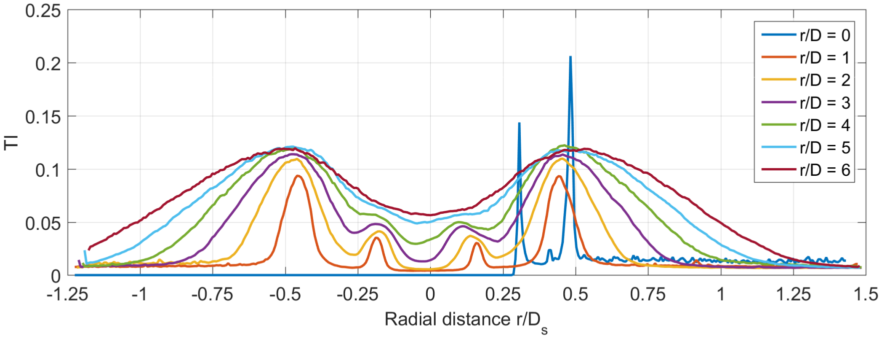

Figure A.71: Turbulence intensity radial profiles at several axial distances.

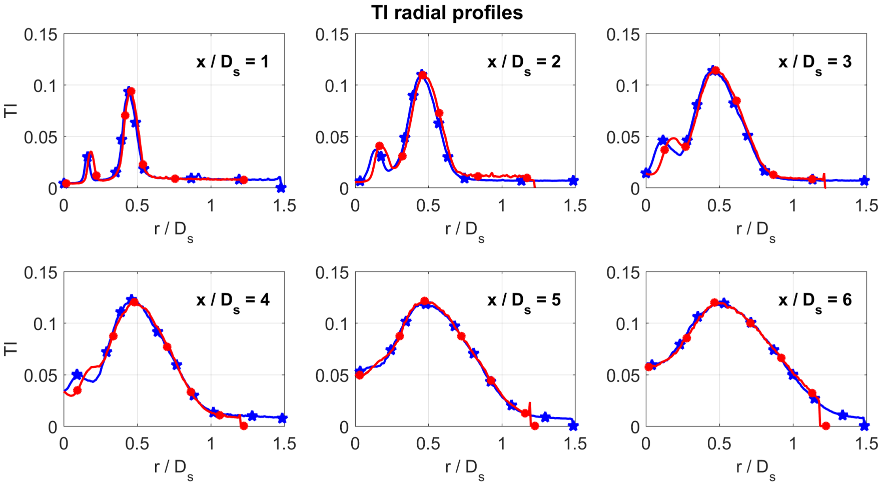

Figure A.72: Comparison of the TI radial profiles between the upper part (in blue, stars) and the lower part (in red, circles) at several axial distance.

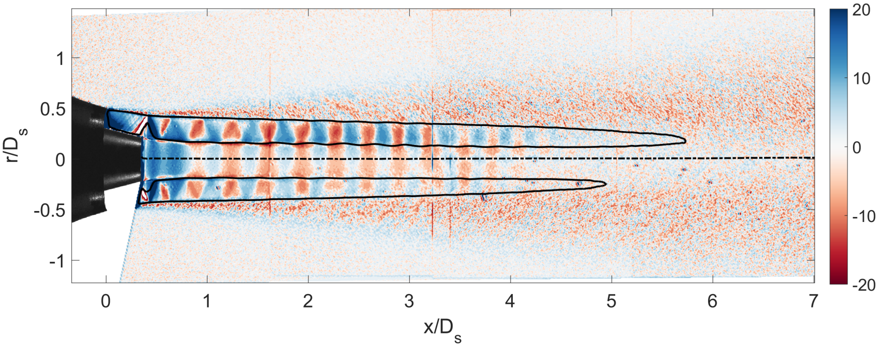

Figure A.73: Square root of the mean velocity divergence flow field $\nabla \cdot V/\sqrt{|\nabla \cdot V|}$. The image shows how the primary and secondary flows are expanding (in blue) and compressing (in red) with the shock-cells. The black line is the sonic line.

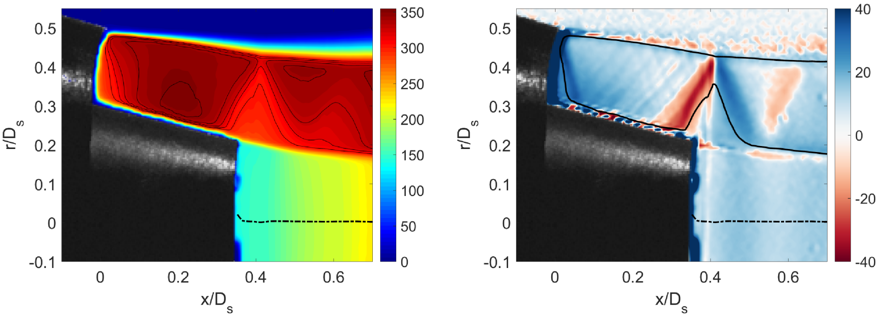

Figure A.74: Detail of the nozzle region. Velocity flow field with M > 1 isolines (left) and velocity divergence flow field (right).

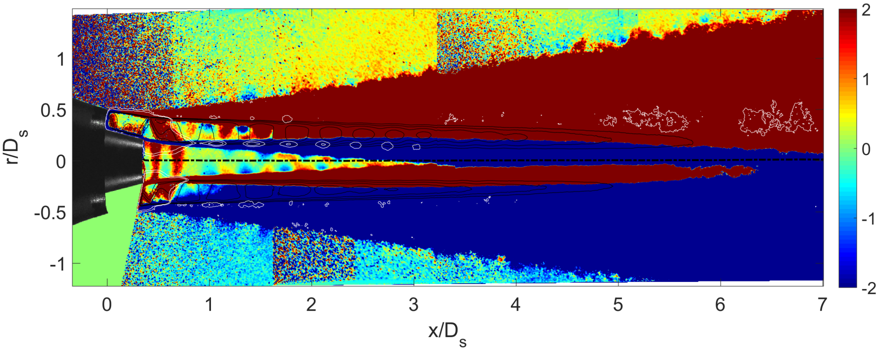

Figure A.75: Flow field of the averaged velocity fluctuations product $u'v'$. The black lines are M = [1:0.05:1.325] isocontour lines. In white, the isocontour lines of the mean radial velocity field (Fig. A.62). The scale enhances the lobes outside the jet shear layer.

A.6 Condition 08

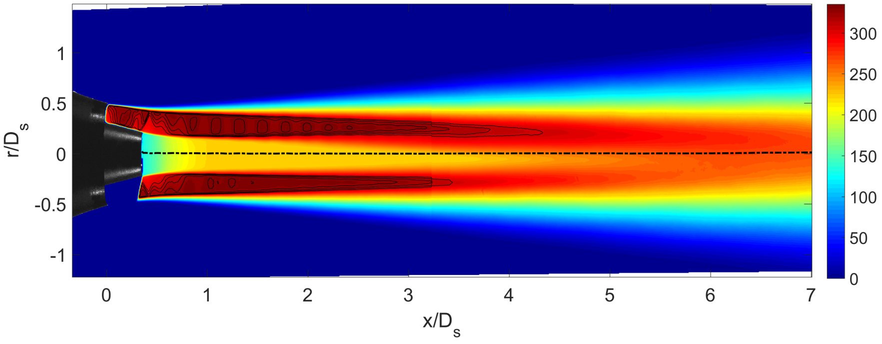

Figure A.76: Mean velocity module flow field with M > 1 isolines at condition 08.

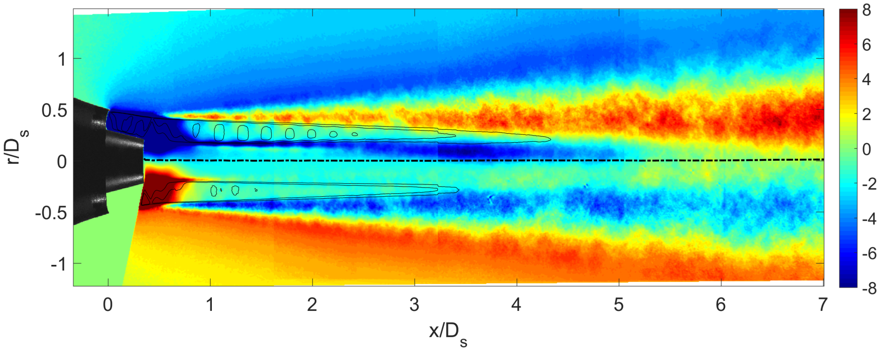

Figure A.77: Mean radial velocity flow field with M > 1 isolines.

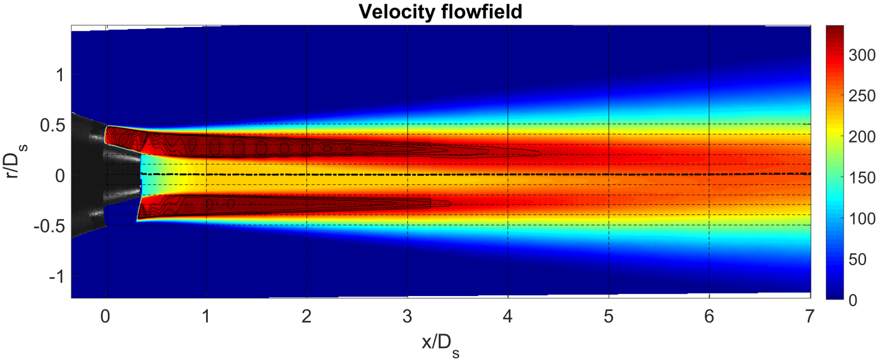

Figure A.78: Same as for Fig. A.76, the dashed lines represents the locations where radial and axial profiles for Mach number and turbulence intensity have been extracted.

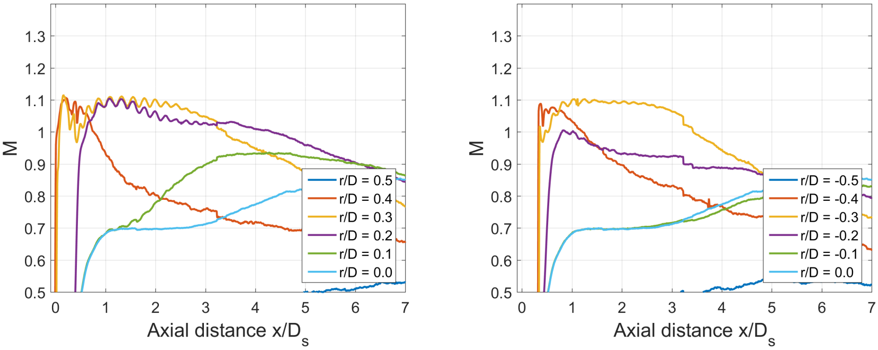

Figure A.79: Mach number axial profiles at several radial position for the upper part (left) and lower part (right) of the image.

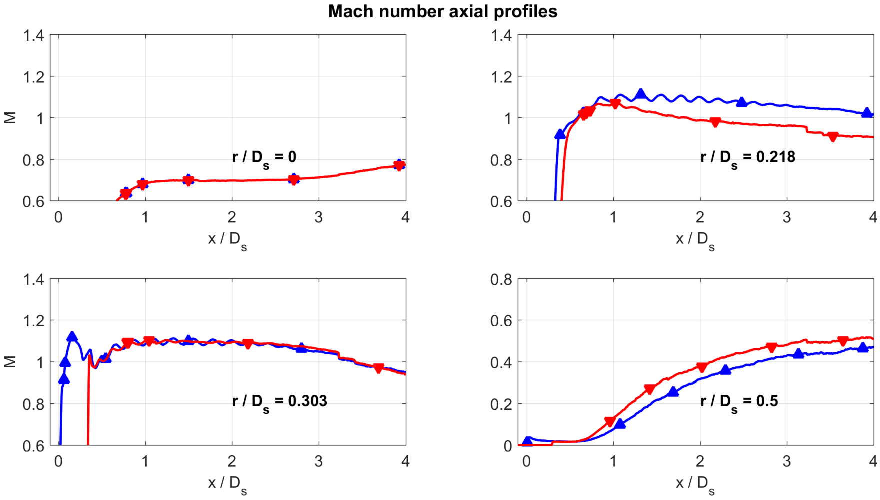

Figure A.80: Comparison of the Mach axial profiles between the upper part (in blue, up pointing triangles) and the lower part (in red, down pointing triangles) at several radial distance. The radial positions corresponds to the jet centerline (r/D = 0), the internal nozzle lip (r/D = 0.218), the ideal intersection point between the internal nozzle wall and the secondary nozzle exit area (r/D = 0.303). the secondary nozzle lip (r/D = 0.5).

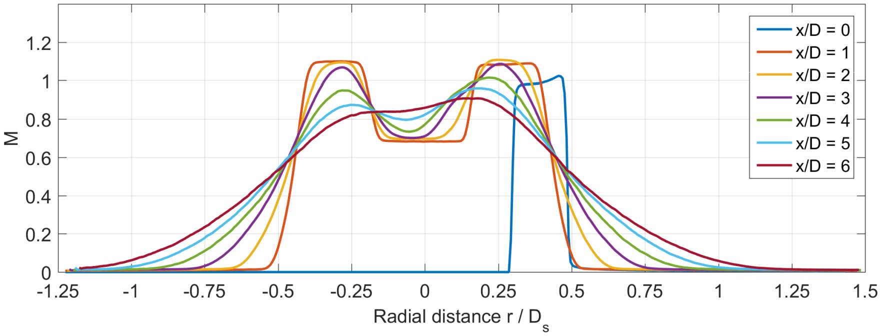

Figure A.81: Mach number radial profiles at several axial distance.

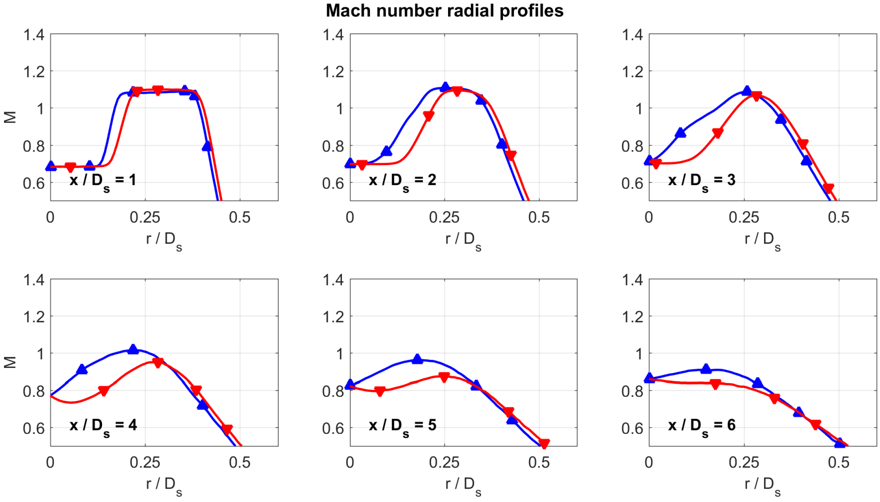

Figure A.82: Comparison of the Mach radial profiles between the upper part (in blue, up pointing triangles) and the lower part (in red, down pointing triangles) at several axial distance

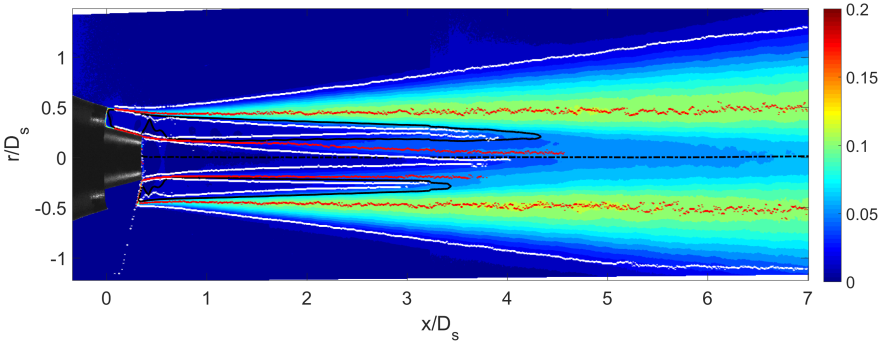

Figure A.83: Turbulence intensity flow field. In black, the M = 1 isoline, in red, the TI maxima locations, and in white, the computed limit of the shear layer.

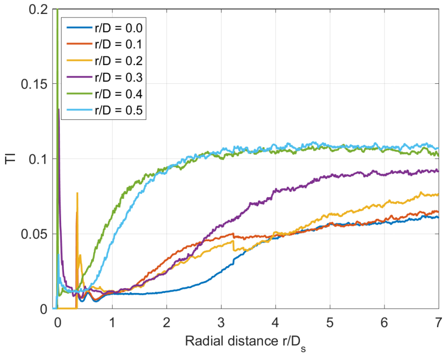

Figure A.84: Turbulent intensity axial profiles at several radial position for the upper part of the image.

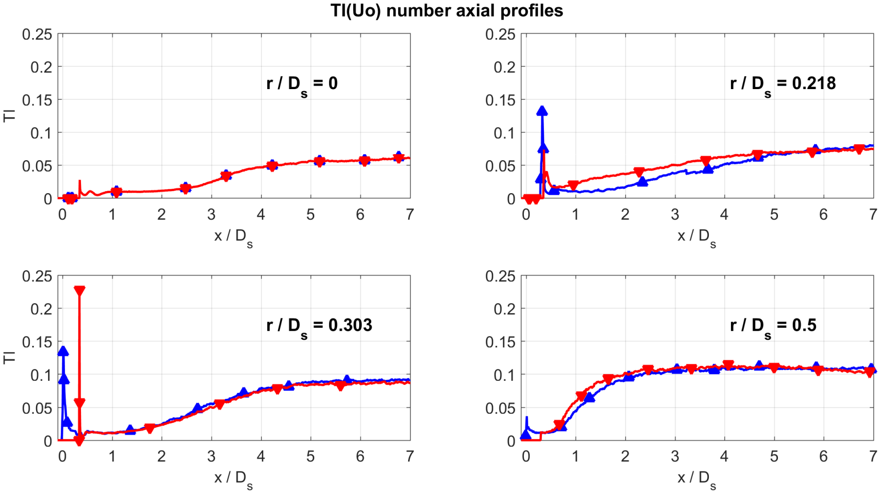

Figure A.85: Comparison of the TI axial profiles between the upper part (in blue, up pointing triangles) and the lower part (in red, down pointing triangles) at several radial distance. The radial positions corresponds to the jet centerline (r/D = 0), the internal nozzle lip (r/D = 0.218), the ideal intersection point between the internal nozzle wall and the secondary nozzle exit area (r/D = 0.303). the secondary nozzle lip (r/D = 0.5).

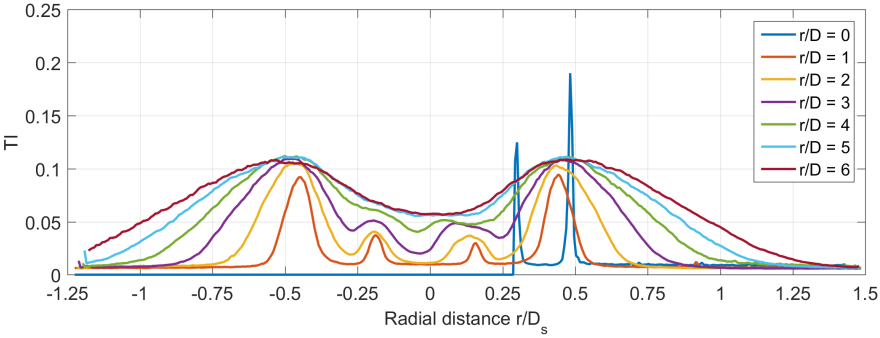

Figure A.86: Turbulence intensity radial profiles at several axial distances.

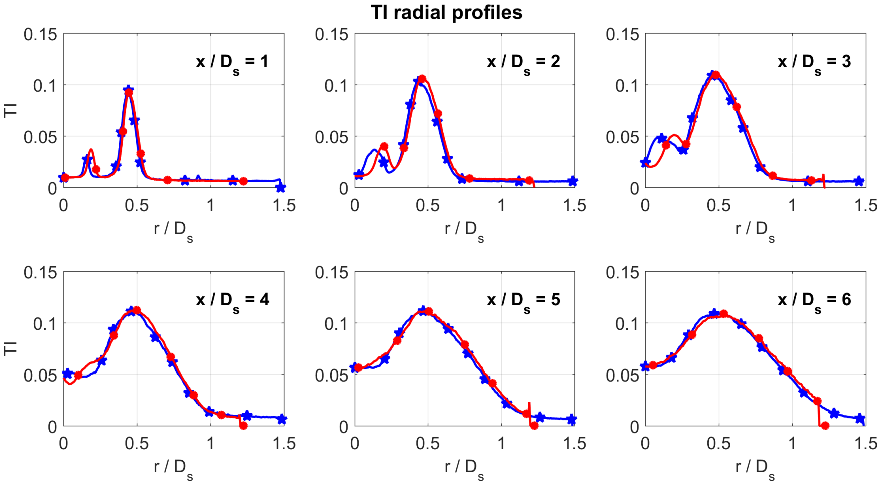

Figure A.87: Comparison of the TI radial profiles between the upper part (in blue, stars) and the lower part (in red, circles) at several axial distance.

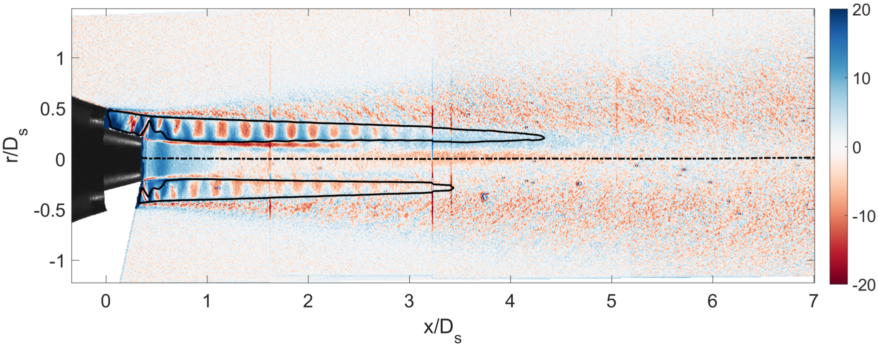

Figure A.88: Square root of the mean velocity divergence flow field $\nabla \cdot V/\sqrt{|\nabla \cdot V|}$. The image shows how the primary and secondary flows are expanding (in blue) and compressing (in red) with the shock-cells. The black line is the sonic line.

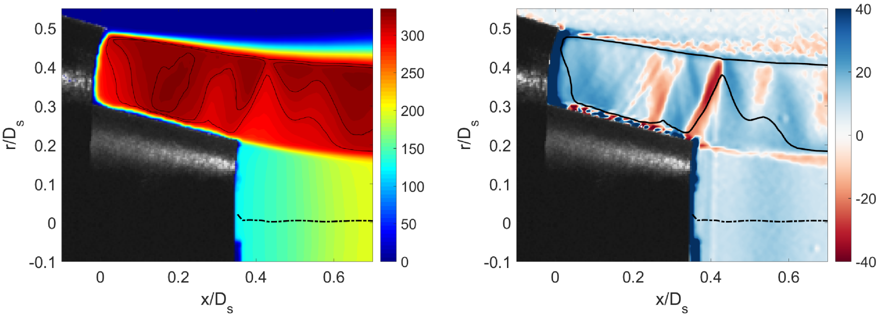

Figure A.89: Detail of the nozzle region. Velocity flow field with M > 1 isolines (left) and velocity divergence flow field (right).

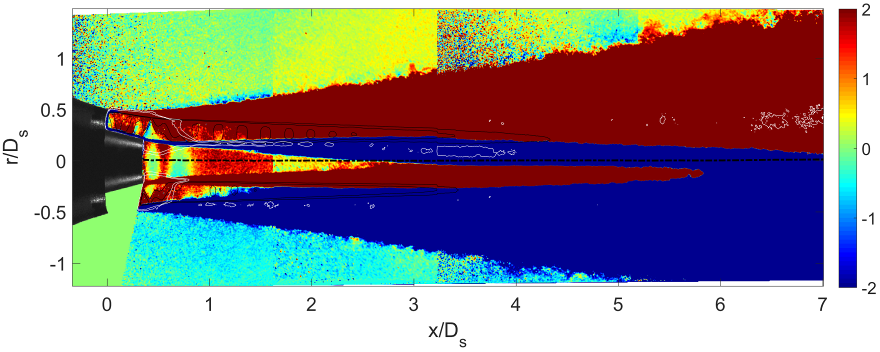

Figure A.90: Flow field of the averaged velocity fluctuations product $u'v'$. The black lines are M = [1:0.05:1.325] isocontour lines. In white, the isocontour lines of the mean radial velocity field (Fig. A.77). There are no visible lobes outside the shear layer.

A.7 Condition 09

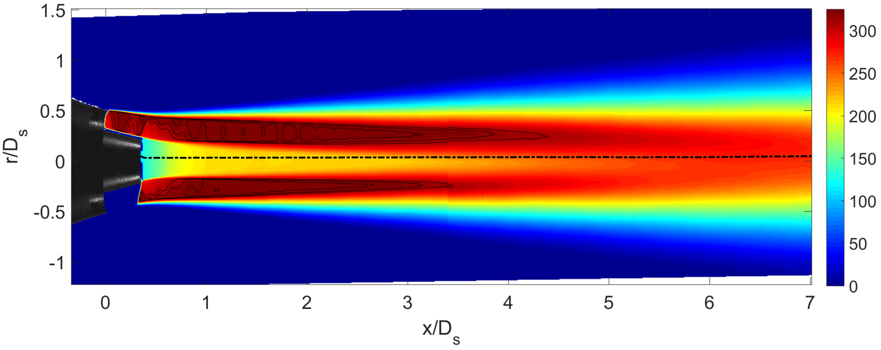

Figure A.91: Mean velocity module flow field with M > 1 isolines at condition 09.

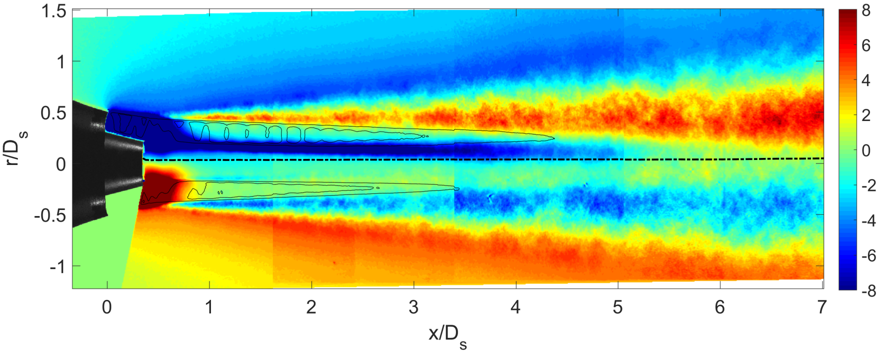

Figure A.92: Mean radial velocity flow field with M > 1 isolines.

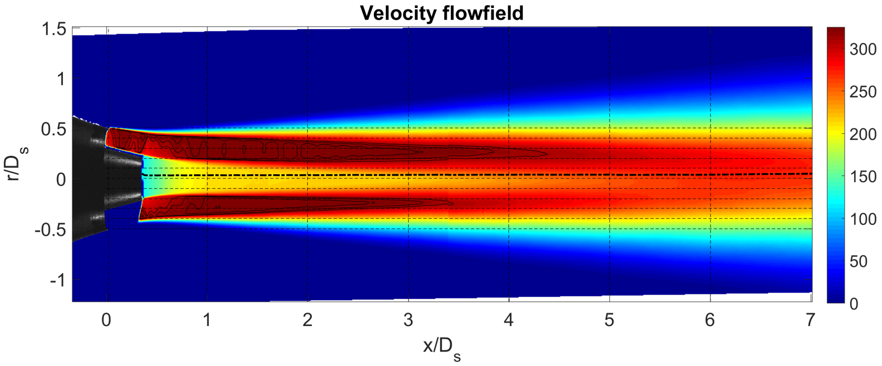

Figure A.93: Same as for Fig. A.91, the dashed lines represents the locations where radial and axial profiles for Mach number and turbulence intensity have been extracted.

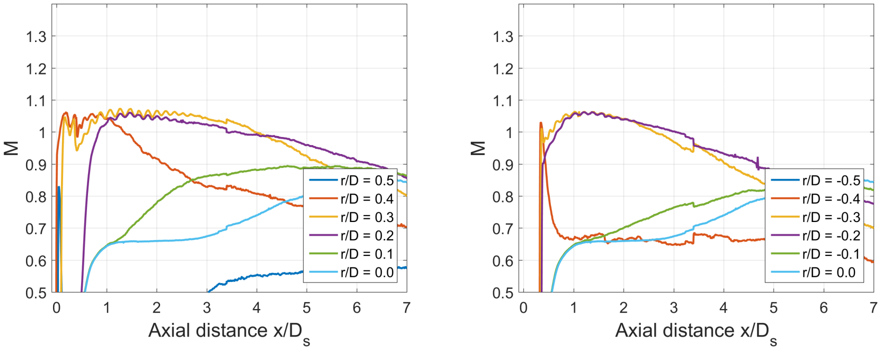

Figure A.94: Mach number axial profiles at several radial position for the upper part (left) and lower part (right) of the image.

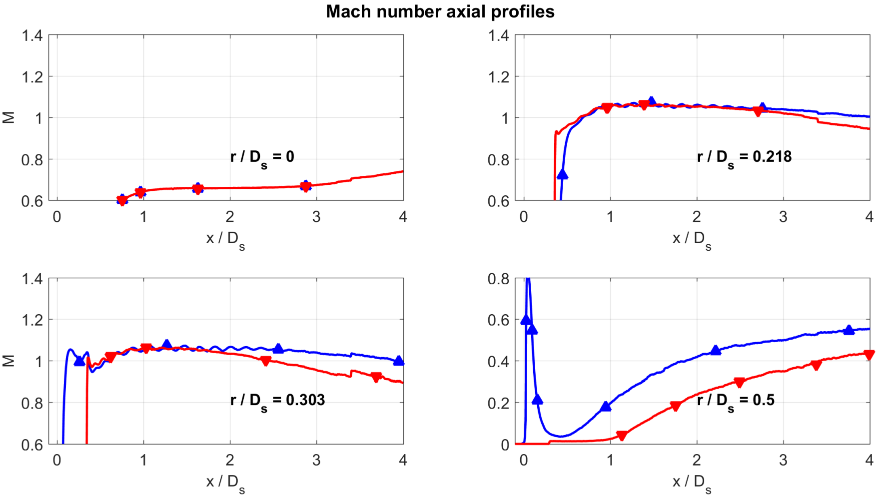

Figure A.95: Comparison of the Mach axial profiles between the upper part (in blue, up pointing triangles) and the lower part (in red, down pointing triangles) at several radial distance. The radial positions corresponds to the jet centerline (r/D = 0), the internal nozzle lip (r/D = 0.218), the ideal intersection point between the internal nozzle wall and the secondary nozzle exit area (r/D = 0.303). the secondary nozzle lip (r/D = 0.5).

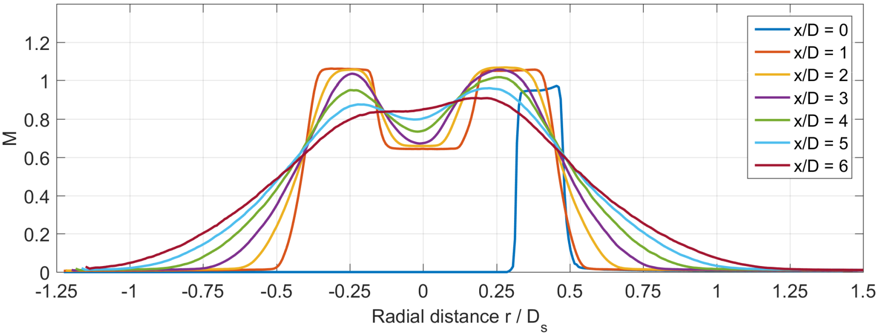

Figure A.96: Mach number radial profiles at several axial distance.

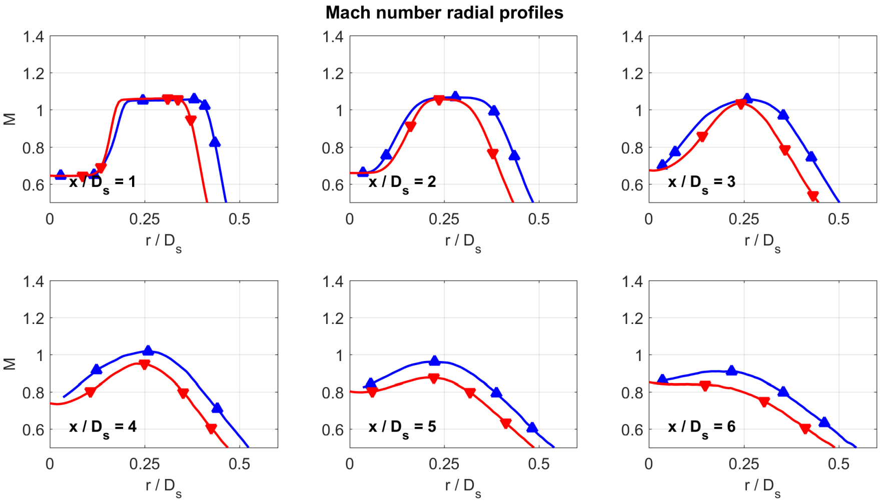

Figure A.97: Comparison of the Mach radial profiles between the upper part (in blue, up pointing triangles) and the lower part (in red, down pointing triangles) at several axial distance

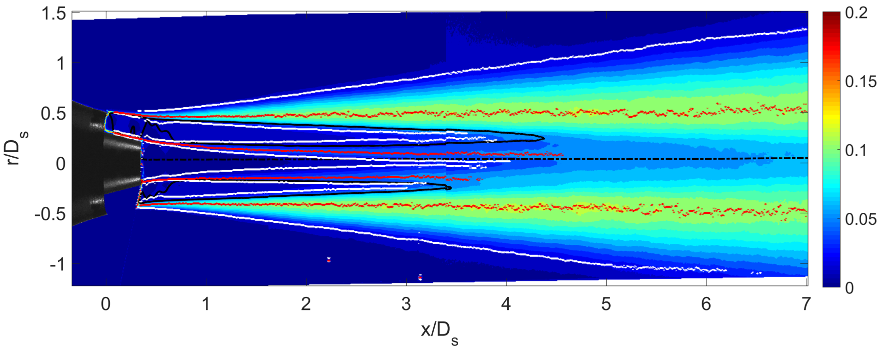

Figure A.98: Turbulence intensity flow field. In black, the M = 1 isoline, in red, the TI maxima locations, and in white, the computed limit of the shear layer.

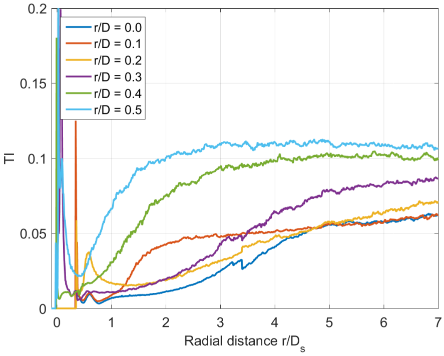

Figure A.99: Turbulent intensity axial profiles at several radial position for the upper part of the image.

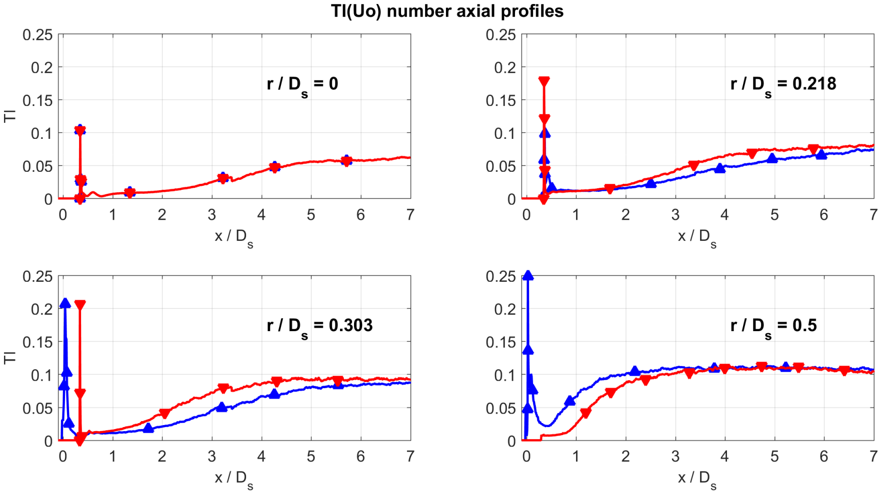

Figure A.100: Comparison of the TI axial profiles between the upper part (in blue, up pointing triangles) and the lower part (in red, down pointing triangles) at several radial distance. The radial positions corresponds to the jet centerline (r/D = 0), the internal nozzle lip (r/D = 0.218), the ideal intersection point between the internal nozzle wall and the secondary nozzle exit area (r/D = 0.303). the secondary nozzle lip (r/D = 0.5).

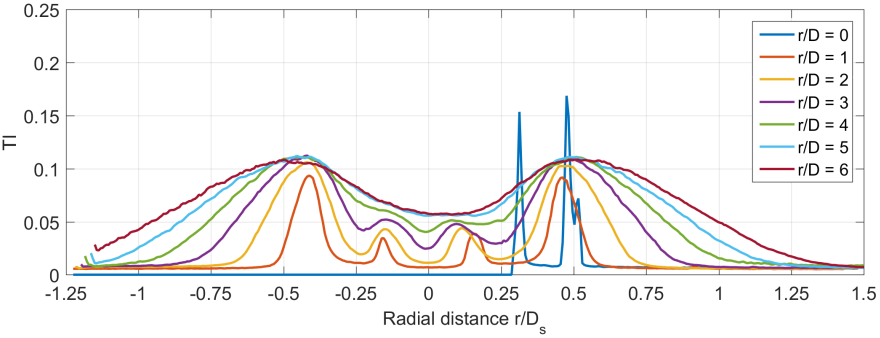

Figure A.101: Turbulence intensity radial profiles at several axial distances.

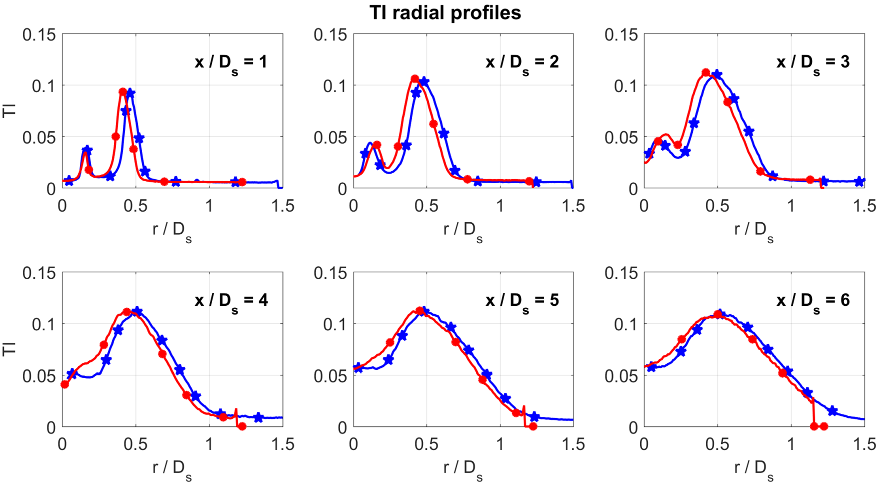

Figure A.102: Comparison of the TI radial profiles between the upper part (in blue, stars) and the lower part (in red, circles) at several axial distance.

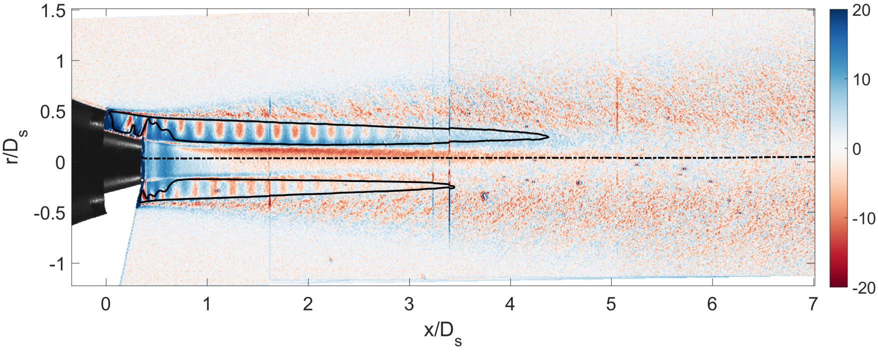

Figure A.103: Square root of the mean velocity divergence flow field $\nabla \cdot V/\sqrt{|\nabla \cdot V|}$. The image shows how the primary and secondary flows are expanding (in blue) and compressing (in red) with the shock-cells. The black line is the sonic line.

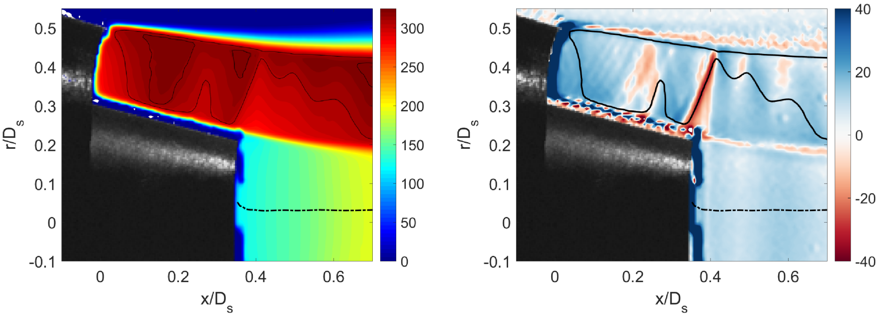

Figure A.104: Detail of the nozzle region. Velocity flow field with M > 1 isolines (left) and velocity divergence flow field (right).

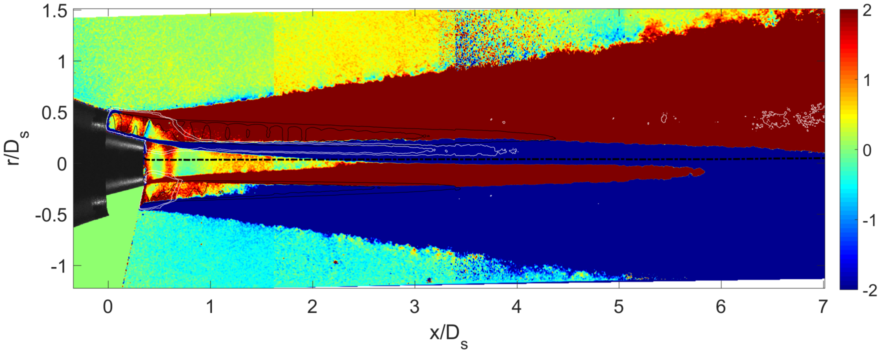

Figure A.105: Flow field of the averaged velocity fluctuations product $u'v'$. The black lines are M = [1:0.05:1.325] isocontour lines. In white, the isocontour lines of the mean radial velocity field (Fig. A.92). There are no visible lobes outside the shear layer.

Appendix B

Acoustic Measurements

B.1 Condition 01: FNPR = 2.45, CNPR = 1.68

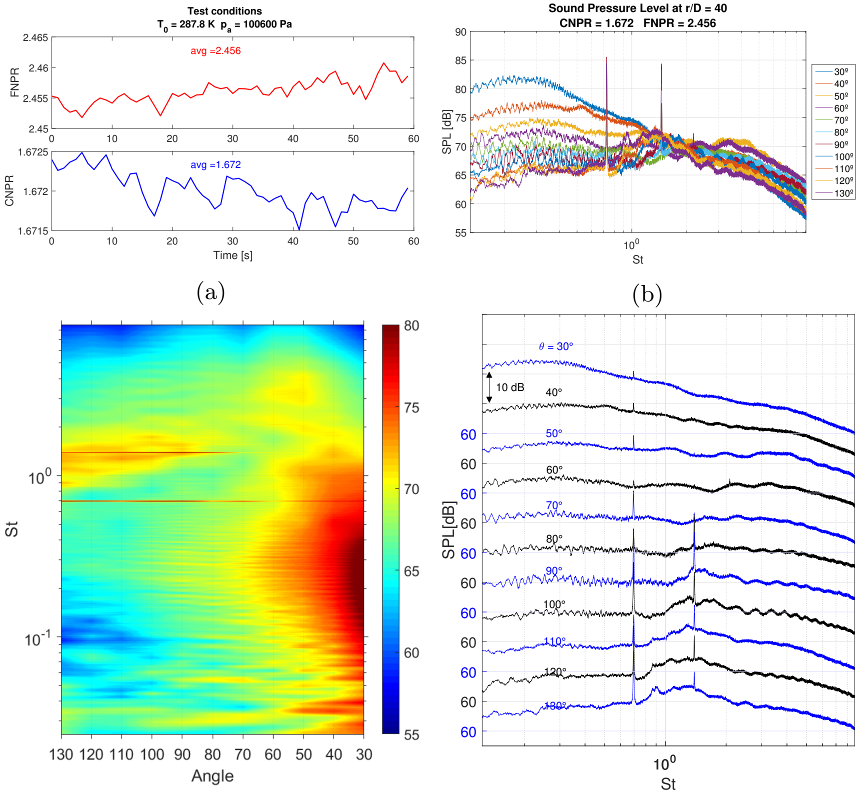

(a) (b)

(c) (d)

Figure B.1: Overview of SPL (ref. $2 \cdot 10^{-5}$ Pa) for condition 01 at all the measured angles in St. a) Pressure conditions measured by the transducers during the acquisition. b) Superposition of the SPL at all measured angles. c) Contour map of the SPL interpolated along the angles. d) Staggered acoustic spectra.

B.2 Condition 02: FNPR = 2.5, CNPR = 1.72

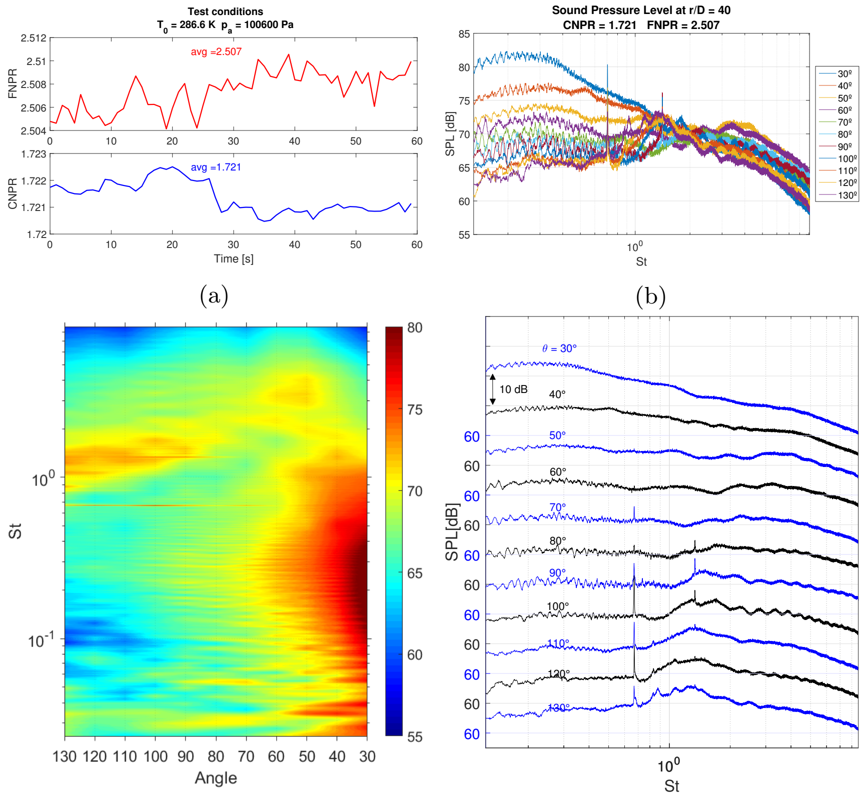

(a)

(b)

(c)

(d)

Figure B.2: Overview of SPL (ref. $2 \cdot 10^{-5}$ Pa) for condition 02 at all the measured angles in St. a) Pressure conditions measured by the transducers during the acquisition. b) Superposition of the SPL at all measured angles. c) Contour map of the SPL interpolated along the angles. d) Staggered acoustic spectra.

B.3 Condition 03: FNPR = 2.42, CNPR = 1.65

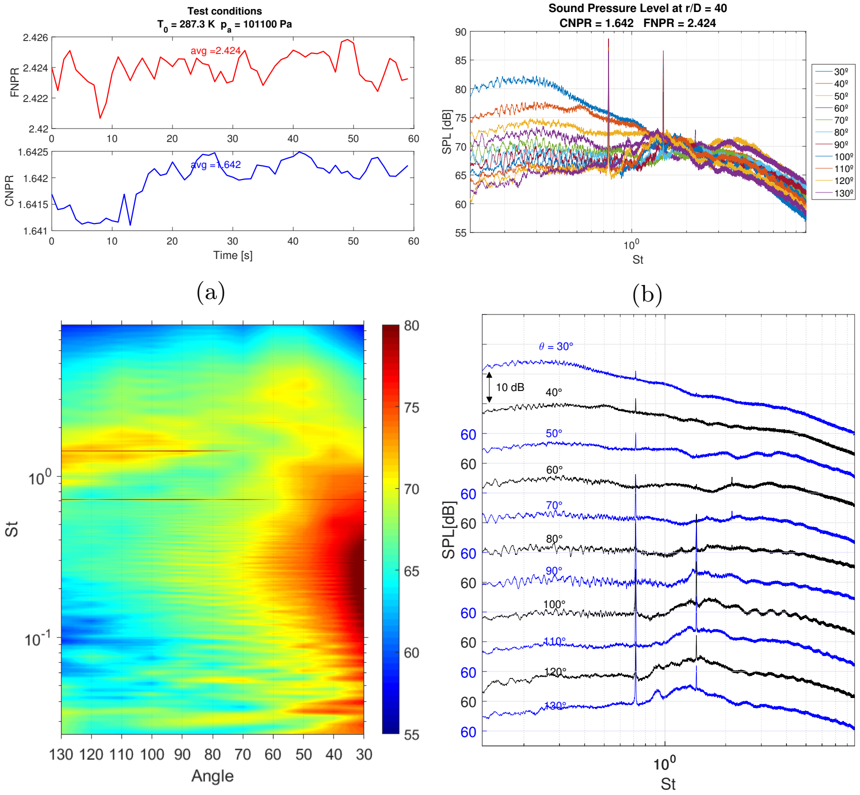

(a) (b)

(c) (d)

Figure B.3: Overview of SPL (ref. $2 \cdot 10^{-5}$ Pa) for condition 03 at all the measured angles in St. a) Pressure conditions measured by the transducers during the acquisition. b) Superposition of the SPL at all measured angles. c) Contour map of the SPL interpolated along the angles. d) Staggered acoustic spectra.

B.4 Condition 04: FNPR = 2.4, CNPR = 1.63

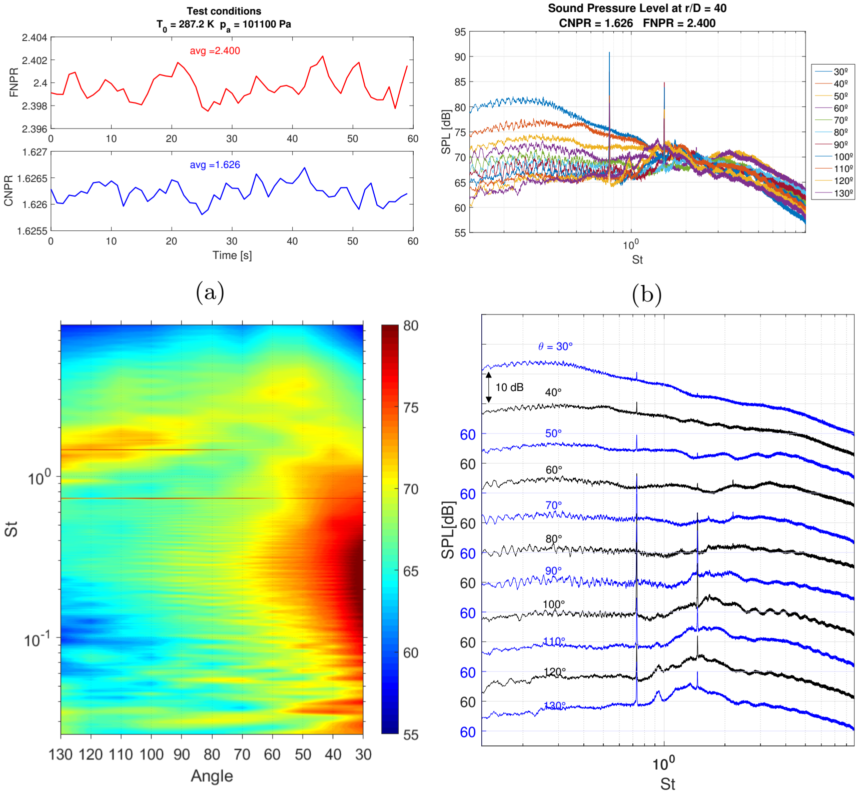

(a) (b)

(c) (d)

Figure B.4: Overview of SPL (ref. $2 \cdot 10^{-5}$ Pa) for condition 04 at all the measured angles in St. a) Pressure conditions measured by the transducers during the acquisition. b) Superposition of the SPL at all measured angles. c) Contour map of the SPL interpolated along the angles. d) Staggered acoustic spectra.

B.5 Condition 05: FNPR = 2.35, CNPR = 1.59

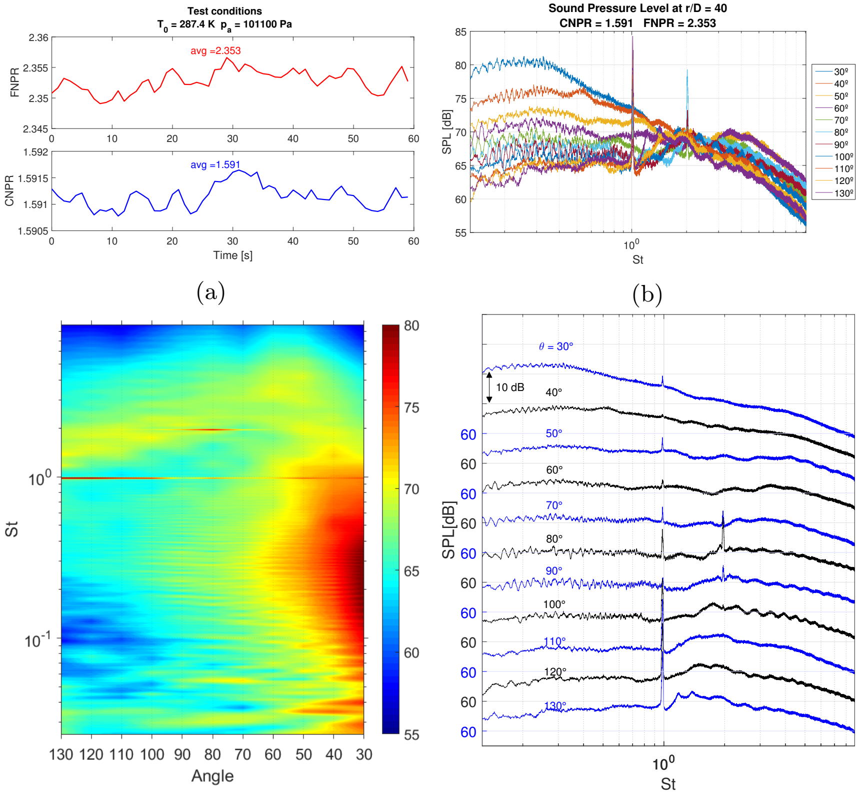

(a)

(b)

(c)

(d)

Figure B.5: Overview of SPL (ref. $2 \cdot 10^{-5}$ Pa) for condition 05 at all the measured angles in St. a) Pressure conditions measured by the transducers during the acquisition. b) Superposition of the SPL at all measured angles. c) Contour map of the SPL interpolated along the angles. d) Staggered acoustic spectra.

B.6 Condition 06: FNPR = 2.25, CNPR = 1.52

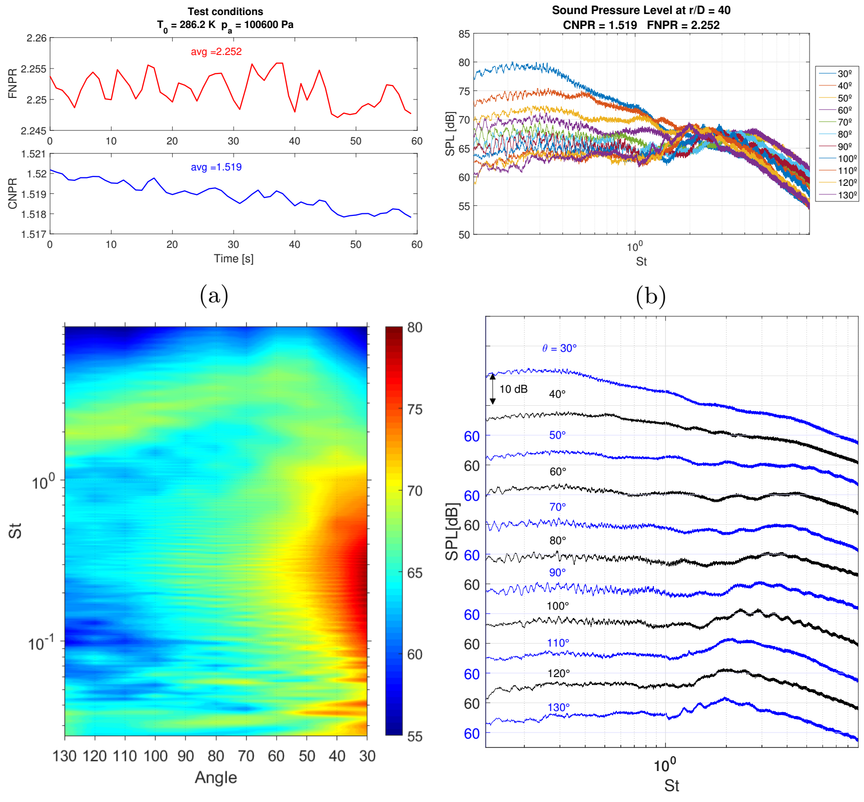

(a) (b)

(c) (d)

Figure B.6: Overview of SPL (ref. $2 \cdot 10^{-5}$ Pa) for condition 06 at all the measured angles in St. a) Pressure conditions measured by the transducers during the acquisition. b) Superposition of the SPL at all measured angles. c) Contour map of the SPL interpolated along the angles. d) Staggered acoustic spectra.

B.7 Condition 07: FNPR = 2.15, CNPR = 1.45

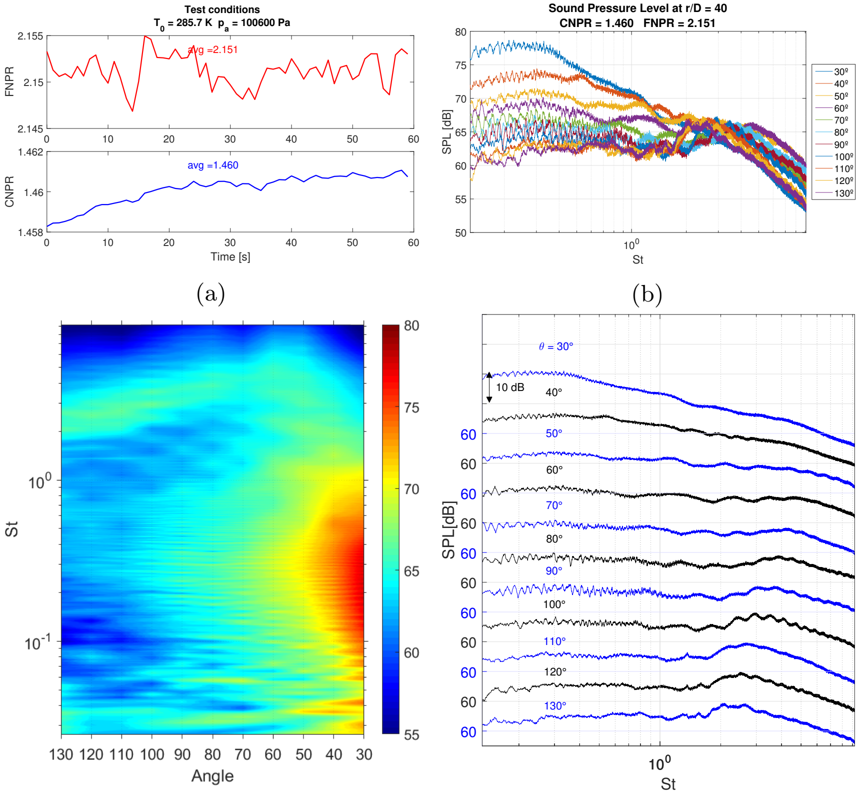

(a) (b)

(c) (d)

Figure B.7: Overview of SPL (ref. $2 \cdot 10^{-5}$ Pa) for condition 07 at all the measured angles in St. a) Pressure conditions measured by the transducers during the acquisition. b) Superposition of the SPL at all measured angles. c) Contour map of the SPL interpolated along the angles. d) Staggered acoustic spectra.

B.8 Condition 08: FNPR = 2.05, CNPR = 1.39

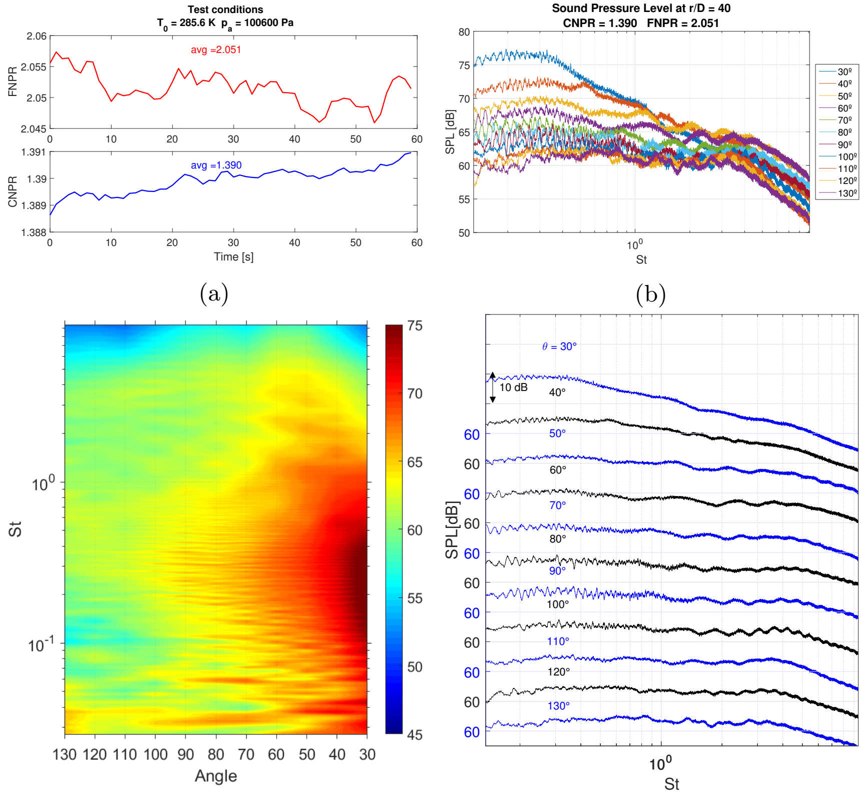

(a) (b)

(c) (d)

Figure B.8: Overview of SPL (ref. $2 \cdot 10^{-5}\ Pa$) for condition 08 at all the measured angles in *St*. a) Pressure conditions measured by the transducers during the acquisition. b) Superposition of the SPL at all measured angles. c) Contour map of the SPL interpolated along the angles. d) Staggered acoustic spectra.

B.9 Condition 09: FNPR = 2, CNPR = 1.35

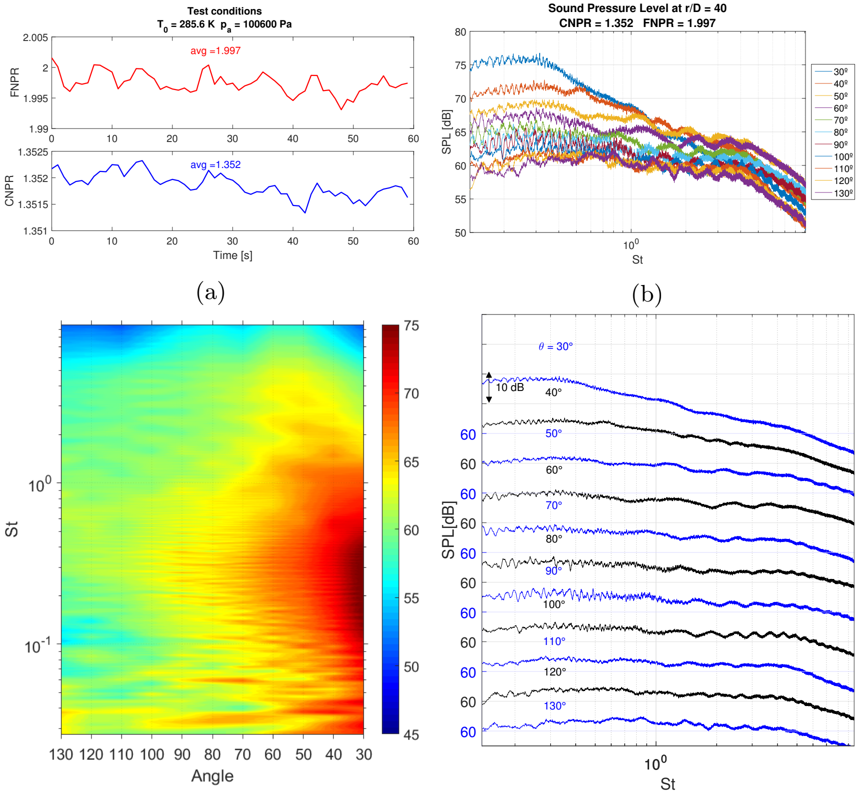

(a) (b)

(c) (d)

Figure B.9: Overview of SPL (ref. $2 \cdot 10^{-5}$ Pa) for condition 09 at all the measured angles in St. a) Pressure conditions measured by the transducers during the acquisition. b) Superposition of the SPL at all measured angles. c) Contour map of the SPL interpolated along the angles. d) Staggered acoustic spectra.

B.10 Condition 10: FNPR = 2.5, CNPR = 1.65

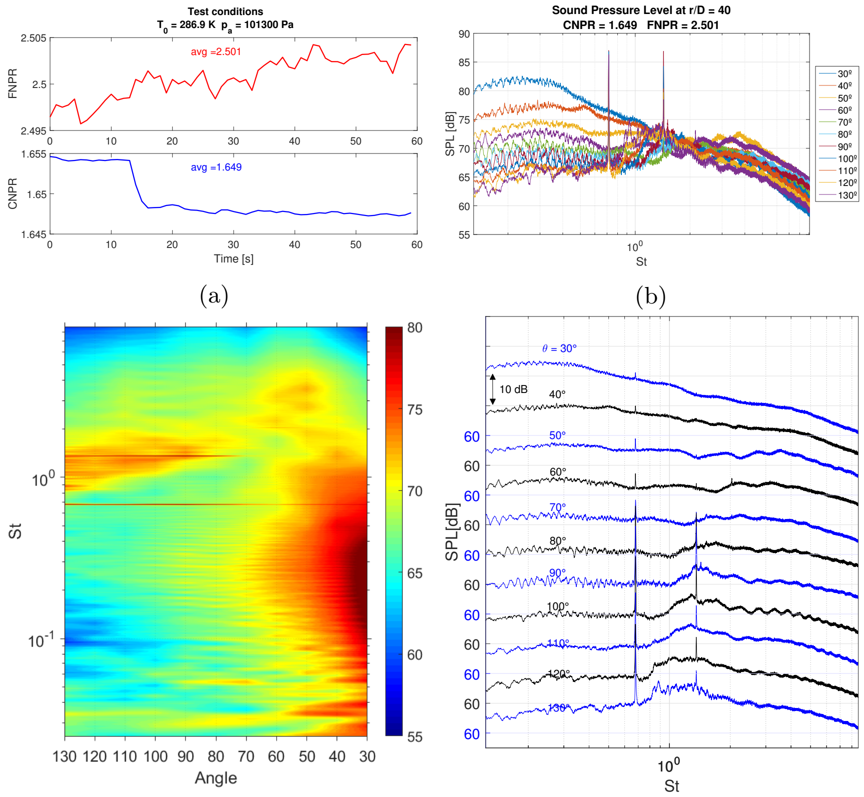

(a) (b)

(c) (d)

Figure B.10: Overview of SPL (ref. $2 \cdot 10^{-5}$ Pa) for condition 10 at all the measured angles in St. a) Pressure conditions measured by the transducers during the acquisition. b) Superposition of the SPL at all measured angles. c) Contour map of the SPL interpolated along the angles. d) Staggered acoustic spectra.

B.11 Condition 11: FNPR = 2.45, CNPR = 1.59

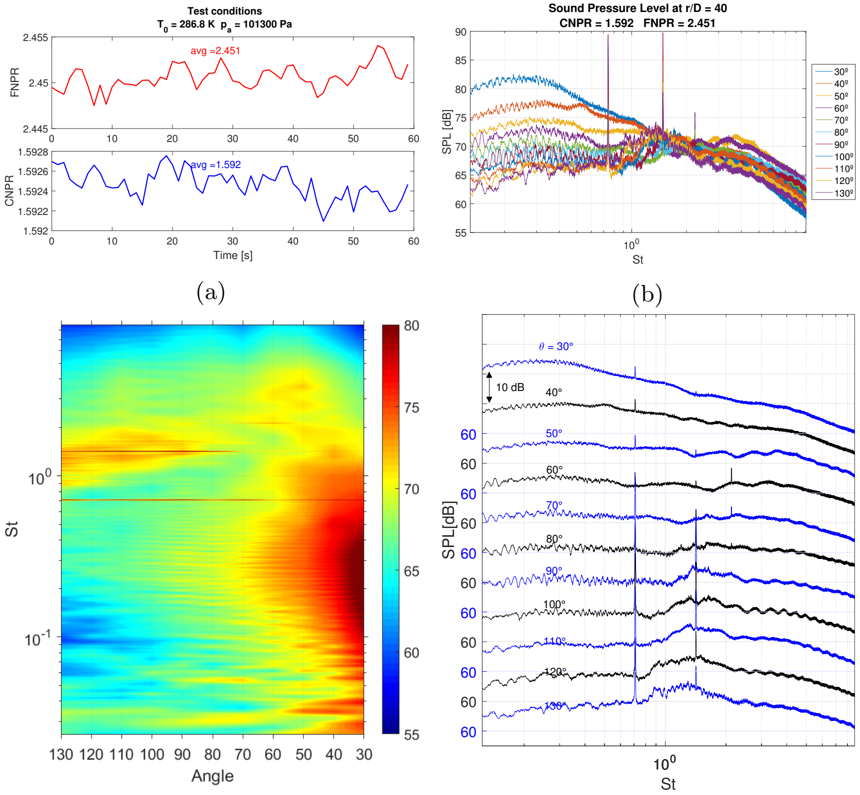

(a) (b)

(c) (d)

Figure B.11: Overview of SPL (ref. $2 \cdot 10^{-5}$ Pa) for condition 11 at all the measured angles in St. a) Pressure conditions measured by the transducers during the acquisition. b) Superposition of the SPL at all measured angles. c) Contour map of the SPL interpolated along the angles. d) Staggered acoustic spectra.

B.12 Condition 12: FNPR = 2.35, CNPR = 1.52

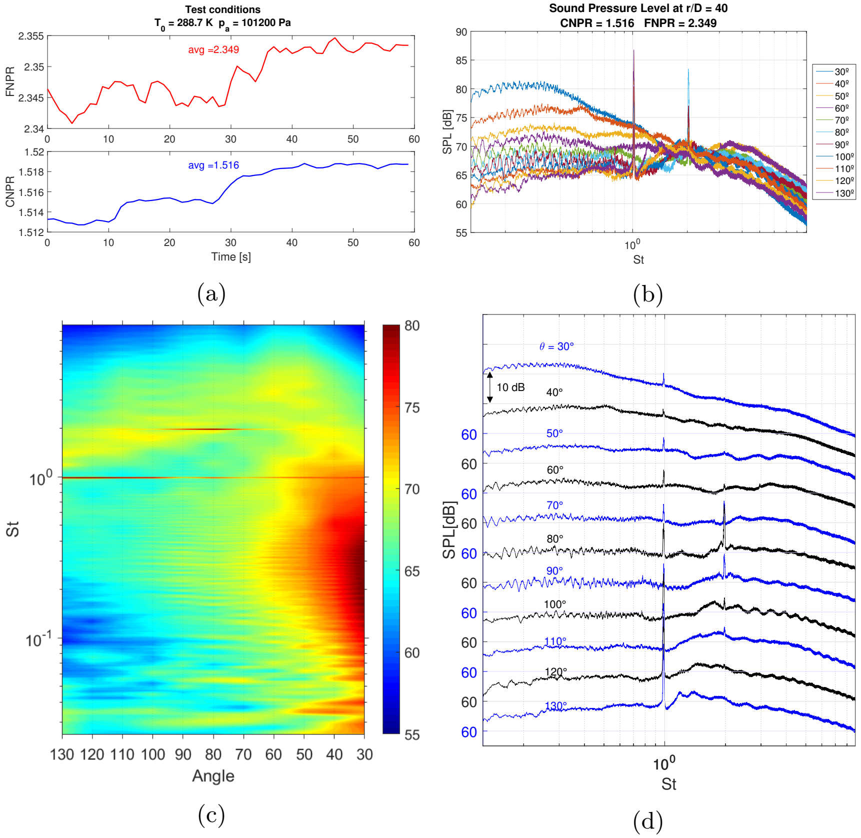

(a) (b)

(c) (d)

Figure B.12: Overview of SPL (ref. $2 \cdot 10^{-5}$ Pa) for condition 12 at all the measured angles in St. a) Pressure conditions measured by the transducers during the acquisition. b) Superposition of the SPL at all measured angles. c) Contour map of the SPL interpolated along the angles. d) Staggered acoustic spectra.

B.13 Condition 13: FNPR = 2.25, CNPR = 1.45

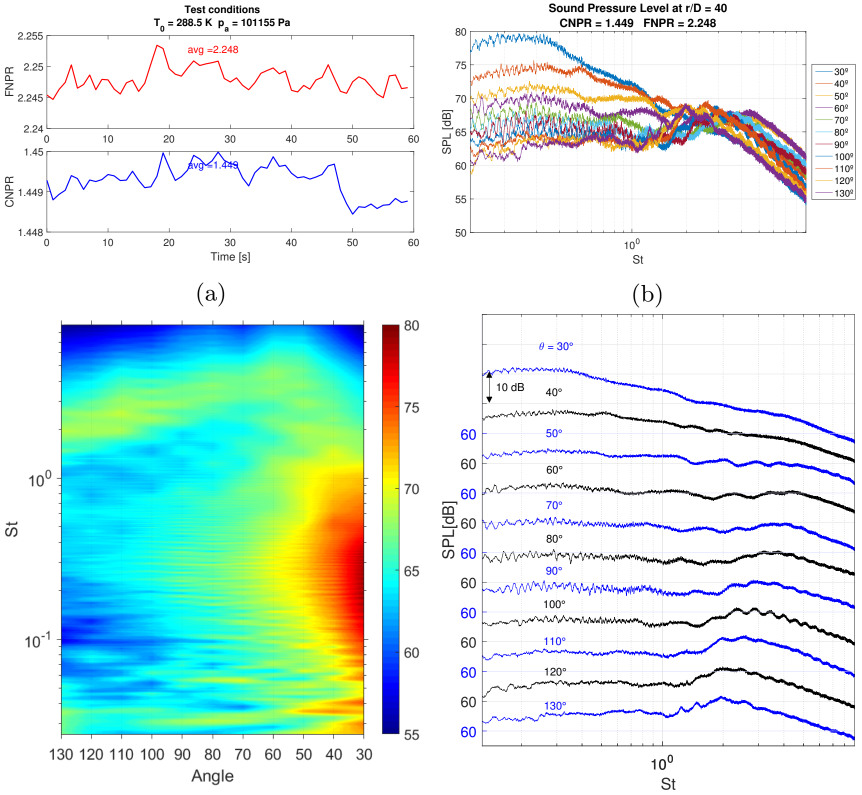

(a) (b)

(c) (d)

Figure B.13: Overview of SPL (ref. $2 \cdot 10^{-5}$ Pa) for condition 13 at all the measured angles in St. a) Pressure conditions measured by the transducers during the acquisition. b) Superposition of the SPL at all measured angles. c) Contour map of the SPL interpolated along the angles. d) Staggered acoustic spectra.

B.14 Condition 14: FNPR = 2.15, CNPR = 1.39

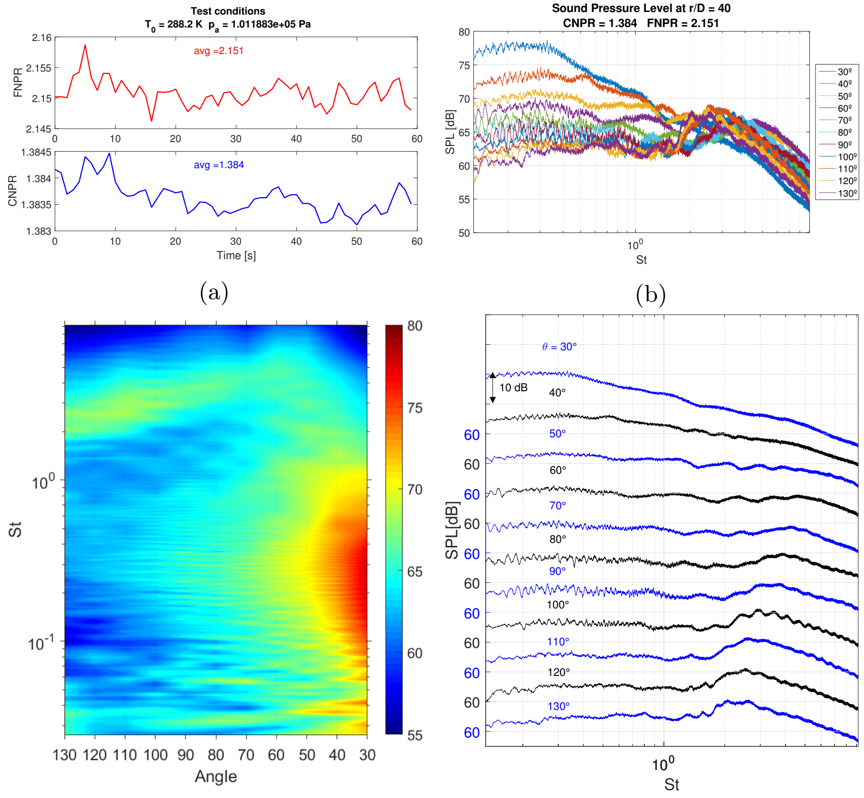

(a)

(b)

(c)

(d)

Figure B.14: Overview of SPL (ref. $2 \cdot 10^{-5}\ Pa$) for condition 14 at all the measured angles in St. a) Pressure conditions measured by the transducers during the acquisition. b) Superposition of the SPL at all measured angles. c) Contour map of the SPL interpolated along the angles. d) Staggered acoustic spectra.

B.15 Condition 15: FNPR = 2.05, CNPR = 1.33

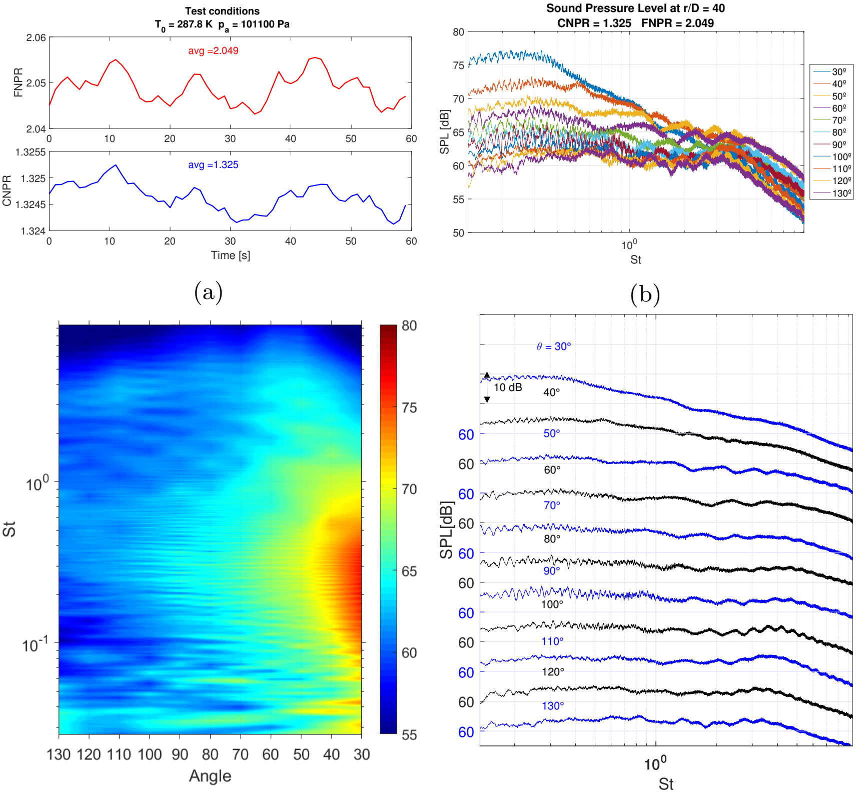

(a) (b)

(c) (d)

Figure B.15: Overview of SPL (ref. $2 \cdot 10^{-5}$ Pa) for condition 15 at all the measured angles in St. a) Pressure conditions measured by the transducers during the acquisition. b) Superposition of the SPL at all measured angles. c) Contour map of the SPL interpolated along the angles. d) Staggered acoustic spectra.

B.16 Condition 16: FNPR = 2.45, CNPR = 1.75

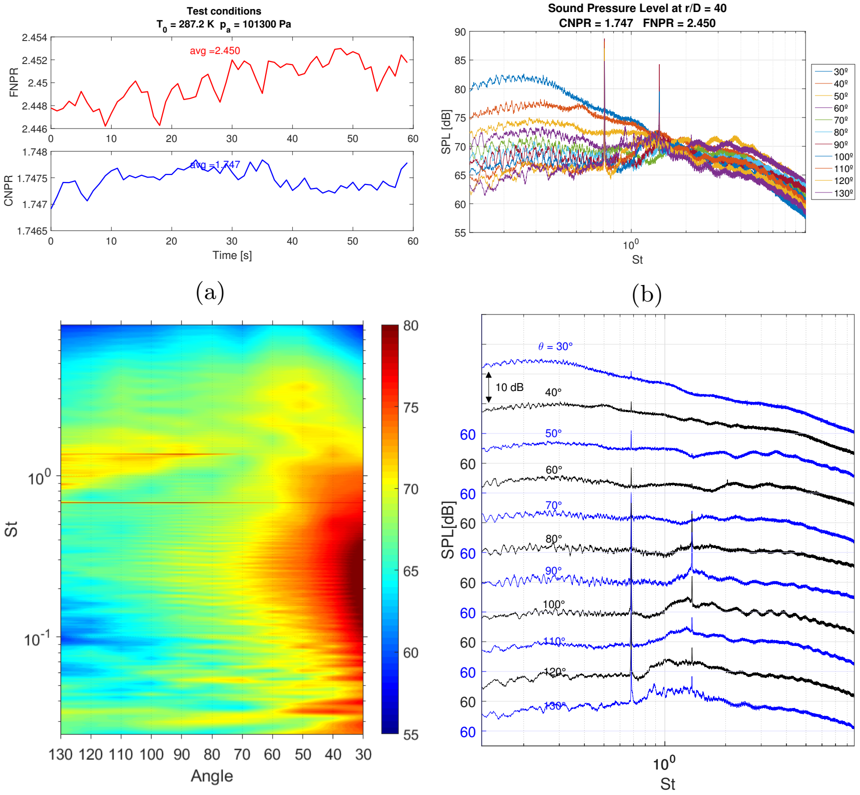

(a) (b)

(c) (d)

Figure B.16: Overview of SPL (ref. $2 \cdot 10^{-5}$ Pa) for condition 16 at all the measured angles in St. a) Pressure conditions measured by the transducers during the acquisition. b) Superposition of the SPL at all measured angles. c) Contour map of the SPL interpolated along the angles. d) Staggered acoustic spectra.

B.17 Condition 18: FNPR = 2.25, CNPR = 1.59

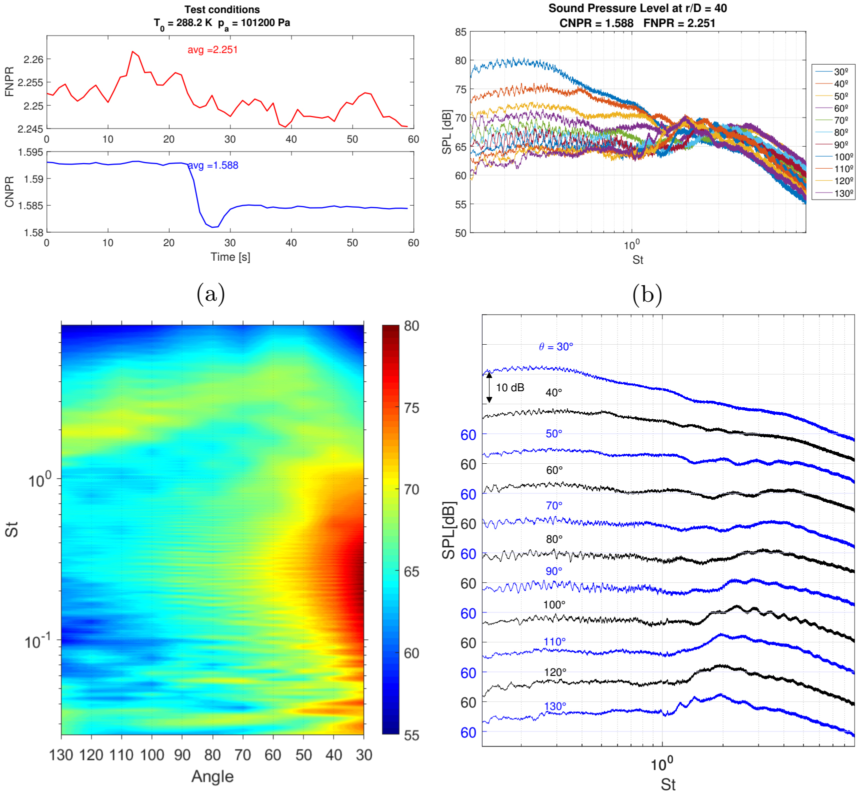

(a) (b)

(c) (d)

Figure B.17: Overview of SPL (ref. $2 \cdot 10^{-5}$ Pa) for condition 18 at all the measured angles in St. a) Pressure conditions measured by the transducers during the acquisition. b) Superposition of the SPL at all measured angles. c) Contour map of the SPL interpolated along the angles. d) Staggered acoustic spectra.

B.18 Condition 19: FNPR = 2.15, CNPR = 1.52

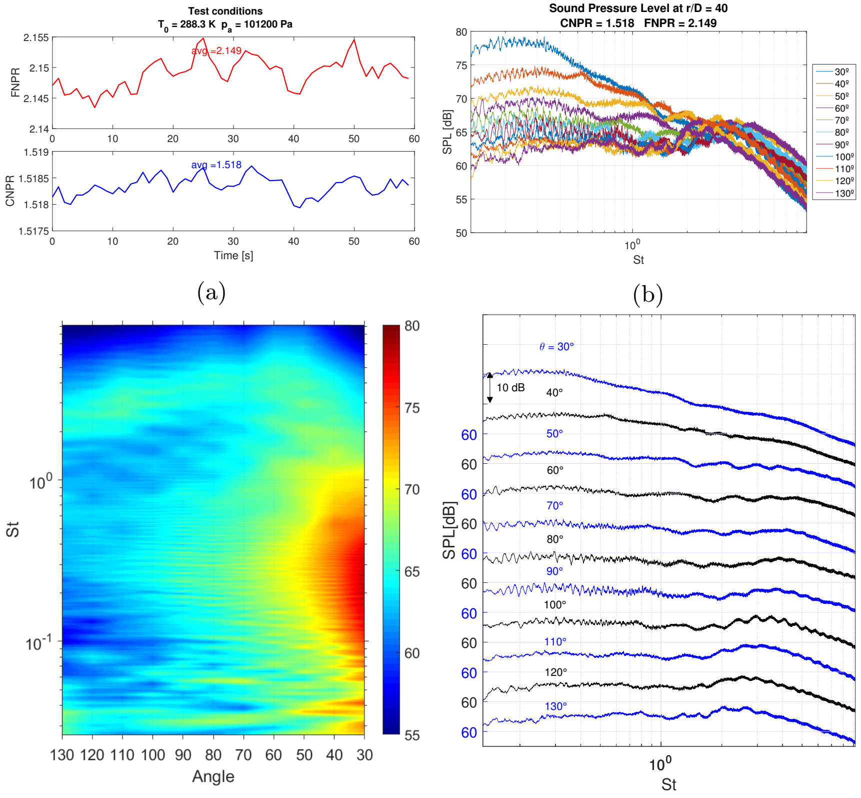

(a) (b)

(c) (d)

Figure B.18: Overview of SPL (ref. $2 \cdot 10^{-5}$ Pa) for condition 19 at all the measured angles in St. a) Pressure conditions measured by the transducers during the acquisition. b) Superposition of the SPL at all measured angles. c) Contour map of the SPL interpolated along the angles. d) Staggered acoustic spectra.

B.19 Condition 20: FNPR = 2.05, CNPR = 1.45

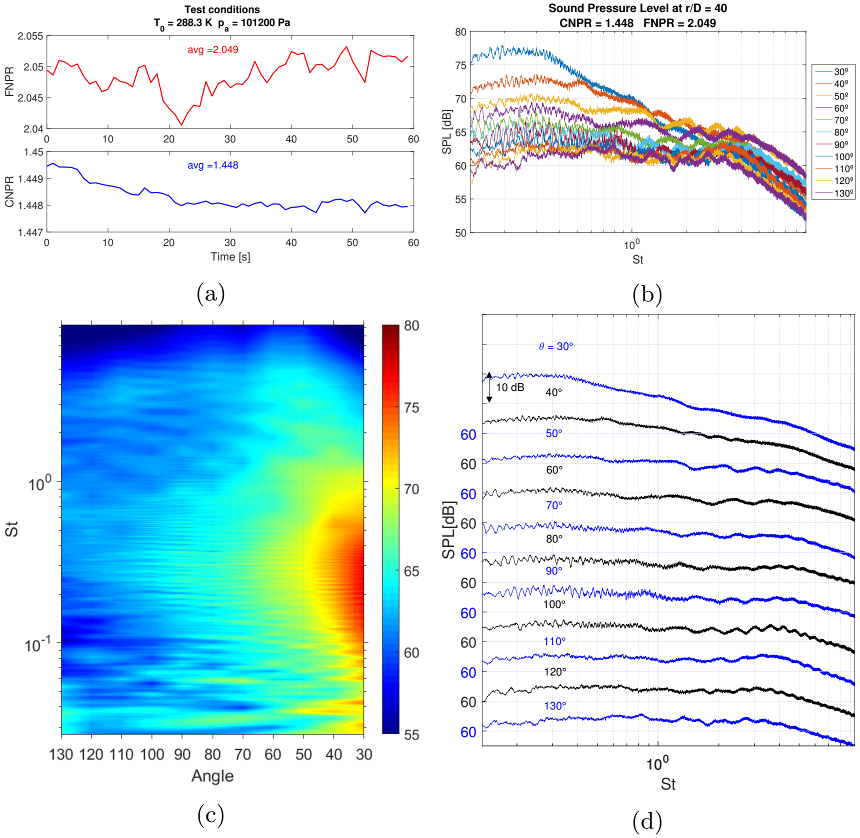

(a) (b)

(c) (d)

Figure B.19: Overview of SPL (ref. $2 \cdot 10^{-5}$ Pa) for condition 20 at all the measured angles in St. a) Pressure conditions measured by the transducers during the acquisition. b) Superposition of the SPL at all measured angles. c) Contour map of the SPL interpolated along the angles. d) Staggered acoustic spectra.

B.20 Condition 21: FNPR = 2.1, CNPR = 1.9

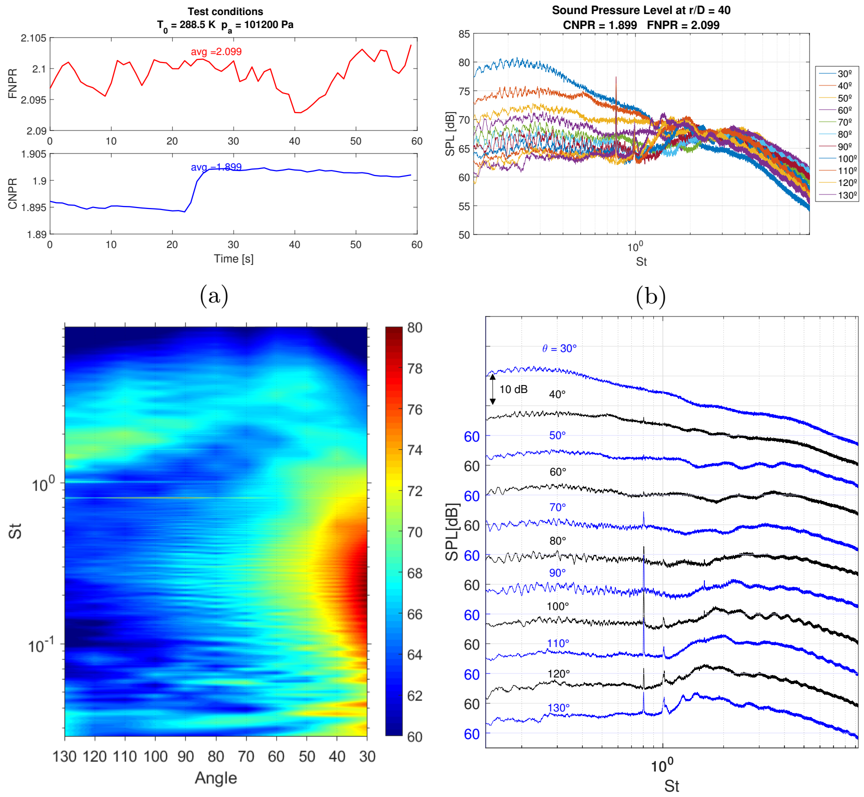

(a) (b)

(c) (d)

Figure B.20: Overview of SPL (ref. $2 \cdot 10^{-5}$ Pa) for condition 21 at all the measured angles in St. a) Pressure conditions measured by the transducers during the acquisition. b) Superposition of the SPL at all measured angles. c) Contour map of the SPL interpolated along the angles. d) Staggered acoustic spectra.

B.21 Condition 22: FNPR = 2.1, CNPR = 2

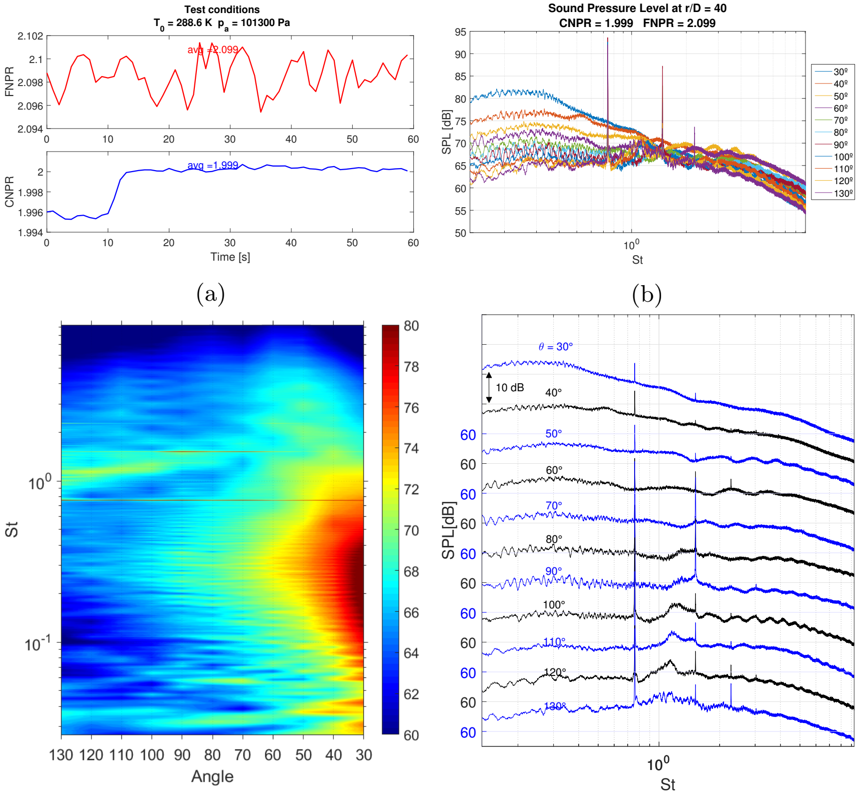

(a) (b)

(c) (d)

Figure B.21: Overview of SPL (ref. $2 \cdot 10^{-5}$ Pa) for condition 22 at all the measured angles in St. a) Pressure conditions measured by the transducers during the acquisition. b) Superposition of the SPL at all measured angles. c) Contour map of the SPL interpolated along the angles. d) Staggered acoustic spectra.

B.22 Condition 23: FNPR = 2.1, CNPR = 2.1

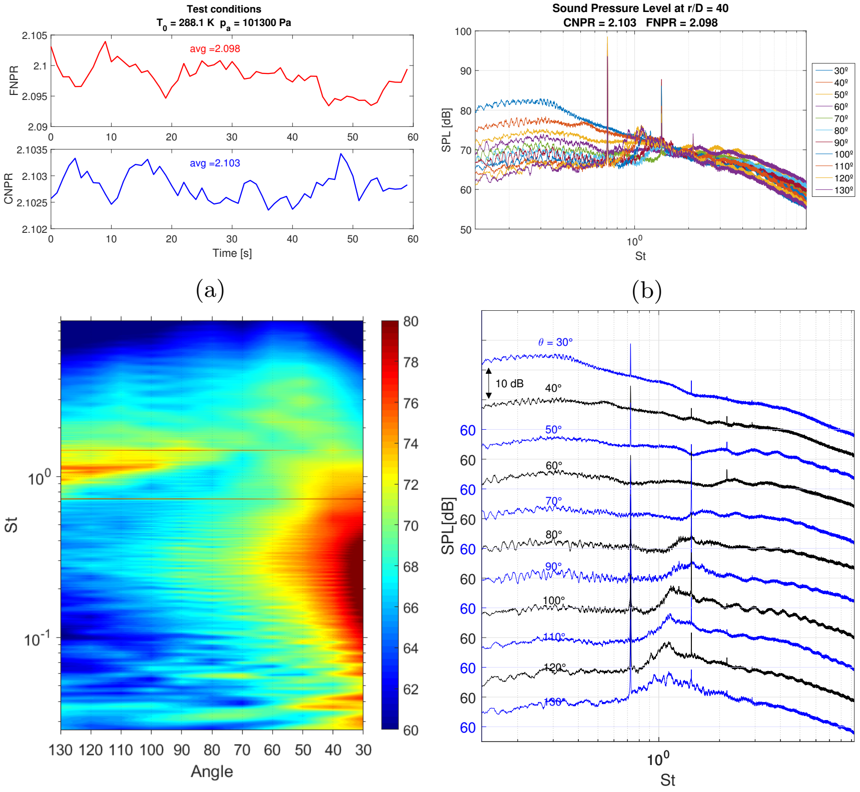

(a) (b)

(c) (d)

Figure B.22: Overview of SPL (ref. $2 \cdot 10^{-5}$ Pa) for condition 23 at all the measured angles in St. a) Pressure conditions measured by the transducers during the acquisition. b) Superposition of the SPL at all measured angles. c) Contour map of the SPL interpolated along the angles. d) Staggered acoustic spectra.

B.23 Condition 24: FNPR = 2.1, CNPR = 2.2

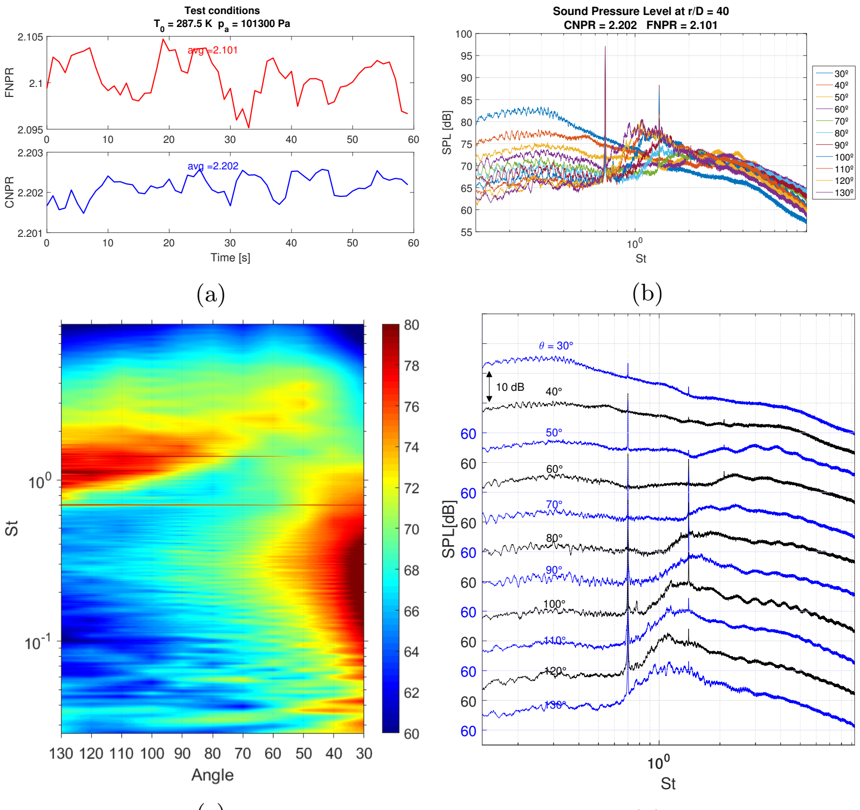

(a) (b)

(c) (d)

Figure B.23: Overview of SPL (ref. $2 \cdot 10^{-5}$ Pa) for condition 24 at all the measured angles in St. a) Pressure conditions measured by the transducers during the acquisition. b) Superposition of the SPL at all measured angles. c) Contour map of the SPL interpolated along the angles. d) Staggered acoustic spectra.

B.24 Condition 25: FNPR = 2.2, CNPR = 1.9

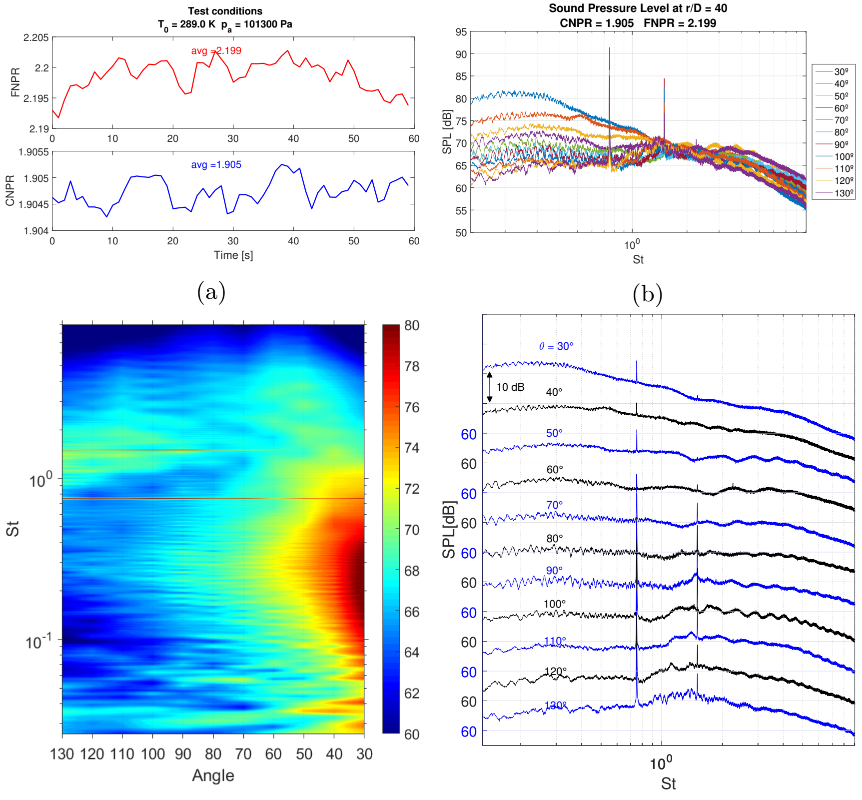

(a) (b)

(c) (d)

Figure B.24: Overview of SPL (ref. $2 \cdot 10^{-5}\ Pa$) for condition 25 at all the measured angles in *St*. a) Pressure conditions measured by the transducers during the acquisition. b) Superposition of the SPL at all measured angles. c) Contour map of the SPL interpolated along the angles. d) Staggered acoustic spectra.

B.25 Condition 26: FNPR = 2.2, CNPR = 2

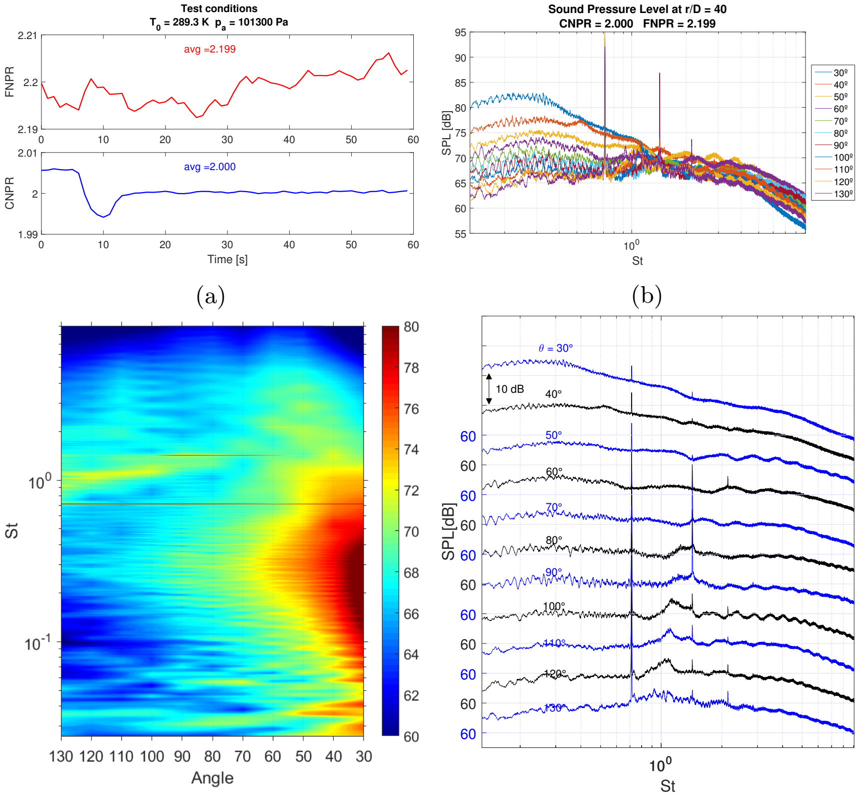

(a)

(b)

(c)

(d)

Figure B.25: Overview of SPL (ref. $2 \cdot 10^{-5}$ Pa) for condition 26 at all the measured angles in St. a) Pressure conditions measured by the transducers during the acquisition. b) Superposition of the SPL at all measured angles. c) Contour map of the SPL interpolated along the angles. d) Staggered acoustic spectra.

B.26 Condition 27: FNPR = 2.2, CNPR = 2.1

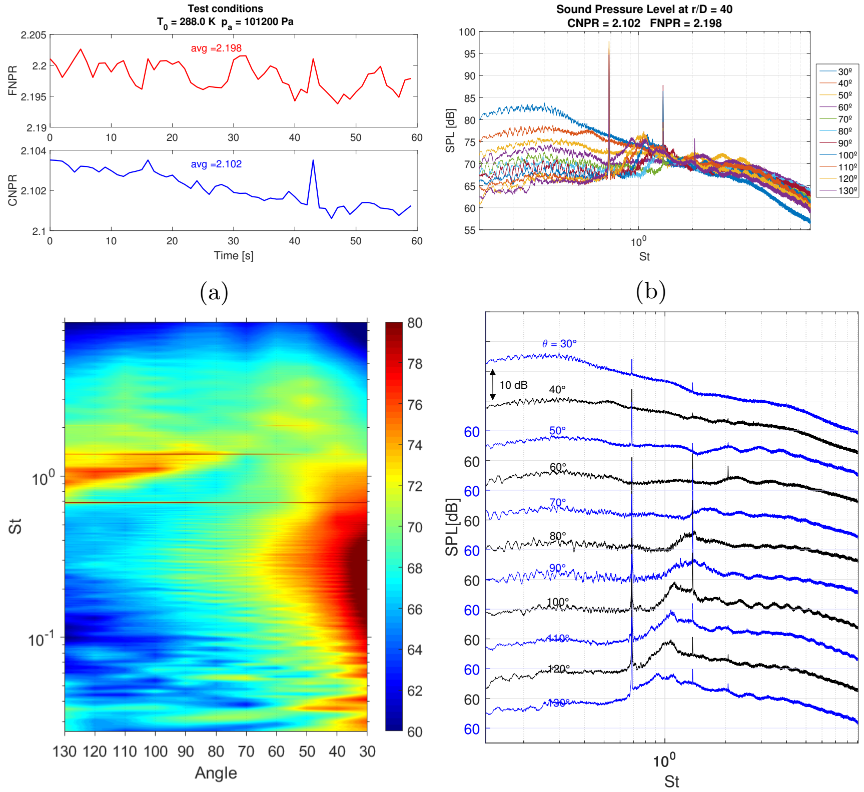

(a) (b)

(c) (d)

Figure B.26: Overview of SPL (ref. $2 \cdot 10^{-5}$ Pa) for condition 27 at all the measured angles in St. a) Pressure conditions measured by the transducers during the acquisition. b) Superposition of the SPL at all measured angles. c) Contour map of the SPL interpolated along the angles. d) Staggered acoustic spectra.

B.27 Condition 28: FNPR = 2.2, CNPR = 2.2

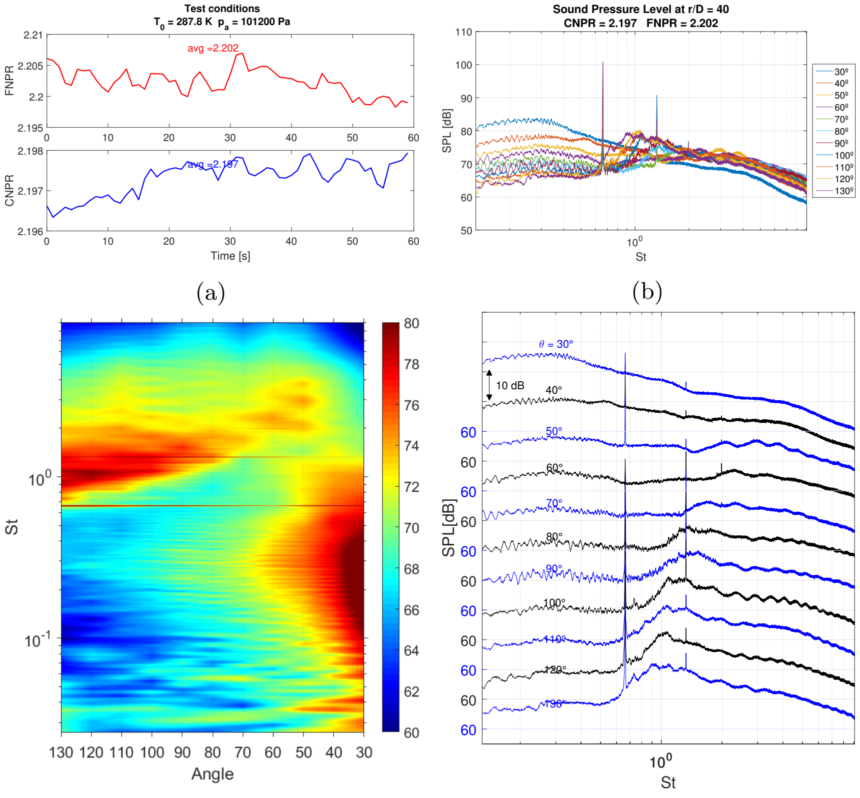

(a) (b)

(c) (d)

Figure B.27: Overview of SPL (ref. $2 \cdot 10^{-5}$ Pa) for condition 28 at all the measured angles in St. a) Pressure conditions measured by the transducers during the acquisition. b) Superposition of the SPL at all measured angles. c) Contour map of the SPL interpolated along the angles. d) Staggered acoustic spectra.

B.28 Condition 29: FNPR = 2.3, CNPR = 1.9

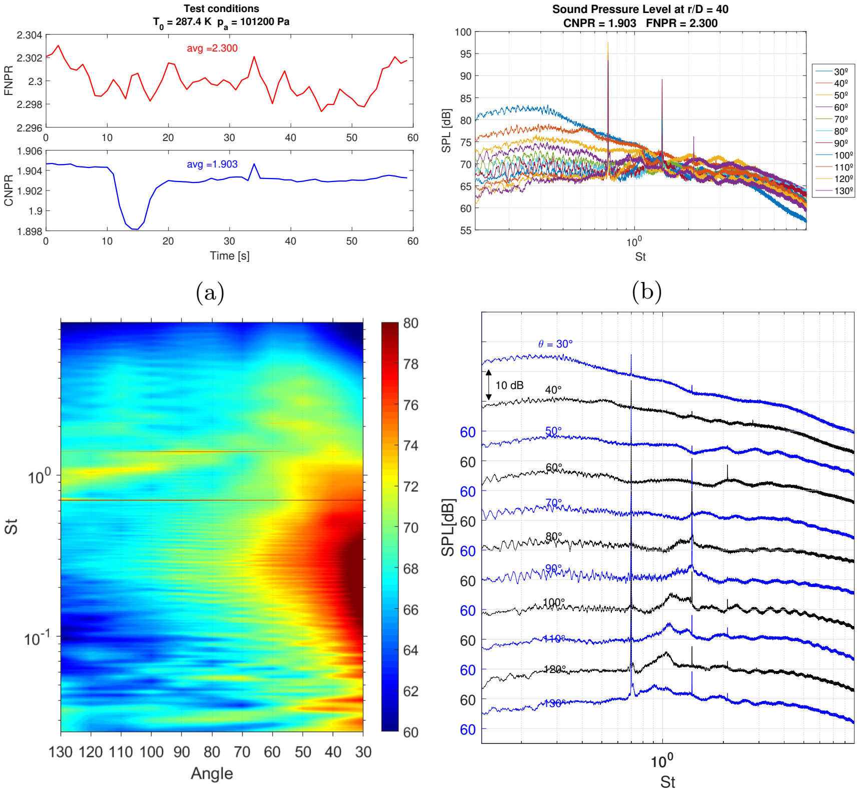

(a) (b)

(c) (d)

Figure B.28: Overview of SPL (ref. $2 \cdot 10^{-5}$ Pa) for condition 29 at all the measured angles in St. a) Pressure conditions measured by the transducers during the acquisition. b) Superposition of the SPL at all measured angles. c) Contour map of the SPL interpolated along the angles. d) Staggered acoustic spectra.

B.29 Condition 30: FNPR = 2.3, CNPR = 2

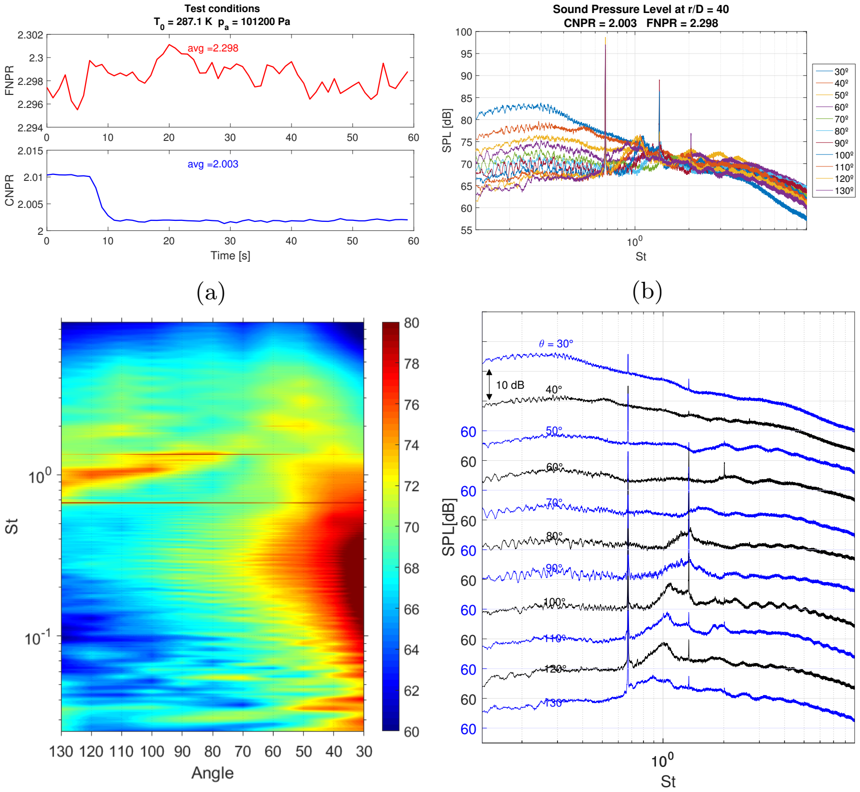

(a) (b)

(c) (d)

Figure B.29: Overview of SPL (ref. $2 \cdot 10^{-5}$ Pa) for condition 30 at all the measured angles in St. a) Pressure conditions measured by the transducers during the acquisition. b) Superposition of the SPL at all measured angles. c) Contour map of the SPL interpolated along the angles. d) Staggered acoustic spectra.

B.30 Condition 31: FNPR = 2.3, CNPR = 2.1

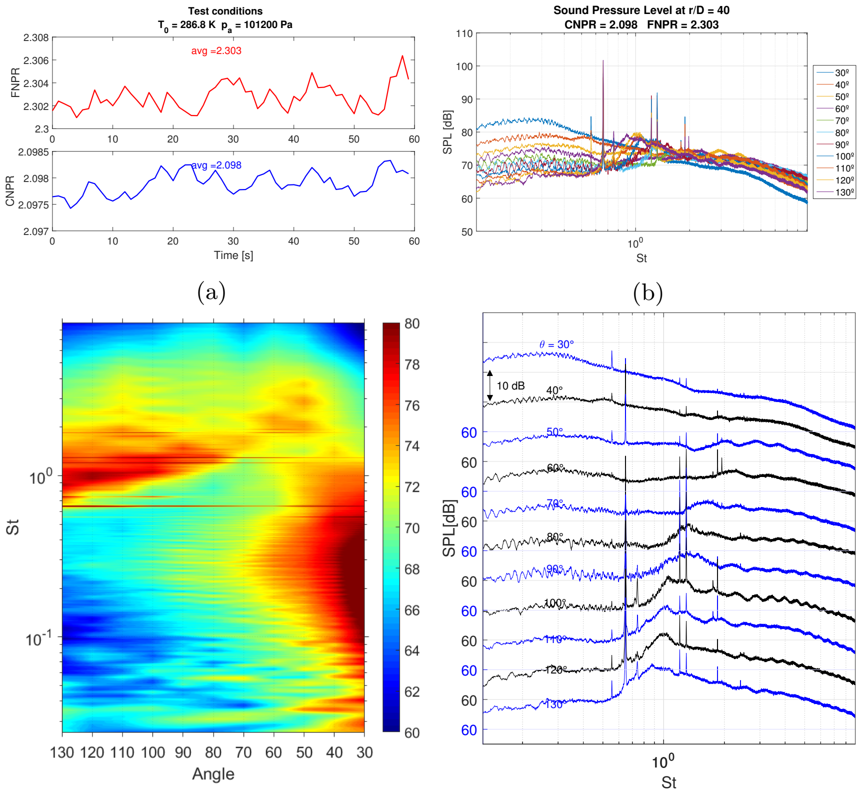

(a)

(b)

(c)

(d)

Figure B.30: Overview of SPL (ref. $2 \cdot 10^{-5}$ Pa) for condition 31 at all the measured angles in St. a) Pressure conditions measured by the transducers during the acquisition. b) Superposition of the SPL at all measured angles. c) Contour map of the SPL interpolated along the angles. d) Staggered acoustic spectra.

B.31 Condition 32: FNPR = 2.3, CNPR = 2.2

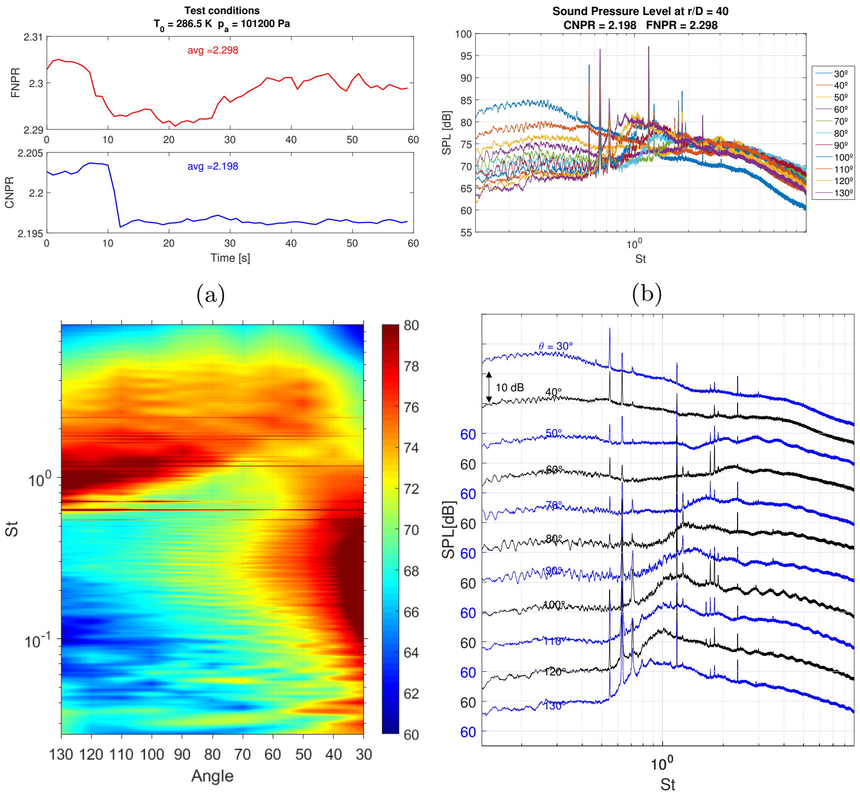

(a) (b)

(c) (d)

Figure B.31: Overview of SPL (ref. $2 \cdot 10^{-5}$ Pa) for condition 32 at all the measured angles in St. a) Pressure conditions measured by the transducers during the acquisition. b) Superposition of the SPL at all measured angles. c) Contour map of the SPL interpolated along the angles. d) Staggered acoustic spectra.

B.32 Condition 33: FNPR = 2.4, CNPR = 1.9

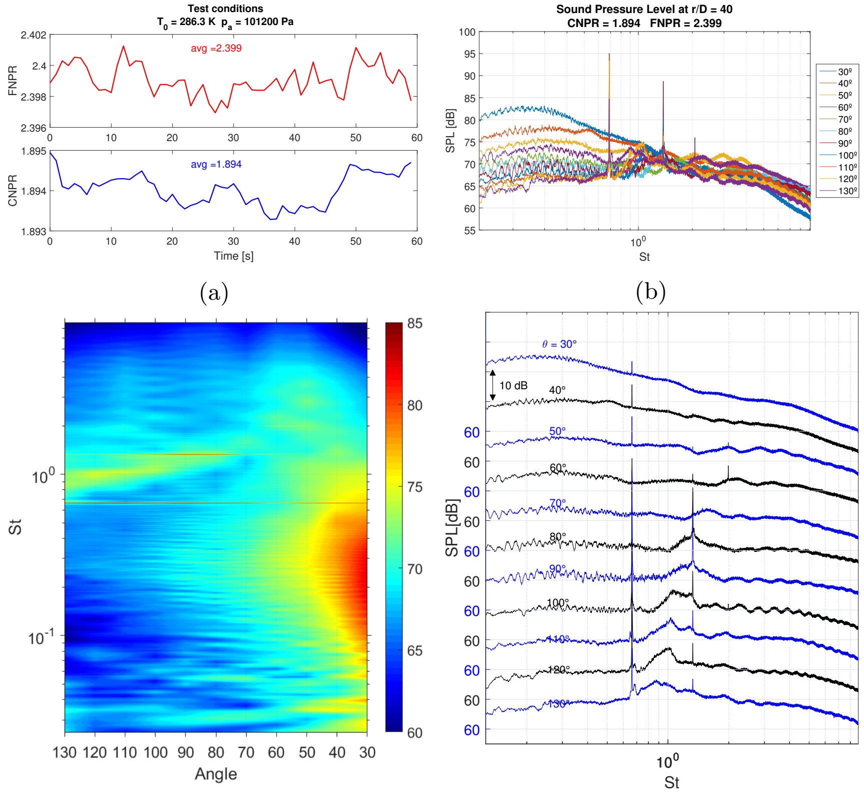

(a)

(b)

(c)

(d)

Figure B.32: Overview of SPL (ref. $2 \cdot 10^{-5}$ Pa) for condition 33 at all the measured angles in St. a) Pressure conditions measured by the transducers during the acquisition. b) Superposition of the SPL at all measured angles. c) Contour map of the SPL interpolated along the angles. d) Staggered acoustic spectra.

B.33 Condition 34: FNPR = 2.4, CNPR = 2

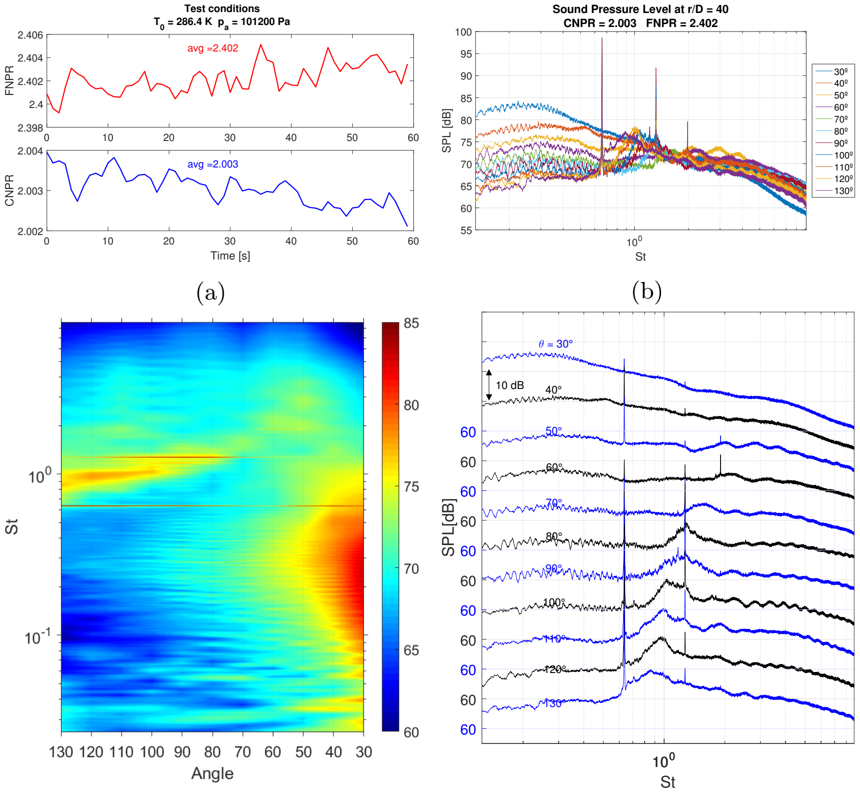

(a)

(b)

(c)

(d)

Figure B.33: Overview of SPL (ref. $2 \cdot 10^{-5}\ Pa$) for condition 34 at all the measured angles in St. a) Pressure conditions measured by the transducers during the acquisition. b) Superposition of the SPL at all measured angles. c) Contour map of the SPL interpolated along the angles. d) Staggered acoustic spectra.

B.34 Condition 35: FNPR = 2.4, CNPR = 2.1

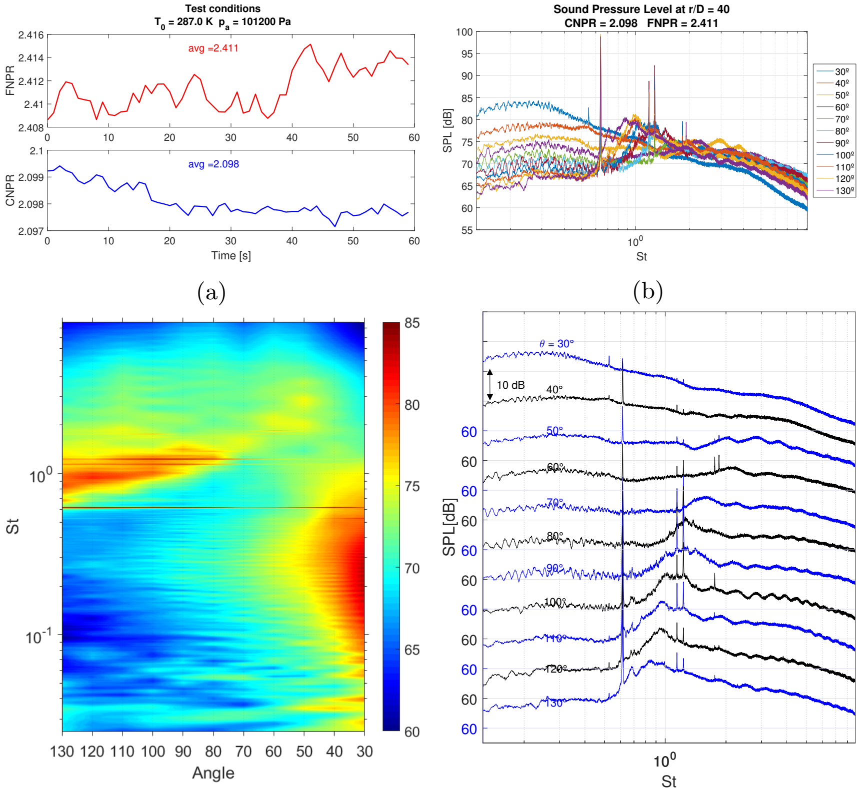

(a)

(b)

(c)

(d)

Figure B.34: Overview of SPL (ref. $2 \cdot 10^{-5}$ Pa) for condition 35 at all the measured angles in St. a) Pressure conditions measured by the transducers during the acquisition. b) Superposition of the SPL at all measured angles. c) Contour map of the SPL interpolated along the angles. d) Staggered acoustic spectra.

B.35 Condition 36: FNPR = 2.4, CNPR = 2.2

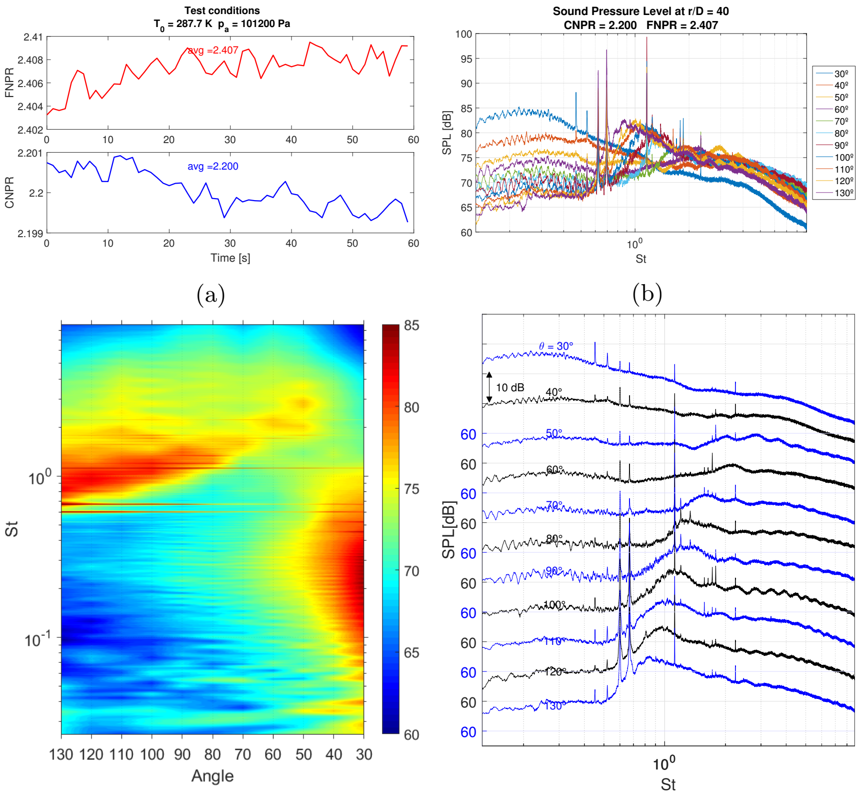

(a)

(b)

(c)

(d)

Figure B.35: Overview of SPL (ref. $2 \cdot 10^{-5}\ Pa$) for condition 36 at all the measured angles in St. a) Pressure conditions measured by the transducers during the acquisition. b) Superposition of the SPL at all measured angles. c) Contour map of the SPL interpolated along the angles. d) Staggered acoustic spectra.

Bibliography

[1] Adrian, R. J. Particle imaging techniques for experimental fluid mechanics. *Annual review of fluid Mechanics*, **23** (1991), 261. Available from: `https://doi.org/10.1146%2Fannurev.fl.23.010191.001401`, `doi:10.1146/annurev.fluid.23.1.261`.

[2] André, B. *Etude experimentale de leffet du vol sur le bruit de choc de jets supersoniques sous-detendus.* Ph.D. thesis, Thse de Doctorat, Ecole Centrale de Lyon (2012).

[3] André, B., Castelain, T., and Bailly, C. Experimental study of flight effects on screech in underexpanded jets. *Physics of Fluids*, **23** (2011), 126102. Available from: `http://scitation.aip.org/content/aip/journal/pof2/23/12/10.1063/1.3671735`, `doi:10.2514/6.2011-2794`.

[4] André, B., Castelain, T., and Bailly, C. Broadband shock-associated noise in screeching and non-screeching underexpanded supersonic jets. *AIAA Journal*, **51** (2013), 665. Available from: `https://doi.org/10.2514%2F1.j052058`, `doi:10.2514/1.j052058`.

[5] André, B., Castelain, T., and Bailly, C. Investigation of the mixing layer of underexpanded supersonic jets by particle image velocimetry. *International Journal of Heat and Fluid Flow*, **50** (2014), 188 . Available from: `http://www.sciencedirect.com/science/article/pii/S0142727X14000976`, `doi:10.1016/j.ijheatfluidflow.2014.08.004`.

[6] Bailly, C., Andr, B., Castelain, T., Henry, C., Bodard, G., and Porta, M. An analysis of shock noise components. *AerospaceLab Journal*, **7** (2014).

[7] Bailly, C., Lafon, P., and Candel, S. Subsonic and supersonic jet noise predictions from statistical source models. *AIAA Journal*, **35, no. 11** (1997), 1688. Available from: `https://doi.org/10.2514%2F3.13733`, `doi:10.2514/3.13733`.

[8] Balsa, T. F. and Gliebe, P. R. Aerodynamics and noise of coaxial jets. *AIAA Journal*, **15** (1977), 1550. Available from: `http://dx.doi.org/10.2514/3.60822`, `doi:10.2514/3.60822`.

[9] Bauer, A. B. Impedance theory and measurements on porous acoustic liners. *Journal of Aircraft*, **14** (1977), 720. Available from: `https://doi.org/10.2514%2F3.58844`, `doi:10.2514/3.58844`.

[10] Bent, P. H., Blackner, A. M., Newsum, S. A., and Nesbitt, E. H. Shock associated noise of dual flow nozzles. *AIAA J.*, **2323** (1998). Available from: `https://doi.org/10.2514%2F6.1998-2323`, `doi:10.2514/6.1998-2323`.

[11] Berland, J., Bogey, C., and Bailly, C. Numerical study of screech generation in a planar supersonic jet. *Physics of Fluids*, **19** (2007), 075105. Available from: `http://scitation.aip.org/content/aip/journal/pof2/19/7/10.1063/1.2747225`, `doi:10.1063/1.2747225`.

[12] Bhat, T., Ganz, U., and Guthrie, A. Acoustic and flow-field characteristics of shock-cell noise from dual flow nozzles. In *Aeroacoustics Conferences*, pp. –. American Institute of Aeronautics and Astronautics (2005). Available from: `https://doi.org/10.2514%2F6.2005-2929`, `doi:10.2514/6.2005-2929`.

[13] Bies, D. and Hansen, C. Flow resistance information for acoustical design. *Applied Acoustics*, **13** (1980), 357. Available from: `https://doi.org/10.1016%2F0003-682x%2880%2990002-x`, `doi:10.1016/0003-682x(80)90002-x`.

[14] Bouanati, N. *Acoustic Beamforming for Aeroacoustics.* Research master report, von Karman Institute for Fluid Dynamics (2016).

[15] Bridges, J. and Wernet, M. Turbulence associated with broadband shock noise in hot jets. *NASA Technical Memorandum 215274*, (2008). Available from: `https://doi.org/10.2514%2F6.2008-2834`, `doi:10.2514/6.2008-2834`.

[16] Carlomagno, G. M. and Astarita, T. *Slides from course of Gasdynamics, University of Naples 'Federico II'.* Università degli Studi di Napoli "Federico II" (2009).

[17] Casalino, D., F.Diozzi, Sannino, R., and Paonessa, A. Aircraft noise reduction technologies: A bibliographic review. *Aerospience Science and Technology*, **12** (2008), 429. Available from: `https://doi.org/10.1016%2Fj.ast.2007.10.004`, `doi:10.1016/j.ast.2007.10.004`.

[18] Colonius, T. and Jordan, P. Wave packets and turbulent jet noise. *Annual review of fluid mechanics*, **145** (2012), 173. Available from: `https://doi.org/10.1146%2Fannurev-fluid-011212-140756`, `doi:10.1146/annurev-fluid-011212-140756`.

[19] Colonius, T. and Lele, S. K. Computational aeroacoustics: progress on nonlinear problems of sound generation. *Progress in Aerospace Sciences*, **40** (2004), 345 . Available from: `http://www.sciencedirect.com/science/article/pii/S0376042104000570`, `doi:10.1016/j.paerosci.2004.09.001`.

[20] Coquelet, N. *Development of beamforming techniques for the investigation of aeroacoustic applications.* Research master report, von Karman Institute for Fluid Dynamics (2015).

[21] Cox, T. J. and D'antonio, P. *Acoustic absorbers and diffusers: theory, design and application.* CRC Press (2009). Available from: `https://doi.org/10.1201%2F9781315369211`, `doi:10.1201/9781315369211`.

[22] Dahl, M. D. and Morris, P. J. Noise from supersonic coaxial jets, part 1: Mean flow predictions. *J. Sound Vib.*, **200, no. 5** (1997), 643663. Available from: `https://doi.org/10.1006%2Fjsvi.1996.0723`, `doi:10.1006/jsvi.1996.0723`.

[23] Dahl, M. D. and Morris, P. J. Noise from supersonic coaxial jets, part 2: normal velocity profile. *J. Sound Vib.*, **200, no. 5** (1997), 665699. Available from: `https://doi.org/10.1006%2Fjsvi.1996.0724`, `doi:10.1006/jsvi.1996.0724`.

[24] Dahl, M. D., Papamoschou, D., and Hixon, R. Supersonic coaxial jets: Noise predictions and measurements. Tech. rep., Tech. Memo. 1998-207422, NASA (1988). Available from: `https://doi.org/10.2514%2F6.1998-2294`, `doi:10.2514/6.1998-2294`.

[25] Daviller, G., Lehnasch, G., and Jordan, P. Numerical investigation of the influence of upstream conditions on properties of shock noise in shock/mixing layer interaction. In *Eighth International Symposium on Turbulence and Shear Flow Phenomena* (2013).

[26] De Santana, L. *Semi-analytical methodologies for airfoil noise prediction.* Ph.D. thesis, KU Leuven (2015).

[27] Delany, M. and Bazley, E. Acoustical properties of fibrous absorbent materials. *Applied Acoustics*, **3** (1970), 105. Available from: `https://doi.org/10.1016%2F0003-682x%2870%2990031-9`, `doi:10.1016/0003-682x(70)90031-9`.

[28] EMERSON. Conditioning orifice plate technology; taking the standard to a new level of capability. Tech. rep., 1595_2_01_*AA* (2004).

[29] Fleury, V., Bailly, C., Jondeau, E., Michard, M., and Juve, D. Space-time correlations in two subsonic jets using dual particle

image velocimetry measurements. *American Institute of Aeronautics and Astronautics*, **46** (2008), 2498. Available from: `https://doi.org/10.2514%2F1.35561`, `doi:10.2514/1.35561`.

[30] Givoli, D. and Neta, B. High-order non-reflecting boundary scheme for time-dependent waves. *Journal of Computational Physics*, **186** (2003), 24. Available from: `https://doi.org/10.1016%2Fs0021-9991%2803%2900005-6`, `doi:10.1016/s0021-9991(03)00005-6`.

[31] Grizzi, S. and Camussi, R. Experimental investigation of the near-field noise generated by a compressible round jet. *Journal of Physics: Conference Series*, **318** (2011), 092003. Available from: `http://stacks.iop.org/1742-6596/318/i=9/a=092003`, `doi:10.1088/1742-6596/318/9/092003`.

[32] Guariglia, D., Carpio, A. R., and Schram, C. Design of a facility for shock-cells noise experimental investigation on a subsonic/supersonic coaxial jet. *Conference: 22nd AIAA/CEAS Aeroacoustics Conference*, (2016). Available from: `https://doi.org/10.2514%2F6.2016-2983`, `doi:10.2514/6.2016-2983`.

[33] Harper-Bourne, M. and Fisher, M. The noise from shock waves in supersonic jets. In *AGARD Conference on Noise Mechanisms* (1973).

[34] Harper-Bourne, M. and Fisher, M. J. The noise from shock waves in supersonic jets. *In proceedings No.131 of the AGARD Conference on Noise Mechanisms*, (1973), 11.

[35] Heeb, N., Kastner, J., Gutmark, E., and Kailasanath, K. Supersonic jet noise reduction by chevrons and fluidic injection. *International Journal of Aeroacoustics*, **12** (2013), 679. Available from: `https://doi.org/10.1260%2F1475-472x.12.7-8.679`, `doi:10.1260/1475-472x.12.7-8.679`.

[36] Henry, C., Bailly, C., and Bodard, G. Statistical modeling of bbsan including refraction effects. *8th AIAA/CEAS Aeroacoustics Conference, AIAA Paper 2012-2163*, (2012), 2012. Available from: `https://doi.org/10.2514%2F6.2012-2163`, `doi:10.2514/6.2012-2163`.

[37] Horvath, I. *PIV Data Processing by Rabon.* Rhode Saint Genese: Von Karman Institute (2011).

[38] Horvath, I. *PIV Image Pre-processing by Tucsok.* Rhode Saint Genese: Von Karman Institute (2011).

[39] Horvath, I. *Extreme PIV Applications: Simultaneous and Instantaneous Velocity and Concentration Measurements on Model and Real*

Scale Car Park Fire Scenarios. Ph.D. thesis, Universit libre de Bruxelles, Ecole polytechnique de Bruxelles Electromcanicien, Bruxelles. (2012). Available from: `http://hdl.handle.net/2013/ULB-DIPOT:oai:dipot.ulb.ac.be:2013/209641`.

[40] Huber, J., Sylla, A. A., Fleury, V., Bulte., J., Britchford, K., Laurendeau, E., and Long, D. Understanding and reduction of cruise jet noise at model and full scale. *American Institute of Aeronautics and Astronautics*, (2009), 1. Available from: `https://doi.org/10.2514%2F6.2009-3382`, `doi:10.2514/6.2009-3382`.

[41] ISO/TR 15377:2007. Measurement of fluid flow by means of pressure-differential devices guidelines for the specification of orifice plates, nozzles and venturi tubes beyond the scope of iso 5167. Tech. rep. Available from: `https://doi.org/10.3403%2F30131338u`, `doi:10.3403/30131338u`.

[42] Jeronimo, A., Riethmuller, M., and Chazot, O. Application of piv to a supersonic jet. *Von Karman Institute Technical Report*, (2001).

[43] Jeronimo, A., Riethmuller, M., and Chazot, O. Piv application to mach 3.75 overexpanded jet. *11th International Symposium on Application of Laser Techniques to Fluid Mechanics*, (2002), 1.

[44] Kuznetsov, V. M. and Munin, A. G. Coaxial jet noise and isothermal jets. *Soviet Physics Acoustics*, (1978).

[45] Landefeld. *Atlas 8 Catalog* (2015). Available from: `www.landefeld.de`.

[46] Lele, S. K., Mendez, S., Ryu, J., Nichols, J., Shoeybi, M., and Moin, P. Sources of high-speed jet noise: Analysis of les data and modeling. *Procedia Engineering*, **6** (2010), 84 . Available from: `http://www.sciencedirect.com/science/article/pii/S1877705810005564`, `doi:http://dx.doi.org/10.1016/j.proeng.2010.09.010`.

[47] Lepicovski, J. and Ahuja, K. K. Experimental results on edge-tone oscillations in high speed subsonic jets. *AIAA Journal*, **23** (1985), 1463. Available from: `https://doi.org/10.2514%2F3.9111`, `doi:10.2514/3.9111`.

[48] Lighthill, M. J. On sound generated aerodinamically i: General theory. *Proceedings of the royal society of London*, **211** (1952), 564. Available from: `https://doi.org/10.1098%2Frspa.1952.0060`, `doi:10.1098/rspa.1952.0060`.

[49] Mandon, J.-B. *Acoustic Dumping by Spray Curtains.* Master's thesis, von Karman Institute (2016).

[50] Manning, T. A. *A numerical investigation of sound generation in supersonic jet screech.* Ph.D. thesis, STANFORD UNIVERSITY (2000). Available from: `https://doi.org/10.2514%2F6.2000-2081`, `doi:10.2514/6.2000-2081`.

[51] Massey, K. C. and Ahuja, K. K. Screech frequency prediction in light of mode detection and convection speed measurements for heated jets. *American Institute of Aeronautics and Astronautics Journal*, (1997), 315. Available from: `https://doi.org/10.2514%2F6.1997-1625`, `doi:10.2514/6.1997-1625`.

[52] Mendez, M., Raiola, M., Masullo, A., Discetti, S., Ianiro, A., Theunissen, R., and Buchlin, J.-M. Pod-based background removal for particle image velocimetry. *Experimental Thermal and Fluid Science*, **80** (2017), 181 . Available from: `http://www.sciencedirect.com/science/article/pii/S0894177716302266`, `doi:10.1016/j.expthermflusci.2016.08.021`.

[53] Miller, S. and Morris, P. The Prediction of Broadband Shock-Associated Noise from Dualstream and Rectangular Jets Using RANS CFD. In *Aeroacoustics Conferences.* American Institute of Aeronautics and Astronautics (2010). Available from: `https://doi.org/10.2514%2F6.2010-3730`, `doi:10.2514/6.2010-3730`.

[54] Miller, S. A. E. and Morris, P. J. The prediction of broadband shock associated noise from dualstream and rectangular jets using rans-cfd. *American Institute of Aeronautics and Astronautics Journal*, (2010), 1. Available from: `https://doi.org/10.2514%2F6.2010-3730`, `doi:10.2514/6.2010-3730`.

[55] Nichols, J., Ham, F., Lele, S., and Moin, P. Prediction of supersonic jet noise from complex nozzles. *Center for Turbulence Research Annual Research Briefs*, (2011), 3.

[56] Norum, T. Screech suppression in supersonic jets. *AIAA Journal*, **21** (1983), 235. Available from: `https://doi.org/10.2514%2F3.8059`, `doi:10.2514/3.8059`.

[57] Norum, T. D. and Seiner, J. M. Broadband shock noise from supersonic jets. *AIAA Journal*, **20** (1982), 68. Available from: `https://doi.org/10.2514%2F3.51048`, `doi:10.2514/3.51048`.

[58] Norum, T. D. and Seiner, J. M. *Measurements of Mean Static Pressure and Far Field Acoustics of Shock-Containing Supersonic Jets.* NASA TM84521d (1982).

[59] Oseen, C. W. *Neuere Methoden und Ergebnisse in der Hydrodynamik*. Akademische Verlagsgesellschaft m. b. h., Leipzig (1927).

[60] Pack, D. A note on prandtls formula for the wave length of a supersonic gas jet. *Quarterly Journal of Mechanics and Applied Mathematics*, **3** (1950), 173. Available from: `https://doi.org/10.1093%2Fqjmam%2F3.2.173`, `doi:10.1093/qjmam/3.2.173`.

[61] Panda, J. An experimental investigation of screech noise generation. *Journal of Fluid Mechanics*, **378** (1999), 71. Available from: `https://www.cambridge.org/core/article/an-experimental-investigation-of-screech-noise-generation/20019CF223DAFF7C1051B3706E5BCAFD`, `doi:10.1017/s0022112098003383`.

[62] Panda, J., Raman, G., and Zaman, K. B. M. Q. Underexpanded screeching jets from circular, rectangular and elliptic nozzles. *American Institute of Aeronautics and Astronautics Paper*, **97-1623** (1997). Available from: `https://doi.org/10.2514%2F6.1997-1623`, `doi:10.2514/6.1997-1623`.

[63] Panda, J. and Seaholtz, R. G. Measurement of shock structure and shock -vortex interaction in underexpande jets using rayleigh scattering. *Physics of Fluids*, **11** (1999), 3761.

[64] Pao, S. and Seiner, J. Shock associated noise in supersonic jets. *AIAA Journal*, **21** (1983), 687. Available from: `https://doi.org/10.2514%2F3.8134`, `doi:10.2514/3.8134`.

[65] Pérez Arroyo, C. Private communication (2016).

[66] Pérez Arroyo, C. *Large eddy simulations of a dual stream jet with shock-cells and noise emission analysis*. Ph.D. thesis, lInstitut National Polytechnique de Toulouse (INP Toulouse) (2016 (Unpublished)).

[67] Pérez Arroyo, C., Daviller, G., Boussuge, J.-F., and Arieau, C. Large eddy simulation of shock-cell noise from a dual stream jet. In *AIAA/CEAS Conference. Lyon.* American Institute of Aeronautics and Astronautics (AIAA) (2016). Available from: `https://doi.org/10.2514%2F6.2016-2798`, `doi:10.2514/6.2016-2798`.

[68] Pérez Arroyo, C., Daviller, G., Puigt, G., and Ariau, C. Shock-cell noise of supersonic underexpanded jets. In *Workshop Direct and large-Eddy Simulation 10 (DLES 10), Limassol (Cyprus)* (2015).

[69] PIVTEC GmbH. *Aerosol Generator PivPart45-M series User Manual.* Stauffenbergring 21, D-37075 Gottingen - Germany (2013).

[70] Powell, A. On the mechanism of choked jet noise. *Proceedings of the Physical Society. Section B*, **66** (1953), 1039. Available from: `https://doi.org/10.1088%2F0370-1301%2F66%2F12%2F306`, `doi:10.1088/0370-1301/66/12/306`.

[71] Prandtl, L. *Uber die stationaren wellem in einem gasstrahl.* Physikalische Zeitschrift (1904). Available from: `https://doi.org/10.1007%2F978-3-662-11836-8_74`, `doi:10.1007/978-3-662-11836-8_74`.

[72] Raman, G. Advances in understading supersonic screech: Revire and perspective. *Progress in Aerospace Sciences*, **34** (1998), 45.

[73] Raman, G., Panda, J., and Zaman, K. B. M. Q. Feedback and receptivity during jet screech: influence of an upstream reflector. *American Institute of Aeronautics and Astronautics Paper*, **97-0144** (1997). Available from: `https://doi.org/10.2514%2F6.1997-144`, `doi:10.2514/6.1997-144`.

[74] Raman, G. and Rice, E. Instability modes excited by natural screech tones in a supersonic rectangular jets. *Physics of Fluids*, **6** (1994), 3999. Available from: `https://doi.org/10.2514%2F6.1993-4321`, `doi:10.2514/6.1993-4321`.

[75] Rao, T. V. R., Kumar, R. R., and Kurian, J. Near field shock structure of dual co-axial jets. *Shock Waves*, **6, no. 6** (1996), 361. Available from: `https://doi.org/10.1007%2Fbf02511326`, `doi:10.1007/s001930050054`.

[76] Regert, T., Grossir, G., Paris, S., and Blay Esteban, L. Schlieren visualization for high-speed flows based on laser-induced fluorescence. *Experiments in Fluids*, **55** (2014), 1. Available from: `http://dx.doi.org/10.1007/s00348-014-1668-x`, `doi:10.1007/s00348-014-1668-x`.

[77] Rubio Carpio, A. *Experimental Investigation on Shock-Cell Noise.* Research master report, von Karman Institute for Fluid Dynamics (2016).

[78] Savarese, A. *Experimental study and modelling of shock cell noise.* Ph.D. thesis, Ecole Nationale Superieure d'Ingegneurs de Poitiers (2014).

[79] Savarese, A., Jordan, P., Girard, S., Collin, E., Porta, M., and Gervais, Y. Experimental study of shock-cell noise in underexpanded supersonic jets. In *Aeroacoustics Conferences*, pp. –. American Institute of Aeronautics and Astronautics (2013). Available from: `https://doi.org/10.2514%2F6.2013-2080`, `doi:10.2514/6.2013-2080`.

[80] Scarano, F. and Riethmuller, L. M. Iterative multigrid approach in piv image processing with discrete window offset. *Experiments in Fluids*, **26** (1999), 513. Available from: `http://dx.doi.org/10.1007/s003480050318`, `doi:10.1007/s003480050318`.

[81] Schram, C. *Data acquisition and processing course notes.* Von Karman Institute for Fluid Dynamics (2016).

[82] Seiner, J. Advances in high speed jet aeroacoustics. *AIAA Paper*, **84-2275** (1984), 1. Available from: `https://doi.org/10.2514%2F6.1984-2275`, `doi:10.2514/6.1984-2275`.

[83] Seiner, J. M. and Yu, J. C. Acoustic near field properties associated with broadband shock noise. *American Institute of Aeronautics and Astronautics*, **22** (1984), 1207. Available from: `https://doi.org/10.2514%2F3.8762`, `doi:10.2514/3.8762`.

[84] Shur, M. L., Spalart, P. R., and Strelets, M. K. Noise prediction for underexpanded jets in static and flight conditions. *AIAA Journal*, **49** (2011), 2000. Available from: `http://dx.doi.org/10.2514/1.J050776`, `doi:10.2514/1.j050776`.

[85] Stanislas, M., Okamoto, K., Kahler, C. J., Westerweel, J., and Scarano, F. Main results of the third international piv challenge. *Experiments in Fluids*, **45** (2008), 27. Available from: `https://doi.org/10.1007%2Fs00348-008-0462-z`, `doi:10.1007/s00348-008-0462-z`.

[86] Suzuki, T. {L1} generalized inverse beam-forming algorithm resolving coherent/incoherent, distributed and multipole sources. *Journal of Sound and Vibration*, **330** (2011), 5835 . Available from: `http://www.sciencedirect.com/science/article/pii/S0022460X11004068`, `doi:10.1016/j.jsv.2011.05.021`.

[87] Suzuki, T. and Lele, S. K. Shock leakage through an unsteady vortex-laden mixing layer: application to jet screech. *Journal of Fluid Mechanics*, **490** (2003), 139. Available from: `https://doi.org/10.1017%2Fs0022112003005214`, `doi:10.1017/s0022112003005214`.

[88] Swagelok. Pressure-reducing regulator flow curves. Technical bulletin (2016).

[89] Tam, C. Proposed relationship between shock associated noise and screech tones. *Journal of Sound and Vibration*, **110** (1986), 309.

[90] Tam, C. Broadband shock-associated noise of moderately imperfectly expanded supersonic jets. *Journal of Sound and Vibration*, **140** (1990), 55 . Available from: `https://doi.org/10.1016%2F0022-460x%2890%2990906-g`, `doi:10.1016/0022-460x(90)90906-g`.

[91] Tam, C. Supersonic jet noise. *Annu. Rev. Fluid Mech.*, **27** (1995), 17. Available from: `https://doi.org/10.1146%2Fannurev.fl.27.010195.000313`, `doi:10.1146/annurev.fluid.27.1.17`.

[92] Tam, C., Pastouchenko, N., and Viswanathan, K. Broadband Shock-Cell Noise from Dual Stream Jets. In *Aeroacoustics Conferences*. American Institute of Aeronautics and Astronautics (2008). Available from: `https://doi.org/10.2514%2F6.2008-2833`, `doi:10.2514/6.2008-2833`.

[93] Tam, C., Seiner, J., and Yu, J. Proposed relationship between broadband shock associated noise and screech tones. *Journal of Sound and Vibration*, **110** (1986), 309 . Available from: `https://doi.org/10.1016%2Fs0022-460x%2886%2980212-7`, `doi:10.1016/s0022-460x(86)80212-7`.

[94] Tam, C. and Tanna, H. Shock associated noise of supersonic jets from convergent-divergent nozzles. *Journal of Sound and Vibration*, **81** (1982), 337 . Available from: `https://doi.org/10.1016%2F0022-460x%2882%2990244-9`, `doi:10.1016/0022-460x(82)90244-9`.

[95] Tam, C. and Tanna, H. Shock associated noise of supersonic jets from convergent-divergent nozzles. *Journal of Sound and Vibration*, **81** (1982), 337. Available from: `https://doi.org/10.1016%2F0022-460x%2882%2990244-9`, `doi:10.1016/0022-460x(82)90244-9`.

[96] Tam, C. and Tanna, H. Shock associated noise of inverted-profile coannular jets, part ii: Condition for minimum noise. *Journal of Sound and Vibration*, **98** (1985), 115 . Available from: `http://www.sciencedirect.com/science/article/pii/0022460X85904067`, `doi:10.1016/0022-460x(85)90406-7`.

[97] Tam, C. and Tanna, H. Shock associated noise of inverted-profile coannular jets, part iii: Shock structure and noise characteristics. *Journal of Sound and Vibration*, **98** (1985), 127 . Available from: `http://www.sciencedirect.com/science/article/pii/0022460X85904079`, `doi:10.1016/0022-460x(85)90407-9`.

[98] Tam, C. K. W. and Burton, D. E. Sound generated by instability waves of supersonic flows. part 1. two-dimensional mixing layers,. *J. Fluid Mech.*, **138** (1984), 249271. Available from: `https://doi.org/10.1017%2Fs0022112084000112`, `doi:10.1017/s0022112084000112`.

[99] Tam, C. K. W. and Burton, D. E. Sound generated by instability waves of supersonic flows. part 2. axisymmetric jets. *J. Fluid*

Mech., **138** (1984), 273. Available from: `https://doi.org/10.1017%2Fs0022112084000124`, `doi:10.1017/s0022112084000124`.

[100] Tam, C. K. W., Parrish, S. A., and Viswanathan, K. Harmonics of jet screech tones. *AIAA Journal*, **52** (2014), 2471. Available from: `http://dx.doi.org/10.2514/1.J052850`, `doi:10.2514/1.j052850`.

[101] Tan, D., Soria, J., Honnery, D., and Edgington-Mitchell, D. A novel method for decoupling the velocity fluctuations in screeching axisymmetric jets. *22nd AIAA/CEAS Aeroacoustics Conference*, (2016).

[102] Tanna, H. An experimental study of jet noise part ii: Shock associated noise. *Journal of Sound and Vibration*, **50** (1977), 429 . Available from: `https://doi.org/10.1016%2F0022-460x%2877%2990494-1`, `doi:10.1016/0022-460x(77)90494-1`.

[103] Tanna, H., Brown, W., and Tam, C. Shock associated noise of inverted-profile coannular jets, part i: Experiments. *Journal of Sound and Vibration*, **98** (1985), 95 . Available from: `http://www.sciencedirect.com/science/article/pii/0022460X85904055`, `doi:http://dx.doi.org/10.1016/0022-460X(85)90405-5`.

[104] Tanna, H. K., Tam, C. K. W., and Brown, W. H. Shock associated noise reduction from inverted-velocity-profile coannular jets. *National Aeronautics And Space Administration, Scientific And Technical Information Branch*, (1981). Available from: `https://doi.org/10.2514%2F6.1981-1972`, `doi:10.2514/6.1981-1972`.

[105] Tanna, H. K., Tester, B. J., and Lau, J. C. The noise and flow characteristics of invertedprofile coannular jets. Tech. rep., Ctr. Rep. 158995, NASA, (1979).

[106] Tchen and Chan-Mou. *Mean value and correlation problems connected with the motion of small particles suspended in a turbulent fluid.* Nijhoff, The Hague (1947). Available from: `https://doi.org/10.1007%2F978-94-017-6101-7`, `doi:10.1007/978-94-017-6101-7`.

[107] Timmoneri, A. *Aeroacoustic generalized inverse beamforming applied to a rod-airfoil configuration.* Short training program report, von Karman Institute for Fluid Dynamics (2014).

[108] Toolbox, T. E. The definition of stp - standard temperature and pressure and ntp - normal temperature and pressure (2016). Available from: `http://www.engineeringtoolbox.com/stp-standard-ntp-normal-air-d_772.html`.

[109] Toth, P. *Beamforming development for open-jet wind tunnel configuration.* Research master report, von Karman Institute for Fluid Mechanics (2010).

[110] Veltin, J. and McLaughlin, D. Noise mechanism investigation in shock containing screeching jets using optical deflectometry. *14th AIAA/CEAS Aeroacoustics Conference*, (2008), 12,53. Available from: `https://doi.org/10.2514%2F6.2008-2889`, `doi:10.2514/6.2008-2889`.

[111] Viswanathan, K. Parametric study of noise from dual-stream nozzles. *J. Fluid Mech*, **521** (2004), 36. Available from: `https://doi.org/10.1017%2Fs0022112004000813`, `doi:10.1017/s0022112004000813`.

[112] Viswanathan, K. True farfield for dual-stream jet noise measurements. *AIAA J.*, **49** (2011), 443. Available from: `https://doi.org/10.2514%2F1.j050771`, `doi:10.2514/1.j050771`.

[113] Viswanathan, K., Alkislar, M. B., and Czech, M. J. Characteristics of the shock noise component of jet noise. *AIAA Journal*, **48** (2010), 25. Available from: `https://doi.org/10.2514%2F1.38521`, `doi:10.2514/1.38521`.

[114] Viswanathan, K., Czech, M. J., and Lee, I. C. Towards prediction of dual-stream jet noise: Database generation. *AIAA J.*, **49** (2011), 2695. Available from: `https://doi.org/10.2514%2F1.j051124`, `doi:10.2514/1.j051124`.

[115] Westley, R. and J.H-Woolley. The near field sound pressures of a choked jet during a screech cycle aircraft engine noise and sonic boom. *AGARD*, **42** (1969), 1.

[116] Westley, R. and Woolley, J. H. Flow and sound visualization of an axisymmetric choked jet (10 in schlieren). (16 mm, silent film, running time 8.5 min). Tech. rep., National Research Council of Canada, National Aeronautical Establishment YC. NRC, ME. Film No. 13, June (1968).

[117] Westley, R. and Woolley, J. H. An investigation of the near noise fields of a choked axisymmetric air jet. Tech. rep., National Research Council of Canada, National Aeronautical Establishment, Aeronautical Report R-506, (1968).

[118] Westley, R. and Woolley, J. H. An investigation of the near noise fields of a choked axisymmetric jet. In *Aerodynamic Noise (H. B. RIBNER, editor). Toronto: University of Toronto Press. Proceedings of AFOSR-V.T.A.S. Symposium held at Toronto, 20-21 May* (1968).

[119] Westley, R. and Woolley, J. H. The nearfield sound pressures of a choked jet when oscillating in the spinning mode. *American Institute of Aeronautics and Astronautics Paper*, **75-479.** (1975). Available from: `https://doi.org/10.2514%2F6.1975-479`, `doi:10.2514/6.1975-479`.

[120] Wikipedia, t. f. e. Pressure regulator. (2016). Available from: `https://en.wikipedia.org/wiki/Pressure_regulator`.

[121] Zaman, K., Bridges, J., and Huff, D. Evolution from tabs to chevron technology: A review. *International Journal of Aeroacoustics*, **10** (2011), 685.

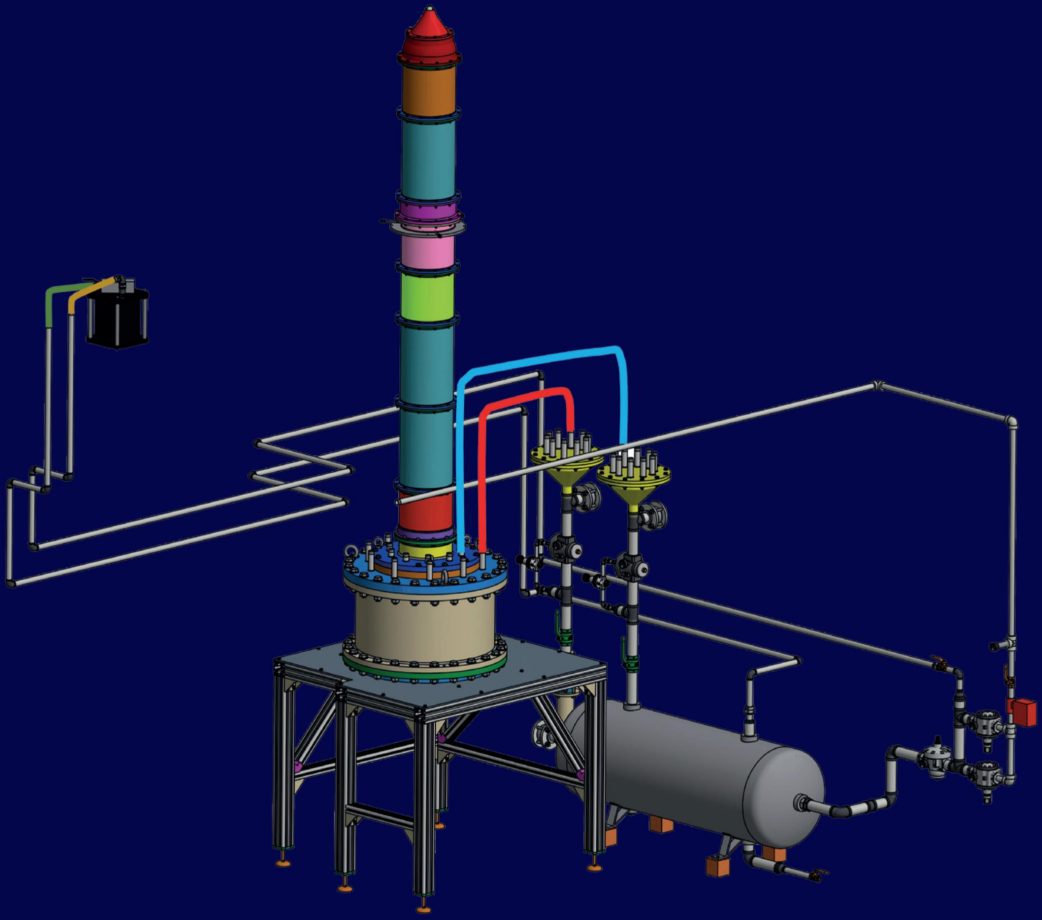

ISBN 978-2-87516-113-0

VON KARMAN INSTITUTE FOR FLUID DYNAMICS

WATERLOOSESTEENWEG, 72
B-1640 SINT-GENESIUS-RODE
BELGIUM

PHONE: +32 (02) 359 96 11
FAX: +32 (02) 359 96 00
E-MAIL: BIBLIO@VKI.AC.BE
WEBSITE: HTTPS://WWW.VKI.AC.BE